Doctoral theses at NTNU, 2023:278

Robin André Rørstadbotnen

Acoustic and Elastic wave Exploration and Monitoring using Dense Passive Arrays

Doctoral thesis

NTNU
Norwegian University of Science and Technology
Thesis for the Degree of
Philosophiae Doctor
Faculty of Information Technology and Electrical Engineering
Department of Electronic Systems

NTNU
Norwegian University of
Science and Technology

Robin André Rørstadbotnen

Acoustic and Elastic wave Exploration and Monitoring using Dense Passive Arrays

Thesis for the Degree of Philosophiae Doctor

Trondheim, September 2023

Norwegian University of Science and Technology
Faculty of Information Technology and Electrical Engineering
Department of Electronic Systems

NTNU

Norwegian University of
Science and Technology

NTNU
Norwegian University of Science and Technology

Thesis for the Degree of Philosophiae Doctor

Faculty of Information Technology and Electrical Engineering
Department of Electronic Systems

ISBN 978-82-326-7256-1 (printed ver.)
ISBN 978-82-326-7255-4 (electronic ver.)
ISSN 1503-8181 (printed ver.)
ISSN 2703-8084 (online ver.)

Doctoral theses at NTNU, 2023:278

Printed by NTNU Grafisk senter

Abstract

Passive recording systems have become increasingly popular and important in various marine acoustic and geophysics branches. Data from these systems provide valuable information and can be used in various applications, e.g., to characterize whales, earthquakes, or, more generally, the subsurface. These applications contain different frequency ranges, and various recording systems have been developed to capture them all. For example, strainmeters are sensitive to the lowest frequencies, like those generated by Earth's tide, while hydrophones, geophones and broadband seismometers can pick up higher frequencies, such as those produced by whales and small-magnitude earthquakes. Hence, the choice of receiving system depends on the application. These systems contain point-sensors, therefore making it challenging to sufficiently instrument the whole world. This is mainly due to the cost of installation and maintenance, hence leaving the world sparsely instrumented. In recent years, new technologies have been developed to increase instrumentation. One example is Permanent Reservoir Monitoring (PRM) systems, which have been installed near oil and gas fields to improve recovery. Such a system typically contains 1000s of 4-component sensors per PRM system and is placed near interesting features in the subsurface. Another example is Distributed Acoustic Sensing (DAS), which has, in recent years, emerged as a new technology to help increase the density of sensors worldwide. The receiver unit, the DAS interrogator, is connected to an optical fiber within a fiber telecommunication cable. This can re-purpose the fiber to a distributed sensor, sensing acoustic signal every meter for up to 150 km, thus creating a far-reaching, easily accessible receiver unit.

This thesis consists of several manuscripts investigating how dense passive receiver arrays can extract information from the water column through whale songs and the subsurface through different seismic waves. Most of the work has focused on DAS data from three datasets. The first DAS dataset was acquired in 2020 in Svalbard by re-purposing one of two telecommunication cables connecting Longyearbyen and Ny-Ålesund. The data were used to study the signals from a local earthquake. Standard preprocessing techniques were used to enhance the on-set of P- and S-waves, which were further used to locate the event. The obtained epicenter location was compared to those found using conventional receiver systems. The second DAS dataset was acquired in 2022 in Svalbard by re-purposing both telecommunication cables connecting Longyearbyen and Ny-Ålesund. We used data recorded on the cables to track up to eight whales for five hours, using two different localization methods. Additionally, seismic shots from a single air gun were used as ground truth information to assess the accuracy of the tracking methods. The third DAS dataset was acquired using a dedicated fiber in Rissa, Norway, trenched roughly 40 cm into a known quick clay area. This data were used to monitor the quick clay as a new road was built on top of the clay by investigating changes in the shear-wave velocity depth profile. Inversion of the dispersion curves of Rayleigh waves was used to estimate the shear-wave velocity profiles. Moreover, the Rayleigh waves were generated from sledge-

hammer shots and the ambient background noise. The final dataset used in this thesis was recorded on a PRM system South of the Oseberg C platform in the Norwegian North Sea at a water depth of 107 m. The data were used to estimate the average quality factor of a sedimentary package under the platform by applying a spectral ratio of earthquake signals recorded on a station pair, one station placed on sediments near the Oseberg C platform and one on bedrock in Bergen, Norway. Three different earthquakes were analyzed.

By studying the local earthquakes in the Svalbard 2020 dataset, we showed how a simple beamforming procedure could find the direction of the earthquake, the apparent velocity and help to increase the onset of P- and S-waves. In addition, we could estimate the epicenter location of a local earthquake within $\simeq$17 km of the estimates from conventional receiver systems.

Using the two fiber cables in Svalbard, we could see when the various whales vocalized whilst accurately locating them. A dedicated single air gun fired at known positions close to the fibers allowed us to estimate the average localization error to be $\simeq$100 m. These capabilities demonstrate the potential for near-real-time whale tracking using DAS that could be applied anywhere in the world where whales and fiber-optic cables are present.

Using the Rayleigh waves recorded in the quick clay DAS data, we could estimate shear-wave velocity depth profiles over a seven-month acquisition period. The obtained dispersion curves, and shear-wave velocity profiles, showed small time-lapse variation during the acquisition period, suggesting that the construction work did not alter the quick clay's property. Nevertheless, the obtained results capture the non-repeatability effects within the acquisition period and provide reference curves for the study at undisturbed conditions.

From the Oseberg PRM data, we found average Q_p and Q_s values for the sedimentary sequence underneath the PRM system. The Q_p values were found to be more scattered and hence more uncertain than the Q_s values due to the P-wave being closer to the background noise level. The quality factors for one of the studied earthquakes were found to be 92 ± 18 for the P-wave and 84 ± 13 for the S-wave, suggesting more attenuation of S-waves than P-waves in this sedimentary layer.

Preface

This thesis is submitted in partial fulfillment of the requirements for the degree of Philosophiae Doctor at the Norwegian University of Science and Technology (NTNU).

This doctoral work has been performed at the Department of Electronic Systems, NTNU, Trondheim with Professor Hefeng Dong as main-supervisor and Professor Martin Landrø as co-supervisor.

The research was funded by Geophysics and Applied Mathematics in Exploration and Safe production (GAMES) project supported by the Norwegian Research Council and petroleum companies.

Acknowledgments

Firstly, I want to thank my supervisor Professor Hefeng Dong and co-supervisor, Professor Marin Landrø, for the fruitful discussions and guidance throughout my four-year Ph.D. There were always plenty of interesting and exciting ideas to pursue! I also want to thank Martin for giving me the possibility to go on various field trips, giving me valuable experience.

A special thanks to my partner Tora for her continuous love and support during these four years. I also want to thank you for all the discussions on various geophysical topics, even though I didn't always want/ask to be part of them.

I am grateful to all the professors and staff at NTNU for many great discussions and help. I am especially grateful to those who helped me with the analysis and writing the different papers, which greatly improved the content and presentation of the work. Special thanks to Léa, Jo, Kenneth, John, Jan, and Ståle.

Thanks to the partners and researchers of GAMES and CGF, who made my work possible. A special thanks to Frode for the good times during our field trip to Longyearbyen and Ny-Ålesund in August 2022 and Joacim for all the help with the different interrogators I have been fortunate to deploy and use.

During this period, I have met many new people I am glad to call friends today. You have all made the period so fun. A special thanks to three groups of people: the 'Acoustic gang' Xiaoyu, Andreas, Léa, and Jun. The 'CGF gang' Nick, Léa, Kristoffer, Kevin, Umed, Kit, Riccardo, Helene, Lukas, Franz, Bhargav, Shun, Kristina, Ole Edvard, Maren, Tor, Tobias, Claudie, Isabella, Andrea, Mohammed, Mina (and so on). And finally, 'the training gang' Nick, Kristoffer, and Umed.

Special thanks also to Nick and Kristoffer for many good laughs in the office and outside the office! Thanks Nick for proof-reading my articles.

Thanks to Todd and Charlotte for taking the time to read through the introduction and the concluding remark. I apologize for hurting your brain and exposing you to my Norwegian-influenced English writing!

Last but not least, I would like to thank my parent, Gunn, and Norodd, for creating me and raising me to be who I am. I would also like to thank my siblings, Steffen, Fredrick, and Preben, for many memorable moments (good and bad) throughout my life, which also formed me into who I am today (also good and bad). Thank you all for the support through this work and generally through my life so far.

Tusen takk!

Contents

Chapter 1

Introduction

1.1 Motivation

Passive recording of acoustic and seismic data provides valuable information on various processes. The main goal of the work performed during this Ph.D. project has been to examine the potential of state-of-the-art dense passive receiver systems, focusing on fiber-optic sensing and conventional 4-component systems for both bioacoustic and geophysical applications. Dense receiver arrays give valuable information about the impinging wave field, which cannot be captured by individual sensors spread over large areas. By exploiting a large number of receivers in such arrays, more statistically significant estimates can be obtained, and local variations in the wave field caused by local structures in the subsurface can be observed. However, the instrumentation worldwide is generally sparse, and much important information is not recorded. This undersampling depends on geographical location, which can usually be attributed to how accessible and acoustically/seismically interesting a specific area is. The ocean is an example of an acoustically active domain, but undersampled due to accessibility issues. The undersampling issue is typically a question of cost, often in terms of the price of installation and maintenance, and how many sensors are needed to be installed/maintained. For example, in an inactive region, the sensor deployment is often not cost-efficient, as the effort of instrumenting the area is greater than the value of the information recorded, or it is simply too expensive to keep the sensors operational. For remote geographical areas, the cost rapidly increases. Even though there is valuable information to be recorded, keeping a sufficient number of receivers running for the needed time window might not be realistic. In recent years, new technologies have been developed to increase instrumentation worldwide, where Distributed Acoustic Sensing (DAS) is one of the latest examples. The DAS interrogator, holding the source laser and the receiver unit, contains all the hardware and is placed at the termination point of the fiber-optic cable, generally in an easily accessible area, such as in a room where the fiber cable terminates. The convenient placement of the interrogator unit

will decrease the cost associated with installation and maintenance whilst generating data quickly available for post-processing and analysis. The cost will rapidly increase if the fiber cable installation is part of the experiment, especially when it needs to be trenched into the sea floor, and the interrogator unit is still relatively expensive. However, more than 1.3 million km of fiber-optic cable is already in the oceans alone, which could be re-purposed as sensor arrays. The longest portion of a fiber cable an interrogator unit manages to cover is, to date, between 120 and 150 km. Having dense channel sampling for such distances will considerably contribute to mitigating the undersampling problem, which is especially important for the ocean, where the cost of installing and maintaining receiver systems is greater than onland.

This thesis is a paper collection of several independent papers. It starts by introducing various theories and concepts which provide valuable background information to the papers. Then it continues describing the motivation of the work, and finally, a summary of the individual paper. After the introduction, the individual papers are given in separate chapters. In the final chapter of the thesis, concluding remarks are given together with a description of other work carried out during the Ph.D. and a future outlook.

1.2 Sensing systems

To map the sounds produced in the air around us, underneath our feet and above our heads, we need various recording systems that capture the signals and convert them into a format that can be interpreted and studied. The most obvious sound sensor is the human ear. The ear is an efficient transducer converting sound pressures into neural-electrical signals and is capable of discriminating sounds between 20 Hz and 20 kHz. Other receiver systems complement the frequency range of the human ear and can record signals from all environments with a great dynamic and frequency range, capturing both infra- and ultra-sounds (below 20 Hz and above 20 kHz, respectively). The ocean, the solid earth, and the atmosphere are examples of sound environments.

In geophysical applications, we are interested in ground motion, or particle displacement, which is normally recorded on the lower portion of the frequency spectrum, typically from 10^{-5} (Earth tides) to 1000 Hz (body waves from earthquakes with magnitudes less than 2). The amplitude range over these frequencies is vast, with a highly frequency-dependent background noise level. This background noise limits the particle displacement we can measure, and the lowest is typically 1 nm and the longest 1 m (giving a dynamic range of 10^9; Havskov and Alguacil (2010, Chapter 1)). Given the vast frequency range and the large dynamic range, it is hard to construct receivers that measure all ground motions or even portions of them.

Another fundamental problem is that the particle displacement cannot be measured directly. The most common way of obtaining the displacement is to record the particle

acceleration instead and integrate it twice

$$\ddot{u} \propto f^2 u, \tag{1.1}$$

where u denotes the particle displacement, the dots the differentiation with respect to time, and f the frequency. We can identify another issue from this equation: low-frequency displacement will produce low acceleration. Therefore, a seismic receiver needs an extensive dynamic range to capture all signals within the different frequency bands. In principle, it should be able to record the small accelerations at low frequencies and not saturate when recording the large accelerations at high frequencies. However, building a stable sensor that can capture all the wanted frequencies is difficult, and various recording systems covering different portions of the frequency spectrum are therefore available (Havskov and Alguacil 2010).

The most popular receivers for geophysical exploration are the hydrophone (recording acoustic pressure) and the geophone (recording particle velocity or acceleration), from which strong motion signals at frequencies above the 2 to 14 Hz band can be recorded (depending on the natural frequency of the receiver). The broadband seismometer is normally used for earthquake applications, recording small ground motion for frequencies between 3 mHz and 100 Hz. To record the lowest frequencies, strainmeters are used. These sensors can measure from a few Hz down to periods of years. More recently, Distributed Acoustic Sensing (DAS) has emerged as a technology capable of capturing a wide range of frequencies from μHz to kHz (Waagaard et al. 2021, Williams et al. 2022).

These geophysical recording systems will be introduced in the following sections.

1.2.1 Conventional recording systems

Hydrophones

Hydrophones respond to variations in acoustic pressure by converting a small length change of a particular material into an electrical signal proportional to the amplitude of the impinging pressure wave. There are different types of hydrophones on the market constructed for different applications, and the most common are piezoelectric transducers/hydrophones and fiber-optic hydrophones. When the hydrophones are placed on the sea floor over a long period, the conventional piezoelectric hydrophones might become unreliable due to possible electrical leakage, corrosion, or general sensor degradation. To overcome these issues, new hydrophones employ fiber-optic systems with no electrical components or electrical power requirements in the water. The required electronics are in the interrogator system onshore. These should be more reliable on the sea floor (Langhammer et al. 2010, Landrø and Amundsen 2018).

A piezoelectric transducer can be used as both source and receiver. The latter is primarily used in geophysical applications, mainly within the ocean domain and based on Micro-Electro-Mechanical-Systems (MEMS). MEMS technology uses the techniques of micro-

fabrication to make micro-scale transducers with the same or better performance than the traditional transducers (Amiri et al. 2020). Such elements are small; one example is the HTI-97-DA hydrophones (by High Tech (2023)) which have a cylindrical shape with a length of 7.32 cm and a diameter of 2.54 cm. A piezoelectric transducer records the pressure wave in the water through the deformation the wave induces on the piezoelectric material. This mechanical deformation will create an electrical voltage that can be recorded and saved. Since the recorded electrical voltage is proportional to the amplitude of the pressure wave, it can be readily converted back when processing the recorded voltage data. Many piezoelectric materials exist and come in different geometrical shapes, like rods, cylindrical tubes, and many others. Common materials include synthetic ceramics, such as lead zirconate titanate ($PbZrTi_3$ or simply PZT; Hovem (2012, Chapter 8.2)).

Piezoelectric hydrophones are used in a wide range of applications, including, but not limited to, bioacoustic monitoring, target detection, underwater acoustic communication, and subsurface exploration. For example, Hendricks et al. (2019) used four icListen HF hydrophones to track killer whales, fin whales, and humpback whales in the Squally Channel on the West coast of Canada. Hydrophones are used in several receiver array systems for subsurface exploration and monitoring. They are used in hydrophone streamers in marine geophysical acquisitions and as one of the 4-components in Life-of-Field Systems (LoFS), also known as Permanent Reservoir Monitoring (PRM) systems.

In recent years, the fiber-optic hydrophone has become increasingly popular, especially for applications where hydrophones must be placed on the sea floor. Fiber-optic hydrophones make up a cylinder made of a plastic-like material with fiber coiled around the cylinder. The hydrophone responds to a change in the length of the cylinder as the pressure wave passes it. This length change can be measured using the shift in the reflection time (or phase delay) between two identical Bragg grating[1] on opposite sides of the fiber coil. Hence, the change in length in the fiber is proportional to the amplitude of the pressure wave (Landrø and Amundsen 2018).

Geophones

Geophones respond to vibrations in the ground, for example, those generated by earthquakes, a person walking, or a moving car. The geophone converts the ground motion, either particle velocity or acceleration, into voltage, which is recorded and saved. This is done by investigating how the voltage deviates from a known baseline level. The most basic geophone is a coil suspended around a permanent magnet. When the coil moves relative to the magnet, a voltage is created and can be saved to disk. The main limitations of this system are the excursion of the coil and the limited frequency response. The limited excursion is due to the coil only being able to move relative to the permanent magnet.

[1] A fiber Bragg grating is a fiber where the refractive index changes from high- to low-index along its length (about 1 cm). This modulation in refractive index acts as a light reflector that reflects certain wavelengths and transmits others. For more derails see Hartog (2017) or Landrø and Amundsen (2018).

In contrast, the limited frequency is related to the response of the sensor system rolling off under its natural frequency. Several improvements have been introduced to reduce these limiting factors; two examples are: (1) Barzilai et al. (1998) added a separate displacement measurement to improve the response for lower frequencies; (2) Brincker et al. (2005) used the geophone as is and applied an inverse filter to improve the low frequencies response. Various geophones are available with different natural frequencies. The standard sensors are built to have a natural frequency between 4 and 10 Hz (Hearn et al. 2019), with some as low as 2.5 Hz (Seis Tech 2023).

MEMS geophones, or accelerometers, are other types of ground motion recording systems. The main difference to the conventional geophone is that this system is smaller and responds primarily to particle acceleration. The MEMS technology typically converts the ground motion to an electrical response through an active feedback circuit to maintain the position of a small piece of material (e.g., silicon). This electrical response is proportional to the ground particle acceleration.

Fiber-optic accelerometers measure the particle acceleration of the ground, similar to MEMS accelerometers. In the same way as the fiber-optic hydrophones, the accelerometers do not have any electronics present or any electrical power requirements. The main difference is that the accelerometer is a directional system that aims to measure acceleration in three orthogonal directions, normally East-West, North-South, and vertical components. To measure the directional acceleration, the fiber-optic system uses two half-spheres at each side of a rod. This design ensures that only seismic waves impinging the system parallel to the rod are measured, whereas it is in-sensitive to waves hitting perpendicular to the rod. When hitting the wave parallel to the rod, the coil length will change, and the seismic signal can be measured. The sensor can be tuned to a flat frequency response over a wide frequency range from 1 to 250 Hz (Langhammer et al. 2010, Landrø and Amundsen 2018).

4-component Permanent Reservoir Monitoring (PRM) systems

It is increasingly normal to instrument the offshore oil and gas fields with 4-component (4C) sensors containing one hydrophone and three orthogonal geophones. These usually are laid out in massive arrays and called Permanent Reservoir Monitoring (PRM) systems. The systems aim to improve oil and gas recovery by optimizing the placement of production and water injection wells, increasing the yearly saving by reducing the drilling cost of new wells, and providing better sensor position repeatability for time-lapse monitoring, among other reasons.

The first full-field PRM system, containing 2400 4C component receivers, was introduced over the Valhall field in 2003, where 120 km of seismic cables, covering 45 km^2, were trenched roughly 1 m into the seafloor. One receiver unit contains a Deepener piezoelectric pressure sensor and three orthogonal OMNI-X-LT geophones (Van Gestel et al. 2008, Landrø and Amundsen 2018).

In the Snorre 'focused seismic monitoring project,' a sensor system entirely based on fiber-optic sensor technology was deployed 3 km North of the Snorre A platform in 2003 (Thompson and Andersen 2008). The system consisted of two multicomponent fiber-optic seismic cables, each containing 100 4C seismic sensors, three orthogonal fiber-optic accelerometers, and a fiber-optic hydrophone. The cables were placed 'back-to-back' with an inter-station spacing of 50 m, giving a total array length of roughly 10 km. The interrogator unit for the system was placed on the platform. A related study before deploying the fiber-optic systems showed it to have a similar performance to the conventional systems (Thompson et al. 2006). Later in December 2012, Statoil deployed a larger PRM system on the Snorre license. This system covered an area of 195 km^2, with 10000 seismic receivers (Landrø and Amundsen 2018).

Another example is the PRM system installed in 2013 South of the Oseberg C platform. This system contains 172 4C receivers connected by seismic cables laid out in a 'V' shape (Bussat et al. 2016). This system uses three orthogonal MEMS VectorSeis sensors and an HTI-97-DA High Tech Inc. hydrophone in one receiver node.

One of the newest 4C PRM systems is installed at the Johan Sverdrup oil and gas field. This field is monitored by permanent 4C fiber-optical cables trenched into the subsurface. A total of 380 km of fiber-optic seismic cables have been installed, holding over 6500 receiving stations and covering an area of more than 120 km^2 (Offshore-Energy 2019, Fayemendy et al. 2021).

Strainmeter

Strainmeters are on the other end of the frequency spectrum compared to hydrophones and geophones, measuring "ultra-low" frequencies (periods as long as years). The basic principle behind strainmeters is to measure the changes in the distance between two points using some solid materials like an iron pipe or a quartz rod. Focusing on these low frequencies, it captures signals originating from Earth's tides and gradual displacement build-up near plate boundaries and volcanoes.

One of the earliest strainmeters, made by Benioff (1959), was a 24 m long quartz rod attached to the ground at one end and extended through a capacitance transducer on the other end. Newer strainmeters, and hydraulic sensors, achieve a dynamic range of 130 dB and a strain sensitivity of 10^{-12}. Other examples are based on laser technology and measure normal horizontal strain over longer distances, such as faults (Stein and Wysession 2003). Araya et al. (2017) presented a new example of a laser strainmeter that measures the change in distance between two retroreflectors housed in two separate vacuum chambers placed 1500 m apart. They reported that the lowest background noise obtained was below 10^{-12} in the mHz scale.

Broadband seismometers

Modern broadband seismometers are usually based on the Force Balanced Accelerometer (FBA) principle (Havskov and Alguacil 2010). The FBA consists of a spring, a force coil around a mass, a displacement transducer with a capacitor, and a resistor. The final component, a feedback coil, can exert a force equal to and opposite to the inertia force generated by the particle acceleration. The displacement transducer sends a current to the force coil through a resistor in a negative feedback loop. The current produces a polarity opposite to the motion of the mass and hence tries to prevent movement from the mass (with respect to the frame). The current is proportional to the ground acceleration, and the voltage over the resistor directly measures acceleration. Havskov and Alguacil (2010) noted that the low-frequency limit of broadband receivers is 0.0025 Hz and that the dynamic range of FBA sensors is $10^6 - 10^8$. The typical high-frequency limit is 100 Hz.

1.2.2 Distributed Acoustic Sensing (DAS)

Distributed Acoustic Sensing (DAS) technology has emerged over the last two decades as a paradigm shift in remote sensing for many different applications. The DAS technology evolved in the oil and gas industry using dedicated vertical fibers in downhole operations (Mestayer et al. 2011). Later it was applied to horizontal fibers, and a range of examples was investigated; earthquake seismology (Lindsey et al. 2017), near-surface monitoring (Dou et al. 2017), passive acoustic monitoring of ships (Rivet et al. 2021), and whales (Landrø et al. 2022, Bouffaut et al. 2022). As mentioned in Section 1.1, one of the major limitations within conventional remote sensing is that only some geographical regions are sufficiently instrumented. This generates a statistical bias in the reporting of a wide range of acoustic and seismic signals. For the earthquake catalogs, the small-magnitude local earthquakes might go undetected, while vital information from bioacoustic acoustic signals might be missed in areas with few-to-no receivers. DAS is broadly considered part of the solution to this issue, as it can interrogate down to mHz and up to kHz, covering distances up to 150 km, with the spatial sample around one meter. The advantages of using fiber-optic cables as sensing elements are that they are cheap, flexible, and durable, with a lifetime somewhere between 25 and 40 years (most of the fiber installed 30 years ago was expected to last 25–30 years, and the majority are still in operation).

For many applications, receivers every meter for up to 150 km is more than enough to capture the wanted signals. However, other applications need a longer range. For instance, some of the undersampled areas are at such distances from where the interrogator units can be installed and cannot be reached with the current technology. When we want to monitor the integrity of fiber cables, the current interrogation range will not suffice as the cables are usually much longer than the 150 km range. It is worth noting that a high noise region is present after $\simeq$100 km, depending on fiber quality, connector quality and the interrogator unit used. However, the DAS technology is rapidly improving, and we

can hopefully interrogate longer fiber cables soon. Another issue is that laser repeaters are placed every 60-70 km, potentially stopping the laser signal and limiting the length coverage. It is worth noting that the distance to the first repeater depends on the system used, it might be as low as 50 km and as long as 100 km along some cables.

Rayleigh scattering

Rayleigh scattering is essential to the DAS measurement principles. It is the elastic distribution of light in all directions, caused by the refractive index being non-uniform on a distance scale which is much smaller than the wavelength of the light sent into the fiber. The portion of the light being scattered back towards the light source is referred to as the Rayleigh backscattering. The non-uniform distribution of refractive index occurs during fiberglass manufacturing, where thermodynamically driven density fluctuations, or impurities, in the glass, are created (Hartog 2017).

Measurement principle of the OptoDAS interrogator

Many DAS interrogator systems are available and based on different optical approaches and principles. DAS is also known by other names, such as Distributed Vibration Sensing, Coherent Optical Time-Domain Reflectometery, Coherent Optical Frequency-Domain Reflectometery, or phase-sensitive Optical Time Domain Reflectometry (Lindsey et al. 2020). In this section, we will focus our discussion on the measurement principle behind the OptoDAS interrogator, which is based on long-duration Linear Frequency Modulated (LFM) optical pulses and coherent detection combined with a low noise fiber laser (Waagaard et al. 2021).

Interrogation of an optical fiber is performed by sending LFM pulses into the cable and recording the backscattered signal from the whole fiber for consecutive pulses. The instrument can compute phase changes by comparing the backscatter response from one pulse to the next. Usually, light pulses are repeatedly sent with a free-space wavelength (λ_0[2]), in which the sampling period at the optical receiver is 1×10^{-8} s ($\Delta\tau$). This can be used to find the spatial sampling interval (SSI) through

$$\text{SSI} = \left(\frac{c}{2n_g}\right)\Delta\tau, \tag{1.2}$$

where c is the speed of light in vacuum, and n_g is the refractive index. These values are normally set to $c = 299792458$ m/s and $n_g = 1.47$ (for SMF-28 fibers), which gives a SSI ≈ 1.02 m (Taweesintananon et al. 2021). If the cable lies perfectly still, the backscatter response between two pulses is the same, and no linear phase change will be observed. In contrast, when an acoustic or elastic wave hits the fiber cable (or

[2]The free-space wavelength is normally set to 1550 nm as this wavelength gives the minimum total loss in the cable, corresponding to a $\simeq$0.18 dB loss per km. The total loss is a combination of scattering loss, infrared absorption, and UV-absorption (Hartog 2017).

is disturbed by some other source) at a specific position, it will slightly strain the fiber at this point. This will induce a change to the position of inherent impurities, which can be detected as a linear change in the phase response between the two consecutively recorded backscattered signals. The interrogator extracts this rate of phase change, or the time-differentiated phase ($\dot{\phi}_x$), for every spatial sampling location x along the cable. This process is schematically depicted in Figure 1.1.

The time-differentiation process is done for the entire fiber length, where local impurity position changes are measured within different scattering regions, resulting in strain measurements as a function of time and fiber position. In the OptoDAS system, the distance between the center points of two adjacent scattering regions is defined as the spatial sample separation, dx, as well as constituting the gauge length, GL (we will discuss the GL in more detail in a later subsection). When the time-differentiated phase response is computed, a spatial moving average is applied with an averaging length (N_{avg}) similar to the gauge length, resulting in a spatially averaged time-differentiated phase $\dot{\phi}_{avg,x}$ around the location x. The spatial averaging is used to decimate the SSI to a desired spatial resolution and to suppress the Rayleigh fading effect[3]. For example, when a gauge length of 4.08 m is used, the new spatial resolution is calculated by averaging across four spatial samples ($N_{avg} = 4$; Taweesintananon et al. (2021)). After successfully applying the spatial averaging, spatial differentiation between the average time-differentiated phase from two adjacent spatial sampling locations ($N_{\Delta\tau}$, normally the same as N_{avg}) is computed

$$\Delta\dot{\phi}_x = \dot{\phi}_{avg,x+\mathrm{GL}/2} - \dot{\phi}_{avg,x-\mathrm{GL}/2}, \tag{1.3}$$

where the GL $= N_{\Delta\tau} \times$ SSI, $\Delta\dot{\phi}_x$ is the time-differential phase change data saved to the disc, and x indicates spatial sampling location.

To convert the recorded time-differentiated phase change data to in-line strain, three signal conditioning steps are usually needed:

1. The in-line strain rate ($\dot{\epsilon}_{11,x}$) of position x can be computed from the time-differentiated phase change (Taweesintananon et al. 2021):

$$\dot{\epsilon}_{11,x} = \frac{\lambda_0}{4\pi n_g \zeta \mathrm{GL}} \Delta\dot{\phi}_x, \tag{1.4}$$

   where ζ[4] is the strain-optic coefficient (0.78 is used for silica fibers).

2. The data is normally phase wrapped along the spatial dimension, and spatial unwrapping is applied to the data. The unwrapping is done over a range defined in the meta-data and depends on the measurement set-up.

[3] Rayleigh fading is a random attenuation of a signal from the destructive interference of multipath arrivals, which will degrade the sensor performance (see, e.g., Lin et al. (2019)).

[4] The strain-optic coefficient ζ is often described by the Pockel photoelastic constants (P_{11}, P_{12}) and the Poisson's ratio of the fiber material ν. It can be computed by $\zeta = 1 - \frac{n_g^2}{2}[P_{12} - \nu(P_{11} + P_{12})]$.

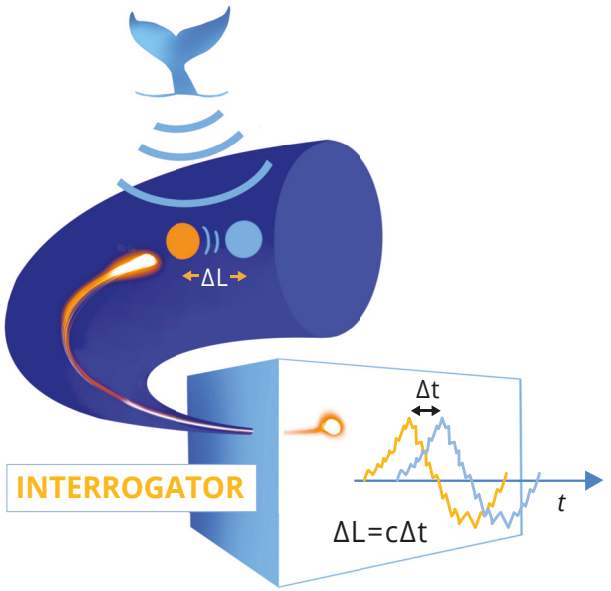

Figure 1.1: Distributed acoustic sensing measurement principle. The acoustic signal, in this case from a whale, will displace the impurity (the orange dot) with a small length, ΔL. Two consecutive laser signals are backscattered from two slightly different points along the cable, which can be observed as a phase shift, Δt. This is illustrated by the two curves where the orange curve is shifted relative to the original blue curve. By interrogating the phase shift, the length change in the cable can be computed using the speed at which the laser travels within the fiberglass (c), $\Delta L = c\Delta t$. Figure from Landrø et al. (2022).

3. The final step is an integration along the time axis to get the measurement in the strain unit:

$$\epsilon_{11,x} = \int_0^t \dot{\epsilon}_{11,x} dt. \tag{1.5}$$

The output from the third step is the strain data analyzed in this thesis.

Various factors can help us understand the inherent restrictions of DAS. The first factor is that the pulse has a finite travel distance within the cable (x_{max}) due to the laser energy being attenuated (scattered or absorbed) as it propagates through the cable. This distance depends on the input laser energy, quality of the fiber, as well as the connectors along the cable. Waagaard et al. (2021) have, to date, shown the longest achieved interrogation range of 171 km using a low-loss cable. Commercial cables absorb more of the input laser sweep, and the maximum range with signal above the noise floor is approximately between 140 and 150 km (if a 0.19 dB/km is achieved). Additionally,

the index of refraction dictates at which speed the laser propagates through the cable. In the case of silica fibers, the refractive index is $n_g \approx 1.47$. The laser speed is then $c_n = c/n_g = 3 \cdot 10^8/1.47 = 2.04 \cdot 10^8$ m/s. The maximum fiber length possible to interrogate (L) depends on the sampling frequency used (the interrogating optical pulse interval) and c_n and can be computed by:

$$L = \frac{c_n}{2f_s}. \tag{1.6}$$

Therefore, if we want to interrogate 171 km the sample rate would be 598 Hz. However, if we want to capture high frequencies, say a sampling frequency of 100 kHz, "only" the first $\simeq$1022 m of the cable will be covered.

The gauge length

Gauge length (GL) may be the most crucial variable in an interrogation system, and a poorly chosen value will distort the recorded signal and might render some data useless. It is defined as the length of fiber over which distributed measurements are taken to obtain the phase signal (Dean et al. 2017). A longer GL will result in a higher signal-to-noise ratio (SNR) but at the cost of reduced resolution and increased signal distortion. The optimal GL depends on the velocity and frequency of the wave under investigation. Dean et al. (2017) found the optimal GL to be when the GL over wavelength ratio (GL/λ) is $\simeq$0.6. This leads to the following "rule-of-thumb" for choosing the optimal length value:

$$\mathrm{GL}_{optimum} = 0.6\frac{v}{f}, \tag{1.7}$$

where v is the velocity and f the frequency of the wave studied. When (GL/λ) approaches one the signal becomes distorted.

Using a Ricker wavelet with a central frequency of 40 Hz and velocity of 1000 m/s, Dean et al. (2017) investigated how the wavelet would respond in terms of SNR and resolution to a variation of GLs. Increasing the GL reduced the high frequency content of the wavelet and decrease the frequency of the notches. When wavelengths between 5 and 15 m were used (resulting in GL/λ between 0.2 and 0.6), the wavelet was well represented with one clear peak. However, when increasing the GL to 20 m the wavelet appeared to posses a flat-topped appearance (GL/λ = 0.8) before developing two peaks at a 25 m GL value (GL/λ = 1.0), producing a distorted representation of the signal.

Directional response of DAS

DAS arrays measure the in-line stain component, i.e., one component of the 3D strain tensor, and not 3D vector velocity, as is often the case for conventional geophone receivers. Hence, the DAS directional sensitivity is vital to understand as the array is only sensitive to how the fiber is strained along the fiber direction. This sensitivity depends on how the fiber cable is installed, i.e., if it is a straight line, slightly curved, or makes a 90° turn. For simplicity, we will limit this discussion to the former case.

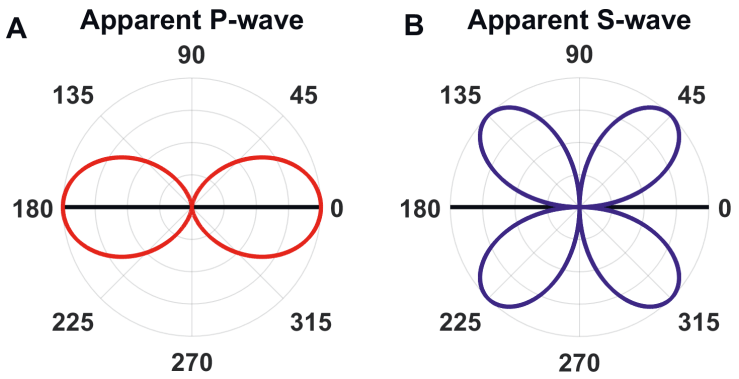

Figure 1.2: DAS directivity response of a straight fiber (the black line) to apparent compressional, P, waves (A) and apparent transverse, S, waves (B; Li et al. (2022).

The directivity of DAS depends on the type of wave and the relative position between the array and the source, i.e., the angle the incident wave hits the cable. For apparent P-waves it is given as (Li et al. 2022, Chapter 1.1.2)

$$D_p(\theta) = \cos^2\theta, \tag{1.8}$$

where θ is the angle of incidence. For apparent S-waves it is

$$D_s(\theta) = \sin\theta\cos\theta. \tag{1.9}$$

The resulting directionality patterns are depicted in Figure 1.2. Papp et al. (2017) test the P-wave sensitivity in a laboratory experiment using walkaround geometry for the acquisition. They found the same patterns for P-waves as in equation (1.8), where the arrivals at a 90° angle (fiber perpendicular to the source direction) have the lowest amplitude with increasing amplitude towards 0° and 180° (fiber parallel to the source direction). Moreover, Papp et al. (2017) observe that the fiber is not sensitive to the P-wave polarity and cannot distinguish between waves arriving from opposite directions.

1.3 Seismic wave propagation

A seismic source generates several seismic waves. Seismic waves are normally divided into the compressional wave arrivals (also known as Primary waves, P-waves), the shear wave arrivals (also known as transverse and Secondary wave, S-waves), and the slower surface waves. These waves are separated by their particle motion and where they occur/propagate. The waves can be described in various media, with attributes dependent on the medium under investigation. To highlight the basic wave propagation ideas used in the acoustic and geophysical application studied in Chapters 2, 3, and 4, we limit the discussion to the acoustic medium and the elastic isotropic case.

1.3.1 Equation of motion

The equation of motion expresses Newton's second law in terms of surface and body forces and is given as (Stein and Wysession 2003, Chapter 2.4.1)

$$\nabla \boldsymbol{\sigma}(\boldsymbol{x}, t) + \boldsymbol{f}(\boldsymbol{x}, t) = \rho(\boldsymbol{x}) \frac{\partial^2}{\partial t^2} \boldsymbol{u}(\boldsymbol{x}, t), \tag{1.10}$$

where $\boldsymbol{u}(\boldsymbol{x}, t)$ is the displacement vector as a function of the geographical coordinates $\boldsymbol{x}$ and time t, $\rho(\boldsymbol{x})$ the density, $\boldsymbol{\sigma}(\boldsymbol{x}, t)$ the stress tensor and $\boldsymbol{f}(\boldsymbol{x}, t)$ the body force, or source, term. From hereafter, we will omit the arguments $(\boldsymbol{x})$ and $(\boldsymbol{x}, t)$ to simplify the notation and neglect the body force term. The displacement vector and the stiffness tensor are first- and second-order tensors, respectively, and are given as

$$\boldsymbol{u} = u_i = \begin{bmatrix} u_1 \\ u_2 \\ u_3 \end{bmatrix}, \quad \boldsymbol{\sigma} = \sigma_{ij} = \begin{bmatrix} \sigma_{11} & \sigma_{12} & \sigma_{13} \\ \sigma_{21} & \sigma_{22} & \sigma_{23} \\ \sigma_{31} & \sigma_{32} & \sigma_{33} \end{bmatrix}, \tag{1.11}$$

where the index in u_i $(i = 1, 2, 3)$ denotes the direction, while the indices in the stress tensor σ_{ij} describe the stress applied in the i direction on the surface with normal j $(j = 1, 2, 3)$.

Stress is related to strain through Hook's law:

$$\sigma_{ij} = C_{ijkl} \epsilon_{kl}, \tag{1.12}$$

where C_{ijkl} is the fourth-order elastic stiffness tensor and the strain ϵ_{kl} can be expressed in terms of the displacement components:

$$\epsilon_{kl} = \frac{1}{2} \left(\frac{\partial u_k}{\partial x_l} + \frac{\partial u_l}{\partial x_k} \right) \tag{1.13}$$

The fourth-order elastic stiffness tensor has 81 entries. However, due to symmetry in the strain tensor and, by extension, the stress tensor, there are 21 independent elastic components (which is the case for a triclinic medium). The elastic tensor can be written as

$$C_{IJ} = \begin{bmatrix} C_{11} & C_{12} & C_{13} & C_{14} & C_{15} & C_{16} \\ C_{21} & C_{22} & C_{23} & C_{24} & C_{25} & C_{26} \\ C_{31} & C_{32} & C_{33} & C_{34} & C_{35} & C_{36} \\ C_{41} & C_{42} & C_{43} & C_{44} & C_{45} & C_{46} \\ C_{51} & C_{52} & C_{53} & C_{54} & C_{55} & C_{56} \\ C_{61} & C_{62} & C_{63} & C_{64} & C_{65} & C_{66} \end{bmatrix}, \tag{1.14}$$

using a simplified notation of the full C_{ijkl} tensor, known as the Voigt notation. In equation (1.14) we have used the following: $11 \rightarrow 1$, $22 \rightarrow 2$, $33 \rightarrow 3$, $23 \rightarrow 4$, $13 \rightarrow 5$, $12 \rightarrow 6$, i.e., $ij \rightarrow I$ and $kl \rightarrow J$. In the case of an elastic isotropic medium, the elastic

tensor is greatly simplified. Using the Lamé parameters (λ and μ), we can re-write the elastic tensor and, for the sake of completeness, plug it into Hook's law (equation (1.12))

$$\begin{bmatrix} \sigma_1 \\ \sigma_2 \\ \sigma_3 \\ \sigma_5 \\ \sigma_5 \\ \sigma_6 \end{bmatrix} = \begin{bmatrix} \lambda+2\mu & \lambda & \lambda & 0 & 0 & 0 \\ \lambda & \lambda+2\mu & \lambda & 0 & 0 & 0 \\ \lambda & \lambda & \lambda+2\mu & 0 & 0 & 0 \\ 0 & 0 & 0 & \mu & 0 & 0 \\ 0 & 0 & 0 & 0 & \mu & 0 \\ 0 & 0 & 0 & 0 & 0 & \mu \end{bmatrix} \begin{bmatrix} \epsilon_1 \\ \epsilon_2 \\ \epsilon_3 \\ \epsilon_4 \\ \epsilon_5 \\ \epsilon_6 \end{bmatrix}. \tag{1.15}$$

1.3.2 The acoustic wave equation

The simplest case of wave propagation is when there is no shear motion ($\mu = 0$), where pressure wave propagation in a fluid medium is investigated. For such cases, pressure is normally used instead of displacement. There are three main reasons for starting with this simple medium: (1) The equations are easier to understand and derive; (2) It is often used in practice as a simple approximation of compressional-waves in solid models (Cervenỳ 2001); (3) It must be used when modeling signals in the water column.

One example of the acoustic wave equation (assuming constant density) is given as

$$\nabla^2 p(\boldsymbol{x}, t) - \frac{1}{c(\boldsymbol{x})^2} \frac{\partial^2}{\partial t^2} p(\boldsymbol{x}, t) = -f(\boldsymbol{x}, t), \tag{1.16}$$

where $p(\boldsymbol{x}, t)$ is the acoustic pressure field in a three-dimensional (3D) spatial volume, $\boldsymbol{x}$, at time t, $c(\boldsymbol{x})$ denotes the P-wave velocity, and $f(\boldsymbol{x}, t)$ the body force.

There are different methods of solving the acoustic wave equation. One example of such a function is that of plane waves:

$$\mathbf{p}_{plain} = \mathbf{A} \exp(i(\omega t - \mathbf{k} \cdot \mathbf{x})) + \mathbf{B} \exp(i(\omega t + \mathbf{k} \cdot \mathbf{x})), \tag{1.17}$$

which are in- and out-going plane waves, where $\mathbf{A}$, $\mathbf{B}$ are two complex constants, ω the angular frequency and $\mathbf{k}$ the angular wavenumber vector. However, in some scenarios, other representations of the wavefront are more realistic. For example, in the water column, describing them as cylindrical or spherical waves gives better representations. The type of radiation model used depends on the range in which the waves propagate, as the horizontal dimension is much larger than the vertical. The wave will spread spherically until it hits the sea floor and the ocean surface and can be treated as cylindrical after.

In Chapter 2, we will use pressure waves propagating in the water column to track whales and seismic signals produced by an air gun.

1.3.3 Waves in an elastic isotropic medium

While acoustic media can describe wave propagation in the ocean, treating the earth as an elastic isotropic medium provides a better approximation for seismic wave propagation. The equation of motion for an elastic isotropic medium can be written in terms of displacement by combining equations (1.10), (1.12) and (1.13), and the relevant stiffness components given in equation (1.15) (Stein and Wysession 2003, Chapter 2.4):

$$(\lambda + 2\mu)\nabla(\nabla \cdot \boldsymbol{u}) - \mu\nabla \times (\nabla \times \boldsymbol{u}) = \rho\frac{\partial^2}{\partial t^2}\boldsymbol{u}, \tag{1.18}$$

where $\cdot$ and $\times$ denote the dot and cross products, respectively. Equation (1.18) can be rewritten using the relation between the particle displacement ($\boldsymbol{u}$) and the scalar potential (ϕ) and the vector potential ($\boldsymbol{\psi}$):

$$\boldsymbol{u} = \nabla\phi + \nabla \times \boldsymbol{\psi}. \tag{1.19}$$

Inserting this into equation (1.18), rearranging the equation, and applying some vector identities, we obtain

$$\nabla\left[(\lambda + 2\mu)\nabla^2\phi - \rho\frac{\partial^2}{\partial t^2}\phi\right] = -\nabla \times \left[\mu\nabla^2\boldsymbol{\psi} - \rho\frac{\partial^2}{\partial t^2}\boldsymbol{\psi}\right]. \tag{1.20}$$

By setting each of the brackets equal to zero, we can obtain two wave equations, one scalar equation for compression waves and one vector equation for shear waves:

$$\nabla^2\phi = \frac{1}{\alpha^2}\frac{\partial^2}{\partial t^2}\phi, \tag{1.21}$$

$$\nabla^2\boldsymbol{\psi} = \frac{1}{\beta^2}\frac{\partial^2}{\partial t^2}\boldsymbol{\psi}, \tag{1.22}$$

where the velocities are given as $\alpha = ([\lambda + 2\mu]/\rho)^{1/2}$ and $\beta = (\mu/\rho)^{1/2}$, for P- and S-waves, respectively.

To better understand the nature of the P- and S-waves, we can investigate how their wave equations react to plain wave propagation. This will reveal some fundamental properties of their wave propagation in terms of their displacement polarization. By introducing a plane wave propagating in the z-direction, we can introduce the scalar potential for the harmonic P-wave and the vector potential for harmonic S-waves:

$$\phi(z,t) = A\exp(i(\omega t - kz)), \tag{1.23}$$

$$\boldsymbol{\psi}(z,t) = (A_x, A_y, A_z)\exp(i(\omega t - kz)). \tag{1.24}$$

Using that equation (1.19) can be divided into a displacement for the P- and S-waves, we find that their respective displacement vectors are

$$\boldsymbol{u}_p(z,t) = \nabla\phi(z,t) = (0,0,-ik)A\exp(i(\omega t - kz)), \tag{1.25}$$

$$\boldsymbol{u}_s(z,t) = \nabla \times \boldsymbol{\psi}(z,t) = (ikA_y, -ikA_x, 0)\exp(i(\omega t - kz)). \tag{1.26}$$

These equations show that the P-wave has a non-zero displacement component along the propagation direction z. In contrast, the S-wave displacement is non-zero perpendicular to the propagation direction. It is also worth noting that there is a dilatation present for the P-wave displacement:

$$\nabla \cdot \boldsymbol{u}_p(z,t) = -k^2 A \exp(i(\omega t - kz)), \tag{1.27}$$

whereas the S-wave displacement has no volume change:

$$\nabla \cdot \boldsymbol{u}_s(z,t) = 0. \tag{1.28}$$

This is one way of showing that the first arriving wave in an elastic isotropic medium is a compressional wave and the secondary comprises two perpendicular polarized shear waves.

In Chapter 4, we will investigate how P- and S-waves generated by local earthquakes can be used to estimate the average attenuation of a sedimentary layer.

1.3.4 Surface waves

In addition to recording P- and S-waves, seismic sensors will detect waves trapped near the Earth's surface, or near layer boundaries, known as surface or interface waves. There are two types of surface waves, Rayleigh and Love waves, named after their discoverers and separated by their particle displacement patterns. Firstly, the displacement patterns of the Rayleigh wave will be introduced by investigating it in a homogeneous half-space. Secondly, the dispersion relation for Love waves in a layer over a half-space will be introduced. In principle, the same procedures can be carried out to find the displacement pattern of Love and Rayleigh waves, but with some modifications. Love waves do not exist in a homogeneous half-space, and Rayleigh waves are not dispersive in this model. Both need to be extended to a layer over a half-space model. Most generally, they need a velocity structure that varies with depth. We will follow the notation of Stein and Wysession (2003, Chapter 2.7)) in the following paragraphs.

Rayleigh waves particle displacement

The term 'Rayleigh waves' is used when the waves are trapped near the air-solid boundary. Alternative names are used for waves along other layer interface types. For the fluid-solid boundary at the sea floor, it is known as Scholte waves, and at the solid-solid boundary, within the Earth, it is known as Stoneley waves (Ewing et al. 1957). Here, only Rayleigh waves will be considered. In the case of a homogeneous half-space, Rayleigh waves are a combination of compression motion and vertically polarized shear motion, i.e., SV motion, and we can therefore investigate it in, for example, the $x-z$ plane. To describe the particle displacement of Rayleigh waves, we use the potentials for P- and SV-plane waves

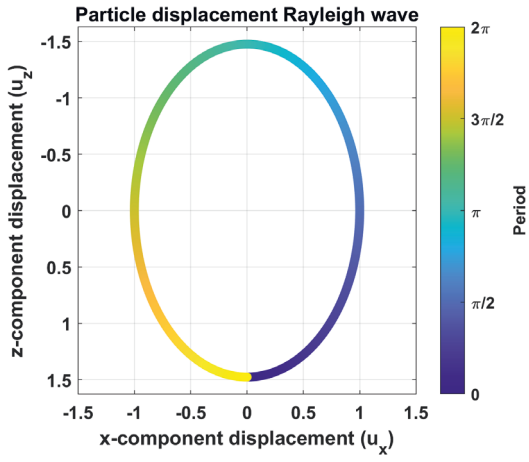

Figure 1.3: The basic behavior of surface waves. The particle displacement of the Rayleigh wave along the surface displays its retrograde elliptical motion, and the maximum displacement in the z-direction is 1.5 greater than the maximum in the x-direction. In this example, the wave is propagating from left to right along the x-axis.

defined for a free surface boundary condition at $z = 0$, where z is positive downward

$$\phi = A \cdot \exp(i(\omega t - k_x x - k_x r_\alpha z)), \tag{1.29}$$

$$\psi = B \cdot \exp(i(\omega t - k_x x - k_x r_\beta z)), \tag{1.30}$$

where A and B are constants, ω is the angular frequency, k_x the x-component of the wavenumber, and

$$r_\alpha = (c_x^2/\alpha^2 - 1)^{1/2}, \quad r_\beta = (c_x^2/\beta^2 - 1)^{1/2}, \tag{1.31}$$

where c_x is the apparent velocity along the surface. For these potentials to describe Rayleigh wave motion, i.e., energy trapped near $z = 0$, two conditions must be adhered to: (1) the energy must not propagate away from the free surface, and (2) satisfy the free surface boundary condition.

The first condition is known as the radiation condition and is met when the energy of the wave decay with depth. This is the case when the argument in $\exp(-ik_x r_\alpha z)$ and $\exp(-ik_x r_\beta z)$ are negative real, which only happens when $c_x < \beta < \alpha$. We then get that

$$r_\alpha = -i(1 - c_x^2/\alpha^2)^{1/2}, \quad r_\beta = -i(1 - c_x^2/\beta^2)^{1/2}, \tag{1.32}$$

which results in a negative real argument, and when substituted back into equations (1.29) and (1.30), will result in an exponential decay of the potentials with depth.

The second condition is a boundary condition and is satisfied when σ_{xz} and σ_{zz} vanish at the free surface. We use this to find the values of either A or B. The stress components

at $z = 0$, expressed in terms of the potentials in equations (1.29) and (1.30), satisfy the continuity equation (where the boundary condition is satisfied without an incident wave)

$$\sigma_{xz}(x,0,t) = \mu\left(\frac{\partial u_x}{\partial z} + \frac{\partial u_z}{\partial x}\right) = \mu\left(2\frac{\partial^2\phi}{\partial x \partial z} + \frac{\partial^2\psi}{\partial x^2} - \frac{\partial^2\psi}{\partial z^2}\right) \tag{1.33}$$

$$= 2r_\alpha A + \left(1 - r_\beta^2\right) B = 0, \tag{1.34}$$

$$\sigma_{zz}(x,0,t) = \lambda\theta + 2\mu\frac{\partial u_z}{\partial z} = \lambda\left(\frac{\partial^2\phi}{\partial x^2} + \frac{\partial^2\phi}{\partial z^2}\right) + 2\mu\left(\frac{\partial^2\phi}{\partial z^2} + \frac{\partial^2\psi}{\partial x \partial z}\right) \tag{1.35}$$

$$= \left[\lambda\left(1 + r_\alpha^2\right)\right] + 2\mu r_\alpha^2\Big] A + 2\mu r_\beta B = 0, \tag{1.36}$$

where $\theta = \nabla \cdot \boldsymbol{u}$ is the dilatation. This system of two equations has a nontrivial solution if its determinant is zero. The algebra will not be shown here, but a fourth-order polynomial containing four roots is obtained by writing out the determinant (Stein and Wysession 2003, Chapter 2.7). Each root corresponds to one possible apparent velocity of the Rayleigh wave. However, only one satisfies the radiation condition, $c_x < \beta$. This root gives an apparent velocity of the Rayleigh wave $c_x = (2 - 2/\sqrt{3})\beta = 0.92\beta$, providing a simple relation between the apparent velocity of the Rayleigh wave and the velocity of the SV-wave. Furthermore, we use this root to express B in terms of A:

$$B = A\left(2 - \frac{c_x^2}{\beta^2}\right) \Big/ (2r_\beta). \tag{1.37}$$

We insert this back into the potential and find the resulting displacement for the x- and z-components:

$$u_x = \frac{\partial\phi}{\partial x} - \frac{\partial\psi}{\partial z} = Ak_x \sin(\omega t - k_x x)\left(\exp(-0.85k_x z) - 0.58\exp(-0.39k_x z)\right), \tag{1.38}$$

$$u_z = \frac{\partial\phi}{\partial z} + \frac{\partial\psi}{\partial x} = Ak_x \cos(\omega t - k_x x)\left(-0.85\exp(-0.85k_x z) + 1.47\exp(-0.39k_x z)\right), \tag{1.39}$$

where the real parts of the displacement exponential have been taken, the displacement pattern is harmonic waves propagating in the x-plane, decaying exponentially with depth propagating with a retrograde particle motion (Stein and Wysession 2003, Chapter 2.7). Figure 1.3 shows a numerical implementation of equations (1.38) and (1.39) and illustrates the retrograde motion of particle displacement colorcoded as a function of time (one period in this case).

Love waves and the dispersion relation

Contrary to Rayleigh waves, Love waves have the same name for all interfaces and result from interaction between horizontally polarized shear waves, SH-waves. The Love wave's particle motion is entirely horizontal, 90° relative to the propagation direction, and decays

with depth. Another difference from Rayleigh waves is that the simplest case where Love waves exist is in a layer over a half-space model. Generally, it exists in media where the velocity structure varies with depth. To investigate the dispersion behavior of Love waves, we introduce a sum of up- and down-going SH-wave in the top layer (1) and down-going waves in the half-space (2):

$$u_y^{(1)} = B_1 \exp(i(\omega t - k_x x - k_x r_{\beta_1} z)) + B_2 \exp(i(\omega t - k_x x + k_x r_{\beta_1} z)), \tag{1.40}$$

$$u_y^{(2)} = B' \exp(i(\omega t - k_x x - k_x r_{\beta_2} z)), \tag{1.41}$$

where β_1 is the shear-wave velocity in layer 1, β_2 is the shear-wave velocity in layer 2. For the layer over half-space medium, the boundary conditions needed to produce the Love waves are: (1) the radiation condition where the energy should not travel into the half-space as propagating waves. This is the case when $c_x < \beta_2$, and $r_{\beta_2} = -i(1 - c_x^2/\beta_2^2)^{1/2}$ (as in equation (1.32)). (2) The boundary condition at the free surface ($z = 0$) and at the layer interface ($z = h$) need to be satisfied. The traction force at the free surface should vanish and be continuous for both the displacement and the stress components over the $z = h$ layer interface. Inserting the particle displacement into these conditions, we find two new expressions (for more details, see Stein and Wysession (2003, Chapter 2.7)):

$$2B_1 \cos(k_x r_{\beta_1} h) = B' \exp(-ik_x r_{\beta_2} h), \tag{1.42}$$

$$2i\mu_1 r_{\beta_1} B_1 \sin(k_x r_{\beta_1} h) = -\mu_2 r_{\beta_2} B' \exp(-ik_x r_{\beta_1} h). \tag{1.43}$$

By taking the ratio of these two equations (equation (1.43) by equation (1.42)), we find the dispersion relation of the Love wave:

$$\tan(k_x r_{\beta_1} h) = -\frac{\mu_2 r_{\beta_2}}{i\mu_1 r_{\beta_1}}, \tag{1.44}$$

which is an essential property of surface waves illustrating how Love waves in a layer over half-space are dispersive, meaning that different frequencies propagate at different apparent velocities[5].

To find dispersion curves, we rewrite the dispersion relation in terms of the apparent velocity (c_x) and the angular frequency (ω):

$$\tan(\omega\xi) = \frac{\mu_2(1 - c_x^2/\beta_2^2)^{1/2}}{\mu_1} \frac{h}{c_x \xi}, \quad \xi = \frac{h}{c_x} \left(\frac{c_x^2}{\beta_1^2} - 1 \right)^{1/2}. \tag{1.45}$$

This equation is best solved graphically where the function of the left-hand side equals the right-hand side, i.e., where they intersect. These points provide the modes of the

[5] It is also worth noting that dispersion can be derived from reflection and transmission. This derivation emerges from the radiation condition, $c_x < \beta_2$, which also means we are looking at critically reflected SH-waves corresponding to a wave trapped within the layer with an evanescent wave in the half-space.

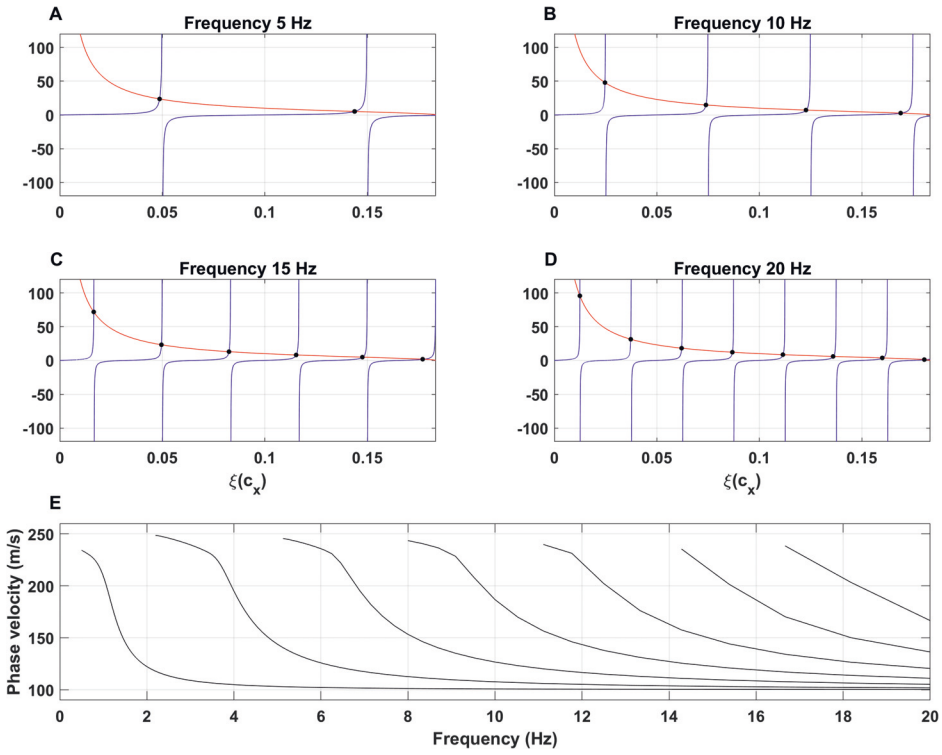

Figure 1.4: Illustration of how dispersion curves are computed. A layer over half-space model is used. Layer 1 is 20 m thick with a shear-wave velocity of 100 m/s and density of 1.825 g/cm^3. Layer two has a velocity of 250 m/s and a density of 1.9 g/cm^3. (A, B, C, D) The left- (the blue) and right-hand (the red) sides of equation (1.45) with their intersection points (black dots). When there are several intersection, each is associated with a dispersion curve. (A) Using 5 Hz, (B) 10 Hz, (C) 15 Hz, (D) 20 Hz. (E) The dispersion curves are estimated by saving the velocity values for each dot on the frequency range 1–20 Hz.

Love wave and can only be found on the interval defined by the $\tan$ function, as it is only defined for real values. Hence, the available range is $\beta_1 < c_x < \beta_2$. The tangent function will have several repeating curves and several intersections between the curves in equation (1.45). The number of $\tan$ graphs depends on the frequency used, and the modes are, therefore, frequency dependent.

Figures 1.4A, B, C, D illustrate how equation (1.45) can be solved graphically for the layer over half-space model. The medium parameters are chosen to be comparable to the case investigated in the second paper of this thesis (Chapter 3), where the first layer has a thickness of 20 m, S-wave velocity of 100 m/s and density of 1.825 g/cm^3, while layer two has a S-wave velocity of 250 m/s and density of 1.9 g/cm^3. The blue and red curves represent the left- and right-hand sides of the equation, and the black dots are their intersection points. It also depicts how different frequencies produce a different number

of modes and how we can find the dispersion curves by investigating several frequencies. Extending the frequency interval to range from 1 to 20 Hz, we can find the dispersion curve for the fundamental mode and the higher-order modes by saving the $\xi(c_x)$ values for each frequency. The resulting dispersion curves are depicted in Figure 1.4E, where the first mode from the left is the fundamental mode, followed by the higher-order modes. A total of eight modes are present.

The dispersion observed in the layer over the half-space model is the simplest in which surface wave dispersion occurs. It will also be a prominent effect in more complicated models, where the properties vary with depth, and in such subsurface models, the dispersion curves will exist for both Love and Rayleigh waves. There are different ways of computing these curves, where one approach extends the method just discussed by introducing the necessary layer conditions. This is used in Chapter 3, where a different number of horizontal homogeneous layers are used to estimate the shear-wave velocity profile over seven months to map changes in a quick clay area.

1.3.5 The effect of viscosity on wave propagation

Before going into the details on the effect viscosity has on seismic wave propagation, we will shortly discuss a simpler case, the damped harmonic oscillator. This oscillating system provides a relatively easy way of understanding some fundamental concepts related to viscosity and damping, which are also applicable to seismic processes.

The un-damped and damped harmonic oscillator

The un-damped harmonic oscillator is depicted in Figure 1.5A and composes a spring with a stiffness constant κ connected to a mass m. Using Newton's second law, we can describe the particle displacement of the mass through the following equation of motion:

$$m\frac{d^2}{dt^2}u(t) + \kappa u(t) = 0, \tag{1.46}$$

where the second term is related to the restoring force of the spring. Since there is no damping to the system, it will never stop once set in motion, which can be described through

$$u(t) = A\exp(i\omega_0 t) + B\exp(i\omega_0 t), \tag{1.47}$$

where A and B are constants, t is time, and $\omega_0 = (\kappa/m)^{1/2}$ is the natural frequency of the system. Equation (1.47) has a general solution on the form

$$u(t) = A_0\cos(\omega_0 t). \tag{1.48}$$

If we introduce a dashpot to the system with a damping factor γ (see Figure 1.5B), the mass will not oscillate forever. This damping term is proportional to the velocity of the

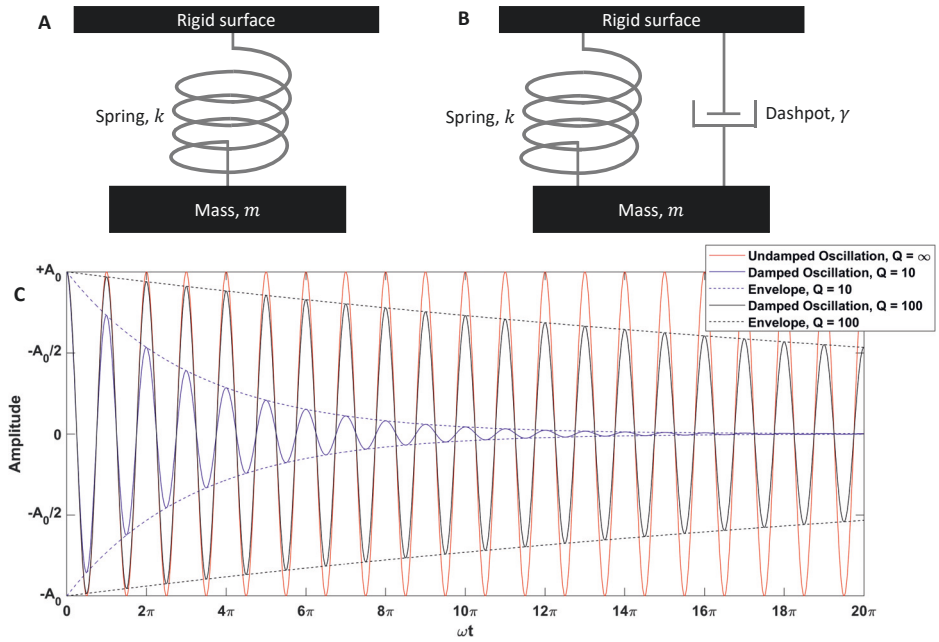

Figure 1.5: A simple introduction to attenuation, and quality factor, through the un-damped (A) and damped (B) harmonic oscillator. (C) The oscillations for various quality factors $Q = \infty$ (un-damped), $Q = 10$, and $Q = 100$. Note that the damping factor γ is inversely proportional to Q, $Q = \omega_0/\gamma$, where ω_0 is the system's natural frequency.

mass and will oppose its motion, which modifies the equation of motion:

$$\frac{d^2}{dt^2}u(t) + \frac{\omega_0}{Q}\frac{d}{dt}u(t) + \omega_0^2 u(t) = 0, \tag{1.49}$$

where $Q = \omega_0/\gamma$ is the quality factor. The general solution of this system can be found by assuming that the particle displacement is given as

$$u(t) = A_0 \exp(ipt), \tag{1.50}$$

where p is a complex frequency. We will not go into the derivation here but rather give the general solution directly (which can be obtained by inserting equatino 1.50 into equation (1.49), see Stein and Wysession (2003, Chapter 3.7)):

$$u(t) = A_0 \exp(-\omega_0 t/2Q)\cos(\omega t), \tag{1.51}$$

where $\omega = \omega_0(1 - 1/4Q^2)^{1/2}$.

Figure 1.5C shows the response of the damped harmonic oscillator to an impulse source at time zero when $Q = \infty$, $Q = 10$, and $Q = 100$. The main difference is that the

exponential term in equation (1.51):

$$A(t) = A_0 \exp(-\omega_0 t/2Q), \tag{1.52}$$

expresses the decay of the signal's envelope introduced by the dashpot. When $Q = \infty$, this term vanishes, and equation (1.51) breaks down to equation (1.48), meaning we have the un-damped case. Another effect is that the natural frequency of the harmonic oscillator changes depending on the value of the quality factor. We can observe in Figure 1.5 that a smaller Q value means a higher attenuation, which conversely means that a higher damping factor gives a higher attenuation, as expected.

Attenuation and physical dispersion

It is normal to consider seismic waves as acoustic or elastic, where the main attenuation of the wave is through the geometrical spreading and losses over layer interfaces. However, it is well known that dissipation (energy converted to heat) follows wave propagation. Various disturbances within the Earth cause this dissipation; each converts some energy to heat. Several mechanisms contribute to energy dissipation, generally collected under the term internal friction (Ewing et al. 1957, Chapter 5.5). Internal friction has two main effects: wave attenuation and physical dispersion.

The seismic attenuation is often described in terms of the quality factor Q, a measure of the efficiency of the wave propagation, which is inversely related to attenuation. Moreover, attenuation is often described as the anelastic structure of the Earth. It can be further described as an analog to the elastic velocity structure, where Q is the imaginary part of the velocity (Stein and Wysession 2003, Chapter 3.7).

Physical dispersion is the second important consequence of seismic attenuation. We already discussed dispersion when looking at surface waves, but the dispersion related to attenuation and the dispersion from surface waves are different. For surface waves, the dispersion (also known as geometrical dispersion) results from the subsurface having a depth-dependent velocity structure. Surface waves at different frequencies sample different parts of the subsurface (low frequencies penetrate deeper, while the high frequencies focus on upper parts). Conversely, the intrinsic velocity of waves in the medium varies with frequencies for physical dispersion.

To illustrate how physical dispersion results from attenuation, we look at how a seismic wave, a delta pulse in this case, changes shape as it attenuates. The delta pulse is of infinite height and unit area and is made up of waves of all frequencies, which can be seen through its Fourier transform pair:

$$u(x,t) = \delta\left(t - \frac{x}{c}\right) \longleftrightarrow F(\omega) = \exp(-i\omega x/c). \tag{1.53}$$

We will start by looking at how the pulse attenuates when assuming no velocity dispersion. To see the attenuation effect, we recall how the signal of the damped harmonic oscillator

decays as a function of time (equation (1.51)), but instead write it as a function of distance ($t = x/v$; Q is assumed constant) and frequency:

$$A(\omega) = \exp(-\omega x/2vQ). \tag{1.54}$$

From this equation, we can observe that higher frequencies decay faster with distance than the lower frequencies. Multiplying equation (1.54) with the frequency response of the delta pulse in equation (1.53) and taking the Fourier transform back to the time domain, we find (Stein and Wysession 2003, Chapter 3.7):

$$u(x,t) = \left(\left(\frac{x}{2vQ} \right) \Big/ \left(\left(\frac{x}{2vQ} \right)^2 + \left(\frac{x}{v} - t \right)^2 \right) \right) \Big/ \pi, \tag{1.55}$$

which is a broadened version of the delta pulse, symmetric around $t = x/v$. The problem with this solution is that the tails stretch to infinity, meaning that some energy arrives before the pulse arrives at a receiver and even before the earthquake has started. This is an un-physical situation known as non-causality, meaning we cannot treat seismic wave velocity as the same for all frequencies. Instead, we need physical dispersion, i.e., the mechanisms that create attenuation must also prevent seismic waves from propagating at the same speed. Dispersion makes the lower frequencies travel slower than the higher frequencies, hence arriving later. From this, we can introduce a mathematical condition that ensures causality of the arrivals: all $u(x,t) = 0$ when $t = x/c_\infty < 0$, where c_∞ is the velocity of the infinite-frequency wave, the first arriving frequency. For completeness, it is useful to introduce a dispersion relation that takes the causality into account. One such example is Azimi's attenuation law given as (Aki and Richards 2002)

$$v(\omega) = v_0 \left(1 + \frac{1}{\pi Q} \ln \left(\frac{\omega}{\omega_0} \right) \right), \tag{1.56}$$

where v_0 and ω_0 are the reference velocity and frequency. In this formulation, the high frequencies arrive at, or soon after, the infinity-frequency wave and, subsequently, the lower frequencies. The times of arrival depend on the Q value.

In Chapter 4, we estimate the average P-wave quality factor Q_p and S-wave quality factor Q_s values for a sediment layer using a dense 4C ocean-bottom-node array installed on top of the sediment layer and a reference broadband seismometer installed on bedrock.

1.3.6 Ray Tracing – an approximate solution to wave propagation

The wave equations can sometimes be challenging to solve, with analytical solutions only existing for some specific models, initial conditions, and boundary conditions. Hence, approximate solutions are often used, and in the most complex scenarios, they must be used. Modeling the seismic wavefield is important in many branches of exploration and earthquake seismology and can be done in many different ways. The most common methods are finite difference, finite element, and ray tracing. In this thesis, only the latter has

been used and will be introduced in the following paragraphs (following the notation of Cervenỳ (2001)).

To get an overall picture of the simplifications needed to get to a ray tracing system, we start by introducing the general elastodynamic equation in terms of particle displacement:

$$\nabla \cdot \left(C_{ijkl} \frac{\partial u_k}{\partial x_l} \right) + f_i = \rho \frac{\partial^2 u_i}{\partial t^2}, \quad i = 1, 2, 3, \tag{1.57}$$

where C_{ijkl} are components of the elastic tensor and f_i the Cartesian components of the the body force (we assume a source free region, $f_i = 0$, in the following discussion).

The elastodynamic equation represents a system of three coupled second-order partial differential equations for the particle displacement vector $\boldsymbol{u}$. Solving this problem is significantly complex for most media, which leads us to the first approximation, namely the high-frequency approximation. The high-frequency approximation requires a smoothly varying medium, and the material properties, slowness, and amplitude vectors do not vary significantly over a distance similar to the wavelength. Applying this approximation to the elastodynamic equation, it is possible to derive equations controlling the traveltime function of the ray (eikonal equation) and the amplitude function (transport equation) for both P- and S-waves. For simplicity, we will show how this is done using the acoustic wave equation, and a similar approach can be done for the elastic wave equation (see Cervenỳ (2001, Chapter 2.4.2)).

We start by introducing an approximate time-harmonic high-frequency solution (a generalization of the plane-wave approach):

$$p(x_i, t) = P(x_i) \exp(-i\omega(t - T(x_i))). \tag{1.58}$$

To adhere to the high-frequency approximation condition, $P(x_i)$ and $T(x_i)$ are smoothly varying models. Note that $t = T(x_i)$ represents the moving wavefront and $T(x_i)$ is the traveltime function. We insert this into the acoustic wave equation given in equation (1.16) and find:

$$-\omega^2 P[(\nabla T)^2 - 1/c^2] + i\omega[2\nabla P \cdot \nabla T + P\nabla^2 T] + \nabla^2 P = 0. \tag{1.59}$$

This equation should be satisfied for all frequencies ω, meaning each term in brackets must be equal to zero. However, there are three equations and only two unknowns (T and P). As we are interested in high frequencies the first two terms will be most prominent, and we require only these to be equal to zero (and neglect the third term). This leads to

$$(\nabla T)^2 - 1/c^2 = 0, \tag{1.60}$$

known as the eikonal equation, and

$$2\nabla P \cdot \nabla T + P\nabla^2 T = 0, \tag{1.61}$$

known as the transport equation (Cervenỳ 2001, Chapter 2.4.1). As mentioned, a similar approach can be carried out by inserting another generalized plane-wave solution into the elastodynamic equation, which will, after some work, give similar eikonal and transport equations for both P- and S-waves. In this work, we are interested in the traveltimes and focus only on the eikonal equation.

The eikonal equation is still challenging to solve as it is a first-order non-linear partial differential equation and, when solved, finds the wavefronts radiating from a seismic source. The next step is to solve for the rays propagating perpendicular to these wavefronts. This can be done in different ways, but the most common is to solve the eikonal equation in terms of the characteristic curve producing 3D trajectories through the medium, i.e., the ray paths (for a complete discussion, see Cervenỳ (2001, Chapter 3.1.1) and references therein). This produces the ray equations, a system of ordinary differential equations. These equations give the position $x_i(t)$ of a ray at time t, given a P-wave velocity model v_p and a source position:

$$\frac{d}{dt}x_i(t) = v_p(x_i)^2 p_i, \tag{1.62}$$

$$\frac{d}{dt}p_i(t) = -\frac{1}{v_p(x_i)}\frac{\partial}{\partial x_i}v_p(x_i), \tag{1.63}$$

where $p_i(t)$ denotes slowness as a function of time and x_i is the Cartesian coordinate along the ray. This can be numerically implemented using, e.g., the modified Euler method:

$$x_{i,k+1} = x_{i,k} + \Delta t v_p^2(x_{i,k}) p_{i,k}, \tag{1.64}$$

$$p_{i,k+1} = p_{i,k} - \Delta t \left(\frac{1}{v_p(x_{i,k+1})}\frac{\partial}{\partial x_i}v_p(x_{i,k+1}) \right), \tag{1.65}$$

where k denotes the position along the ray and Δt is the time step.

1.4 Acoustic and elastic wave monitoring

An increased sensor coverage provides new possibilities in terms of monitoring as information not available with single sparse receivers can now be captured. We use DAS data for two monitoring studies, one to track whales in Isfjorden at Svalbard and the other to monitor subsurface changes in a known quick clay area in Norway as a road was built on top of the clay.

1.4.1 Whale monitoring

Baleen whales were brought to the brink of extinction during large-scale commercial whaling, but many are now recovering (Thomas et al. 2016). Nevertheless, anthropogenic stressors associated with modern and industrialized ocean exploration still affect the whale population. This is especially clear in the Arctic, an area with abundant baleen whales, both endemic and boreal visitor species (Hamilton et al. 2021). Additionally, due

to global warming, the sea-ice melt has increased in recent years (Stroeve et al. 2007, Comiso et al. 2008). This melt will open new shipping routes, intensifying human activities in local species-rich areas. Increasing ship traffic will further increase the threat of ship strikes, which is one of the main stressors for whales, in addition to entanglement in fishing gear (Greene and Pershing 2004, Thomas et al. 2016). Global warming will also induce alteration in sea-surface temperatures and circulation patterns. This could force cetaceans to change their seasonal habits, such as the migratory route or force them to change their feeding patterns (Van Gestel et al. 2008).

Considering the effects of increasing human activity in Arctic habitats and the potential changes in whale migration, it is urgent to develop robust monitoring procedures to track and map the changes in whale migration routes and habitats. The methods should also enable close to real-time monitoring of the whale locations, which can be used to avoid deadly ship strikes. There are several common tracking methods; some examples are visual surveys (Cummings and Thompson 1971), satellite tracking (Lydersen et al. 2020), and location estimation based on hydrophone data (McDonald et al. 1995). Long-term installation of hydrophone arrays has been widely used for Passive Acoustic Monitoring (PAM), but suffers from uneven spacing and general undersampling. DAS might be part of the solution to this problem, as it provides a dense spatial sampling of receivers over a long range. To monitor whales, accurate location methods are needed as well as an estimation of the heading and speed. Hendricks et al. (2019) argued that an accuracy of 100 m is needed to perform real-time ship strike risk management for whales. One simple location method is the grid search (see, e.g., Wilcock (2012)). This method will compute the whale's position and provides valuable information on the accuracy of the location through mismatch maps. Another example that estimates the location heading and speed is a state space model and Bayesian filtering approach (see, e.g., Eidsvik and Hokstad (2006)).

1.4.2 Quick clay monitoring

Many devastating quick clay landslides have occurred in Norway the last 50-60 years. These slides are triggered by changes in the near-surface properties through anthropogenic and/or natural impacts. Many factors play a role in triggering the clay liquefaction associated with such events; examples are vibrations from earthquakes, alteration in the material balance in the clay, massive rainfall over time, and/or local erosion (Gregersen et al. 1981, Lundström et al. 2009, Ryan and Riekeles 2021).

Quick clay can only be found in areas that were previously covered by glaciers. The clay was deposited on the seafloor as marine clay during or shortly after the last ice age. The pore fluid of the marine clay deposit consisted primarily of salt water. When the glaciers melted, the clay areas were uplifted due to isostatic rebound. After some time, the area emerged from the sea and was no longer covered by saltwater. The marine clay material was then exposed to freshwater that passed through the material. Over time, the

salt leached out of the clay and became increasingly unstable; it turned quick. In such quick clay, a little disturbance to the internal structure of the clay could cause it to liquefy and flow, generating massive damage to the landscape and the local population.

In Norway, there have been several devastating quick clay landslides, and the most recent example is the Gjerderum slide in 2020 (Ryan and Riekeles 2021). This slide had very unfortunate consequences, where eleven people were killed, and it caused at least 875 MNOK worth of damages. This highlights the importance of developing robust monitoring systems for such areas. Such a monitoring system can be based on different methods and set up in several ways. One possibility is to quantify the changes in the shear-wave velocity depth profile in a time-lapse manner while processes previously known to trigger events are ongoing. When an avalanche is triggered, the shear strength of the clay will drastically decrease before the landslide and vanish when the clay liquefies. Since the shear strength is related to the shear-wave velocity (see equation (1.22)), these changes can be detected as changes in the shear-wave velocity. It is worth noting that the time scale for these changes in shear modulus is unknown and represents a significant challenge in such monitoring projects.

1.5 Thesis structure

The main part of this thesis consists of three independent papers, either published or submitted to peer-review journals, organized into separate chapters. Additionally, one paper published and presented at the 83rd EAGE (European Association of Geoscientist and Engineers) annual conference and exhibition is presented in Appendix A. In Appendices E, F, G, H the abstract of papers co-authored during the Ph.D. are given and a summary of these papers are given in Section 5.2. A summary of the published/submitted papers is presented in the following:

Chapter 2 presents how two parallel fiber-optic cables can be used to track whales simultaneously using two fiber-optic cables, over a distance range of 60 km. Two different localization methods (a grid search and a Bayesian filter) are investigated and compared. These methods are found to provide complementary information. The grid search estimates individual locations (with detailed mismatch maps), which can be connected to tracks. In contrast, the Bayesian filter estimates the tracks directly and the associated swim direction and speed. A total of eight fin whales were successfully tracked within a five hours along cable section between 40 and 95 km from the interrogator unit. Additionally, we used ground truth data from geo-referenced seismic shots to assess the accuracy of the methods for both the locations and velocities obtained, finding the location accuracy to be roughly 100 m.

In Chapter 3, we investigate the feasibility of using Rayleigh wave dispersion curves to monitor a known quick clay area in Norway. The dispersion curves can be used to estimate the shear-wave velocity of the quick clay. As the shear stiffness is related to the

shear-wave velocity and will drastically decrease before a quick clay landslide, a potential monitoring system can look for changes in the shear-wave velocity over time. We test the concept by acquiring both active and passive data over seven months as a road is constructed on top of the clay. Such construction activities might influence the mass balance of the clay and potentially trigger a landslide. The data were recorded on a dedicated DAS array trenched roughly 40 cm into the clay before the road construction started. Shear-wave profiles were computed using two different surface wave inversion methods, one linearized and one non-linear method. The time-lapse analysis of the obtained shear-wave velocity profiles and the extracted dispersion curves show no significant variation in velocity over the monitoring period. Nevertheless, the obtained velocity profiles can be used as references to the current steady state of the quick clay.

In Chapter 4, we present a new spectral ratio method to estimate the average P- and S-wave quality factors, Q_p and Q_s, of the sedimentary package under the Oseberg C platform in the Norwegian North Sea. Quality factors are important for more accurate characterization of the subsurface and to obtain added information on physical processes within the earth. However, few methods compute the average quality factor value in sediments for both P- and S-waves. The proposed spectral ratio method uses data recorded on a station pair, one on bedrock and one on sediments. Data from a 3C broadband seismometer was used for the station placed on bedrock, and 172 4C receivers just south of the Oseberg C platform were used for the station placed on sediments. Each receiver gives individual Q estimates ranging from 64 to 137 for P-waves and 29 to 123 for S-waves. The Q_p estimates are more scattered, and hence, more uncertain than the Q_s values, due to the P-wave signal being closer to the background noise level. The method can be used for various regions, using appropriate raypath configurations connecting the source and the receiver.

In Appendix A, we describe a case study using a local earthquake recorded on a 120 km DAS array in Svalbard, Norway. Standard preprocessing methods and a simple beamforming method are used to improve the signal-to-noise ratio of the earthquake to extract better first-break arrivals, which are subsequently used in a grid search procedure to localize the event. The result is compared to those reported by the NORSAR and the Norwegian National Seismic Network (NNSN). The locations are found to be similar in a 17 km range of each other.

1.6 Contributions

The contributors to the papers presented in the thesis are as follows:

- **Paper 1, Chapter 2**: Simultaneous tracking of multiple whales using two fiber-optic cables in the Arctic. *Published in Frontiers in Marine Science.*

  This work was carried out by Robin André Rørstadbotnen. Jo Eidsvik provided the Bayesian Filter location method, which was adapted to the application in the

paper. Marin Landrø, Jo Eidsvik, John Potter, and Léa Bouffaut participated as supervisors. The rest of the authors participated in writing and editing the manuscript and carrying out the data acquisition.

- **Paper 2, Chapter 3**: Quick clay monitoring using distributed acoustic sensing: A case study from Rissa, Norway. *Submitted to Geophysics.*

  This work was carried out by Robin André Rørstadbotnen. Hefeng Dong provided the surface wave inversion methods, which were adapted to the applications in the paper. Kenneth Duffaut provided the rock physics modeling. Hefeng Dong, Martin Landrø, and Kenneth Duffaut participated as supervisors. The rest of the authors participated in writing and editing the manuscript and carrying out the data acquisition.

- **Paper 3, Chapter 4**: Average Q_p and Q_s estimation in marine sediments using a dense receiver array. *Published in Geophysics.*

  This work was carried out by Robin André Rørstadbotnen. Martin Landrø participated as supervisor.

- **Paper 4, Appendix A**: Analysis of a local earthquake in the Arctic using a 120 km long fiber-optic cable. *Published and presented as conference paper in EAGE 83rd annual conference & exhibition.*

  This work was carried out by Robin André Rørstadbotnen. Marin Landrø participated as supervisor. The rest of the authors participated in writing and editing the manuscript and carrying out the data acquisition.

Chapter 2

Paper 1: Simultaneous Tracking of Multiple Whales using two Fibre-Optic Cables in the Arctic

Robin André Rørstadbotnen[1,2], Jo Eidsvik[2,3], Léa Bouffaut[4], Martin Landrø[1,2], John Potter[1,2], Kittinat Taweesintananon[1,2,5], Ståle Johansen[1,2,6], Frode Storvik[2,7], Joacim Jacobsen[3], Olaf Schjelderup[2,7], Susann Wienecke[3], Tor Arne Johansen[9], Bent Ole Ruud[9], Andreas Wuestefeld[2,10], Volker Oye[2,10]

1 - Department of Electronic Systems, Norwegian University of Science and Technology (NTNU), 7491 Trondheim, Norway,

2 - Centre for Geophysical Forecasting, NTNU, 7491 Trondheim, Norway,

3 - Department of Mathematical Sciences, NTNU, 7491 Trondheim, Norway,

4 - K. Lisa Yang Center for Conservation Bioacoustics, Cornell Lab of Ornithology, Cornell University, Ithaca, NY, United States,

5 - PTT Exploration and Production Public Company Limited, Bangkok, Thailand,

6 - Department of Geoscience and Petroleum, NTNU, 7491 Trondheim, Norway,

7 - Sikt, 7037 Trondheim, Norway,

8 - Alcatel Submarine Networks Norway AS, 7075 Tiller, Norway,

9 - Department of Earth Science, University of Bergen, 5007 Bergen, Norway,

10 - NORSAR, Gunnar Randers vei 15, 2007 Kjeller, Norway.

Published by Frontiers in Marine Science 28 April 2023 (Rørstadbotnen et al. 2023)

Abstract

Climate change is impacting the Arctic faster than anywhere else in the world. As a response, ecosystems are rapidly changing. As a result, we can expect rapid shifts in whale migration and habitat use concurrent with changes in human patterns. In this context, responsible management and conservation requires improved monitoring of whale presence and movement over large ranges, at fine scales and in near-real-time compared to legacy tools. We demonstrate that this could be enabled by Distributed Acoustic Sensing (DAS). DAS converts an existing fiber-optic telecommunication cable into a widespread, densely sampled acoustic sensing array capable of recording low-frequency whale vocalizations. This work proposes and compares two independent methods to estimate whale positions and tracks; a brute-force grid search and a Bayesian filter. The methods are applied to data from two 260 km long, nearly parallel telecommunication cables offshore Svalbard, Norway. First, our two methods are validated using a dedicated active air gun experiment, from which we deduce that the localization errors of both methods are 100 m. Then, using fin whale songs, we demonstrate the methods' capability to estimate the positions and tracks of eight fin whales over a period of five hours along a cable section between 40 and 95 km from the interrogator unit, constrained by increasing noise with range, variability in the coupling of the cable to the sea floor and water depths. The methods produce similar and consistent tracks, where the main difference arises from the Bayesian filter incorporating knowledge of previously estimated locations, inferring information on speed, and heading. This work demonstrates the simultaneous localization of several whales over a 1800 km^2 area, with a relatively low infrastructural investment. This approach could promptly inform management and stakeholders of whale presence and movement and be used to mitigate negative human-whale interaction.

2.1 Introduction

Baleen whales play crucial ecosystemic roles in the oceans, from predators to prey, climate regulators, nutrient reservoirs, niche constructors enhancing biodiversity, and connectors between ecosystems (Roman et al. 2014, Lavery et al. 2014). After being brought to the brink of extinction, many species are recovering following the cessation of large-scale commercial whaling (Thomas et al. 2016). Nevertheless, their recovery is hampered by anthropogenic stressors associated with modern and industrialized ocean exploitation where pollution (acoustic, chemical, and thermal) coupled with ocean acidification, add to the primary threats of ship strikes and entanglement in fishing gear (Greene and Pershing 2004, Thomas et al. 2016).

In the Arctic, the climate is changing faster than anywhere else in the world (IPCC 2022), and the Svalbard archipelago is one of the fastest warming regions (Maturilli et al. 2013,

Nordli et al. 2014). This can be observed in many ways; e.g., through the rapid retreat of glaciers in the Svalbard area (Hagen et al. 1993, Schuler et al. 2020) and by the decrease in Arctic sea-ice (Stroeve et al. 2007, Comiso et al. 2008). The "Atlantification" of the Arctic alters sea-surface temperatures and circulation patterns, forcing some cetaceans to change their seasonal habits; e.g., the timing of their migration, the migration route itself, or even forcing them to seek alternative habitats (van Weelden et al. 2021). This impacts both endemic Arctic species and boreal visitor species (Hamilton et al. 2021); e.g., fin whales have recently been observed to change their observed presence in Arctic regions from late spring/early summer to the fall to year-round (Klinck et al. 2012). At the same time, human activities, their intensity, and impacts are also evolving with sea-ice loss; e.g., with the impending development of cross-Arctic shipping routes and openings for natural resource exploitation (Jaskólski 2021, Townhill et al. 2021). Hence, we can expect that human activities will intensify in species-rich areas (Hamilton et al. 2021).

Considering the region's dynamism, it is urgent to develop robust and scalable methods to draw the baseline of species' geographic range and habitat use to understand their ecology, which is challenging for highly mobile and pelagic baleen whales (Ahonen et al. 2021). The methods should also enable close to real-time monitoring to identify rapid changes and mitigate anthropogenic impacts. A key element is to be able to evaluate whales' positions both at large- and fine-scales. Current and common methods for tracking baleen whales include visual surveys (Cummings and Thompson 1971), satellite tracking (Lydersen et al. 2020, Höschle et al. 2021) or deploying widespread arrays of hydrophones to determine a whale's position from time difference of arrival and hyperbolic intercepts of its calls (McDonald et al. 1995). Nowacek et al. (2016) presents a review of recent technologies used for conservation-oriented behavioral studies of cetaceans while Harcourt et al. (2019) focuses specifically on methods applied to the conservation of right whales. Under the scope of localization and tracking, passive acoustic monitoring (PAM), using long-term hydrophone installations or towing arrays during short field trial periods, has proven reliable and cost-effective and has been used extensively since the late 1980's to quantify the seasonal presence of whales (Širović et al. 2013, Ahonen et al. 2021) and to estimate locations (see, e.g., McDonald and Fox (1999), Thode et al. (2000), Bouffaut et al. (2021)). However, individual hydrophones are often unevenly spaced, making fine-scale movement analysis difficult, and they are often sparse, resulting in undersampling of the vast ocean habitat of baleen whales (Ahonen et al. 2017; 2021). The sparse instrumentation can be largely attributed to the cost of purchasing, installing and maintaining these systems and the finite life span of their batteries. Therefore, we are in need of continuous-monitoring PAM systems that are cost-effective, spread over large areas and with sufficient spatial density to fill the gaps in existing capabilities. In addition, it would be highly desirable to be able to get measurements in near-real-time, rather than having to wait until recording instruments are recovered.

Over the last two decades, a new technology, Distributed Acoustic Sensing (DAS), has

emerged as a game-changer in remote acoustic sensing, with the potential to fill many of the monitoring gaps in the ocean. Connecting an 'interrogator' to the end of a 'dark' (unused) fiber in a fiber-optic cable allows acoustic data to be acquired continuously. Virtual acoustic sensors can be generated at spatial intervals along the cable as frequently as every meter, for up to 171 km along the fiber (Waagaard et al. 2021). Over 1.3 million km of offshore telecommunication cables are installed worldwide, creating an opportunity to increase remote acoustic sensing coverage both onshore and offshore. Currently, these virtual sensors do not have the sensitivity to rival dedicated hydrophones. However, with thousands lying along an extended cable, the beamforming gain available through signal processing, together with the ability to 'focus' on sources using the very long array, offers unique potential. DAS technology has already been applied to many different fields ranging from earthquake seismology (Lindsey et al. 2017) to geophysical exploration (Mestayer et al. 2011, Taweesintananon et al. 2021), near-surface monitoring (Dou et al. 2017), oceanography (Taweesintananon et al. 2023), water-born sound sources (Matsumoto et al. 2021), and passive acoustic monitoring of ships (Rivet et al. 2021) and baleen whales (Bouffaut et al. 2022, Landrø et al. 2022). Until recently, DAS has been collected from single fibers. However, there is growing interest in combining two different fibers, either in the same or in separate telecommunication cables, when configuration and access allow it (Wilcock et al. 2023).

Fiber-optic cables are often trenched for protection against anchoring and fish trawling. Depending on the sea bed type, the cables are usually laid in a line that covers the shortest possible distance to minimize cost and reduce latency. When interrogating straight-line cable segments, we generally encounter the well known left-right ambiguity (also known as 180° ambiguity) associated with linear arrays, in which it is impossible to determine which side of the array the source is located. Bouffaut et al. (2021) experienced this problem when tracking whales using the inner cable between Longyearbyen and Ny-Ålesund from a similar experiment in 2020 and Landrø et al. (2022) had the same issue when tracking a cargo ship. While it may sometimes be possible to resolve the left-right ambiguity if the environment breaks the symmetry, the only sure solution is to make the array two-dimensional. This can be achieved by curving the array (as it negotiates a 'corner', for example) or using a second array separated by a sufficient distance to provide a resolvable time of arrival difference, yet close enough to receive the same source signals. We exploit the availability of two such cables in this work.

We investigate and compare two different methods to track baleen whales using DAS: a Grid Search (GS) method (Havskov and Ottemoller 2010) and a Bayesian Filter (BF; see, e.g., Särkkä (2013)). These two methods were applied to data recorded on two fiber-optic cables connecting Longyearbyen and Ny-Ålesund in the Svalbard archipelago (Figure 2.1). We first exploited the ground truth generated by a single geo-referenced air gun source for calibration and evaluation of the accuracy of these two methods. A small air gun was used, in accordance with the permissions given by the authorities in Svalbard, to

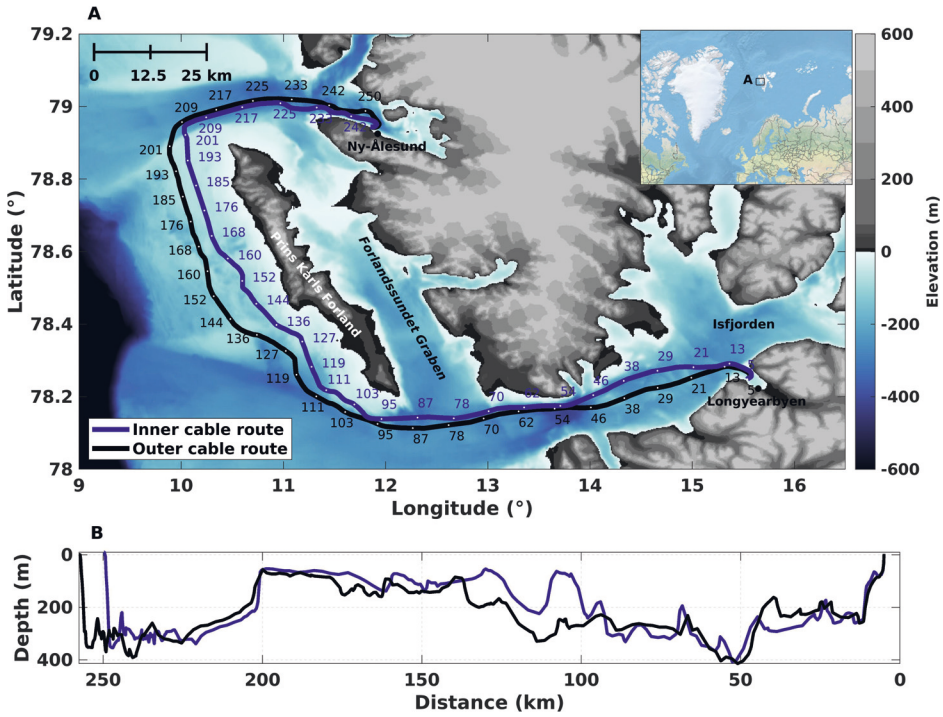

Figure 2.1: An overview map of the study area. (A) The fiber-optic telecommunication cables are located between Longyearbyen and Ny-Ålesund. Starting in Longyearbyen, the cables enter the Adventsfjorden 5 km after the interrogator unit; they then cross Isfjorden into the open ocean, bypassing Prins Karls Forland before entering the Kongsfjorden north of the settlement at Ny-Ålesund. The entire length of both telecommunication cables was interrogated using four interrogator units. However, only data from the two units located in Longyearbyen have been used in this work. (B) The ocean depth profiles along the fiber paths, the cables are trenched an additional 0–2 m into the seafloor.

minimize disturbance and potential harm to marine life. Then, over a 5.1 h period recorded on a 60 km portion of the cable, up to eight fin whales (*Balaenoptera physalus*) were successfully tracked.

The chapter is organized into five main parts. First, the distributed acoustic sensing data are presented, where the experimental set-up, the air gun, and fin whale data are introduced. The second part contains information on the methods used to obtain the results. The data conditioning, time of arrival picking and computation of empirical detection range are first presented, followed by the localization methods, the GS and the BF. Then, the results from the air gun and fin whale tracking are given, as well as individual fin whale song characteristics. The results are discussed in part four. Firstly, the localization errors are discussed, followed by comparing the two localization methods and, finally,

DAS-based localization for whale conservation. We conclude the chapter by presenting the conclusions.

2.2 Distributed acoustic sensing data

2.2.1 Experimental set up

Currently, it is common practice to include more optical fibers than initially required within one fiber-optic telecommunication cable, to enable network growth and increase redundancy at a minimal incremental cost. Using Alcatel Submarine Network Opto-DAS interrogators, we tapped into two out of 24 standard single mode G.652D fiber bundles within each of two existing submarine telecommunication cables connecting Longyearbyen and Ny-Ålesund in Svalbard, Norway (Figure 2.1). The OptoDAS interrogators send linear optical frequency-modulated swept pulses into the fiber and interrogate the Rayleigh backscattering caused by inherent inhomogeneities in the fibers (Waagaard et al. 2021). Such inhomogeneities are displaced by, e.g., acoustic waves from whales impinging on the fiber, which can be detected as phase changes in the Rayleigh backscatter. The time-differentiated phase is obtained by continuously comparing the backscattered response from one pulse to the next. This is typically done in two steps: first, the phase is spatially differentiated between regularly spaced channels along the optical fiber, then compared to the next pulse's response. The time differentiated phase is stored by the interrogator and later converted to fiber strain during the data processing (for more information on this conversion, see, e.g., Hartog (2017)). Normal signal strength decay along the fiber is about 0.2 dB/km, depending on the quality of the optical fibers and connectors. The returned signal strength from 100 km is, therefore, $\simeq -40$ dB with respect to 1 km. To date, the maximum cable length that has been interrogated with a signal above the noise floor is 171 km, applying low-loss cables. On commercial telecommunication cables, the range is typically 140–150 km (Waagaard et al. 2021). Therefore, to collect data on the entire 260 km length of each separate telecommunication cable, four interrogator units were deployed; two in Ny-Ålesund and two in Longyearbyen, one for each direction on each telecommunication cable. Both optical fibers were dark, i.e., not used for data transfer. We denote the two telecommunication cables as the 'inner cable' (the cable closest to Prins Karls Forland) and the 'outer cable' (the cable furthest from Prins Karls Forland; see Figure 2.1). The first 5 km portions of the telecommunication cables at the Longyearbyen and Ny-Ålesund ends are trenched on land. The subsequent 248 km portion of the inner cable and the 252 km for the outer cable are sub-sea cables buried 0–2 m below the seafloor. Only data recorded on the sub-sea part of the telecommunication cables have been analyzed in this work.

The four interrogators were installed over two periods in the summer of 2022. The first interrogator started recording in Ny-Ålesund 02 June 20222 and is still recording as of 21 April 2023. The latter three were installed roughly two months later, the first two in Longyearbyen on 17 August 2022 and the last unit on 19 August 2022 in Ny-Ålesund.

The OptoDAS interrogators were each connected to a different optical fiber within the inner and outer telecommunication cables. The same optical fiber was not used with more than one interrogator for two reasons: (1) The laser pulses emitted by an interrogator at one end of a fiber could damage a unit connected to the same fiber at the other end. (2) There could be unknown interference effects arising from two overlapping laser pulses traveling in opposite directions in the same fiber. All four interrogators used a gauge length of 8.16 m with virtual channels sampled every 4.08 m over a 136 km distance. The recorded data were transferred near-real-time to NTNU in Trondheim, Norway, using the network infrastructure described in Landrø et al. (2022). The data were also saved locally on Network Attached Storage (NAS) discs on the interrogator units as a backup. We used light pulses with a free-space wavelength of 1550 nm with a sampling period of 1×10^{-8} s at the optical receiver. The data were recorded at a sampling frequency of 625 Hz. The interrogated distance ensured that the entire length of both telecommunication cables was covered, with a $\simeq$10 km overlap east of Prins Karls Forland (roughly $\pm$5 km of the 127 km mark in Figure 2.1A). The three interrogators installed in mid-August recorded data continuously for roughly two months (with some breaks due to, e.g., power outages) before being shipped back to mainland Norway. Only data recorded by the interrogators in Longyearbyen have been analyzed in this work.

2.2.2 Air gun data

A dedicated air gun survey was performed on 06 September 2022 to allow us to estimate the errors related to the two localization methods used in this work. Permission was given by the authorities in Svalbard to minimize disturbance and potential harm to marine life. No whale vocalizations were observed in the DAS data from the survey period. The air gun was towed 10 m behind the ship, which recorded its position every second from an onboard Global Positioning System (GPS).

The chamber of the air gun was 0.1311 m^3 (20 in^3), and the average chamber pressure used was 12000 kPa (120 bar), producing a source of 100–200 kPa-m (1–2 bar-m; the pressure one meter from the source, corresponding to 220 dB re. 1 μPa at 1 m). Note that fin whale source levels observed along the Norwegian coast is reported to be 190.5 ± 7.4 dB (Garcia et al. 2019). The air gun shots produced a valuable data set that we have used to calibrate the analysis in this paper.

The air gun data were acquired for roughly 3.5 h on 06 September 2022 with an inter-shot interval of $\simeq$60 s (with some longer breaks due to malfunctions in the acquisition system), resulting in a total of 183 shots. For this work, we selected a 41-shot sub-set covering source locations above each cable and in between (see Figure 2.2). When fired directly above one of the cables, an air gun signal could be observed over $\simeq$6 km in each direction along the cable as well as on the adjacent fiber-optic cable if the inter-cable distance was lower than 6 km (for an example of a recorded air gun shot, see Supplement Material Figure B.1). It is possible to increase the detection range by applying a filter in

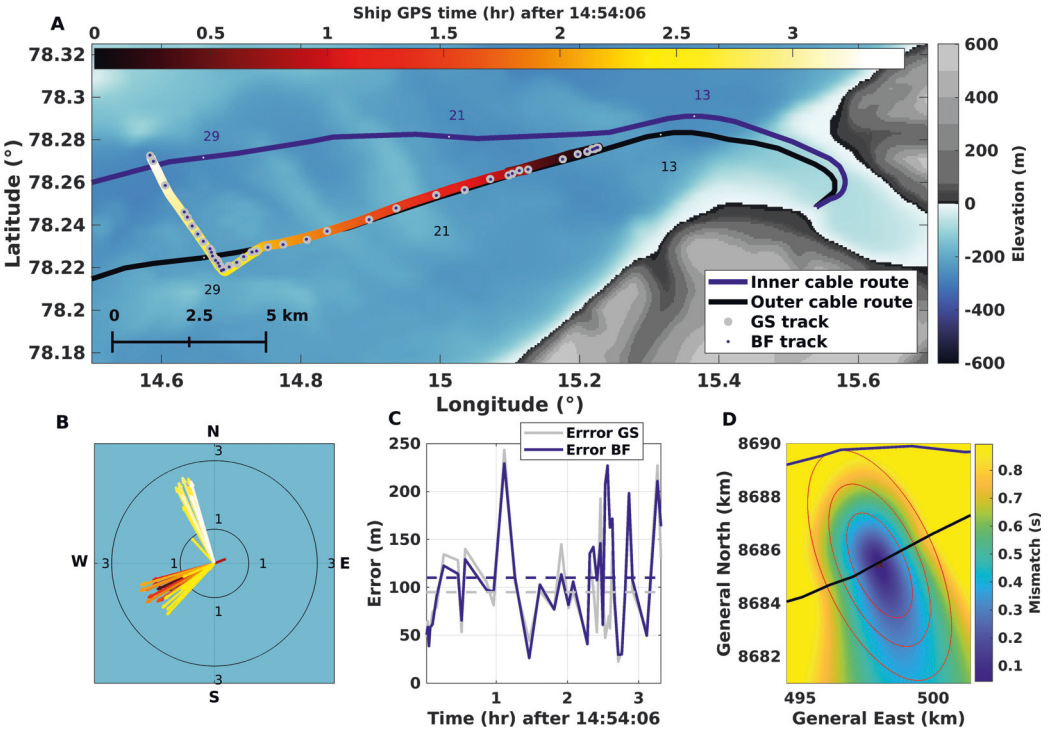

Figure 2.2: Tracking the air gun with known shot locations. (A) Overview of the first 35 km section of cables, showing ship track, color-coded from dark to light (by origin time of shots) overlaid with the estimates from the grid search (GS; big gray circles) and the Bayesian filter (BF; small blue circles). (B) The associated velocities of the ship are estimated by the BF with the same color coding as (A). (C) The error between the estimated location and the known position of the ship at the shot origin time. (D) RMS mismatch from GS overlaid by the error ellipse (1x, 2x, 3x standard deviation) from the BF based on a representative shot with an error (100 m) close to the mean error of all shots.

the frequency-wavenumber domain ($f - k$ filter), which provides processing gain.

2.2.3 Fin whale data

To test our methods for baleen whale tracking, we selected a 5.1 h portion of the DAS dataset acquired on 22 August 2022 that proved to contain 1808 fin whale 20 Hz-calls. Note that we performed laser sweep calibrations on both interrogator units between 11:13 and 11:23 on that day. The fin whale song is described in the literature as a series of 20-Hz-centered down sweeps of $\simeq$1 s duration (Thompson et al. 1992, McDonald et al. 1995). These calls, thought to be produced only by males, have been recorded around Svalbard between July and September/October (Ahonen et al. 2021), in association with local ship-based visual surveys. A subset of 188 calls was used to demonstrate the feasibility of

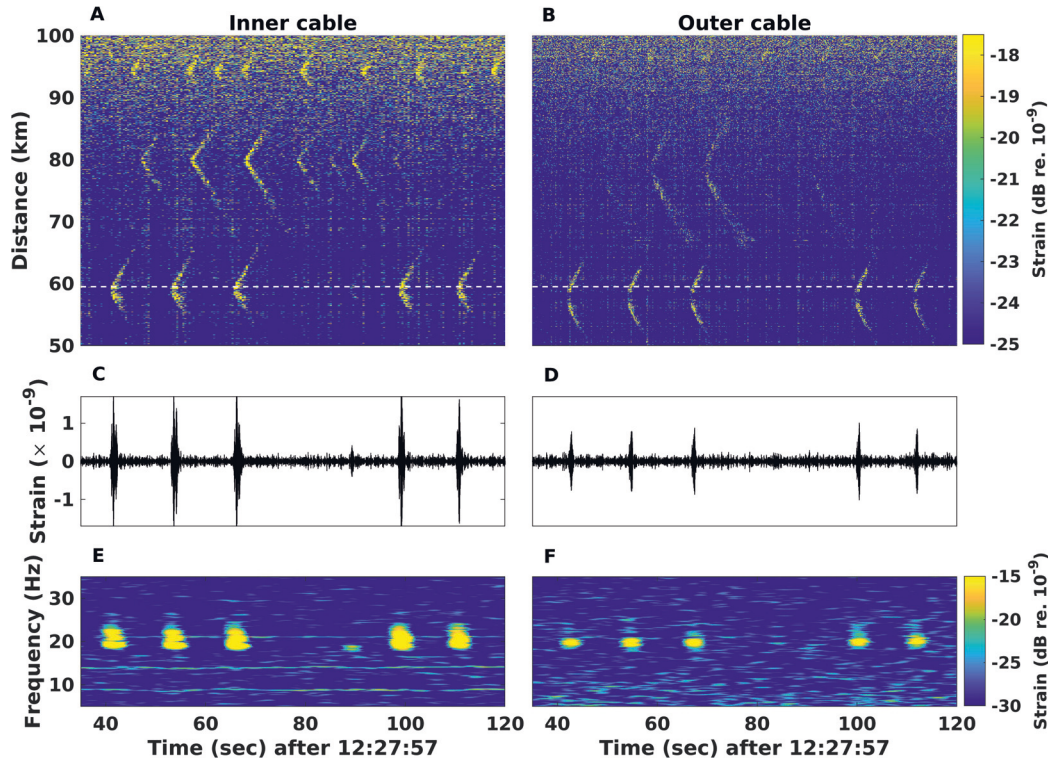

Figure 2.3: Distributed acoustic sensing recording of fin whale vocalizations on two fiber-optic cables on 22 August 2022 at 12:27:57 UTC. (A, B) Spatio-temporal ($t-x$) representation of three simultaneously vocalizing whales on the inner cable (A) and the outer cable (B) between 50 and 100 km. Waveforms (C, D) and corresponding spectrograms ($t-f$; E, F) at 59.52 km, represented by the white dashed line in (A, B), displaying portions of two series of fin whale 20 Hz calls and a back-beat at $\simeq$95 is recorded on both cables with an average inter-call interval of 13 s. The spectrograms were computed using a Hann window of 512 samples with 98% overlap.

using two parallel fiber-optic cables to track several whales simultaneously.

Figure 2.3 shows an example of a fin whale 20 Hz-call series recorded over a 90 s time window on both the inner and outer cables between 50 and 100 km on 22 August 2022 at 12:27:57 UTC, where (A, B) are spatio-temporal representations underlining the presence of at least three vocalizing whales at $\simeq$60 km, $\simeq$80 km and $\simeq$95 km, (C, D) the waveforms of the calls emitted by the whale at 60 km and (E, F) the associated spectrograms. Note that the distances given (in this case, 50 to 100 km) are the length of fiber from the interrogator to the channel recording the vocalization.

From the repetitive 20 Hz down-sweep signals, their frequency span (between [18-25] Hz) with a duration less than 2 s and average inter-call intervals of 13 s (for the whale at 60 km;

the whales at 80 km and 95 km have respective average intervals of 10 s and 9 s), we can clearly identify these as characteristic fin whale 20 Hz song, as well as an example of a back-beat at roughly 90 s (Watkins et al. 1987, Thompson et al. 1992)).

2.3 Methods

2.3.1 Data conditioning

The following preprocessing steps were carried out to prepare the data for analysis and improve the signal-to-noise ratio (SNR). Initially, the time-differentiated phase was converted to longitudinal strain (Hartog 2017). Then the data were resampled in time and space to cover the regions of interest. Recorded air gun signals contained frequencies between 5 and 45 Hz, and the sample rate was reduced by a factor of 5, from 625 Hz to 125 Hz. Similarly, the fin whale vocalization carried frequencies between 18 and 25 Hz and was resampled by a factor of 8 to 78 Hz. The data were tapered and band-pass filtered to focus on the frequency band of interest. A Tukey window was applied to the data and subsequently bandpass filtered using a fourth-order Butterworth filter to focus on each signal of interests' dominant frequencies. The cut-off frequencies were chosen to focus on the frequency range listed above. Next, a 2D median filter over 3×3 datapoints was applied to suppress common-mode noise. Finally, a frequency-wavenumber ($f - k$) fan filter was applied to preserve only acoustic waves propagating around sound speed in sea-water and sediments, keeping everything with a propagation speed between 1000 and 3000 m/s.

2.3.2 Time of arrival picking

The data were visually inspected using spatio-temporal representations to identify signals of interest (Bouffaut et al. 2022). This visualization gave an overview of the recorded signals over several channels and was used by one observer to pick the first times of arrivals manually. The first time of arrivals were chosen at a sudden amplitude and frequency changes in the onset of the acoustic signal. To constrain the time of arrival picking burden, a maximum of 12 arrival times were selected from both cables, with an average inter-channel distance between the picks of 600 m (depending on the range from source to receiver). An exact inter-channel distance was not used due to the variation of SNR along the cable. We avoided using arrivals on the tail and focused on arrivals near the apex to avoid picking in the portions of the data dominated by normal modes. However, due to the known directivity of DAS arrays (see, e.g., Papp et al. (2017)), we did not pick arrivals in close vicinity to the apex. When the signal quality from the two cables was significantly different, which was often the case when a whale was vocalizing near one cable, and at a greater distance to the other, fewer picks were selected from the cable with the poorer quality. In the worst cases, we used only one pick from the cable with lower signal strength only to resolve the left-right ambiguity.

2.3.3 Track estimation

Two different localization methods were developed to estimate the source positions from traveltime information detected at the fiber-optic cables: a Grid Search (GS) method and a Bayesian Filter (BF). We denote the observed time of arrivals at the fiber channel locations by $T_{i,j}^{(obs)}$, $i = 1, \ldots, n_j$, $j = 1, 2$. Here, index i refers to the channel used to pick the time of arrival, and j denotes the telecommunication cable used (e.g., $j = 1$ corresponds to the inner cable and $j = 2$ to the outer cable). Alternatively, one could list these arrival times data in a length $n_1 + n_2$ vector, but the i and j index clarify that data are acquired and processed on two different cables.

In the forward model, we assume that a signal is emitted at time η from location (x, y, z), where x and y are the geographical coordinates and z is the depth. We use a reference depth of $z = z_{ref}$ set to 20 m for whales (known to be a typical call depth for fin whales (Stimpert et al. 2015)) and 3.5 m for the air gun (set prior to the acquisition). The theoretically modeled arrival time, $T_{i,j}(x, y)$, is computed from the origin time of the event studied η and the traveltime for the Euclidean distance from the event to the receiver $t_{i,j}(x, y)$:

$$\begin{aligned} T_{i,j}(x,y) &= \eta + t_{i,j}(x,y), \\ t_{i,j}(x,y) &= \frac{\sqrt{(x - x_{i,j})^2 + (y - y_{i,j})^2 + (z_{ref} - z_{i,j})^2}}{v_p}. \end{aligned} \tag{2.1}$$

where $(x_{i,j}, y_{i,j}, z_{i,j})$ is the coordinate of channel i at fiber j and $v_p = 1440$ m/s is the speed of sound in water. The sound speed is based on previous study of Arctic water (Gavrilov and Mikhalevsky 2006) and the minimum error obtained in the air gun study.

2.3.4 Grid search position estimation

The GS method uses equally spaced grid points around a prior guess of the source location. Such a systematic search computes the traveltime for all possible locations in a survey area to find the best matching source location. This kind of GS procedure has been adapted from earthquake seismology (see, e.g., Havskov and Ottemoller (2010)) and it has been previously applied to earthquakes recorded on DAS arrays by Rørstadbotnen et al. (2022). GS methods are also commonly used for whale localization (see, e.g., Wilcock (2012), Abadi et al. (2017)).

In this work, the grid points are defined from the channels receiving the first signal and laid out on a horizontal grid of (x, y) coordinates. The grid points were set at 25 m intervals, covering a 20 km by 20 km area centered around the receiving channel. For each element of the grid, the reference time η is calculated by shifting the computed origin time to the

'correct' timing, given by

$$\eta = \frac{1}{n_1 + n_2} \sum_{j=1}^{2} \sum_{i=1}^{n_j} \left[T_{i,j}^{(obs)} - t_{i,j}(x, y) \right]. \tag{2.2}$$

When the theoretical traveltime and reference time in equation (2.2) are known for each grid point, the root mean square (RMS) misfit between observed and computed traveltimes is given by

$$M(x, y) = \left(\frac{O(x, y)}{N} \right)^{1/2}, \quad O(x, y) = \sum_{j=1}^{2} \sum_{i=1}^{n_j} (T_{i,j}^{(obs)} - T_{i,j}(x, y))^2, \tag{2.3}$$

where the normalization in the RMS computation is typically performed based on the total number of time of arrival picks used, $N = n_1 + n_2$. The estimated location of the source is the grid point with the lowest misfit, i.e., the global minimum RMS across the GS volume. The misfit function depends on the geometry of the source, the time of arrival picks, and cable pick locations.

Rather than evaluating the mismatch on a dense grid, Newton's method can be used to solve for the position (x, y). Using boldface for vectors and matrices, we start with an initial guess for the position $\boldsymbol{p}^0 = (x^0, y^0)$ and iterate by

$$\boldsymbol{p}^r = \boldsymbol{p}^{r-1} - \left[\frac{d^2 l(\boldsymbol{p}^{r-1})}{d\boldsymbol{p}^2} \right]^{-1} \frac{dl(\boldsymbol{p}^{r-1})}{d\boldsymbol{p}}, \quad r = 1, \ldots. \tag{2.4}$$

Here, $l(x, y) = -O(x, y)/2\tau^2$ is a statistical likelihood version of equation (2.3), where we assume that the traveltime observations are made with additive independent and Gaussian distributed noise with variance τ^2. The guided search provided by equation (2.4) converges within a few iterations r. We denote the resulting optimum value by $\hat{\boldsymbol{p}}$. This kind of optimization involves re-setting the reference time η (see equation (2.2)) at each step of the iterative scheme. By investigating residuals from modeled and known air gun shot positions, the noise standard deviation was found to be $\tau = 5.4$ ms.

A probabilistic view enables uncertainty quantification. In particular, the curvature of $l(\boldsymbol{p})$ at the optimum value can be used to assess the covariance matrix of the position. Together with the optimum, this leads to a Gaussian approximation for the position:

$$\boldsymbol{p} \sim N(\hat{\boldsymbol{p}}, \hat{\boldsymbol{\Sigma}}), \quad \hat{\boldsymbol{\Sigma}} = - \left[\frac{d^2 l(\hat{\boldsymbol{p}})}{d\boldsymbol{p}^2} \right]^{-1}, \tag{2.5}$$

where $N(\hat{\boldsymbol{p}}, \hat{\boldsymbol{\Sigma}})$ denotes a normal distribution with mean $\hat{\boldsymbol{p}}$ and covariance matrix $\hat{\boldsymbol{\Sigma}}$ holding the variance and covariance of the position estimate. The ellipse-shaped contours of the Gaussian probability density function (PDF) provide a comparison with that achieved using the GS, as shown in Figure 2.2D. If there is prior information about the position $\boldsymbol{p}$, a Bayesian approach with a Gaussian approximation for the posterior PDF works similarly.

2.3.5 State space model and Bayesian filtering

With the association of a state space model and a BF, we can connect the predictions at different locations and also consistently estimate the source speed and direction. Similar uncertainty assessments to traveltime data have been applied to, e.g., satellite positioning accuracy (Yigit et al. 2014) and location estimation with borehole seismic data (Eidsvik and Hokstad 2006).

Let s_k, $k = 1, \ldots$ denote time steps and represent positions and swim velocities at time s_k by $\boldsymbol{m}_k = (x_k, y_k, u_k, v_k)$. Position $\boldsymbol{p}_k = (x_k, y_k)$ and east and north velocities u_k and v_k are next coupled over time in a state space model. Traveltime data $T^{(obs)}_{i,j,k}$ at time s_k are modeled via the likelihood model $l(\boldsymbol{m}_k)$ as described below equation (2.4). Note that measurements carry direct information only about the position $\boldsymbol{p}_k$. However, now that a model connects positions and velocities over time, data are implicitly informative about all process variables.

For the dynamical model part, taking state variables from one time to the next, we assume constant velocity and additive noise $\boldsymbol{\epsilon}_k$, obtaining

$$\boldsymbol{m}_k = \boldsymbol{A}_{k-1,k}\boldsymbol{m}_{k-1} + \boldsymbol{\epsilon}_k, \quad \boldsymbol{\epsilon}_k \sim N(\boldsymbol{0}, \boldsymbol{S}_{k-1,k}), \tag{2.6}$$

$$\boldsymbol{A}_{k-1,k} = \begin{bmatrix} 1 & 0 & \Delta_{k-1,k} & 0 \\ 0 & 1 & 0 & \Delta_{k-1,k} \\ 0 & 0 & 1 & 0 \\ 0 & 0 & 0 & 1 \end{bmatrix},$$

where the time interval $\Delta_{k-1,k} = s_k - s_{k-1}$ and the matrix $\boldsymbol{S}_{k-1,k}$ is a 4×4 positive definite covariance matrix for the noise in this process model, accounting for potential acceleration. Equation (2.6) defines a Markovian structure where the state at time s_k depends on the previous states only through the one at time s_{k-1}. An associated formulation of this model in equation (2.6) is provided by a conditional PDF $p(\boldsymbol{m}_k|\boldsymbol{m}_{k-1})$. Initially, at the time of the first detection, we assume a vaguely informative prior model $\boldsymbol{m}_1 \sim N(\boldsymbol{\mu}, \boldsymbol{\Sigma})$, where the mean $\boldsymbol{\mu}$ is composed of the average positions of the cable locations where the first picks are detected and with 0 velocity. The covariance matrix $\boldsymbol{\Sigma}$ is set to have significant standard deviations (1000 m for positions and 5 m/s for velocities).

We denote all data available up to time s_k by

$$\boldsymbol{D}_k = \{T^{(obs)}_{i,j,k'}; \quad i = 1, \ldots, n_{j,k'}; \quad j = 1, 2; \quad k' \leq k\}.$$

The data are assumed to be conditionally independent over time. With the Markovian assumptions and that of conditionally independent measurements, methods from Bayesian filtering allow us to estimate the location and velocity $\boldsymbol{m}_k$ at a time s_k, given all data up to that time k (see, e.g., Särkkä (2013)). For efficient calculations that can be run online, we fit a Gaussian PDF to the filtering distribution at each observation time. This represents

extensions of equations (2.4) and (2.5), where the mean of the predictive distribution given earlier data is used to initiate the Newton search. In terms of probability distributions, this means we are approximating the filtering PDF $p(\boldsymbol{m}_k|\boldsymbol{D}_k)$ by a Gaussian model. This filtering procedure is run recursively over time steps $k = 1, 2, \ldots$, and it offers a highly applicable tool for conducting real-time analysis of the traveltime data.

By having positions and velocities in a state space model, we can obtain probabilistic state estimates and associated uncertainties at any time s_k, not only at the measurement sites and times.

2.3.6 Computation of empirical DAS detection range

Using the estimated whale position $(x_w, y_w, z_{ref} = 20 \text{ m})$ from either the GS or the BF, we estimated an empirical detection range from this position to the position of the DAS channel that detected the last whale signal $(x_{i,j}, y_{i,j}, z_{i,j})$ before it is lost in the background noise level:

$$r_{max} = \sqrt{(x_w - x_{i,j})^2 + (y_w - y_{i,j})^2 + (z_{ref} - z_{i,j})^2}, \tag{2.7}$$

where r_{max} denotes the maximum empirical Detection Range and is taken as a straight line distance.

2.4 Results

2.4.1 Air gun tracking

The geo-referenced air gun survey detailed in Sections 2.2.2 is used to calibrate and evaluate the error of both localization methods (Wuestefeld et al. 2018). Figure 2.2A shows the track obtained from the ship's GPS overlaid with the locations of the 41 shots as obtained using the grid search (GS; Section 2.3.4) and the Bayesian filter (BF; Section 2.3.5). Figure 2.2B displays the BF estimate of the direction and speed of the ship for the whole track. The warm color-scale indicates time on the GPS trajectory on both sub-figures. Figure 2.2C displays the localization error of each method evaluated for air gun locations 10 m behind the ship's GPS positions. Figure 2.2D shows the mismatch between observed and calculated arrival times from the GS overlaid with error ellipses from the BF.

Both methods follow the ship's track for the selected 3.5 h of recordings. The estimated speed is roughly 1.8 m/s, which agrees with the average speed obtained from the GPS position, 1.9 m/s (see supplemental material Figure B.1). There are three areas where the BF underestimates the ship speeds, each associated with the ship making a sharp turn or a loop. In these cases, the BF predictably estimates the ship to travel a shorter distance than it actually does. The estimated mean error standard deviation is 94.9 ± 51.1 m and 108.8 ± 53.7 m for the GS and the BF, respectively. Errors are highest when the ship makes turns and when the signal quality on one cable is poor.

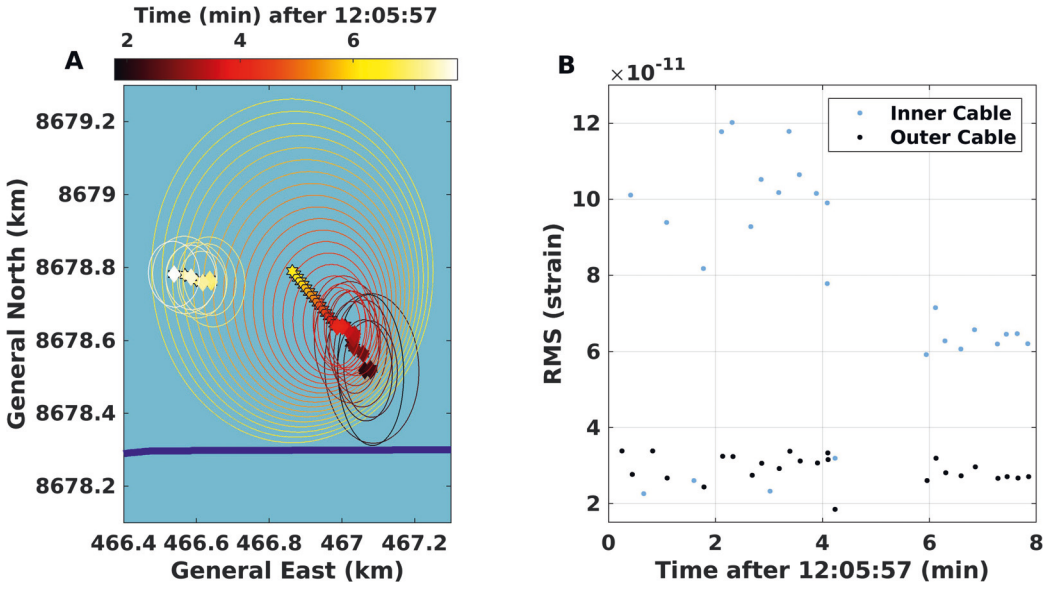

Figure 2.4: Prediction of whale location during an inter-series interval. (A) A subsection of a whale track near the inner cable (the bold blue line; 12:06 – 12:14) with a 1 min 51 s inter-series interval. BF tracks are computed roughly every 10 s, and in inter-pulse intervals, we predict the position without updating (indicated by the hexagram). Diamonds indicate the predictions with observed data, while the ellipses show 90% coverage regions constructed by the BF. (B) The associated RMS amplitude of the calls used in the localization.

2.4.2 Fin whale tracking

Figure 2.4A shows the application of the BF to evaluate a fin whale track over an interrupted series of calls (data at 12:07 to 12:14, later referred to as an 8 min portion of whale track (B)) and 2.4B the corresponding RMS levels of the calls. The RMS levels are computed in the spatio-temporal domain by a rectangular windowen closing the recorded whale call. For example, for the whale call at 60 km in Figures 2.3A, B, a rectangular window covering 5 km on each side of the apex and from the start of the apex to 6 s after the apex is used.

Each diamond in Figure 2.4A indicates predictions based on observed data, while hexagrams represent intermediate predictions without observed data. The ellipses correspond to the error expressed in the BF version of equation (5), with a 90% coverage region. The plot shows a portion of whale B's track lasting roughly 8 min and an Inter-Series interval (ISI) of 117 s. From the BF error ellipses, it is clear that the computed variances decrease as the whale track builds up over many time steps. Locations are computed roughly every 10 s for the track. When the Inter-Call interval (ICI) is longer than 10 s, the BF predicts the location based on the previous track locations and velocities without updated uncer-

tainty. Here, we have an ISI of 2 min, and we compute 12 predictions with a straight-line prediction and increasing uncertainty. When the whale vocalizes after the 2 min pause, the BF finds this new position based on the last prediction, and the new location is within the uncertainty of the prediction. This means that we are, most likely, still tracking the same whale. However, the whale did change course, heading more West during the ISI and it increased its swim speed somewhat, traveling slightly further than the BF prediction. We are thus able to show that interruptions in vocalization can be associated with changes in swim speed and direction.

Figure 2.5A shows the overview plot of all whale tracks colorcoded by the time of vocalizations, where Figures 2.5B, D, F, H are zoomed-in representations of the tracks, and Figures 2.5C, E, G, I the directional swim speeds estimated by the BF. Following the protocol described in the previous paragraph, we found eight distinct whale tracks within the five analyzed hours, denoted by the sequential letters (A) to (F) according to the time of the first vocalization in each track.

Whale track (A) started at a distance of 50 km from the interrogator unit at 09:28 (all times are given in UTC) and headed East for 72 min before contact loss. Just before losing contact with whale (A), whale track (B) started at 54 km, heading North-West for 160 min before the signal ceased. During this period, we also show the start of a vocalization series from three other positions along the cable, around 60 km, 80 km, and 95 km (see Figure 2.3), associated with tracks (F), (D), and (E), respectively.

Whale track (C) started around 72 km and headed North. The contact lasted roughly 10 min from 11:23. The interrogator calibration mentioned in Section 2.2.3 happened between 11:13 and 11:23, and vocalizations from both whale (B) and (C) were lost. No calls associated with whale track (C) are observed in the data prior to 11:13.

Whale track (D) started just after whale track (C), at 11:42, at roughly 80 km from the interrogator unit, lasting 113 min. This track went South before heading North-East over roughly 7 km before looping back West before contact loss. A few vocalizations were localized near track (C) but three hours later (14:20). They are denoted by track (H).

Whale track (E) started the furthest from the interrogator. Calls started at 12:20, South of Prins Karls Forland at 95 km and were detected for 71 min. The background noise level is significant at these long distances, making arrival time picking challenging, especially for the outer cable due to elevated noise and the high inter-cable distance. This increased the uncertainty of the estimated track. Nevertheless, the track headed East for roughly 2.7 km, where it turned and shifted to the North-East. Considering the uncertainty mentioned above and localization error of $\simeq$100 m, two whales could have vocalized simultaneously and parted ways after 1.5 km, one continuing East and the other North-East.

Whale track (F) started at 62 km at 13:30, 18 min after the end of track (B), and headed West. The 4.8 km distance between the two tracks would have required the whale of track

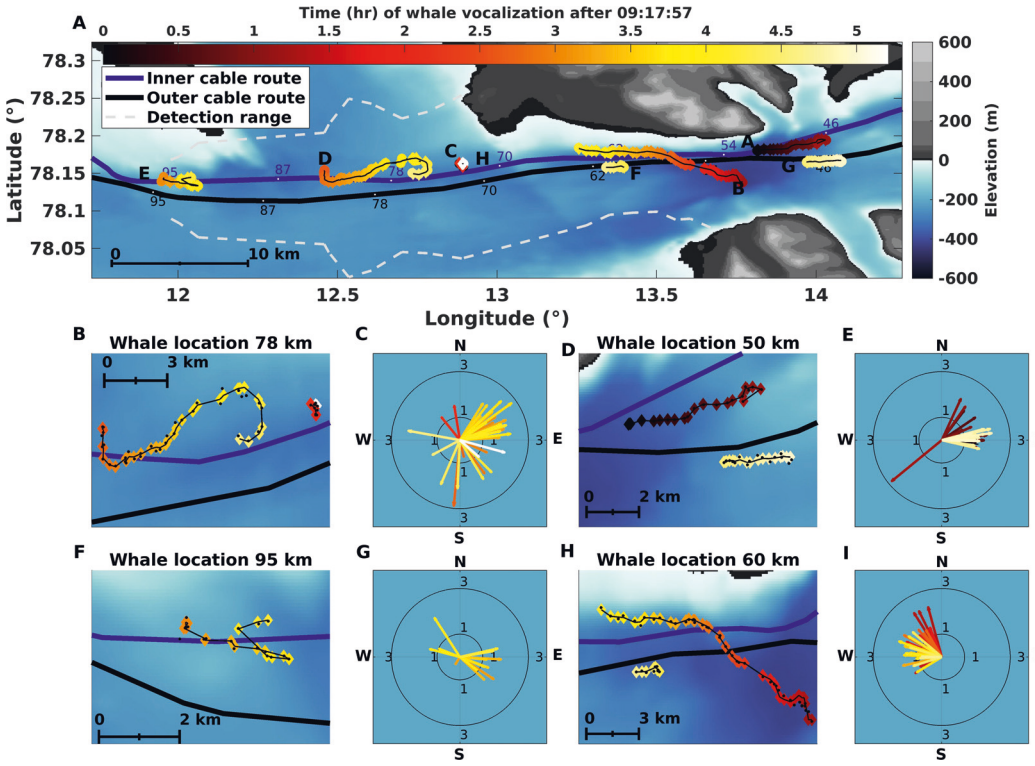

Figure 2.5: Simultaneously tracking multiple whales using fiber-optic cables in the Arctic. (A) Overview of a 60 km long section of the cables, showing the positions and tracks of up to eight acoustically-detected whales, color-coded from dark to light over a 5.1-hour period. Note that the GS and the BF have been plotted in the same color and shape to better illustrate the tracks. The two dashed lines show an attempt to estimate an empirical whale detection range directly from the DAS data using vocalizations every 10 min for each whale track. (B, D, F, H) Show zoomed-in detailed positions and tracks of the four areas with whale detections. We use the same color coding as in (A) for the BF, while GS has been plotted as black dots to better see the differences in the estimated positions. (C, E, G, I) show the corresponding swim velocities as polar plots for these tracks.

(B) to have more than doubled its maximum swim speed (from 2 m/s to 4.4 m/s). While this is not entirely unrealistic (fin whales have been reported to be able to increase swim speed between singing bouts (Clark et al. 2019)) we chose the conservative approach of considering the two tracks separately.

The first column of Figure 2.6 shows the RMS of received fin whale vocalization amplitudes for whale tracks (B), (C), (D), (F), and (H) over the 5.1 h studied (for whales (A), (E), and (G), see supplemental material Figure B.2), calculated as in Figure 2.4B. We assume that a given fin whale produces 20 Hz songs with an almost stable source level over

a short period (Watkins et al. 1987, Garcia et al. 2019). The peaks traced out by the RMS values of detected strain reflect the fact that whale B crosses the outer fiber at a more perpendicular angle than the inner cable, the second peak being less sharp than the first. The minimum strain at which we can detect the vocalizations is observed to be $\simeq 2 \times 10^{-11}$, which constrains the maximum detection range. It is also interesting to note that the RMS amplitude peak of the two whale B crossings are similar, indicating that the two cables have similar sensitivities. The second column in Figure 2.6 shows a zoomed-in version of the calls of whale tracks (B) and (D) to illustrate the ICI and the ISI (for the same plot for whale tracks (A), (E), and (G), see supplemental Figure B.2).

We evaluated an empirical DAS detection range following Section 2.3.6, every 10 min, for all whale tracks. The detection range is represented as white dashed lines in Figure 2.5A. The obtained range does not monotonically decrease with fiber distance as whale track (D) at 80 km shows a longer range, 9.4 km, compared to, e.g., whale track (H) at 60 km with a range of 6.0 km. This suggests that other effects, such as coupling or the sediment properties, play a role or that the whales we observed at 80 km produced higher intensity calls than the whales at 60 km. This is not uncommon, e.g., Garcia et al. (2019) observed a significant variation in call levels and estimated fin whale sound intensity levels along the Norwegian coast to range from 186.3 ± 7.1 to 195.8 ± 4.4 dB. Moreover, whale (E) displays the lowest range (2.4 km). The large difference for whale (E) is believed to mainly be due to the increased background noise level at the location.

2.4.3 Fin whale individual characteristics

Over the 5.1 h of analyzed data, five fin whale tracks were analyzed over a minimum of 45 min, providing insight on a few critical measurements for the species at the individual scale, based on a male 20 Hz song. We analyzed the sounds associated with each fin whale trajectory, reporting the total number of calls, average ICI, average ISI, and average swim speed in Table 2.1. Averages are associated with their standard deviation denoted by the $\pm$ symbol. Note that we excluded the first and last call series in each track as it is not clear if they contain a complete set of vocalizations.

Blue whale song is geographically distinct with differences in call time-frequency characteristics and repetition (ICI and ISI; McDonald et al. (2006)). Our description of fin whale song follows Watkins et al. (1987), where a call series is defined as a group of at least five fin whale vocalizations, ICI corresponds to the time stretch between two consecutive 20 Hz calls that are < 60 s, and ISI when the call interval is longer. Intervals are measured on a spatio-temporal representation of the signals, where the reference timings are picked along the same channel. Note also that the interrogator calibration break interval (11:13 to 11:23) was neither included in the ICI nor the ISI estimations.

While peak frequencies are fairly stable for fin whales, the most regionally-distinctive parameter is the ICI, e.g., Delarue et al. (2009) used ICIs in the North East Atlantic for

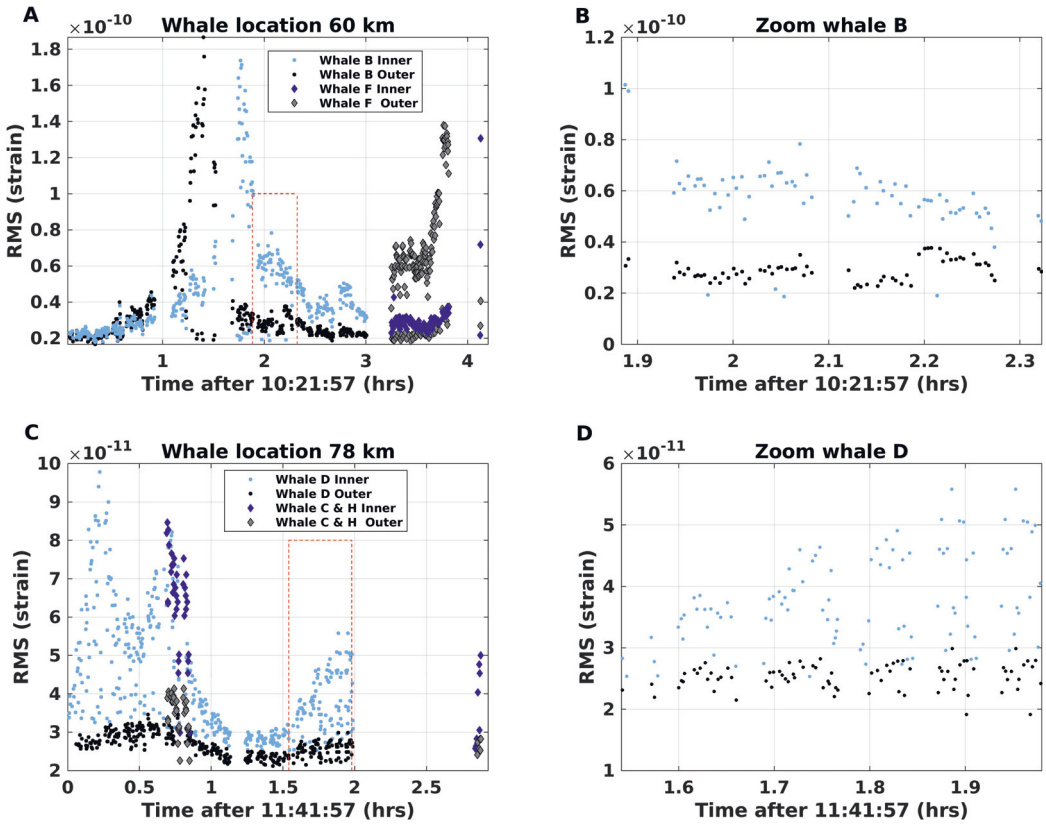

Figure 2.6: Observed RMS amplitudes of fin whale vocalizations in whale locations 60 km and 78 km (see Figure 2.5) computed by a rectangular window around the calls. (A, C) All RMS levels from the vocalizations in the respective locations. (B, D) Zoomed-in versions to illustrate periods with whale calls and the inter-series intervals.

stock differentiation. ICIs were found between 9.3 and 13.8 s, aligning with reports of systematically shorter ICIs in the Barents sea, measured post-2017 close to $\simeq$10 s (Romagosa et al. 2022). Focusing only on the tracks with more than five observed ISI, we denote that the smallest interval was computed for whale (D; 96.9 s) and the longest for whale (B; 167.9 s), consistent with ISI reported by Watkins et al. (1987). ISIs varied substantially along track (B) with a standard deviation of 124.5 s, whereas whale D had the smallest ISI deviation of 22.2 s.

The BF uses 3–4 vocalizations to estimate swim direction. We found swim speeds between 1 and 3 m/s, with "instant" horizontal speeds between 1.24 m/s and 1.86 m/s (4.5–6.7 km/h). It is consistent with previously-reported fin whale swim speeds of 1.2–3.9 m/s during vocal activity (McDonald et al. 1995, Clark et al. 2019), generally lower than cruising speeds (Lydersen et al. 2020).

Table 2.1: Information on the different whale tracks, displaying the call period, the inter-call intervals, the inter-series interval, the mean swim speed and the number of calls during the different intervals. ICI = Inter-Call Intervall, ISI = Inter-Series Interval, MSS = Mean Swim Speed.

Whale	Call period	ICI (s)	N_{calls}	ISI (s)	N_{rest}	MSS (m/s)
(A)	09:20 - 10:32	9.3 ± 5.7	243	126.3 ± 58.8	12	1.53
(B)	10:23 - 13:19	13.8 ± 4.3	452	167.9 ± 124.5	17	1.40
(C)	11:23 - 11:33	13.6 ± 8.7	39	80.0	1	1.27
(D)	11:42 - 13:33	11.7 ± 6.0	447	96.9 ± 22.2	19	1.86
(E)	12:20 - 13:31	10.0 ± 7.4	324	116.7 ± 71.1	8	1.34
(F)	13:37 - 14:25	11.4 ± 3.1	154	83.4 ± 1.8	2	1.24
(G)	13:58 - 14:29	11.2 ± 2.8	137	–	0	1.70
(H)	14:28 - 14:31	12.2 ± 5.6	12	–	0	1.56

2.5 Discussion

2.5.1 Localization error

We used the known ship's GPS associated with the air gun data to evaluate the GS and BF localization errors. The distance between the ship's GPS position and the source was compensated by moving the logged source position from the GPS 10 m behind the ship following the known track. However, this is only a partial solution as the source will drift with abrupt changes in ship's heading and with variations in local conditions, e.g., ocean currents and weather, during the acquisition. These variations could introduce some errors into the air gun position estimate.

Comparing the errors in air gun position estimation to the errors in the telecommunication cable coordinates and the time of arrival picks, we consider the error in the air gun shot location as negligible. The fiber track locations were logged while the cables were trenched into the substrata. Moreover, the DAS system saves data into channels related to the distance the laser has traveled along the cable, which must be calibrated to the known telecommunication cable coordinates. As we know the coordinates along the fiber track, we can compute distances along the cable that roughly correspond to the distances logged by the interrogator equipment. However, the cable is not necessarily fully stretched; hence the distance calculated from the known fiber track position could deviate from the distances logged by the interrogator unit. Using the geo-referenced shot position, a future study could focus on developing an inversion procedure to match the distances that the interrogator logs with the known cable positions and quantify the potential errors.

First arrival times were manually picked on conditioned spatio-temporal representations of the data. We identify manual time-picking as a source of error directly related to the apparent SNR. For a specific DAS configuration and stable source characteristics as in the

air gun example, the SNR will change with the distance between the source and the fiber (both on the horizontal plane and with changes in the water column depth), the ambient noise but also, changes in DAS recording capabilities all along the fiber.

Considering the configuration of (1) a pelagic sound source in the 5–45 Hz (air gun) and 15–25 Hz (fin whale) frequency band, (2) bottom-mounted receivers and, (3) a constrained detection range of 9.4 km we assumed a constant sound speed (and, therefore, straight ray traveltime; see equation (2.1)) to limit the computational costs of the localization methods. When estimating the air gun track, we tested various sound speeds and found the value with the lowest error to be 1440 m/s. The obtained sound speed agrees with average values given for sea-water at 4–6°C, which are typical for Svalbard (Timmermans and Labe 2022), also used in previous studies of Arctic waters (see, e.g., Gavrilov and Mikhalevsky (2006)). We carried out a simple test to see the change in average errors between the known shot position and the estimated track. Increasing the sound speed by 25 and 50 m/s produced a 16 and 31 m increase in average errors. In the event longer detection ranges were available or to reduce the obtained 100 m localization error, 3D propagation modeling might be necessary to account for the complex bathymetry in fjord environments (e.g., using BELLHOP (Ocean-Acoustic-Library 2022)), as highlighted in neighboring fjords (Richard et al. 2023).

The typical depth range for fin whale vocalizations is between 15 and 30 m (Oleson et al. 2014). We investigated a similar depth range using the air gun data to quantify the errors related to using a fixed source depth by changing the source depth of the air gun in the localization algorithms to 20 m while keeping the sound speed constant at 1440 m/s. The BF localization errors deviate less than 1 m, whereas the GS deviates with just over 1 m. The very low deviations in errors are likely because we are investigating depth variation well below the location accuracy.

2.5.2 Comparison of the localization methods

The two localization algorithms provide similar results for both the air gun and the whale vocalization and show similar localization errors of 100 m. For the air gun track, the GS showed a smaller error than the BF (Figure 2.2), whereas, for the whale tracks, the GS generated positions that are more scattered than the BF (Figure 2.5). This is attributed to the BF incorporating knowledge of previous locations, whereas the GS location estimates are independent for each vocalization.

Because of the manual first time of arrival picking, the methods from raw data to a position, swim speed and direction, and ultimately the tracks still need to be fully automated. The manual picks were limited by the SNR of the observed signal, which translated into a minimum received RMS strain of 0.2×10^{-10} on Figure 2.6 which in turn limited the detection and localization range to a maximum offset of 9.4 km from the fiber, for both methods. For fin whales' 20 Hz song, the arrival times selection could be automated, e.g.,

by a time-frequency matched filter (also known as spectrogram correlation; Mellinger and Clark (2000)) or by adapting recent advances in machine learning and convolutional neural networks to analyze the large amount of DAS-collected data and detect whale calls with high accuracy (Shiu et al. 2020). Automating the time of arrival picking could help extend the localization's spatial reach and potentially reduce the localization error.

The implementations of the algorithms used to find the tracks in this paper are computationally different. The GS is a brute force algorithm that finds arrival times for grid points over a pre-defined area and uses, for instance, 1.9 s to locate one air gun shot. Conversely, the BF is more computationally efficient and uses 0.15 s to locate one seismic shot. These computational times denote the applicability and potential for near-real-time whale tracking. The computational efficiency of the methods strongly depends on the computer used, the processing unit (CPU versus GPU), the programming language, and the algorithms' efficiency, and it can be optimized for better performance.

Under the considerations of near-real-time tracking, the BF stands out as the most complete method as it estimates the heading and speed of the whales in addition to its geographical position. In contrast, the GS only estimates the geographical position of the whale call. However, it is a global optimization method with few assumptions in the inversion procedure. It is limited by the grid spacing, the size of the area covered by grid points, and the complexity of traveltime calculations. The latter limitation is also valid for the BF. Additionally, it computes the misfit function for the whole grid area, which might show features in the objective function not captured by the BF. This can serve as a comparison to the BF (as done here) to find local minima in the grid area or provide an accurate starting model for the BF (or a similar local optimization method dependent on an accurate initial model). For example, when one cable is used, it will highlight the left-right ambiguity problem in the misfit function. The contours from the GS position, as depicted in Figure 2.2D, align well with the various error ellipses from the BF, which indicates that the Gaussian approximation used in the BF is a good approximation for situations like those studied here.

2.5.3 Implication of DAS-based localization for whale conservation

Telecommunication cables are available worldwide, and most new cables have more optical fibers than required to create redundancy. These could be repurposed to create distributed sensors from their onshore termination point to the first repeater. However, there are a limited number of places where two parallel fibers are laid a few km apart, as in this study. Even with one fiber, we can still detect and estimate the direction (with a left/right ambiguity) of vocalizing whales, with range inferred by, e.g., the received levels and the directional ambiguity perhaps broken by an asymmetry in the bathymetry (see, e.g., Bouffaut et al. (2022)). However, additional work is needed to quantify the instrument response of DAS, its directivity, and sensitivity at higher frequencies to understand which species can be monitored with this technology and under what circumstances.

The localization accuracy of the two methods presented in this work has been shown to be ≃100 m while offering the possibility to localize whales over a ≃1800 km^2 area (considering whales being detected at a distance of up to 95 km from the interrogators in Longyearbyen, with a detection range of ≃9.4 km). This combination of spatial coverage, relatively low infrastructural investment, and potential for real-time monitoring could bring great value to a range of coastal conservation applications.

For example, driven by the North Atlantic right whale case, several acoustic-based methods are being developed or applied to mitigate the risk of ship strikes (e.g., Gervaise et al. (2021), Baumgartner et al. (2019)). For this application, real-time methods are essential, and the obtained 100 m accuracy compares well with current practices (Hendricks et al. 2019). Such a collision management system is becoming increasingly important in the Arctic, where the decrease in sea-ice coverage opens up new shipping routes that might impact previously untouched whale habitats. At the same time, climate change is likely causing whales to change their habitat use and migration behavior. By automating the tracking procedure presented here, it would be possible to produce near-real-time tracks of whales with species identification, swim speed, and direction. At the very least, this information could be used to inform local management and stakeholders of whale presence and movement in a timely manner and at a very fine spatial resolution, supporting them to take appropriate mitigation measures. Furthermore, detailed information on whale locations and behavior would support science-based decisions and the management of conservation areas where anthropogenic activities should be kept at a minimum. Svalbard is a known summer feeding ground for baleen whales (Storrie et al. 2018), and mapping the common or active feeding areas is important. A final possibility is to find information on how whales respond to the changing marine ecosystem in the Arctic, induced by climate change, which has already been shown to alter baleen whale behavior (Moore et al. 2019). A global effort is needed to obtain such information, in which DAS systems can provide detailed information through high spatial and temporal sampling.

2.6 Conclusion

Examining five hours of data from two fiber-optic telecommunication cables, we have detected 1808 fin whale vocalizations. A subset of these data have been used to track eight whales during this period, with up to four being tracked simultaneously at a detection range from the cable of up to 9.4 km. This capability opens up new possibilities for detailed mapping of the presence and location of whales over large areas (at least 60 km long and ≃19 km wide) over long periods, in near-real-time. The simultaneous tracking of multiple whales also has the potential to provide new insights into the behavior and interaction between whales along a corridor up to ≃9.4 km on either side of the cable. Using shots from a single air gun towed behind a ship, we were able to calibrate our two localization estimators (a grid search and a Bayesian filter) with deterministic signals of similar source characteristics to fin whale calls and found both methods to be computa-

tionally efficient and accurate to $\simeq$100 m. Using two fiber cables, separated by a few km, breaks the symmetry of a single straight-line array, resolving the usual left-right ambiguity. The capabilities demonstrated here establish the potential for a near-real-time whale tracking capability that could be applied anywhere in the world where there are whales and fiber-optic cables. Coupled with ship detection, using a similar approach and/or with fused data from other sources such as AIS, a real-time collision avoidance system could be developed to reduce ship strikes.

Data availability statement

The original contributions presented in the study are publicly available. This data can be found here: https://doi.org/10.18710/Q8OSON.

Author contributions

RR wrote the manuscript with support from JE, LB and JP, which was read and approved by all co-authors. RR carried out the acoustic analysis; RR and JE developed and conducted the whale tracking; RR produced the results shown in the manuscript, interpreted together with JE, LB, ML, JP, and KT. ML, RR, SJ, FS, JJ, OS, SW, VO, and AW, planned the experiment, and RR, JJ, and FS collected the DAS data. ML, VO, and AW provided the OptoDAS interrogator used. BR and TJ conducted the air gun experiment. All authors contributed to the article and approved the submitted version.

Funding

RR and KT are funded by the Geophysics and Applied Mathematics in Exploration and Safe production Project (GAMES) at NTNU (Research Council of Norway; Grant No. 294404). We acknowledge support from the Centre for Geophysical Forecasting - CGF (grant no. 309960). The acquisition of the data was financed by CGF.

Publisher's note

All claims expressed in this article are solely those of the authors and do not necessarily represent those of their affiliated organizations, or those of the publisher, the editors and the reviewers. Any product that may be evaluated in this article, or claim that may be made by its manufacturer, is not guaranteed or endorsed by the publisher.

Supplemental data

The supplemental Material for this article can be found online at: https://www.frontiersin.org/articles/10.3389/fmars.2023.1130898/full#supplementary-material or in Appendix B.

Chapter 3

Paper 2: Quick clay monitoring using distributed acoustic sensing: A case study from Rissa, Norway

Robin André Rørstadbotnen[1,2], Hefeng Dong[1,2], Martin Landrø[1,2], Kenneth Duffaut[2,3], Kevin Growe[1,2], Umedzhon Kakhkorov[2,3], Susann Wienecke[2,4], Joacim Jacobsen[2,4]

1 - Department of Electronic Systems, NTNU, 7491 Trondheim, Norway

2 - Centre for Geophysical Forecasting, NTNU, 7491 Trondheim, Norway,

3 - Department of Geoscience and Petroleum, NTNU, 7491 Trondheim, Norway

4 - Alcatel Submarine Networks Norway AS, 7075 Tiller, Norway

Review 3 (minor revision) was submitted to Geophysics 19 April 2023.

3.1 Abstract

Quick clay avalanche is one of the most devastating landslide types worldwide. Hence, an early warning system is in demand to mitigate the fatal consequences caused by such events. To address this, distributed acoustic sensing data are collected in an area containing quick clay deposits between July 2021 and February 2022 in Rissa, Norway, while a new road is constructed on the quick clay. Road construction can induce unwanted changes to the mass balance in the clay, and previous landslides have been triggered by such changes. For this purpose, passive and active data are collected to test and compare various analysis methods. Using extracted Rayleigh wave dispersion from active sledgehammer shots, shear-wave velocity depth profiles covering the first 15 m could be estim-

ated and compared using a linearized and a non-linear surface wave inversion method. Furthermore, ambient noise cross-correlation is used to obtain the dispersion from the ambient noise and associated shear-wave velocity profiles, providing two possible data collection methods for the early warning system. The obtained dispersion curves and the estimated shear-wave velocity profiles show small time-lapse variation during the acquisition period (up to approximately 23 m/s), where the variation is within one standard deviation. Such a small variation suggests that the construction work and the extra load added to the quick clay do not alter the quick clay's properties. Nevertheless, the obtained results capture the nonrepeatability effects within the acquisition period and provide reference curves for the study area at undisturbed conditions and valuable information for future comparisons to refer to potential failure scenarios. This is the first step in exploring an early warning system for quick clay landslides using fiber-optic cables. Further work will investigate the possibility of automatizing the system and improving the accuracy of the sensing system.

3.2 Introduction

In recent years, several devastating quick clay landslides have been triggered by changes in the near-surface properties of the clay through anthropogenic and natural impacts. Different disturbances have been shown to trigger such liquefaction, e.g., vibrations from earthquakes, altering the material balance in the clay by moving cubic meters of mass, massive rainfalls over time, or erosion from a nearby drainage network (Gregersen et al. 1981, Lundström et al. 2009, Ryan and Riekeles 2021). In Norway, Sweden, and Canada (and other countries previously covered by glaciers), the majority of the devastating landslides can be categorized as quick clay landslides (Lundström et al. 2009). There have been several quick clay slides in Norway over the last 50–60 years. Examples are the slides at Trögstad in 1967, at Rissa in 1978 (Gregersen et al. 1981), and most recently at Gjerdrum in 2020 (Ryan and Riekeles 2021). Moreover, the shear strength of the clay will drastically decrease before such landslides and vanish when the quick clay liquefies (see NGI (2011) for a YouTube video of the Rissa landslide). The time scale for this change in shear modulus is unknown and represents a significant challenge for such monitoring projects as proposed here. As the shear-wave speed is related to the shear strength, the quick clay changes can be monitored by investigating the changes in the shear-wave speed. Therefore, developing an early warning system for quick clay landslides is possible.

Distributed acoustic sensing (DAS) has been shown to be an effective and appropriate near-surface monitoring system (Dou et al. 2017). DAS can repurpose existing "dark" fiber-optic (FO) cables (fibers not used for data transfer) or be part of a dedicated recording system where FO cables are installed for a specific application. Both record inline strain in the cable down to nano strain levels. Historically, DAS has been applied to dedicated vertical fibers in downhole operations (Mestayer et al. 2011) and has only recently been applied to horizontal fibers. The DAS recording system has several advantages com-

pared with conventional seismic sensors; it has a high temporal and spatial resolution, with sample rates down to meters and up to kilohertz. It is a low-maintenance receiver array with possibilities of short- to long-range monitoring by interrogating cables stretching from 500 m (using a 100 kHz sample rate) to 150 km (approximately 667 Hz; Waagaard et al. (2021)). DAS technology has already been applied to many disciplines, including near-surface monitoring (Table 3.1), earthquake seismology (Lindsey et al. 2017), geophysical exploration (Mestayer et al. 2011, Taweesintananon et al. 2021), water-born sound sources (Matsumoto et al. 2021), and passive acoustic monitoring of ships (Rivet et al. 2021) and baleen whales (Landrø et al. 2022, Bouffaut et al. 2022).

Currently, it is common to have more optical fibers than required for the installation of telecommunication cables, as it incurs minimal additional cost and adds redundancy. In terms of telecommunications applications, these additional fibers are typically left unused (dark) and can therefore be exploited for other applications, such as DAS. Alternatively, fiber cables can be installed as part of dedicated recording systems for a specific application, such as in this study. The DAS interrogator (OptoDAS) used in this work repeatedly sends linear frequency-modulated pulses into the fiber and interrogates the Rayleigh backscattering caused by density fluctuations in the fiber (Waagaard et al. 2021). These density fluctuations are displaced when, for instance, a seismic wave impinges upon the fiber. Such displacements can be detected as phase changes in the backscattered light. The time-differentiated phase is obtained by continuously comparing the backscattered response from one pulse to the next. This is done by differentiating the phase spatially between regularly spaced sections (channels) along the fiber in the backscatter response for each pulse separately and subsequently comparing it to the backscatter response from the next pulse. The number of channels over which the phase differentiation is performed is called the gauge length (GL). The effect of a longer GL is an improved signal-to-noise ratio (SNR) observed through stronger arrivals at higher velocities but at the cost of attenuating shorter wavelengths. In addition, the time differentiation is done continuously, at a rate no faster than the time between when the pulse is sent into the fiber and the time at which the backscatter from the end of the fiber has propagated back to the interrogator, constituting the maximal temporal resolution in the DAS data. The time-differentiated phase is stored by the interrogator and is linearly related to the fiber strain. See Hartog (2017) for more information on the conversion.

Previously, there have been several studies on near-surface changes using DAS and other seismic receiver systems. Dou et al. (2017) use two perpendicular DAS segments to image the changes in the shear-wave velocity profile in the near-surface using three weeks of traffic noise. Rodríguez Tribaldos and Ajo-Franklin (2021) analyze five months of ambient noise to monitor seismic velocity variation caused by groundwater changes in Sacramento Valley, US. Shragge et al. (2021) do a case study for on-land DAS in Perth, Australia, using low-frequency signals to show the potential of using DAS for large-scale geophysical and geotechnical analysis finding shear-wave profiles more than 500 m into

the subsurface. Furthermore, Cheng et al. (2021) use offshore fiber cables and ambient noise interferometry from Scholte waves to create 2D shear-wave velocity images of the near-surface shear-wave velocity in marine sediments, thereby improving constraints on submarine features. Olafsdottir et al. (2018) carry out a multichannel analysis of surface waves (MASW) using different geophone setups to find array configurations that increase the dispersion images' frequency bandwidth. Long et al. (2020) use hydrophone streamers and MASW on two data sets from Ireland to find offshore shear-wave velocities from Scholte wave recordings. See Table 3.1 for a comparison of the content in this paper to other publications.

This paper aims to show how surface waves recorded on dedicated FO cables can be used as part of a monitoring procedure to map the changes in quick clay attributes with time, such as the shear stiffness and velocity, as a new highway is built on the clay. The area under investigation consists of a 3–6 m sediment layer (including a 0.5–1 m top layer of soil), followed by a 15 m thick marine clay and quick clay layer overlaying glacial marine deposits (Solberg et al. 2012). The new road will introduce changes in the mass load of the clay and can potentially induce unwanted alterations to the quick clay properties. To address this, two different data sets are collected over seven months using a dedicated FO array trenched in a known quick clay area: (1) using an active seismic source, a sledgehammer on a steel plate, and (2) using different ambient noise sources, directional industrial noise generated by the highway construction and isotropic ambient noise from quiet evenings and weekends. We use a subset of this passive data set to prove the feasibility of using passive seismic interferometry in such a monitoring system. Furthermore, to find the variation in the quick clay layer, dispersion curves obtained from the data sets are used as input to two different inversion algorithms, one linear and one non-linear. These are compared to find the procedure best suited for the monitoring system and to find potential alterations in shear-wave velocity over the seven-month period.

The paper is organized into four parts. The first part describes the data acquisition and data analysis. In the second, the surface wave inversion algorithms are briefly presented. The third part presents and discusses the results. Results from the active data and the background noise from quiet periods are presented and compared in the main text, whereas results using the construction noise are presented in supplemental Material section C.1. Finally, the conclusions are made.

3.2.1 DAS data acquisition

DAS data acquisition

To investigate different monitoring procedures for quick clay avalanches using FO cables, time-differentiated phase data recorded by the OptoDAS interrogator are acquired in Rissa, Norway (see Figure 3.1). The acquisition started in July 2021 and lasted until February 2022, recording data using four 2.02 km long FO cables spliced together, providing

Table 3.1: Content of this paper compared to other publications. AD = Active data, PD = Passive data, SH = Sledghammer, SS = Seismic shots, FS = Frequency sweep, ES = Explosive source, VS = Vibroseis, WD = Weight drop, EQ=Earthquake.

Citation	DAS	AD	PD	Geology	Time-lapse	# modes
This paper	x	SH	x	Quick clay	x	1-4
Dou et al. (2017)	x		x	NA	x	1-2
Shragge et al. (2021)	x		x	Sediments		1
Olafsdottir et al. (2018)		SS		Silty sand		1
Martin et al. (2016)	x		x	Permafrost	x	1
Zeng et al. (2017)	x	FS	x			
Martin and Biondi (2017)	x		x	NA	x	NA
Ajo-Franklin et al. (2019)	x		x	Sediments	x	1-3
Spica et al. (2020)	x		x	Sediments		1-2
Renalier et al. (2010)		SH ES	x	Clayey deposits	x	1
Song et al. (2021)	x	VS	x	NA		1
Maraschini and Foti (2010)		WD SH		Sediments clayey sands		1-4
Arisona et al. (2017)		SS		Sediments		
Yuan et al. (2020)	x		Traffic EQ			2

a total cable length of 8.08 km. The cable layout is depicted in Figure 3.1C. The laser sweep is sent through the interrogator unit into the first cable and propagates south into well 1 (W1) and subsequently into well 2 (W2). When exiting well 2, it turns north and travels on the same path until it reaches the northernmost yellow cross in Figure 3.1C, and then it travels to the base, entering the next cable. The configuration path is repeated four times. Data recorded on the first round (on a Corning loose tube cable) are studied in this work. The cables are trenched at a maximum depth of 40 cm into the subsurface.

Active and passive data are acquired. A total of approximately 2340 sledgehammer shots are recorded for the active data, with passive data recorded at intermittent intervals for the whole seven-month period (with small breaks due to power outages). However, only approximately 300 shots at roughly a 0.5 m distance from well 1 have been analyzed, as well as 28 shots on the northern segment (see the yellow asterisk and the highlighted sections in Figure 3.1C at the 1469 & 1752 m marks). In addition, a follow-up survey was carried out on 22 March 2022 to investigate the effect of varying the GL during acquisition (for the analysis of the various GL, see Appendix 3.A). The acquisition parameters are listed in Table 3.2. Figure 3.2 depicts examples of the recorded data, from the active

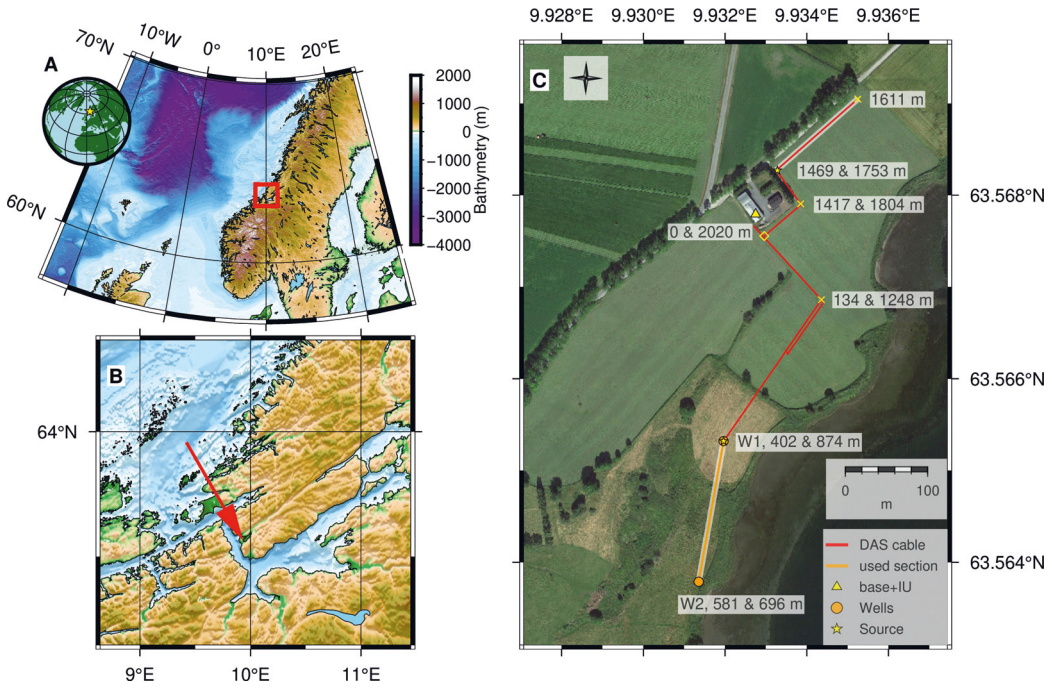

Figure 3.1: (A, B) Overview map indicating the study area, Rissa, in Norway (background map from GEBCO (2021)). (C) Layout and annotation of the DAS fiber-optic cable (the red line). The orange highlighted section depicts the segment inside the quick clay area used in the analysis in this paper. The red highlighted (northern) section indicates the section used to analyze the area outside the quick clay area. The annotations show the distances along the cable for a selection of segments. Note that only the distances for the first route are depicted. Yellow crosses indicate the cable portion corresponding to the distance marking, and the yellow square indicates the point at which the laser enters and exits the northern part of the cable (satellite image from Google (2022)).

and passive periods, at a distance of 100–700 m along the cable from the interrogator to get an overview of the typical signals present during the acquisition period. This study mainly focuses on data recorded on a 168 m section of the Corning loose tube cable inside an area containing quick clay. The segment starts when the cable exits well 1 at a distance of 413 m (where the corresponding trace is used as trace 0 in the following analyses), ending when entering well 2 at 581 m (as indicated by the orange segment in Figure 3.1C). This segment is conveniently placed, as it is easy to define its start and end points due to the clear presence of wells 1 and 2 in the data (see, e.g., Figures 3.2A, C). The wells are observed as two low-amplitude regions at distances of 363–402 and 582–695 m, respectively (the cable in well 2 goes up and down twice). They are drilled 19 m into the quick clay to facilitate additional studies and provide information on subsurface properties, such as the water table level and bedrock depth. Only information from the drilling itself has been used here; the DAS data in the wells are outside the scope of this

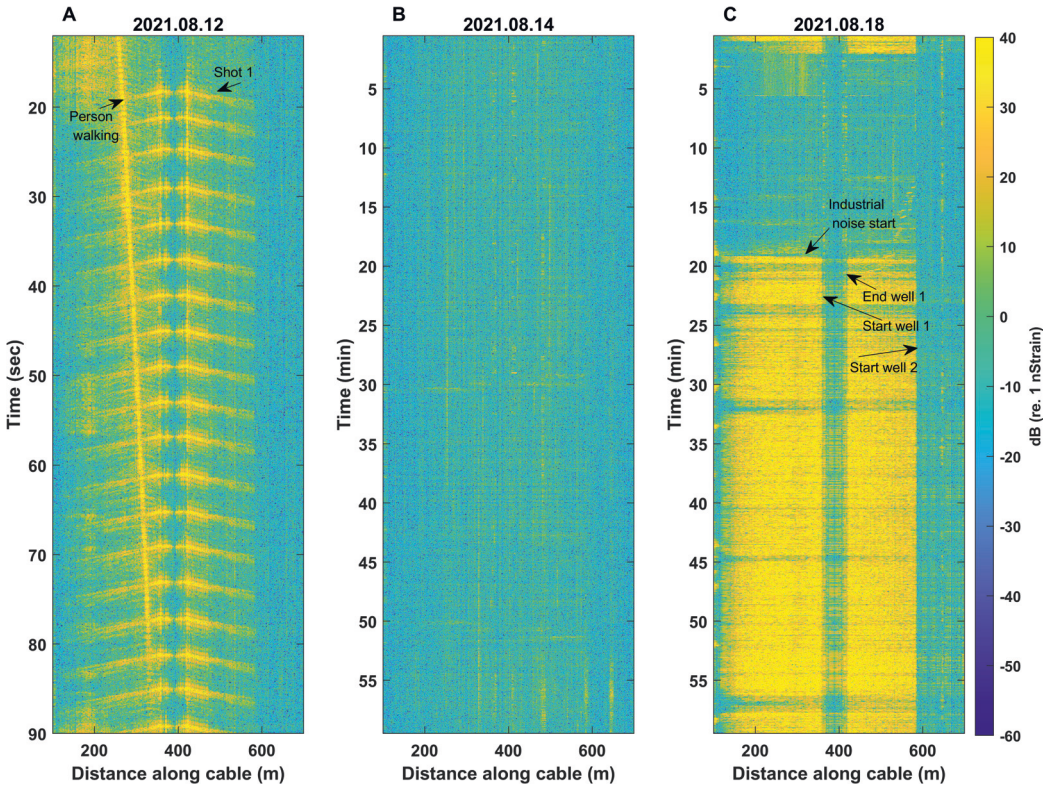

Figure 3.2: Observed data for three different days during the acquisition period in August 2021. (A) Shots from a shot series in 12 August 2021. Two signals are evident. The first is the repeating shots, and the second is a person walking along the cable (the linear event, the slope gives a speed of $\simeq$ 4 km/h). In (B) and (C), two different days of ambient noise are depicted, without (B) and with (C) construction work. The ambient noise without construction, referred to as quiet periods, shows only isotropic noise. In the period with construction noise, it is evident when the work is ongoing (higher amplitudes) and when there are breaks (lower amplitudes, similar to amplitudes in B).

work.

The active data are acquired using sledgehammer shots on a steel plate. Figure 3.2A displays example shots from 12 August 2021. Different types of shots at the same shot position are carried out for each acquisition date: vertical blows (P-shots), horizontal inline with the array (S-shots, H_x), and horizontal cross-line with the array (S-shots, H_y). In practice, the P-shots are executed by the sledgehammer hitting the top of the steel plate. In contrast, for the S-shots, the sledgehammer strikes the vertical sides of the steel plates, parallel with the array for inline shots and perpendicular to it for crossline shots. Figure 3.3A depicts one of the P-shots by well 1 from the acquisition in August 2021, and clear dispersive Rayleigh waves can be observed. The dispersive data inside the black box

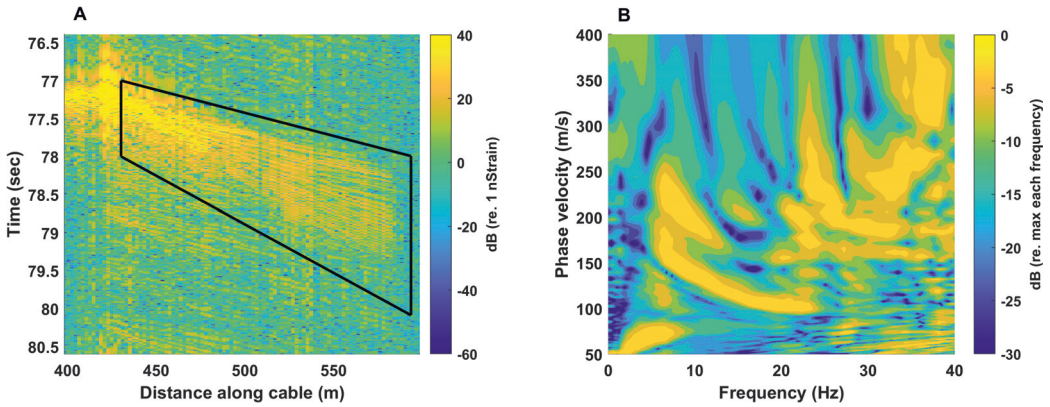

Figure 3.3: (A) One observed shot from 12 August 2021 with the area used to compute the dispersion image indicated (the black trapezium). (B) Resulting dispersion image. Each frequency is normalized by its maximum.

indicated in Figure 3.3A are used to compute the dispersion image shown in Figure 3.3B, where the data outside the black box are muted. The dispersive behavior of the Rayleigh wave is also clear in the obtained dispersive image, and several higher-order modes are present. Furthermore, the different sledgehammer strikes are compared to find which shot type provided the best dispersion image (see supplemental Figure C.5). Data recorded for the inline S-shots showed the most energy, followed by the P-shots and the crossline S-shots, consistent with the radiation patterns in Kähler and Meissner (1983). However, only the P-shots produced clear Rayleigh wave modes, whereas the inline and crossline S-shots generated a mix between the Rayleigh and Love waves. Thus, the P-shots are used to obtain the best Rayleigh wave dispersion image in this analysis and are recommended for surface wave analysis similar to the one presented here. Moreover, the most predominant noise generated during the data acquisition came from road construction, through trucks and excavators. Due to these, some of the shots are masked by noise and unusable for analysis. Even at distances of up to 500 m, the construction work rendered shots useless. However, this could easily be circumvented by carrying out the shots during breaks in work or outside working hours.

Figures 3.2B-C shows two examples of 1 h ambient noise used for the seismic interferometry to extract virtual shot gathers (VSGs). The first segment is acquired during a weekend (14 August 2021), and the second during a weekday at the start of the road construction (18 August 2021). Different events are clearly visible in the data. The noise recorded during the weekend shown in Figure 3.2B is evenly distributed with low amplitude, while the industrial noise in Figure 3.2C shows high amplitudes when road construction is ongoing. The site for acquiring data is, normally, a quiet area, as observed in Figure 3.2B. Only a farmhouse is located close to the buried cables. In addition, a road is located 150–300 m from the cable, and only a few cars pass even during workdays. Pass-

Table 3.2: Acquisition parameters and periods for the data. All data are acquired with a temporal sampling rate of 1000 Hz. Note that the acquisition on 22 March 2022 is solely to investigate the effect of changing the gauge length and is not part of the monitoring study. A = active data, P = passive data, CL = cable length, TSR = temporal sample rate, SSR = spatial sample rate, GL = Gauge length.

Data type	Date	CL (km)	TSR (Hz)	SSR (m)	GL (m)	Shots #
A	2021.07.01	8	1	4	1170	X
P	2021.07.05-07.24	6	2	3	–	–
	2021.08.10-08.12				–	–
A	2021.08.12	6	2	3	250	X
P	2021.08.12-08.20	6	2	3	-	2021.08.14, 08.18
	2021.09.08-09.15	8	2	3	-	–
A	2021.09.15	8	2	3	73	X
P	2021.09.18-11.02	8	2	3	-	2021.09.18–19, 09.22 2021.10.09–10
A	2021.11.02	8	2	3	212	–
P	2021.11.02-11.30	8	2	3	–	X
A	2021.12.01	8	2	3	214	X
P	2021.12.16-12.23	8	2	3	–	–
	2022.01.04-01.14				–	–
	2022.01.17-02.02				–	–
A	2022.02.02	8	2	3	340	X
A	2022.03.22	8	1	2, 4, 6, 8	480	X

ive data are acquired over time to investigate the possibility of monitoring changes in the quick clay. Moreover, the passive data are acquired during quiet periods and construction work. Quiet periods are here defined as periods with no construction work. Weekends are chosen as the quiet periods to analyze as they provide the longest window with isotropic noise sources uninterrupted by construction work. This work focuses on three separate weekends for three consecutive months after the road work started (13–15 August 2021, 17–20 September 2021, and 8–10 October 2021). In addition, different periods of road construction are studied to see how the position of the roadwork, relative to the segment of interest, affects the interferometry results. Two instances are studied and presented in supplemental Material section C.1: (1) when the road construction started by the barn where the interrogator unit is installed (18 August 2021), 200 m from the studied segment slightly broadside, and (2) when the construction is broadside to the segment (22 September 2021).

3.2.2 Data analysis

Phase velocity spectrum

The data are displayed in the phase velocity domain, also known as dispersion images, for easier identification of the different modes present in the recorded surface waves. Such images can be obtained from different methods. In this work, a $\tau - p$ transform (Verschuur 2013) is used (see supplemental Figure C.6). After computing the slant-stack, the ray parameter is inverted, and a Fourier transform along the time-axis is applied to get the phase velocity spectrum ($v_{phase} - f$).

Surface waves from active source

To display the active sledgehammer shots, some simple pre-processing steps are carried out. (1) Data are converted from time-differentiated phase to fiber strain. (2) The mean and linear trends are removed from the data. (3) A Tukey window is applied, and the data are band-pass filtered using cutoff frequencies of 2 and 40 Hz.

In general, 40–50 shots are executed in each series for vertical and in/crossline horizontal shots. All shots generate surface waves and show clear dispersive arrivals when not masked by the construction noise. A window including dispersive arrivals is chosen to capture the dispersion, as depicted in Figure 3.3. The data inside the window are then transformed into the phase velocity spectrum to extract the different phase velocities used to estimate the shear-wave velocity depth profiles ($v_s(z)$).

Surface waves from ambient noise interferometry

Several steps are needed to obtain high-quality VSG, or Green's functions, from the ambient noise interferometry. The first three steps are similar to the active acquisition: (1) data are converted from time-differentiated phase to fiber strain, (2) the mean and linear trends are removed, and (3) the data are tapered by a Tukey window and high-pass filtered with a cut-off frequency of 1 Hz. In addition, (4) spectral whitening is applied by inversely weighting the complex spectrum with a smoothed version of the amplitude spectrum to produce a whitened version of the complex spectrum. This step is meant to broaden the band of the ambient noise signal used in the cross-correlation and decrease the influence of single-frequency sources (Bensen et al. 2007). Finally, (5) temporal normalization is applied to reduce the effect of transient signals in the data, such as earthquakes and instrument irregularities. This work tests both 1-bit normalization and running-absolute-mean-normalization (RAMN). Both show similar results for the ambient noise, so the more adaptable and flexible RAMN method is chosen. A running window of 25 samples is used to compute the RAMN based on half the maximum period of the pass-band criteria introduced by Bensen et al. (2007).

Passive seismic interferometry using noise cross-correlations is applied to estimate the VSG and the Rayleigh wave dispersion. The channel on the segment investigated closest

to well 1 (approximately 413 m along the cable) is chosen as the virtual source. The ambient noise recorded on the virtual source is cross-correlated with the segment's subsequent channels to generate the common VSGs. Shot gathers for 3 s time slices in a 60 min window are computed and stacked to extract the Green's functions. To enhance the coherent arrivals and increase the SNR of the data, a Phase-Weighted Stack (PWS) is applied (Schimmel and Paulssen 1997, Dou et al. 2017). From the VSG, it is possible to pick the dispersion curves in the waveform data. The left and right sides of the time lags are averaged, and the dispersive area is selected as in the active source example and similarly transformed into the phase velocity spectrum. For the weekends, i.e., the quiet periods, the mean stack is first computed for 1 h segments. The PWS is then applied to the minimum amount of mean hourly stacks needed to enhance the surface waves in the VSG. The DAS data from August had a lower noise level than, for example, September and needed a 22 h stack compared with the 26 h stack for September to converge to a stable VSG (see supplemental Figure C.7A). In contrast, the October stack required 30 h (one possible explanation might be variations in weather conditions on the three dates, see supplemental Figure C.8).

Figure 3.4 displays the VSG from the seismic interferometry for ambient noise from a quiet weekend (14 August 2021, column one) compared to an active shot recording (12 August 2021, column two). Note that the VSG has been band-pass filtered between 2 and 40 Hz to have a comparable bandwidth to the active shots. The ambient noise from the weekend is isotropic, as seen through the symmetry in the retrieved Green's functions, producing well-resolved Rayleigh modes (see Figure 3.4D and supplemental Figures C.9E, F). Note that the dispersion images are normalized independently at each frequency (the normalization is similar to spectral whitening, highlighting a broader frequency range). Moreover, there are two noticeable differences between the dispersion curves from the active and ambient noise data: (1) active data contain higher frequencies than the ambient noise data, and (2) the active shots hold more energy and provide higher-order modes. The latter effect can be observed in Figures 3.2 and 3.4.

3.3 Surface wave inversion methods

The dispersion relations obtained from the active shots and the ambient noise interferometry can be used as an input to inversion algorithms to estimate v_s profiles of the near-surface layers. Two different inversion procedures are carried out to obtain the velocity profiles: (1) a linearized inversion (Caiti et al. 1994) and (2) a non-linear inversion, the Adaptive Simplex Simulated Annealing (ASSA) hybrid inversion method (Dosso et al. 2001). These procedures were chosen as they are well-established methods already used in various applications (see, e.g., Dong et al. (2006), Wu et al. (2020)). In addition, we use two different inversion methods to compare their performance and estimated shear-wave velocity profiles.

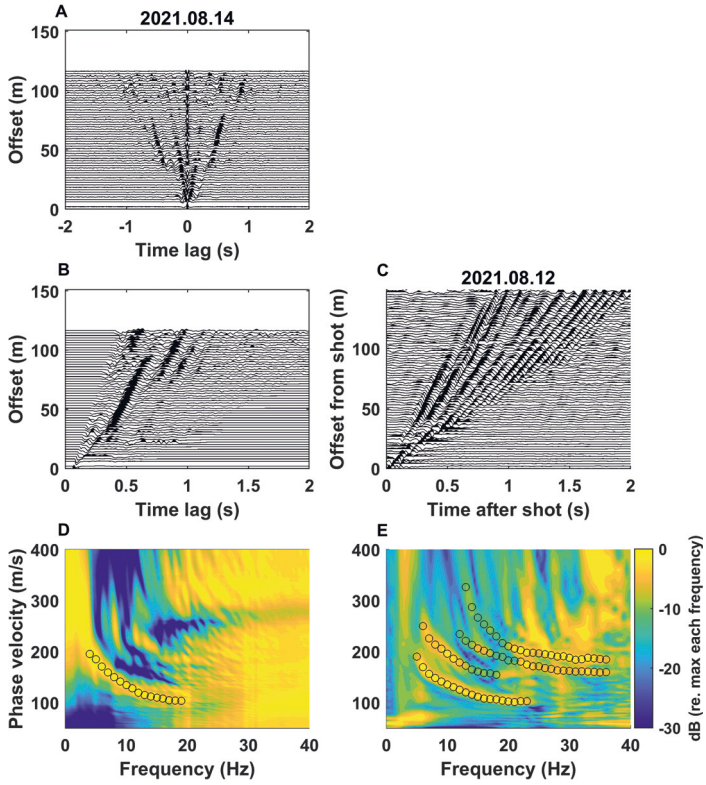

Figure 3.4: Virtual shot gathers and resulting dispersion images for 14 August 2021 (column one). A shot from 12 August 2021 for comparison (column two). (A) The two-sided VSG. (B) Muted one-sided VSG, i.e., the average of positive and negative time lags from the two-sided VSG. (C) Observed dispersion arrivals from one shot, 12 August 2021 (D, E) The resulting dispersion image overlaid with the extracted Rayleigh wave dispersion curves (black circles).

3.3.1 Linearized least-squares inversion

The linearized inversion uses the data's dispersion characteristics to determine the near-surface shear-wave model that best predicts the same observed dispersion curve. The parameters that affect the propagation of elastic waves in the near-surface layers are the compression wave velocity (v_p), the shear-wave velocity (v_s), the compression and shear Q-factor, and the density (ρ). Three assumptions are used in the inversion to simplify the inversion and forward model. The non-linear inversion minimization problem is solved using a deterministic optimization algorithm. It is initiated by a starting model, and an update is sought in the neighborhood of this model. Adding the update to the initial model, the model for the next iteration is found. This is repeated until predefined conditions are met. Furthermore, the linear system is solved in a least-squares sense using singular value decomposition (SVD). However, a part of the SVD is ill-conditioned, and regularization needs to be introduced. Repeating this with a reasonable starting model, the algorithm

Table 3.3: (A) Fixed and initial values used in the linearized inversion. (B) Fixed values and constraints for ASSA.

(A)	Linearized Inversion			
Layer	v_p (m/s)	ρ (kg/m^3)	$v_s^{(0)}$ (m/s)	Thickness, h (m)
1	600	1.825	100	4
2	770	1.85	130	4
3	930	1.875	160	4
4	1100	1.9	190	4
5	1270	1.925	220	4
6	1430	1.95	250	4
7	1600	2.0	280	4
(B)	ASSA			
Layer	v_p (m/s)	ρ (kg/m^3)	v_s (m/s)	Thickness, h (m)
1	600	1.825	0–300	0–10
2	933	1.883	0–350	0–40
3	1266	1.942	0–500	0–40
4	1600	1.9	0–650	0–50

converges to the shear-wave velocity profile of the media. More information on the various aspects of inversion can be found in Caiti et al. (1994).

To initiate the linearized inversion, fixed values and constraints to the P-wave velocity, the density, number of layers, and layer thickness (h) are needed, as well as an initial model of the shear-wave velocities. In this work, six homogeneous layers plus an infinite half-space are used. The values chosen are listed in Table 3.3A, based on a geotechnical report by the Norwegian Geotechnical Institute (NGI; L'Heureux et al. (2015)), work by L'Heureux and Long (2017), and common P-wave velocities for clay (Sauvin et al. 2014, Salas-Romero et al. 2016). However, it is worth noting that the P-wave velocity varies depending on the clay content, porosity, water content, and overburden properties. Hence, the chosen P-wave model might vary depending on local conditions.

Adaptive Simplex Simulated Annealing (ASSA)

This non-linear inversion is a hybrid algorithm that combines local downhill simplex and fast simulated annealing adaptively to find the shear-wave velocities in a stratified media (Dosso et al. 2001). The ASSA algorithm uses a simplex of a predefined number of models and randomly perturbs the parameters after a downhill simplex step. For this, the random perturbations of the unknown parameters are used, and the trial models are either accepted or rejected according to a Metropolis criterion. After a prescribed number of perturbations, the control parameter is reduced. The process is repeated until the difference between the highest and lowest mismatch models relative to their average is less than

a specified convergence factor (Li et al. 2012, Wu et al. 2020). More information on the various aspects of the inversion can be found in Dosso et al. (2001).

In the non-linear inversion, the layer thickness and shear-wave velocity in each layer are estimated parameters. In contrast, the P-wave velocity and the density of each layer are considered constant because the dispersion curves are not sensitive to these parameters. The lower and upper bounds of the estimated parameters and the fixed values of the P-wave velocity and density for all the layers are listed in Table 3.3B. The chosen bounds are based on the NGI report (L'Heureux et al. 2015) and are chosen sufficiently wide to capture the velocities and layer thicknesses of the subsurface. A model with three horizontally homogeneous layers overlying an infinite halfspace is chosen as the subsurface thickness model (note that the number of layers and the constraints of the layer thickness varied for some of the inversions due to the dispersion data's resolvability). The choice of the subsurface thickness model is based on the resistivity report given by Solberg et al. (2012) and tests using different models. In these tests, the inversion consistently resolves three layers which are hence used.

3.4 Results and discussion

In the following, the results from the active data using the first two modes will be presented and discussed (a discussion on the results using the other number of modes can be found in Appendix 3.B). Subsequently, the results using the quiet periods will be presented (results from the construction noise are given in supplemental Material section C.1). Then, the two will be compared, along with a time-lapse comparison between the results from the different acquisitions.

3.4.1 Active Data

Figure 3.5 shows the average dispersion images (from all images obtained in one P-wave shot series) for all acquisition days overlaid with the mean and standard deviation of the extracted dispersion curves. The curves are found by computing the dispersion image and picking the dispersion curves for each shot in a P-wave shot series. Subsequently, the mean and standard deviation of the picked modes are calculated with an interval of 0.5 Hz. Similar to shots acquired in July, the estimated curves from all days show the same trend with four modes within a comparable frequency range (approximately 5–35 Hz). Furthermore, additional shots were executed outside the quick clay area on the northern segment of the array for comparison (see Figure 3.1C). The resulting dispersion image shows more modes than obtained in the quick clay area, with higher frequencies and an overall higher velocity (see supplemental Material section C.2).

The picked dispersion curves in Figure 3.5 are the input data for the linearized and non-linear inversion. The inversion results using the first two modes for all acquisitions are depicted in Figure 3.6 (see Appendix 3.B for inversion results using one, three, and four modes). The shear-wave velocity depth profiles are obtained by applying the constraints,

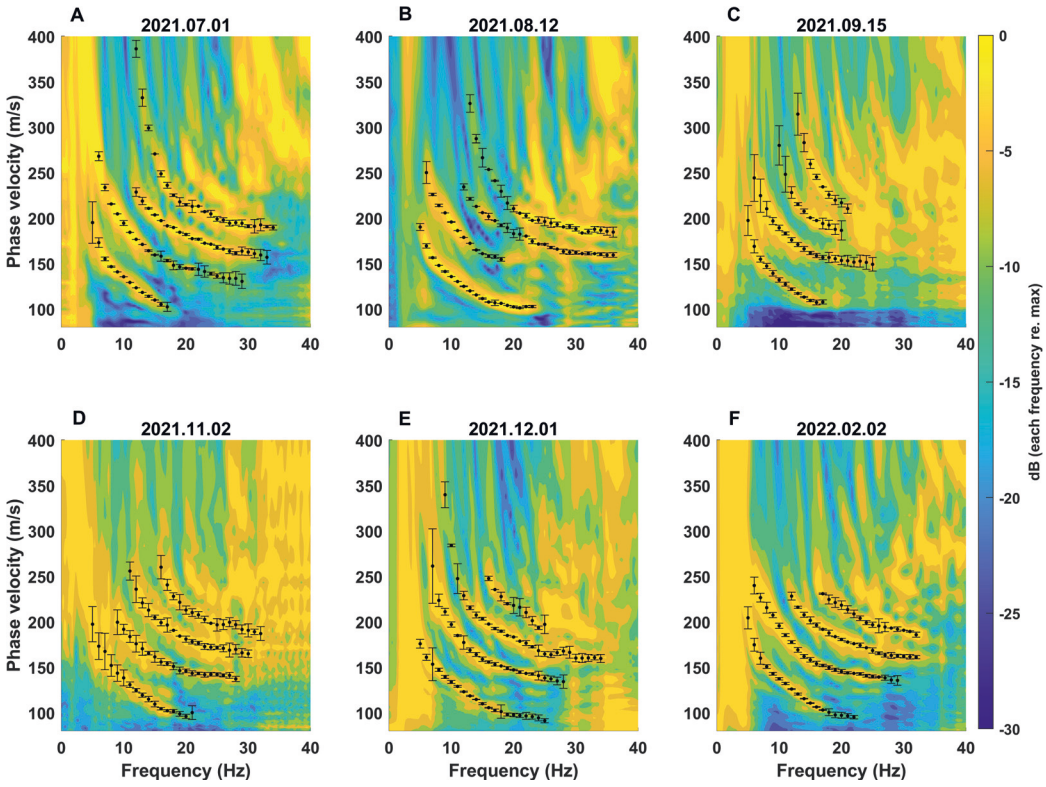

Figure 3.5: Average phase velocity spectrum from one active shot series from different days overlaid with mean and one standard deviation computed using the four extracted dispersion curves.

fixed values, and initial models to the inversion algorithms. Figures 3.6A-F shows the two observed modes from every acquisition, overlaid with the predicted modes from the inversions. The fit between the observed and modeled modes agrees, with some outliers at various frequencies. Figures 3.6G-L displays the resulting shear-wave velocity profiles, where a similar trend is seen for all days. The final v_s profiles overlay a subset of the velocity profiles used during the ASSA inversion to find the best-fitting velocity models to illustrate the uncertainty in the estimates. It is worth noting the resolution general rule stating that the fundamental mode is not sensitive to variation in material properties at depths greater than 1/3 to 1/2 of the maximum resolved wavelength $1/3$ to $1/2$ of the maximum resolved wavelength λ_{max} (Olafsdottir et al. 2018). In the active shot data, the average maximum wavelength for the fundamental mode is 39.2 m yielding a depth resolution between 13.1 and 19.6 m. This is the trend observed in the the inversion results using the fundamental mode only (Figure 3.B.1), where the velocities below approximately 15 m are more spread than that for shallow depths. Similarly, the best-resolved thickness of the top layer is constrained relative to 1/3 and 1/2 of the shortest wavelength λ_{min} (Olafsdottir et al. 2018). The λ_{min} range for the measured fundamental mode is

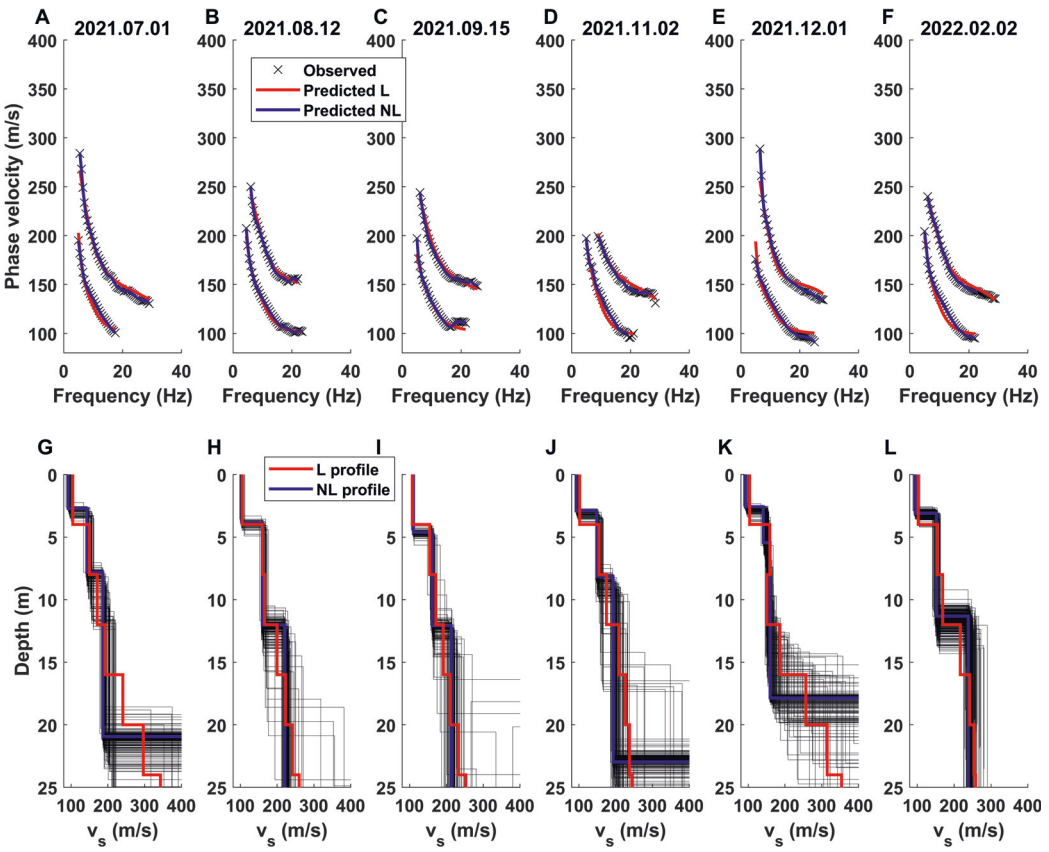

Figure 3.6: Observed and predicted dispersion curves for two modes from active data and the associated inversion results. (A–F) The fit between the observed (the black) and the predicted (the red for linearized, the blue for ASSA) dispersion curves. (G–L) The estimated shear-wave velocity profiles from the linearized (L; the red) and ASSA non-linear (NL; the blue) inversion overlay a subset of the velocity profiles (the black) generated by the ASSA inversion. The ensemble illustrated the uncertainty of the parameter estimation.

3.6–6.3 m, providing a possible resolution between approximately 1.2 and 3.2 m. For the non-linear inversion, the thickness of the first layer varies from 3 to 6 m. Moreover, higher-order modes are known to resolve more of the near-surface shear-wave speed structures, penetrating deeper and providing smaller uncertainties of the estimates (Xia et al. 2003, Li et al. 2012). This effect is also observed in this work, especially prominent using two modes (see Figures 3.7 and 3.B.4). Note that a fixed thickness of 4 m is chosen for all layers for the linearized inversion. By investigating the obtained velocities in the different layers, there are little variations between some of the layers. Therefore, the number of layers could have been reduced, and similar results could have been obtained.

The non-linear inversion analysis provides sensitivity to each parameter. Thus, a multidi-

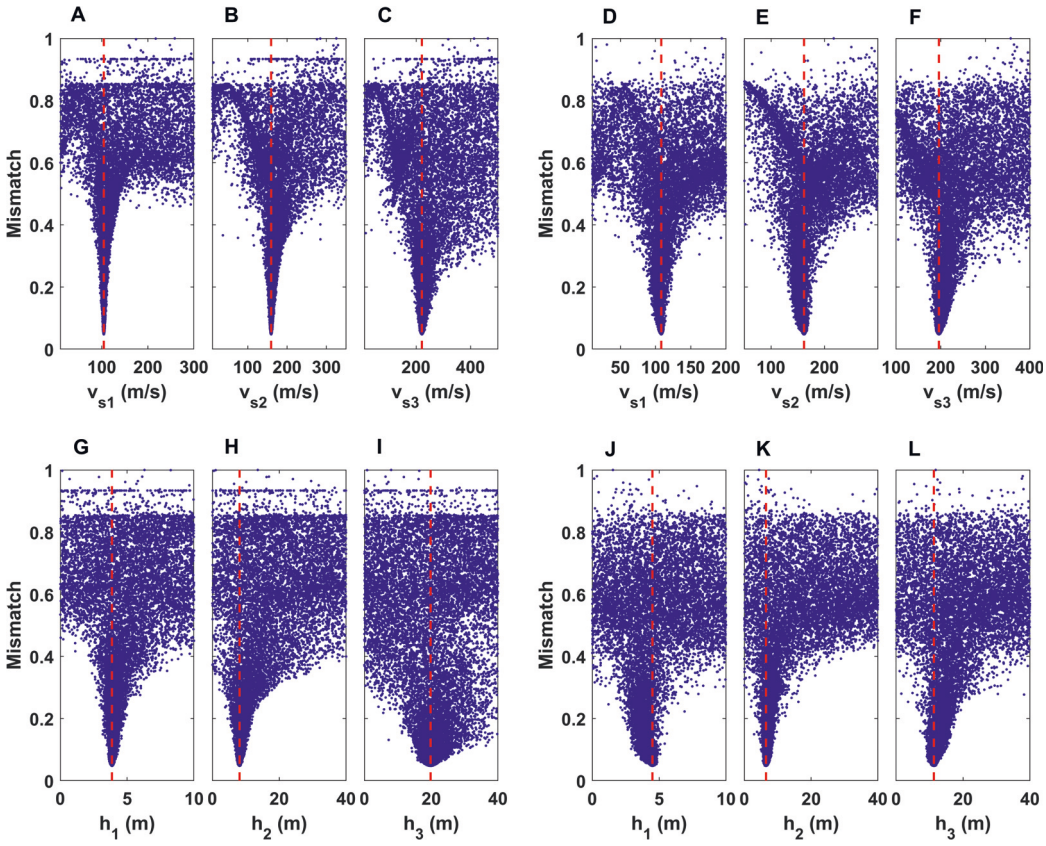

Figure 3.7: Multidimensional sensitivity analysis using two and four modes for active shot data 12 August 2021 (A, B, C) Shear-wave velocity for layers 1–3 using two modes. (D, E, F) Shear-wave velocity for layers 1–3 using four modes. (G, H, I) Thickness for layers 1–3 using two modes. (J, K, L) Thickness for layers 1–3 using four modes. The mismatch gives the normalized difference between observed and predicted data given as values between 0 and 1.

mensional sensitivity (MDS) analysis can be executed using the four modes present in the data. Only the MDS using two and four modes are presented here (for the MDS of one and three modes, see Appendix 3.B). Figure 3.7 illustrates that using two modes as input in ASSA produces better-resolved parameters than using four modes as two modes show more direct and narrow paths to the lowest mismatch values (except for h_3). Therefore, two modes are used hereafter. Similarly, the MDS analysis for the first two modes shows a more direct and narrow path to the lowest mismatch value for the shear-wave velocity than the thickness, suggesting better resolved v_s values. Note that the v_s profiles shown in Figure 3.6 (and later examples) correspond to the models with the lowest misfit in the narrow distribution of the MDS plots.

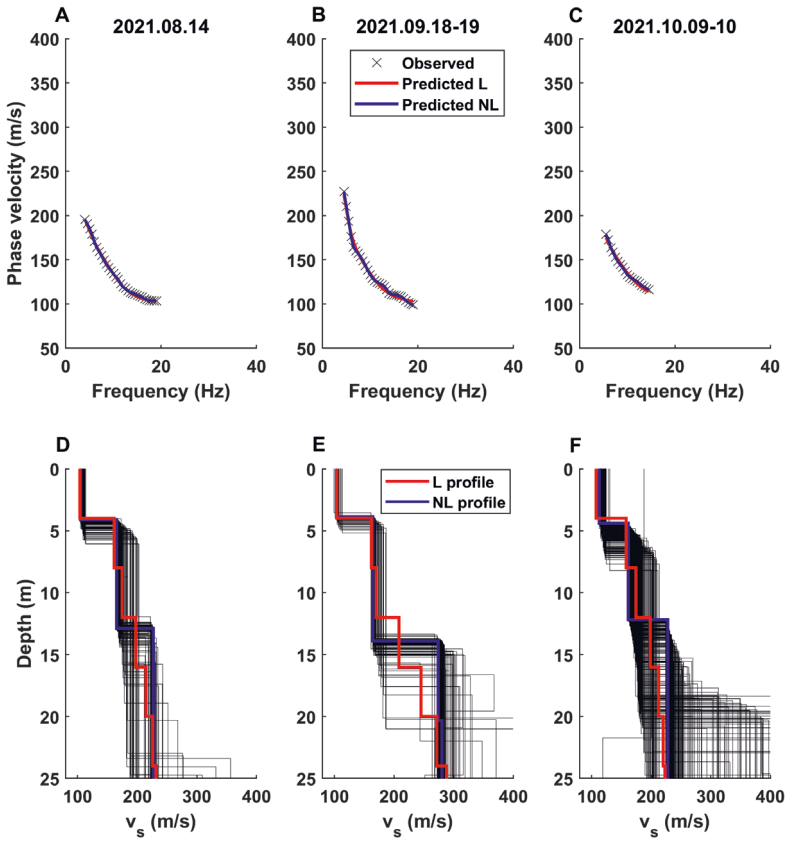

Figure 3.8: Same as Figure 3.6 but for the inversion of one mode obtained from the ambient noise interferometry.

3.4.2 Passive Data

The inversion results for the passive data from various quiet periods are shown in Figure 3.8, where the observed and predicted modes are displayed in the first row, and the resulting v_s profiles, overlaid with a subset of trial v_s profiles from ASSA, in the second. The predicted dispersion curves match the observed ones (Figures 3.8A, B, C), and reliable velocity profiles are obtained. The largest wavelength for the observed dispersion varies depending on the obtained VSG. The values range from 28 to 50 m, providing an in-depth variation resolution of 9–25 m. The shortest wavelength ranges from 5.2 to 8 m, yielding a top-layer resolution of 1.7–4 m.

The associated MDS analysis is shown in Figure 3.9. Using the available fundamental mode for the weekend ambient noise data (14 August 2021), the velocities for all three layers are well determined. Similarly, the thickness mismatch response of layers one and two are well-constrained and reliable. In contrast, the third-layer thickness (h_3) has a flat

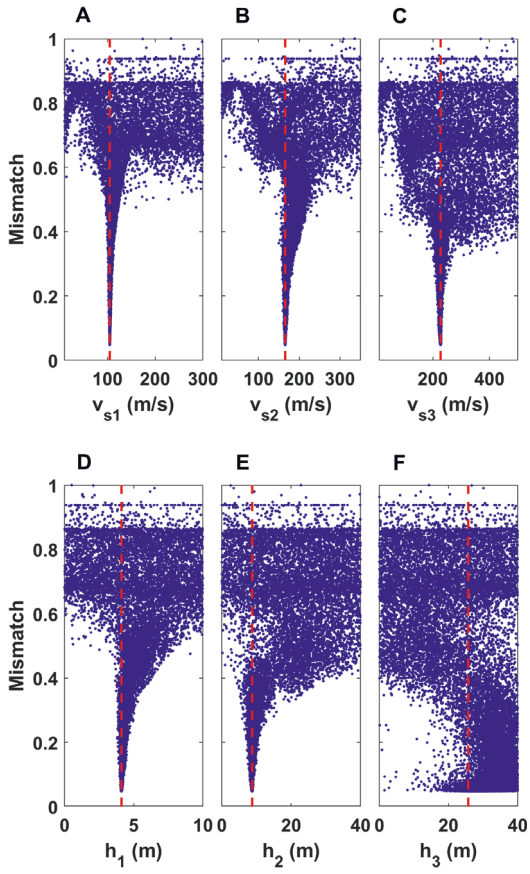

Figure 3.9: Multidimensional sensitivity analysis for ambient noise data on 14 August 2021. (A, B, C) Shear-wave velocity for layers 1-3. (D, E, F) Thickness for layers 1-3.

response, indicating that the data cannot resolve the layer thickness.

3.4.3 Data comparison and discussion

Figure 3.10 summarizes the results from the active and ambient noise data and shows that the inversion results are consistent within the measurement period. The inversion procedures produce the same pattern, where the top approximately 15 m are well resolved and the layers underneath have a larger uncertainty. Figure 3.10A contains all four modes to compare the available information, whereas the inversion profiles in Figures 3.10B, C are obtained using the first two modes as these produce the best-resolved inversion parameters. Furthermore, there are minor differences between the dispersion curves extracted from the different days of active data. This can be observed in Figure 3.10A, where all modes are mostly within one standard deviation of each other. The fundamental modes from all quiet periods investigated are similar and give comparable velocities (Fig-

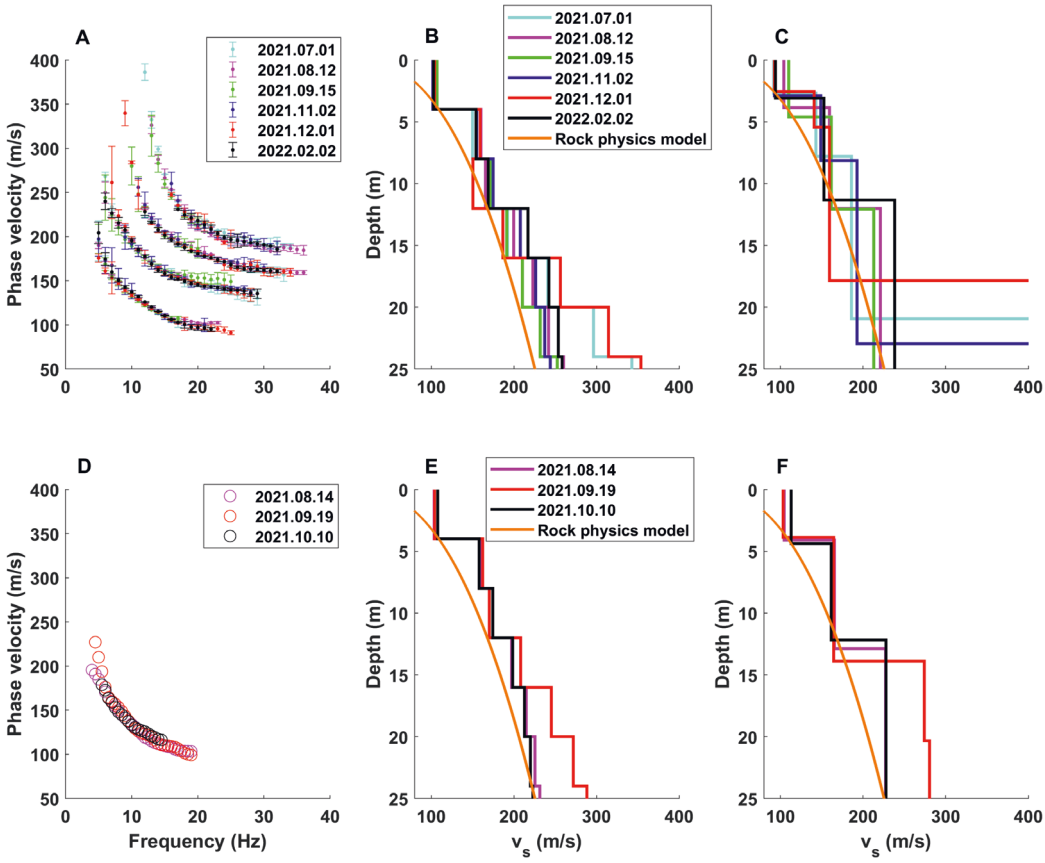

Figure 3.10: Dispersion curves and inversion results from active shots (A, B, C) and ambient noise interferometry (D, E, F). (A) The mean dispersion curves from the different shot days with error bars indicating one standard deviation. (B) The linearized inversion profiles using two modes. (C) The ASSA inversion profiles using two modes. (D) Dispersion curves from the interferometry. (E, F) The linearized and ASSA inversion profiles, respectively. (B, C, E, F) are all overlaid with the predicted v_s profile from the rock physics modeling (see Appendix 3.C for more details).

ure 3.10D). This suggests that the construction work, and extra load added to the quick clay, do not alter the shear-wave properties of the quick clay and remain stable.

The shear-wave velocity profile obtained from the rock-physics modeling shown in Figure 3.10 is consistent with the estimated velocity profiles, providing additional insight into possible rock-physics parameters in the quick clay column. The change in velocity due to the additional weight introduced by the construction is estimated by a strip-load model to be 0.4 m/s at 19 m depth (see Appendix 3.C for more details). These changes in velocity are within one standard deviation of the dispersion curves and cannot be resolved with this method. However, this model is a conservative estimate of the potential velocity change as it assumes the minimum width and thickness of the extra road founda-

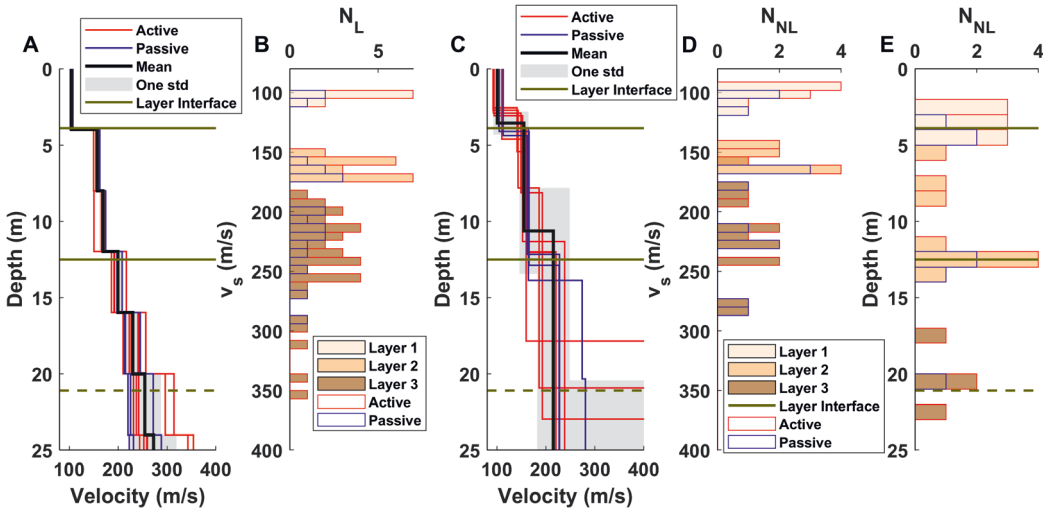

Figure 3.11: Time-lapse analysis of the inversion profiles for the active and passive data over the seven-month acquisition period. (A) Velocity profiles obtained from the linearized inversion for the active (the red) and passive data (the blue) with mean profile (the black) and one standard deviation (std) over velocity profiles found using active and passive data, indicating the variation over the acquisition period (the gray shaded area). Note that the time-lapse of shear-wave velocity profiles have not been separated by color (see Figure 3.10). (B) Associated velocity distribution with N_L velocity values from the linearized inversion, colorcoded by the interpreted layers. (C) and (D) are the same as (A) and (B) but from ASSA inversion with N_{NL} velocity values. (E) Associated depth distribution with N_{NL} depth values from the non-linear inversion. The layers are interpreted from (E), indicated as solid lines for the layers within the resolution rule of thumb, and dashed when outside. For an overview of the individual estimated values from the active and passive data, see Table 3.4.

tion and considers only the resulting stress and pressure changes. The construction work, especially the excavation activity, might add additional unwanted effects to the quick clay that need monitoring (Bjerrum et al. 1971): (1) it might change the drainage network in the subsurface; (2) it will break up the soil cover, which might change the erosion of the underlying material; and (3) it will increase the vibrations in the ground, disturbing the bounds between the clay.

The time-lapse variation, through the distribution of the shear-wave velocities and layer interface depths presented in Figure 3.10, for the selected dates within the measurement period (Table 3.3) is summarised in Figure 3.11. Table 3.4 shows the quantified values from the active and passive data using the two inversion algorithms. Note that the estimates in the halfspace are below the resolution limit and, therefore, are not included in Figures 3.10 and 3.11 and Table 3.4. Furthermore, the layer interface depths found using the ASSA inversion are consistent with the input three-layered model, finding similar depth values. Based on these values and the profiles given in Figure 3.11C, the first layer

Table 3.4: Statistical overview of estimated values for the two inversion algorithms applied to the active (A) and passive (P) data. The mean and the standard deviation are computed for each layer.

Linearized Inversion			
Depth (m)		v_s (m/s)	
		A	P
4.0		105±2	105±2
8.0		156±4	160±2
12.0		167±9	173±3
16.0		199±12	201±6
20.0		233±17	224±18
24.0		263±34	239±28
28.0		285±49	248±35
ASSA			
Depth (m)		v_s (m/s)	
A	P	A	P
3.3±0.8	4.1±0.3	98±8	107±5
9.5±2.7	13.0±0.9	151±8	163±2
26.4±6.7	30.2±9.3	201±28	243±27

interface may be considered to be at approximately 4 m, the second at approximately 12 m, and the third at approximately 21 m, with the uncertainty increasing as a function of depth as highlighted by the increasing standard deviation in Table 3.4, also indicated by the gray shaded area in Figure 3.11C. Based on these results and results from previous resistivity measurements of the area (Solberg et al. 2012), the content of the different layers underneath the studied segment can be interpreted to be (1) sedimentary crust containing agricultural soil, sand, and/or gravel, (2) marine clay, and (3) quick clay. The material below 21 m is interpreted as bedrock. Note that the resistivity profiles given by Solberg et al. (2012) show a significant lateral variation in the depth and thickness of the quick clay layer; hence the layer interpretation will vary along the cable profile (for an example, see supplemental Material section C.2). For this particular segment, the maximum depth range for shear-wave velocity is approximately 15 m, and Solberg et al. (2012) have shown the quick clay layer under the studied profile to be at a depth of roughly 10–20 m. For situations such as this, the procedure needs further development to obtain more reliable shear-wave velocity values for depths below 15 m. One possibility is using an alternative seismic source generating lower frequencies that penetrate deeper. The surface waves will then be able to capture changes occurring in the deeper portions of the quick clay layers. However, the resolution obtained in this study is sufficient for observing changes within the top 15 m.

The distribution of the velocities from the two inversion methods are given in Figures 3.11B,

D, color-coded based on the layer in which the velocities are estimated. The velocity profiles from the various acquisition dates are similar, with a velocity distribution in agreement with a three-layer model and an expected increase in uncertainty with depth. Note that the choice of the bedrock interface has considerable uncertainty. This is visible in the shaded gray area of Figures 3.11A, C and affirmed by the rule of thumb for depth resolution (Olafsdottir et al. 2018). Ultimately, this interface location is chosen based on the results of this study and constrained by the resistivity survey by Solberg et al. (2012).

All modes are within one standard deviation of each other, yet minor time-lapse effects are present in the data. The dispersion curves from 15 September 2021 show some deviation from the other curves for mode two in the frequency range of 20–25 Hz. The soil is reported as wet during this acquisition, and the shots are obtained during noisy construction activity. The wet soil is unlikely to increase the phase velocities as there are other acquisition dates with a higher humidity level that did not show the same trend (see supplemental Figure C.8). In addition, changes between dry, wet, and cold periods could not be resolved in the data. The reason is believed to be due to a very thin weather zone of maybe approximately 0.5–1 m. The non-linear inversion, and the shortest wavelength in the dispersion curves, resolve a minimum thickness of approximately 3 m for the first layer. The estimated velocity in the layer will be an average of the material velocities within, which attenuates the weather-induced changes. Hence, the surface waves cannot resolve the weather changes due to the frequency bandwidth. Other explanations for the observed time-lapse change are variations in the sledgehammer shots and/or influence from the background noise level. Effects from these are evident through the variation in dispersion curves from 15 September 2021, as indicated by the wider error bars in Figure 3.5C. For most acquisition days, the shots produce no or minimal variation in the dispersion curves. The biggest differences are found in the extreme frequency values for each mode (see Figure 3.5). Therefore, it is concluded that most of the time-lapse variations in the dispersive data are caused by nonrepeatability effects. Nevertheless, the shear-wave velocity profile obtained provides reference trends for the quick clay at undisturbed conditions. This agrees with in situ observations from the study area throughout the fieldwork, where no changes to the quick clay area are observed. Moreover, changes during the failure of quick clay are dramatic where its shear strength, and the shear-wave velocity, will decrease towards zero. It is anticipated that changes leading to such conditions will be observable through the proposed methods. However, two problems are not possible to address in this work. (1) The time scale at which failure might occur: for the Gjerdrum quick clay avalanche in 2020 (Ryan and Riekeles 2021) it was possible to compute the minimum time duration of the avalanche based on witness observations and the exact time when the fiber- and power-cable broke along with when the avalanche stopped. The minimum duration was found to be 11 min. However, the changes to the subsurface before the avalanche broke the cables could not be estimated for the event. (2) Deduction of the shear-wave velocity bounds for when the quick clay becomes unstable: developing an automated shot system will make it possible to find the shear-velocity profiles in near-

real-time and make it possible to estimate the shear-wave velocity profile within 11 min (assuming a similar time duration as in the Gjerdrum). This is not the case for the passive data where at least 22 h of recordings are needed to find stable VSGs, maybe less for periods with extreme weather conditions. Another possibility is to take advantage of the surface wave generated by the road construction directly as described by Yuan et al. (2020) and use it as a mobile active source.

Both inversion algorithms produce comparable shear-wave velocity depth profiles and can be used in the proposed monitoring system either together or individually. There are clear advantages and disadvantages to linearized and non-linear inversions. Normally, linearized inversion is less computationally demanding than non-linear inversion. However, the initial values in the linearized inversion are crucial for finding the global minimum, which is circumvented in the non-linear inversion by employing a hybrid method with some predefined constraints. In addition, the non-linear inversion carries out a sensitivity analysis for the estimated shear-wave velocities and layer thicknesses, providing additional information on how well the different values are estimated. In this study, prior information from the NGI report (L'Heureux et al. 2015) is available, providing information for the initial parameterization. When such information is available, the linearized model converges to a stable solution and is therefore preferred due to the low computational cost. However, when the quick clay properties change during an event, the initial model will no longer be accurate, and there is a risk of incorrect and/or unstable inversion results. In such cases, the non-linear method is preferred. Therefore, it is recommended to use a combination of the two. Initially, the linearized method would suffice when there is only natural variation of the subsurface properties, as observed in this study. Subsequently, when the subsurface characteristics vary, the non-linear method (independent of an initial model) should be used. This allows for an accurate shear-wave velocity model or an updated initial model to be used in the linearized approach.

3.5 Conclusion

This work demonstrates the possibilities of establishing an early warning system based on time-lapse analysis of shear wave velocities using FO cables trenched into the shallow soil layer of a known quick clay area in Norway. Exploiting data recorded by DAS, elastic monitoring with high spatial coverage and resolution has been shown to be feasible. By acquiring active and passive data before, during, and after a road construction period, it is possible to extract the clear Rayleigh wave dispersion using both data sets. These dispersion curves are then used as input to two different inversion algorithms, a linearized least-squares inversion and the ASSA inversion algorithm, to compare their performance and the estimated shear-wave velocity profiles. Both inversion algorithms find reliable velocity profiles down to a depth of approximately 15 m. Moreover, the inversion methods produce similar results using active and passive data and could be combined in the early warning system as they complement each other's limitations. The dispersion curves of

the surface waves and the obtained shear-wave velocity profiles for the active and passive data did not change significantly during the acquisition period, suggesting that the quick clay properties remained stable as the road construction proceeded. Nevertheless, the obtained results provide reference shear-wave velocity trends for the study area in undisturbed conditions. This provides valuable information for future comparison to potential failure scenarios. Moreover, the passive data displayed a larger deviation in the picked phase velocities and fewer dispersive modes than the active data. The increased spread in the dispersion curves for the passive data is most likely due to additional noise sources generating energy broadside to the array, producing Love waves in addition to Rayleigh waves.

The results in this work illustrate the feasibility of using both active and passive data, together and separately, recorded on FO cables in an early warning system for quick clay avalanches. However, the main limitation is the depth resolution. Recording data on FO cables is a cost-efficient and easy way of setting up the system for long-term monitoring, as the cable might already be in the quick clay, and all that is needed is to connect an interrogator unit.

3.6 Acknowledgments

We thank the Norwegian Research Council and the industry partners of the GAMES consortium at NTNU for the financial support (grant no. 294404), and the Centre for Geophysical Forecasting at NTNU (grant no. 309960). Furthermore, we want to thank Jonas Dybdahl for permission to use his barn for instrumentation, and Hans Henrik Horneman for permission to trench fibre cables on his land. Norconsult assisted in the drilling of two observation wells, and Bjørnar Buhaug (mayor, Indre Fosen), Tore Solli (Indre Fosen), Olaf Rovik (Trøndelag Fylkeskommune), Emil Cederstrøm (Norconsult) and Kristian Aune (Norconsult) are all acknowledged for help and assistance in planning of these experiments. Finally, we thank the reviewers for the many good and helpful comments that improved the work and the paper.

Appendix

3.A The effect of different gauge lengths

To better understand the effect the Gauge Length (GL) has on the resolution of the surface wave analysis, a follow up survey was carried out on 22 March 2022, acquiring sledge-hammer shots using different GL. During the survey, four different lengths were investigated; 2 m, 4 m, 6 m, and 8 m. These do not include the 3 m GL presented throughout the paper. Figure 3.A.1 shows two clear effects (see Figure 3.5 for similar plots using 3 m GL): (1) shorter GL captures shorter wavelength. Using a 2 m gauge length, more frequencies can be observed for each dominant velocity. In the 8 m GL case, the short wavelengths are not observed. This wavelength high-pass filtering is especially clear for the fundamental mode. For a 2 m GL, the minimum wavelength observed is 2.94 m, compared to 5.56 m for 4 m GL, 7.14 m for 6 m GL, and 10 m for 8 m GL. Previously it has been shown that when the wavelength recorded approaches the GL, the signal significantly distorts (Hartog 2017). This is also observed in Figure 3.A.1 (where the black line denotes this limit, $f = v_{phase}/\text{GL}$), where the majority of the modes can not be observed close to this line. (2) Longer GL contains stronger arrivals for higher velocities.

3.B The effects of using different number of modes

The effects of using a different number of modes are presented and discussed. In addition to using two modes in the inversion (see Figures 3.6), one (Figures 3.B.1), three (Figure 3.B.2) and four (Figure 3.B.3) modes have also been investigated. The inversion results show similar shear-wave velocity profiles, with some variations. These differences are also evident in the multidimensional sensitivity (MDS) analysis presented in Figure 3.B.4 and Figure 3.7 through the differences in the shape of the individual scatter plots. There are various factors producing these variations. The first is related to the different input data to the inversions when increasing or decreasing the number of modes. This should, in general, improve the resolution of the near-surface shear-wave

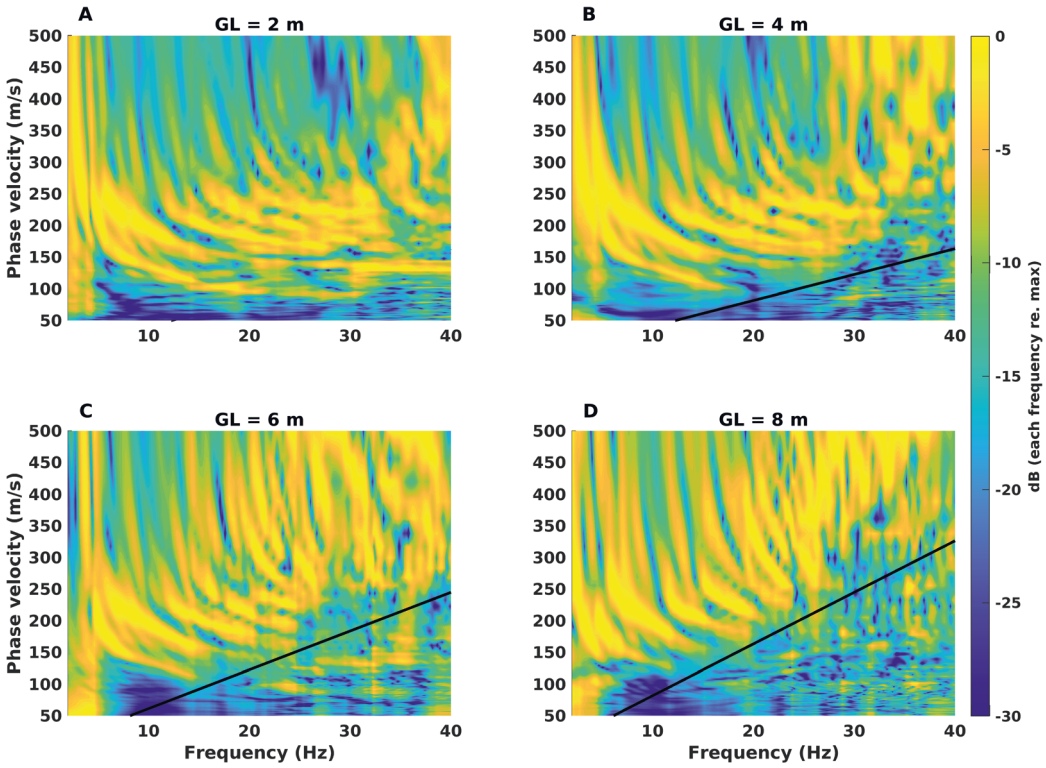

Figure 3.A.1: Comparison of dispersion images from data using different gauge lengths (GL). The black line is computed as the case when the wavelength is equal to GL, i.e., $f = v_{phase}/\mathrm{GL}$.

speed structures, penetrating deeper and providing smaller uncertainties of the estimates (Xia et al. 2003, Li et al. 2012). While this is the case when two modes are used, applying three and four modes produces worse sensitivity for most inverted parameters. Previous work by Li et al. (2012) shows an example where Love and Rayleigh wave modes in close proximity give inaccurate dispersion curves that are inappropriate for inversion and lead to biased velocity profiles. In this study, modeled Love and Rayleigh wave modes (using the v_s profile estimated using two modes from 12 August 2021) are close to each other (Figure C.3). The excited Love wave may have contaminated the extracted Rayleigh wave dispersion curves, which might bias the inversion results.

3.C Rock physics modeling

For comparing the estimated shear-wave velocity profiles through the time-laps surface wave inversion at the Rissa site, a S-wave velocity depth profile is calculated using the empirical equation of Hardin and Blandford (1989) where the elastic shear modulus for

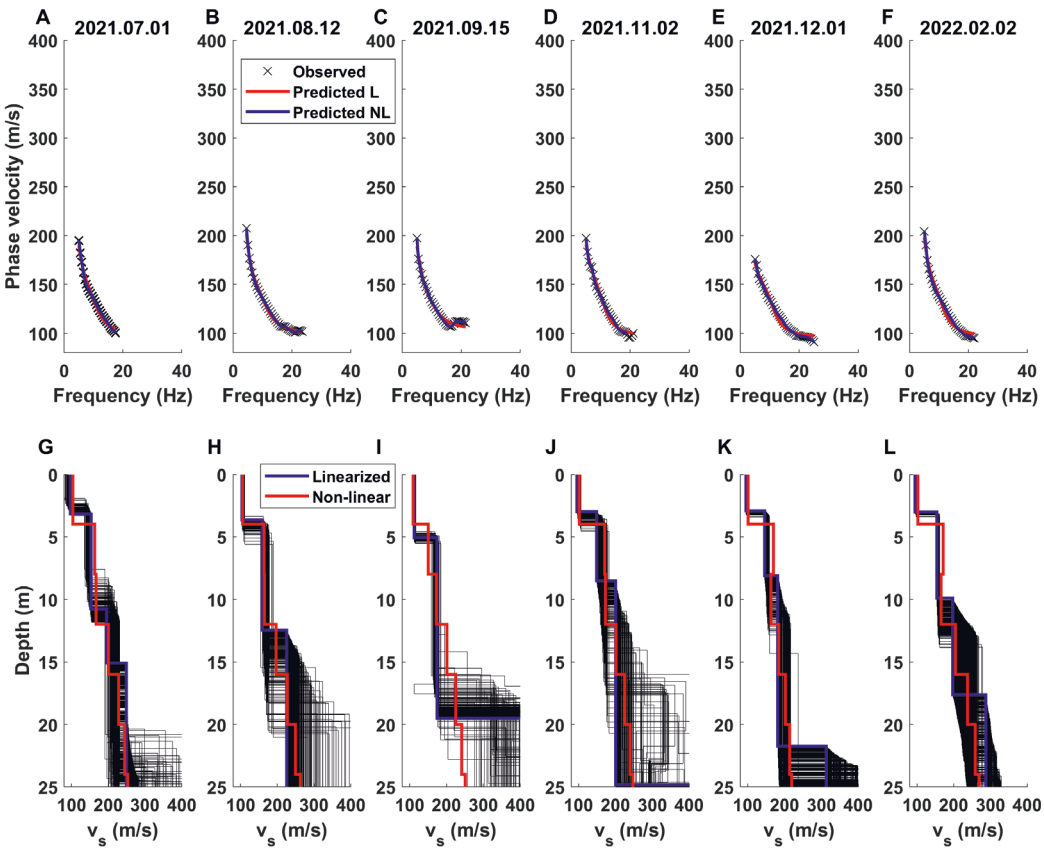

Figure 3.B.1: Observed and predicted dispersion curves for one mode from active data and the associated inversion results. (A-F) The fit between the observed (the black) and the predicted (the red for linearized, the blue for ASSA) dispersion curves. (G-L) The estimated shear-wave velocity profiles from the linearized (L; the red) and ASSA non-linear (NL; the blue) inversion overlay a subset of the velocity profiles (the black) generated by the ASSA inversion. The ensemble illustrated the uncertainty of the parameter estimation.

the vertical direction (c_{44}) is given as

$$c_{44} = \frac{OCR^k}{(0.3+0.7e^2)} \frac{S_{44}}{(2+2\nu)} p_{ref}^{(1-n)} (\sigma'_v \sigma'_h)^{n/2}. \tag{3.1}$$

The model parameters assumed for simulating the shear modulus depth profile are given in Table 3.C.1. The predicted elastic shear modulus is in the plane containing the principal stresses in vertical and horizontal directions. Figure 3.C.1A shows the assumed principal differential stress profiles in vertical (σ'_v) and horizontal (σ'_h) directions when considering hydrostatic pore pressure. Moreover, Figure 3.C.1B displays the simulated void ratio reduction expected across the quick clay column overlaid with values from lab analysis of quick clay samples from Flotten, Norway. The coefficient of earth pressure at rest ($K_0 =$

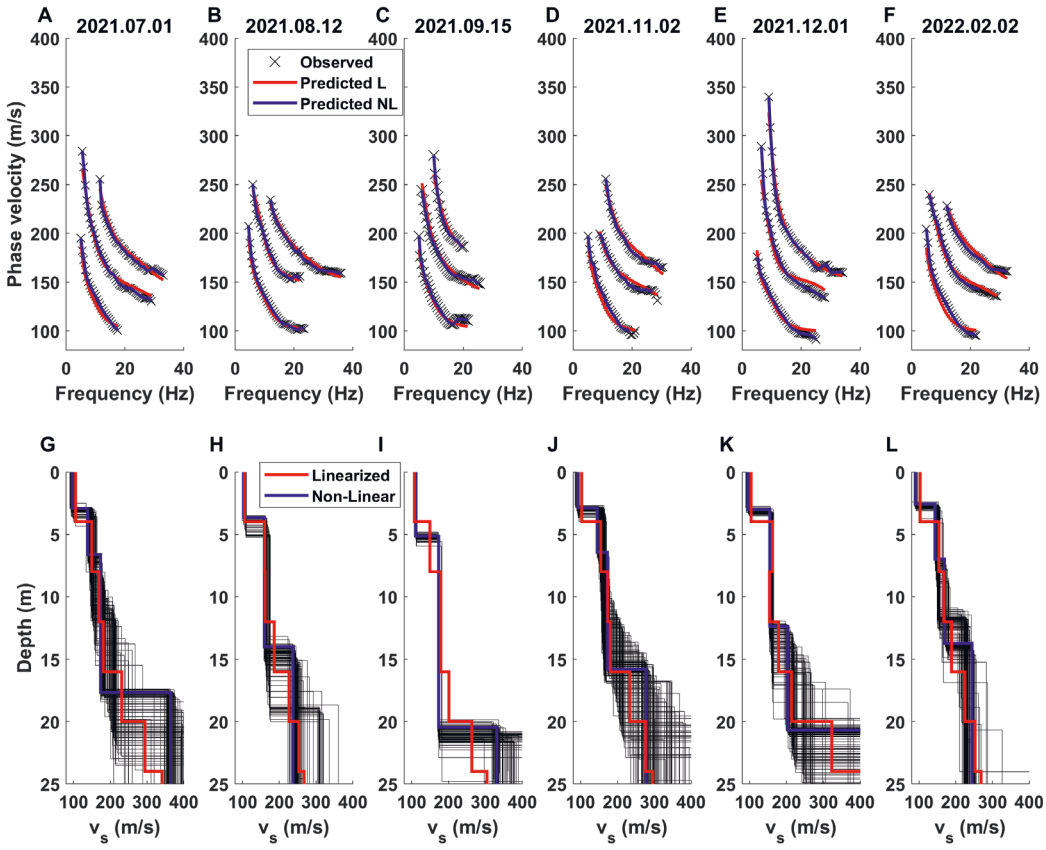

Figure 3.B.2: Same as Figure 3.6 and Figure 3.B.1 but for the inversion of three modes.

σ'_h/σ'_v) is kept constant ($\simeq$0.66) when assuming a friction angle, based on comparable clay material from Gella (2017). The clay is modeled as normally consolidated with an over-consolidation ratio (OCR) equal to one. That is, the *in situ* vertical differential stress is about equal to the past maximum vertical differential stress. A more detailed explanation of the model and its parameters and assumptions can be found in Hardin and Blandford (1989). Furthermore, the shear wave velocity (v_{sv}) is computed as

$$v_{sv} = \sqrt{\frac{c_{44}}{\rho_b}} \tag{3.2}$$

when assuming 100% water saturation. The shear wave is assumed to propagate in the vertical direction along the z-axis, with the particle motion horizontally along the x-axis. The bulk density (ρ_b) is calculated as a volume-weighted average between the mineral and pore fluid densities (see Table 3.C.1). The resulting predicted shear modulus is depicted in Figure 3.C.1C and the corresponding shear-wave velocity depth profile, given the specific *in situ* conditions for a 25 m thick quick clay column, in Figure 3.C.1D.

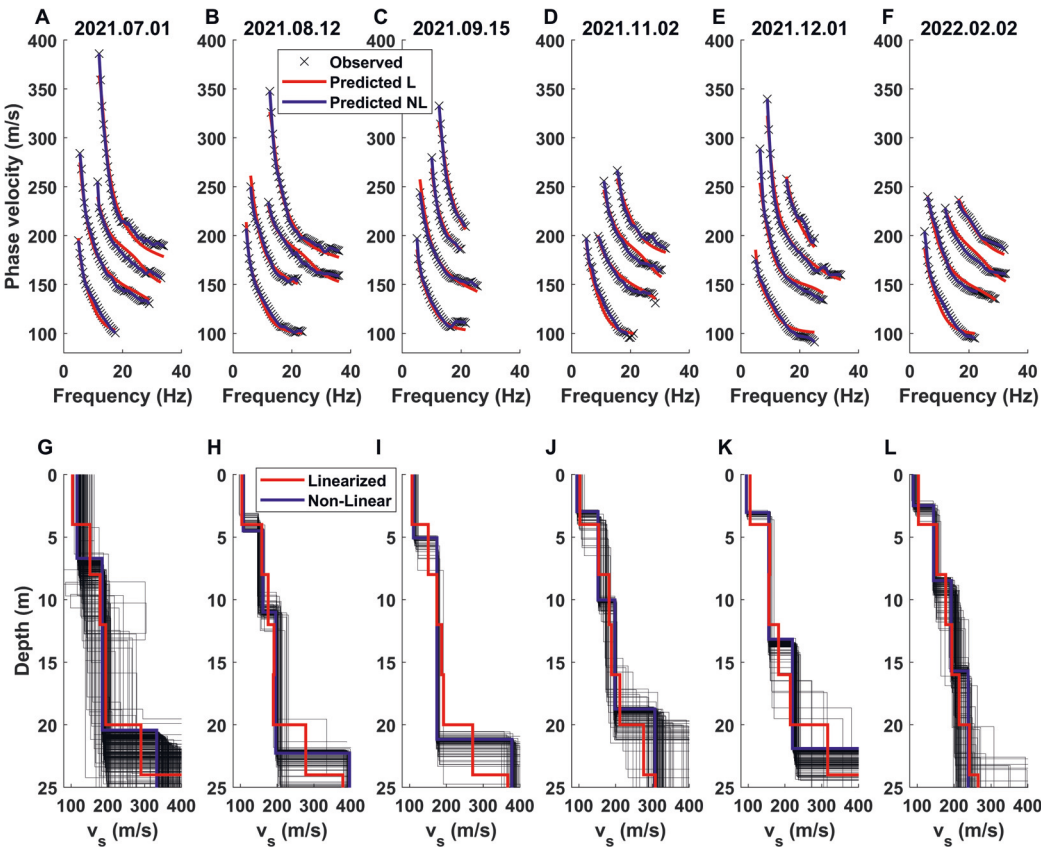

Figure 3.B.3: Same as Figure 3.6 and Figure 3.B.1 but for the inversion of four modes.

In addition to modeling the shear-wave velocity profile, the effect of the applied surface load caused by the new road foundation is investigated using the analytical expression of Boussinesq (1885). Under the assumption of uniform strip load, the vertical total and effective stress changes are estimated as a function of the depth of the 19 m deep well-bore located 30 m from the edge of the new road foundation. The foundation has a minimum width of 30 m and a minimum thickness of about 2.4 m with an assumed bulk density of 1660 kg/m^3. This results in an estimated vertical stress increase of 39 kPa underneath the road stip. The vertical stress change ($\Delta\sigma_z$) can then be computed:

$$\Delta\sigma_z = \frac{q}{\pi}(\alpha + \sin(\alpha)\cos(\alpha + 2\beta)), \tag{3.3}$$

where q is the load per unit area introduced by the road, α the angle between the far end of the foundation and a position along the well-bore make, whereas β is the angle between the closest point of the foundation and the position along the well-bore. The vertical stress change at 19 m depth in the well location is estimated to be about 1.2 kPa

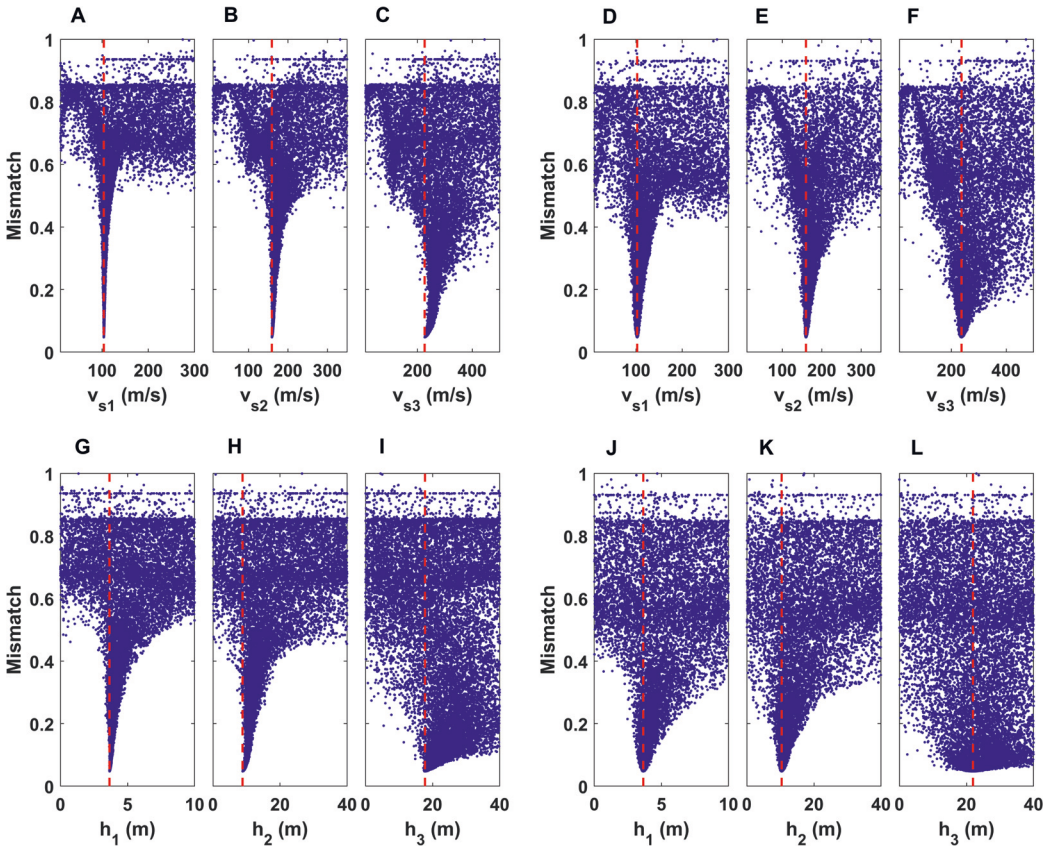

Figure 3.B.4: MDS from 21 August 2021 for one mode (A-C and G-I) and three modes (D-F and J-L).

(see Figure 3.C.1E), which corresponds to a shear-wave velocity increase of about 0.4 m/s or no change in the shear velocity.

In addition to comparing the shear-wave velocities to rock physics, the profiles are compared to an ultrasound test of a $30\times50\times20$ cm^3 sample extracted from the survey area (from a depth of $\simeq$40 cm). Laboratory investigation showed a velocity of 160 m/s using a 100 kHz input signal and a high attenuation level, where the output center frequency decreased to $\simeq$15 kHz.

Table 3.C.1: Modeling parameters used in predicting the elastic shear modulus depth profile as shown in Figure 3.C.1.

Variables	Description	Values
OCR	Over-consolidation-ratio	1.00
k	Dependent on the plasticity index of the soil	0.30
e	Void ratio or pore volume	Void ratio depth profile (Figure 3.C.1B)
ν	Poisson's ratio for wet conditions	0.48
S_{44}	Dimensionless elastic stiffness coefficient	1400.00
n	Stress coefficient	0.50
p_{ref}	Atmospheric pressure	$\simeq$101.31 kPa
ρ_m	Density of mineral material	2.75 g/cm^3
ρ_p	Density of pore water	1.00 g/cm^3

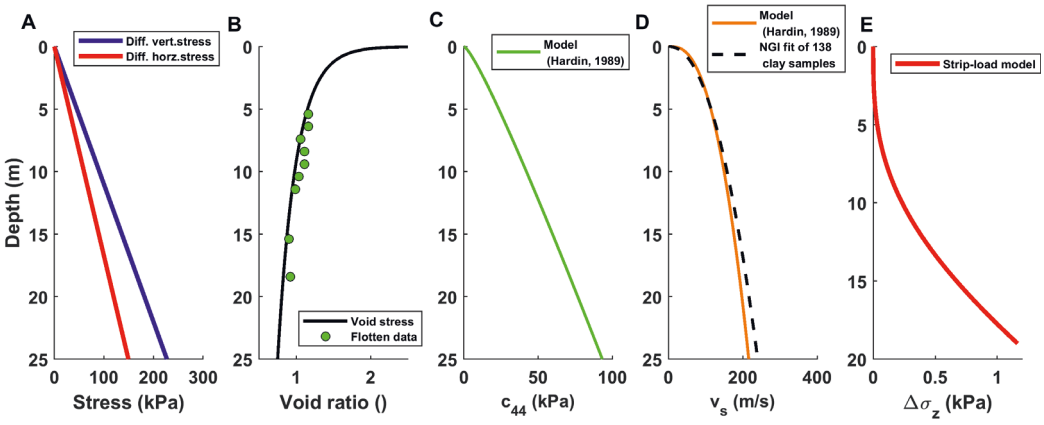

Figure 3.C.1: Stress (A) and void ratio (B) depth profiles are used in estimating the shear modulus depth trend at the Rissa acquisition site when assuming hydrostatic pore pressure conditions. In (B), the green dots represent the average bulk density estimated from lab analysis of quick clay samples of the Tiller site in Trondheim, Norway. (C) The predicted shear modulus depth profile using the model of equation (3.1). (D) The corresponding synthetic shear wave velocity depth profile (the orange) along with NGI's fitted regression line is based on 138 clay cores (the black) acquired from central- and eastern-Norway (L'Heureux et al. 2015). (E) The vertical stress change as a function of depth is estimated using the strip-load model (Boussinesq 1885).

Chapter 4

Paper 3: Average Q_p and Q_s estimation in marine sediments using a dense receiver array

Robin André Rørstadbotnen[1,2], Martin Landrø[1,2]

1 - Department of Electronic Systems, Norwegian University of Science and Technology (NTNU), 7491 Trondheim, Norway,

2 - Centre for Geophysical Forecasting, NTNU, 7491 Trondheim, Norway,

Paper published by Geophysics in February-March 2023 edition (Rørstadbotnen and Landrø 2023).

4.1 Abstract

A new spectral ratio method has been used to compute average P- and S-wave quality factors, Q_p and Q_s, for the sedimentary sequence below the "V"-shaped Oseberg permanent reservoir monitoring (PRM) system. Quality factors are important for a more accurate characterization of the subsurface and to obtain additional information on the physical processes within the earth, such as fluid content and partial melt. However, few methods compute the average Q-value in sediments for P- and S-waves in a region, which can be used as a constraint for attenuation models in more sophisticated inversion techniques such as full-waveform inversion or attenuation tomography. To address this, a spectral ratio method using two receiving stations, one installed on sediment and one installed on bedrock, has been developed. This has resulted in quality factor estimations ranging from approximately 64 to 137 for P-waves and 29 to 123 for S-waves using a

subset of the 172 ocean-bottom nodes in the Oseberg PRM system and a seismometer in Bergen, Norway. The Q_p values are more scattered and hence more uncertain than the Q_s values due to the P-wave signal being close to the background noise level. In the study area, local earthquakes of magnitude as low as M_L 2.4 can be used to obtain Q_p values and earthquakes of magnitude lower than 2.1 to find Q_s values, with the possibility of using lower magnitude events if the epicentral distances to the receivers are similar and smaller. Using this method, the average quality factor in sediment packages, for a variety of regions, can be estimated using appropriate raypath configurations connecting source and receiver.

4.2 Introduction

Seismic waves are known to attenuate when propagating through the subsurface. This wave attenuation will reduce the amplitude of the signal with increasing propagation distance, leading signals at some frequencies to fall below the noise floor, and decreasing the frequency bandwidth. It also will cause a frequency-dependent phase shift and, therefore, a waveform change. The seismic attenuation often is described by the quality factor Q, a measure of the efficiency of wave propagation, or its inverse, Q^{-1}, the internal friction (Stein and Wysession 2003, Romanowicz and Mitchell 2007). The factor Q can be specified for different types of waves, as they show different attenuation behavior when propagating through the same geology. This paper focuses on the average quality factor for P- and S-waves through a given sediment package, Q_p and Q_s. It also has been observed that the quality factor varies for different types of geology. In sedimentary layers, the value is normally much lower than in bedrock. Low Q values mean that the seismic wave amplitudes attenuate more and experience more phase change than high values. In addition, an important consequence of attenuation is physical dispersion, where a high attenuation causes a high dispersion. Conversely, a low attenuation will produce little to no dispersion (Stein and Wysession 2003). In general, two main mechanisms control the level of attenuation: seismic absorption (heat loss) and scattering. No discrimination between the two will be made; instead, the effective, or combined, attenuation is studied. Attenuation is recognized as a significant seismic parameter that, when known and compensated for, may allow for improved interpretation of seismic data. Furthermore, due to the high variation of Q values in the crust and uppermost mantle, this parameter can be related to additional geologic and geophysical information that cannot be found using other geophysical tools. This information can subsequently be used, for example, to more confidently characterize oil and gas reservoirs, monitor CO_2 injection, magnitude estimation of earthquakes, map 3D geologic structures and dynamics within the earth, and provide improved estimates of synthetic seismograms (Aki 1980, Stainsby and Worthington 1985, Tonn 1991, White 1992, Hauksson and Shearer 2006, de Lorenzo et al. 2013, Amalokwu et al. 2014).

In addition to the variation in the crust and the uppermost mantle, the quality factor can

be affected by the regional geology, such as differences observed within and at the interface among the crust, mantle, and core (Mitchell 1995, Romanowicz and Mitchell 2007). To map the crust and mantle attenuation, tomographic analyses have been carried out for the entire earth. Mitchell et al. (2008) map, for example, the overall trend for Eurasia. However, these tomographic models do not capture the local variation of the Q values, e.g., the difference between the local Q value in sediment packages and bedrock as studied here. Moreover, there are several studies that capture the local attenuation in a given area: Beckwith et al. (2017) use prestack Q inversion for a seismic reflection survey in the North Sea, Zollo and de Lorenzo (2001) use a pulse width method in Flegrei Caldera (Italy) and, more recently, Sketsiou et al. (2021) find a 3D attenuation image of the Pollino fault network in Italy. Other studies on oil and gas fields characterize the attenuation values through analysis of well data (see, e.g., Reid et al. (2001), Sams et al. (1997), Carter et al. (2020)). This work aims to add a new spectral ratio method for local attenuation estimation to these studies. The method has been developed to estimate Q values of a sedimentary package for P- and S-waves using station pairs, one station placed on sediment and one placed on bedrock using earthquakes as the source. The method provides average estimates of the given sedimentary package that can serve, for example, as a model constraint for more complicated estimation methods, such as full-waveform inversion and attenuation tomography. The quality factor for a 5–7 km thick sediment package below Oseberg C has been estimated using a permanent reservoir monitoring (PRM) system and a seismometer in Bergen, Norway (Figure 4.1). The method has been applied to three local earthquakes recorded in January 2014.

The method presented in this paper contains aspects comparable to the procedure developed by Teng (1968) and later applied by, e.g., Solomon (1973) and Hwang et al. (2009). Furthermore, others have applied spectral ratios to estimate Q values. Dasgupta and Clark (1998) use spectral division on conventional surface seismic common-midpoint reflection data to find seismic attenuation values in the southern North Sea. Subsequently, Liu et al. (2018) use a modified log spectral ratio method to find Q values, and Mayeda et al. (2007) use a coda spectral ratio of narrowband envelopes to find the attenuation. Hauge (1981) measures attenuation from vertical seismic profiles using spectral ratios between downhole pulses and a reference pulse. The proposed method differs from the listed ones by taking the spectral ratio of a station pair, with one receiver located on sediment and the other located on bedrock, to estimate the quality factor value of a sedimentary sequence for P- and S-waves.

4.3 Data and theory

Earthquakes recorded on receivers at the Oseberg field, the North Sea, and Bergen, Norway (Figure 4.1) were analyzed in this work. The Oseberg data (OSE) were acquired on 172 4C ocean-bottom nodes (OBNs) connected by a seismic cable, containing three orthogonal geophones and one hydrophone, as part of the V-shaped Oseberg PRM system.

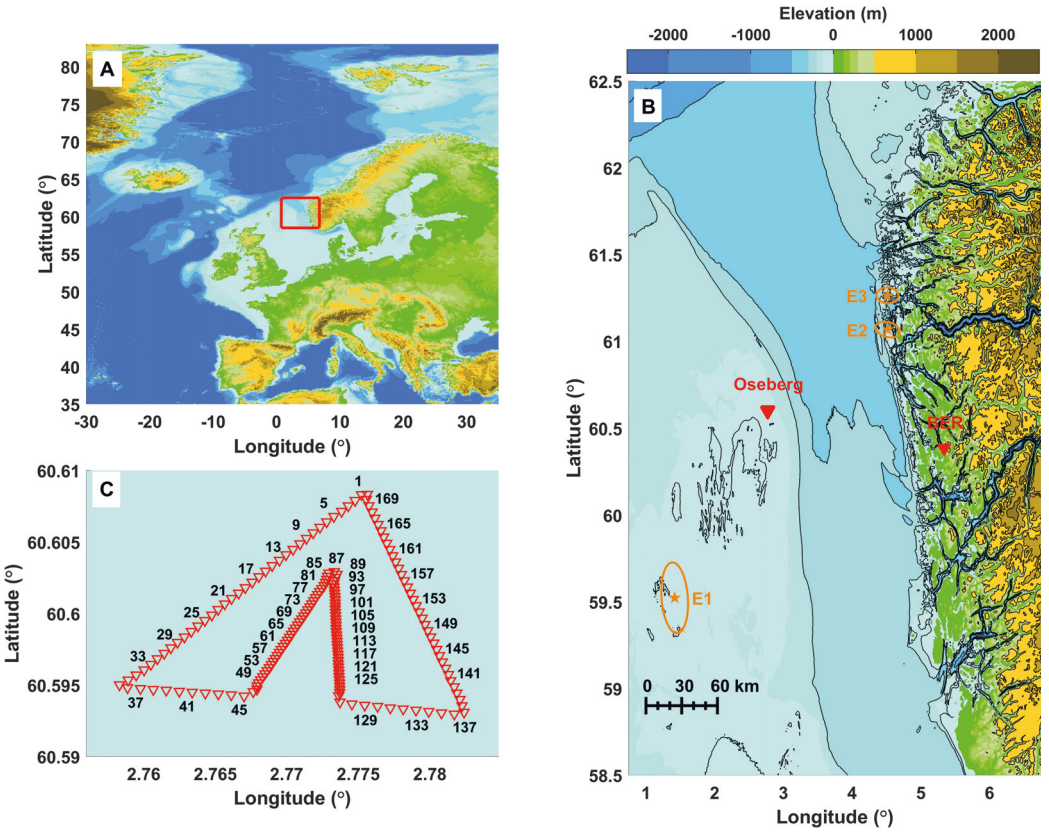

Figure 4.1: Overview of the region of interest. (A) The study area relative to Europe with the red rectangle showing the study area (bathymetry map from GEBCO (2021)). (B) The location of the earthquakes (the orange stars) with associated error ellipses and the receivers (the red triangles). (C) The receiver geometry of the 172 OBN just south of the Oseberg C platform.

The sensor spacing of the outer legs and inner legs was 50 and 25 m, respectively (see Figure 4.1C) and trenched 1–2 m into the seabed at a water depth of 108 m (Bussat et al. 2016). The data recorded in Bergen (BER) were recorded on a 3C broadband seismometer located at the University of Bergen campus. Only one month of data from the Oseberg PRM was available for the analysis (January 2014); three local earthquakes were visible in the data and hence focused on in this analysis. These events will be denoted as E1 for the earthquake on 14 January 2014, E2 for the earthquake on 21 January 2014, and E3 for the earthquake on 23 January 2021. Key facts about the earthquakes are summarized in Table 4.1. Note that no depth estimate was provided for the low-magnitude E1 due to its remote location and distance to the receivers. In addition, six teleseismic earthquakes are reported for January 2014 by USGS (2022) with magnitudes higher than M_{ww} 6.1, with a maximum magnitude of 6.5. There were two main reasons why these were not included in the analysis: (1) As the method estimates the quality factor of the sedimentary layer at the

Table 4.1: Information for the local earthquakes used to estimate the quality factors.

Name	Date	Time	(Lat°, Lon°)	Depth (km)	Mag (M_L)	Station	Distance (km)
E1	2014.01.16	17:03:31	(59.51, 1.47)	-	2.11	BER	239
						OSE	142
E2	2014.01.21	06:39:04	(61.05, 4.72)	13.6	2.35	BER	107
						OSE	88
E3	2014.01.23	04:32:50	(61.24, 4.70)	9.6	2.57	BER	119
						OSE	107

end of the wave propagation path, the teleseismic signal will be dominated by the signal propagating in the bedrock and mantle, and hence not focusing on the effects occurring in the sedimentary layer. (2) The magnitudes of the events were relatively small with a long propagation path (the smallest propagation distance is 2700 km with a magnitude of 6.1).

4.3.1 Preprocessing

To prepare the Oseberg PRM data for Q-value estimation, various preprocessing steps were carried out. (1) Platform noise present in the Oseberg data was suppressed using an $f - x$-filter (Schonewille et al. 2008). The noise was suppressed by four iterations using a noise threshold of seven with five filter points and a frequency band from 1 to 50 Hz. An example of the data from E3 and the effect of the platform noise removal are shown in Figure 4.2. The $f - x$-filter only changed the noise portions of the data, leaving the earthquake signal (and therefore the spectrum) untouched (Schonewille et al. 2008). This also can be observed in the difference plot in Figure 4.2C, in which only the noise part has been affected, whereas the earthquake signal was not. (2) The Oseberg data were converted from g (using a constant factor of 9.81 m/s^2) to particle acceleration and further integrated into particle velocity to match the same measurement unit as the BER seismometer. (3) The data were detrended and (4) all the data were resampled to a common sample rate. Because only frequencies from the local earthquakes were of interest, (5) a Tukey window and a fourth-order Butterworth band-pass filtered with cut-off frequencies at 1 and 40 Hz were applied. The low-cut frequency was set to 1 Hz to remove the most prevalent part of the ocean noise at Oseberg.

4.3.2 Traveltime computation

A ray-tracing algorithm was used to compute the traveltimes needed in the analysis. To calculate these values, a P-wave velocity model representing the geology in the Oseberg area was constructed. This velocity model was generated using the same approach as Jerkins et al. (2020) by combining a local sonic log from well 30/6-1 (Figure 4.3A), and a regional layered velocity model of the area (Havshov and Bungum 1987), as shown in Figure 4.3A, B. The ray-tracing algorithm is a high-frequency approximation to the

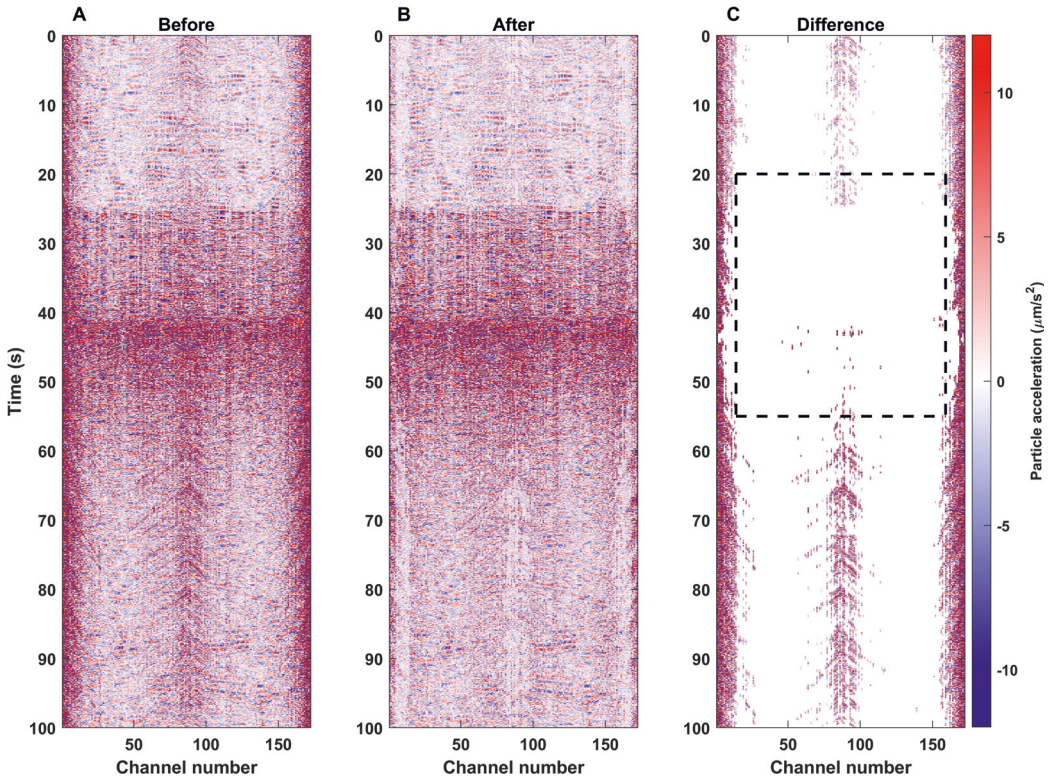

Figure 4.2: Suppression of platform noise from Oseberg C. (A) The raw observed signals. (B) The observed signal after the $f - x$-filter. (C) The difference between (A) and (B). This shows that the noise closest to the platform (channels 1–16, 80–100, and 157–172) has successfully been suppressed. The dashed rectangle indicates the area used for the analysis and the nodes closest to the platform (1–14 and 159–172) are too contaminated by platform noise to give reliable results and are discarded a priori to the analysis

wave equation and therefore requires a smooth velocity model as input (Figure 4.3C). The smoothing ensures that the characteristic dimensions of inhomogeneities were considerably larger than the prevailing wavelength in the model (Cervenỳ 2001). Hence, a four-step workflow to find a smoothed representation of the combined velocity model was used. (1) The rapid changes in the sonic log were smoothed as shown in Figure 4.3A using a 0.76 km moving average window. (2) The end of the sonic log ($\simeq$3.2 km depth) was connected to the regional velocity model at a depth of 8.125 km (Figure 4.3B). (3) Linear interpolation was applied so that the entire model had the same depth sampling interval. Finally, (4) a moving average filter with a window of 3.048 km was applied for the final smoothing. The linear interpolation and moving average filter were chosen for simplicity and efficiently smoothed the data to the desired level.

The ray-tracing algorithm used to model the raypaths through the subsurface is based

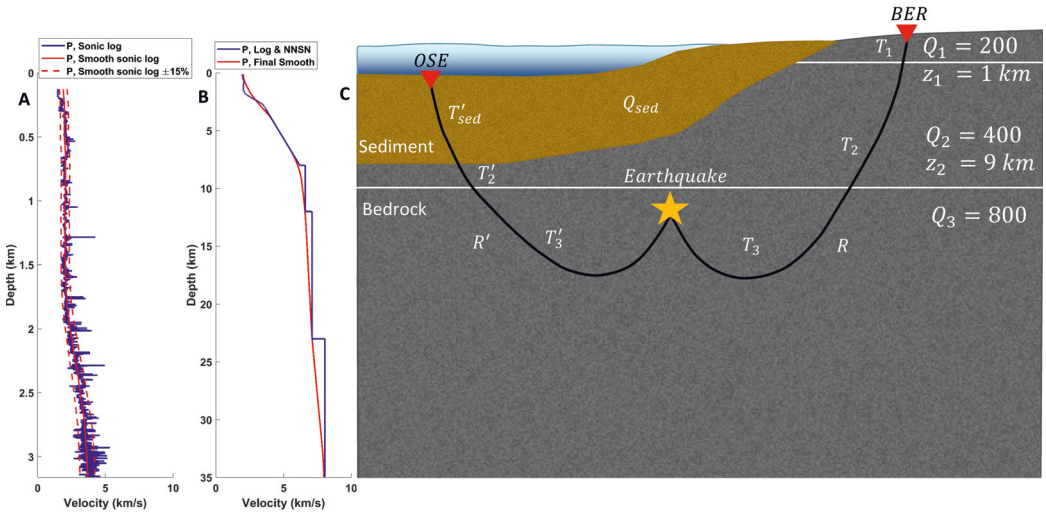

Figure 4.3: Velocity model and conceptual sketch. (A) The sonic log from well 30/6-1 (the blue) and the smoothed version (the red) with the assumed 15% uncertainty indicated (the dashed red lines). (B) The final velocity model (the red), combining the smoothed sonic log and NNSN P-wave crustal velocity model (the blue). (C) The raypaths to BER is assumed to be dominated by attenuation in bedrock, whereas the travel path to Oseberg is affected by attenuation from 5 to 7 km thick sediment package and the same bedrock model as for the raypath to BER. The Q model of the bedrock is assumed known, whereas the value (Q_{sed}) for the sediment package is estimated.

on the ray equations. The ray equations are used to approximate the nonlinear eikonal equations and are given by (Thomson and Chapman 1985, Keers et al. 1997)

$$\frac{d\boldsymbol{x}}{dt} = v^2(\boldsymbol{x})\boldsymbol{p}, \tag{4.1}$$

$$\frac{d\boldsymbol{p}}{dt} = -\frac{1}{v(\boldsymbol{x})}\nabla v(\boldsymbol{x}). \tag{4.2}$$

The modified Euler method is used to numerically implement the equations:

$$\boldsymbol{x}_{i+1} = \boldsymbol{x}_i + \Delta t v^2(\boldsymbol{x}_i)\boldsymbol{p}_i, \tag{4.3}$$

$$\boldsymbol{p}_{i+1} = \boldsymbol{p}_i - \Delta t \left(\frac{1}{v(\boldsymbol{x}_{i+1})} \frac{\partial}{\partial \mathbf{x}} v(\boldsymbol{x}_{i+1}) \right), \tag{4.4}$$

where $\boldsymbol{x}$ is the position along the ray, $v(\boldsymbol{x})$ is the velocity from the velocity model, Δt is the time step and $\boldsymbol{p}$ is the slowness vector.

4.3.3 Q estimation using spectral division of data from two sensors

To estimate the Q value for the sediment package underneath the Oseberg C platform, a spectral division method was applied to the signals recorded on the Oseberg PRM system

and the BER seismometer. Note that the quality factor was assumed to be frequency independent. This was a common, but questionable, assumption as discussed by Douglas (1992), Sams et al. (1997), Romanowicz and Mitchell (2007), Beckwith et al. (2017), among others. As shown in Figure 4.3C, the raypaths to OSE propagated through a layered bedrock model at the start and later through a 5–7 km thick sediment layer before being recorded. In contrast, the raypaths to BER traveled primarily through the layered bedrock model. The layered bedrock model was created based on previous studies from the North Sea (Dasgupta and Clark 1998, Reid et al. 2001, Mitchell et al. 2008). Following these definitions, the predicted amplitudes recorded at OSE (A_1) and BER (A_2) can be given, under the low-loss condition ($Q \gg 1$), as (Stein and Wysession 2003)

$$A_1 = \frac{S}{R_1} \exp\left(-\pi f \frac{T'_{sed}}{Q_{sed}}\right) \exp\left(-\pi f \sum_{i=1}^{N_1} \frac{T'_i}{Q_i}\right), \tag{4.5}$$

$$A_2 = \frac{S}{R_2} \exp\left(-\pi f \sum_{k=1}^{N_2} \frac{T_k}{Q_k}\right), \tag{4.6}$$

where S is the source signature; T'_{sed}, T'_i, and T_k are the traveltime through the sedimentary layer, through layer i to the sediment package and through layer k to BER, respectively; N_1 and N_2 are the numbers of bedrock layers the ray travels through; R_1 and R_2 denote the geometric spreading factors and are given as the travel distances to OSE and BER, respectively; Q_{sed} represents the average attenuation in the sediment package; Q_i and Q_k are the attenuations in the bedrock layers.

By performing a spectral division between the predicted amplitude at OSE with that of BER, the following expression is obtained:

$$\frac{A_1}{A_2} = \frac{R_2}{R_1} \frac{\exp\left(-\pi f \frac{T'_{sed}}{Q_{sed}}\right) \exp\left(-\pi f \sum_{i=1}^{N_1} \frac{T'_i}{Q_i}\right)}{\exp\left(-\pi f \sum_{k=1}^{N_2} \frac{T_k}{Q_k}\right)}, \tag{4.7}$$

which can be rewritten into the following form:

$$\ln\left(\frac{A_1}{A_2}\right) = \ln\left(\frac{R_2}{R_1}\right) - \pi f \left(\frac{T'_{sed}}{Q_{sed}} + \sum_{i=1}^{N_1} \frac{T'_i}{Q_i} - \sum_{k=1}^{N_2} \frac{T_k}{Q_k}\right). \tag{4.8}$$

From this, the coefficients of a straight line with slope a and intercept b can be defined:

$$b = \ln\left(\frac{R_2}{R_1}\right), \tag{4.9}$$

$$a = -\pi \left(\frac{T'_{sed}}{Q_{sed}} + \sum_{i=1}^{N_1} \frac{T'_i}{Q_i} - \sum_{k=1}^{N_2} \frac{T_k}{Q_k}\right). \tag{4.10}$$

Table 4.2: The mean value, with one standard deviation, for the different terms in equation (4.11) using a three-layered bedrock quality factor (Q) model (see Figure 4.3 for Q model). The mean and standard deviation are found from the different values obtained as described in the "Data and theory" section. The quantified uncertainties are presented subsequently.

Name	Wave	$-a/\pi$ (s)	Δt^* (s)	$T_1 - T_2$ (s)	T'_{sed} (s)
E1	S	0.052 ± 0.01	0.052	-34.7 ± 0.08	5.10 ± 0.0006
E2	P	0.035 ± 0.02	0.005	0.84 ± 0.08	3.27 ± 0.002
E2	S	0.060 ± 0.01	0.008	1.46 ± 0.13	5.65 ± 0.003
E3	P	0.044	0.007	-0.84	3.27
E3	S	0.050 ± 0.008	0.012	-1.35 ± 0.14	5.67 ± 0.003

Subsequently, the slope can be found by linear regression of the ratio $\ln(A_1/A_2)$ for a frequency range above the noise floor for both signals. Rearranging, the average quality factor in the sediment package Q_{sed} can be computed using the measured slope a:

$$Q_{sed} = \frac{T'_{sed}}{-\frac{a}{\pi} - \sum_{i=1}^{N_1} \frac{T'_i}{Q_i} + \sum_{k=1}^{N_2} \frac{T_k}{Q_k}}. \tag{4.11}$$

Note that the spectral ratio eliminates the effects of the source term, whereas geometric spreading is accounted for in intercept b, independent from the final Q_{sed} estimation. Furthermore, the effect of instrument response on the recorded earthquakes is expected to be the same for all the receivers because the dominant frequency range is within the flat part of the instrument response for both receiver types used. Common values for the different terms are summarized in Table 4.2, where the notation has been simplified by letting $t^* = \sum t/Q$ and hence:

$$\Delta t^* = -\sum_{i=1}^{N_1} \frac{T'_i}{Q_i} + \sum_{k=1}^{N_2} \frac{T_k}{Q_k}. \tag{4.12}$$

4.3.4 Uncertainty analysis

The quality factor given in equation (4.11) is a function of the slope a, the traveltime through the sediment layer T'_{sed}, and the traveltime differences divided by the assumed quality factor in the bedrock Δt^*. By assuming that the parameters, a, T'_{sed}, and Δt^*, are independent of each other, an estimation of the uncertainty related to Q_{sed} can be found through

$$\delta Q_{sed} = \sqrt{\left(\frac{\partial Q_{sed}}{\partial a}\delta a\right)^2 + \left(\frac{\partial Q_{sed}}{\partial T'_{sed}}\delta T'_{sed}\right)^2 + \left(\frac{\partial Q_{sed}}{\partial \Delta t^*}\delta \Delta t^*\right)^2}, \tag{4.13}$$

where δa is the standard error of the slope found in the regression analysis and $\delta T'_{sed}$ and $\delta \Delta t^*$ are, in this case, the errors related to an erroneous velocity model used to compute

the traveltimes through the sedimentary sequence and the bedrock. The errors in the velocity model are assumed to be 15%, based on the variation in the sonic log from well 30/6-1 (see Figure 4.3A). Moreover, the weak point of this method, in this scenario, is that the parameters T'_{sed} and Δt^* are not fully independent. Therefore, the assumption is that they are weakly related to each other and can thus be treated as independent (Landrø 2002). Furthermore, the uncertainty parts in equation (4.13) are assumed independent, i.e., that they are orthogonal and, hence, a conservative estimate of the total uncertainty of Q_{sed}. The partial derivatives in equation (4.13) are given as

$$\frac{\partial Q_{sed}}{\partial a} = \frac{T'_{sed}}{\pi \left(\frac{-a}{\pi} + \Delta t^*\right)^2}, \tag{4.14}$$

$$\frac{\partial Q_{sed}}{\partial T'_{sed}} = \frac{1}{\frac{-a}{\pi} + \Delta t^*}, \tag{4.15}$$

$$\frac{\partial Q_{sed}}{\partial \Delta t^*} = \frac{-T'_{sed}}{\left(\frac{-a}{\pi} + \Delta t^*\right)^2}, \tag{4.16}$$

and, hence, the uncertainty in the average quality factor as

$$\delta Q_{sed} = \sqrt{\left(\frac{T'_{sed} \cdot \delta a}{\pi \left(\frac{-a}{\pi} + \Delta t^*\right)^2}\right)^2 + \left(\frac{\delta T'_{sed}}{\frac{-a}{\pi} + \Delta t^*}\right)^2 + \left(\frac{-T'_{sed} \cdot \delta \Delta t^*}{\left(\frac{-a}{\pi} + \Delta t^*\right)^2}\right)^2}. \tag{4.17}$$

4.4 Results and discussion

4.4.1 The Q estimation

The Q_{sed} values are computed using a subset of the 172 receivers available at Oseberg. The stations closest to the platform (channels 1–14 and 158–172 inclusive) are visibly highly contaminated by platform noise and are a priori discarded from the analysis. To find reliable channels, two conditions based on signal-to-noise ratios (SNRs) are introduced (for computation of SNR, see Appendix 4.A).

The first SNR condition uses the root mean square (RMS) of equal length windows to compute the SNR. The three windows are (1) before the P-wave arrival assumed to only contain noise (noise RMS), (2) after the P-wave arrival, including the P-wave signal (P-wave RMS), and (3) after the S-wave arrival, including the S-wave signal (S-wave RMS). Figures 4.4A, B, E, F show examples of how the first breaks are found on the OSE and BER data (for a comparison between high and low SNR waveforms from OSE, see Appendix 4.B). The window length is defined as the time interval between the P- and S-wave arrivals for the sensor closest to the event investigated, i.e., the station with the shortest P–S delay. From the resulting RMS values shown in Figures 4.5A, C, D, it is possible to see the differences in signal quality for receivers in different portions of the PRM system.

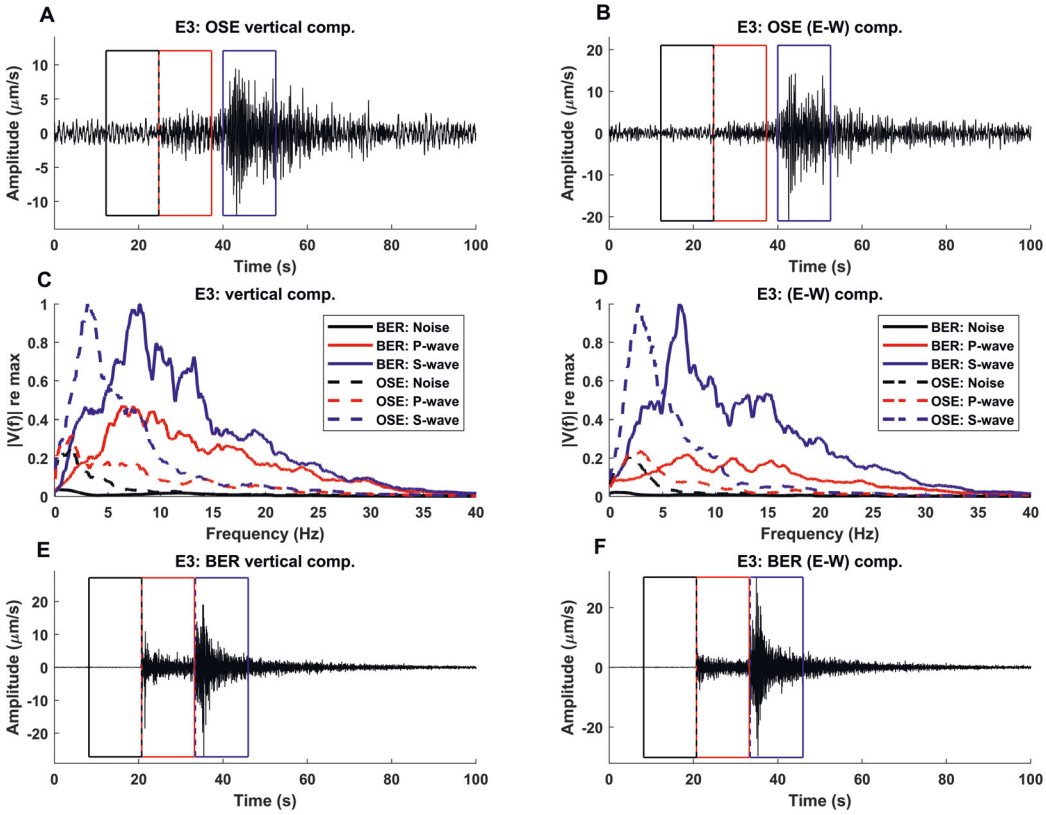

Figure 4.4: The time and frequency content of the different recording sites. (A, B) The time signals on the vertical and (east–west)-geophone components recorded by node 40 in the Oseberg PRM system. The boxes indicate the time window used to compute the noise and P- and S-waves amplitude spectra (and later RMS). (C, D) The respective amplitude spectra normalized to the individual maxima for BER and OSE. The noise is indicated in black, P-wave is indicated in red, and S-wave is indicated in blue. The solid lines represent BER and the dashed lines represent OSE. (E, F) The time signals recorded on the BER seismometer. The boxes indicate the time window (of equal size as in A and B) used to compute the noise and P- and S-waves amplitude spectra.

Channels at distances 3.08–3.58 km (channel number 80–100) are observed to have the highest RMS level for the received P- and S-waves for E2 and E3, perhaps due to better sensor coupling. Comparing the RMS noise from the window just before the P-wave signals with RMS from 3 h of data, assumed to contain noise only, the noise before E2 is lower than the mean for the 3 h of data, whereas the noise for E3 is similar (for mean noise RMS, see supplemental Figure D.1). The lower noise RMS for E2 is most likely due to the platform noise suppression being more efficient for this event compared with E3. The noise level for E2 is on average 0.71 μm/s compared to 0.98 μm/s for E3. The SNR level at which the estimated quality factor becomes stable (7.5 dB for P-wave arrivals, all S-wave arrivals) is then chosen, and channels with SNR above these boundaries

are considered reliable. Figure 4.5 shows the computed RMS values (Figures 4.5A, C, E) and the associated SNR values and boundary (Figures 4.5B, D, F). As expected, E3 shows the highest RMS and SNR values for the S-wave and E1 shows the lowest. It also is evident that the P-wave arrives with low amplitudes, barely above the noise floor for all earthquakes. By investigating the frequency content of the noise and P- and S-wave signals in Figures 4.4C, D, clear differences are observed. The BER amplitude spectrum exhibits more high-frequency components than the OSE amplitude spectra. This is interpreted to be due to the extra attenuation caused by the sediment package under the Oseberg PRM system as schematically shown in Figure 4.3C. Furthermore, the noise level at OSE is higher than BER, especially for low frequencies, even after suppressing the platform noise and ocean swell noise in the preprocessing. This is expected because the OBN network is affected by more low-frequency swell noise than the on-land BER seismometer.

The second condition compares the frequency component of the noise to the P- and S-wave frequency spectra, and the SNR for all components is calculated. Only channels with sufficiently high SNR to adhere to condition one are considered. To estimate reliable slopes from the spectral division, high SNR for as many frequency components as possible is needed. The SNR boundary for both waves is set to 10 dB. The frequency SNR boundary is shown in Figures 4.6G, H together with the spectral ratio for P- and S-wave obtained by taking the ratio between the smoothed amplitude spectra of a station pair as shown in Figures 4.6A, B, D, E. The smoothing is carried out to remove the effects of the frequency component close to zero, resulting in unstable division and a large effect on the final results. The effects of the frequency components close to zero are especially problematic for the higher frequencies as shown in Figures 4.6C, F, I. The bold portion of the spectral ratio shown in Figure 4.6 indicates the frequencies used in the robust regression (MATLAB "robustfit" function was used (Dumouchel and O'Brien 1989)) to estimate the slope and the associated uncertainties, a and δa, respectively (for more examples see supplemental Figures D.2–D.7). The slopes with a 95% confidence interval and the associated standard residual error (SRE) are represented in Figures 4.7A, B.

The estimated traveltimes through the sedimentary layer T'_{sed} and the difference in t^* values from the traveltime in the layered bedrock model Δt^* for all earthquakes analyzed are shown in Figure 4.8 (for examples of computed raypaths used to find these values, see supplemental Figure D.8).

Applying the values from the ray tracing, the SNR conditions, and the obtained slopes, the Q_{sed} values are estimated for the P- and S-wave arrivals. The attenuation results are plotted together in Figure 4.7C and individually along the array layout in Figure 4.9. To find the best boundaries for the first SNR condition, a plot without the introduced SNR boundary is made for comparison (see Figure 4.10). By comparing the estimates and the uncertainty found in equation (4.17) with and without the boundary (Figure 4.7C versus Figure 4.10) and the associated SNR for each channel (Figure 4.5) it is clear that the P-

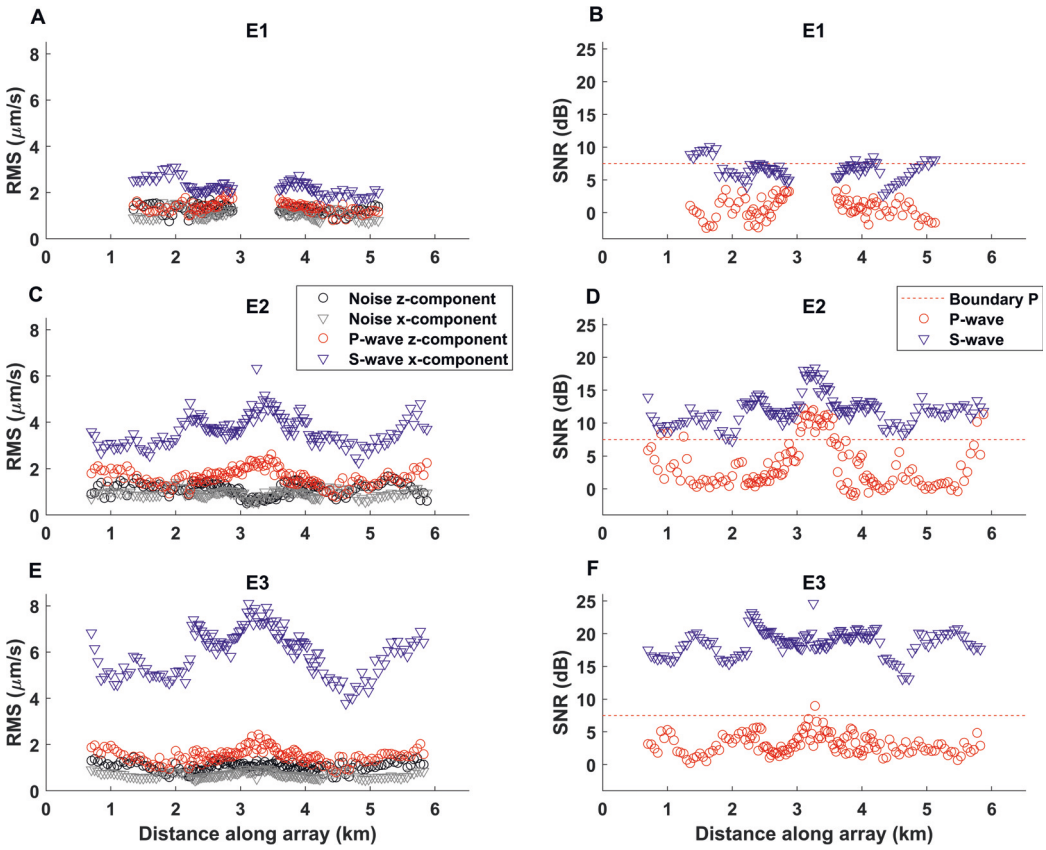

Figure 4.5: The RMS and SNR for the three earthquakes. (A) E1 computed RMS values for the noise recorded on the vertical (the black) and x-component (the gray), the P-waves on the vertical component (the red), and S-waves on the x-component (the blue). (B) The corresponding SNR for the P- and S-wave. The threshold for acceptable P-wave SNR (the dashed red lines) is set to 7.5 dB. (C, D, E, F) The RMS and SNR for E2 and E3.

wave attenuation values become unstable under approximately 7.5 dB, whereas the Q_s values are stable for all channels. For the Q_p values, the total uncertainty is generally high for the rejected values. However, some values have uncertainty close to the accepted values (e.g., the E1 estimates). These are considered unstable due to their low SNR, where their first-break arrivals were hardly visible in the waveforms. From this, a 7.5 dB boundary is set for the Q_p estimation, and no boundary for Q_s is set. This condition provides 27 estimated Q_p values and 378 estimated Q_s values for the events. Note that the estimated quality factor values are given as the mean and one standard deviation from the estimates obtained (see Table 4.2). The values for the quality factor and the associated uncertainties (from equation (4.17)) are given separately.

The results will be presented and discussed in four parts, starting with discussing the ef-

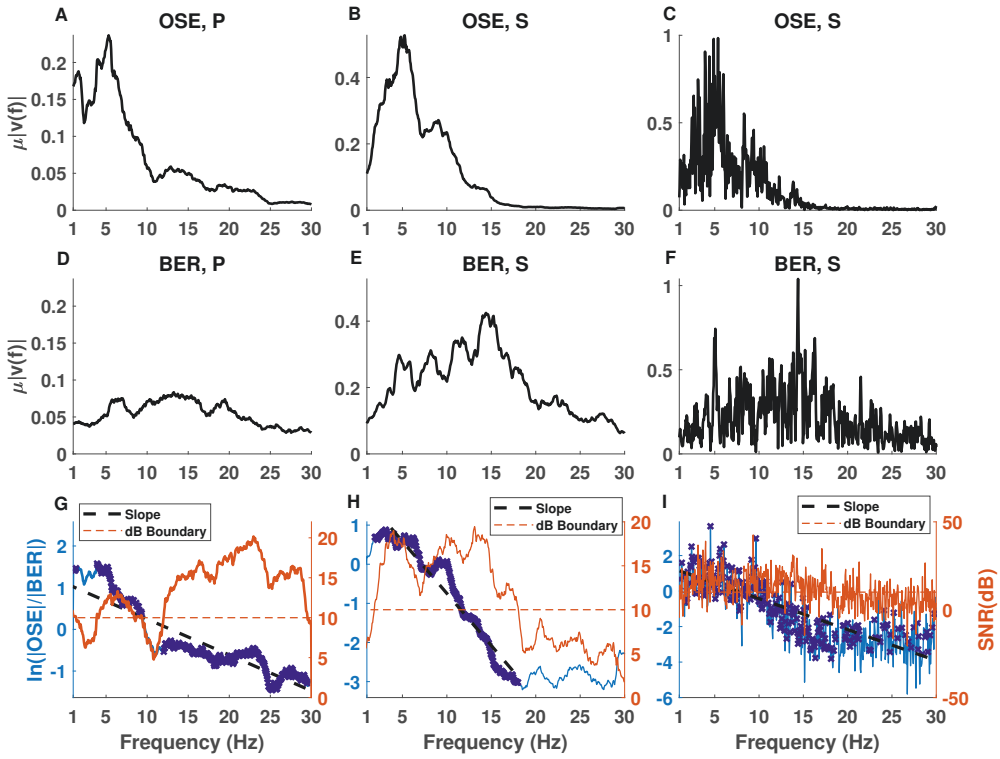

Figure 4.6: Computation of slopes from E2 using node 90 for (A, B, D, E, G, H) smoothed and (C, F, I) unsmoothed representations of the amplitude spectra. (A, B) The smoothed amplitude spectrum for the P- and S-wave phases, respectively, recorded on the Oseberg PRM data. (C) The unsmoothed amplitude spectrum for the S-wave phase for OSE. (D, E) The smoothed amplitude spectrum for the P- and S-wave, respectively, for BER. (F) The unsmoothed amplitude spectrum for the S-wave phase for BER. BER exhibits a higher frequency content than Oseberg, which can be attributed to the extra attenuation in the sediment. (G, H) The computation of the slope (the dashed black line) using the frequency components (the bold blue segments) with SNR above 10 dB (the dashed orange line) used in the Q_{sed} estimation. For more examples of slope estimates, see supplemental Figures D.2–D.7. (I) The computation of the slope using unsmoothed OSE and BER

fects of the assumed values, followed by a presentation and discussion of the results based on the epicenter location, starting with E1 and then E2 and E3. Finally, a comparison of the results will be presented.

4.4.2 Assumptions affecting the results

The model for the bedrock attenuation Q and the constant parameter for the sediment thickness used in the estimation are assumed to be known. These are based on results from previous Q and geologic studies of the North Sea. Mitchell et al. (2008) use attenuation

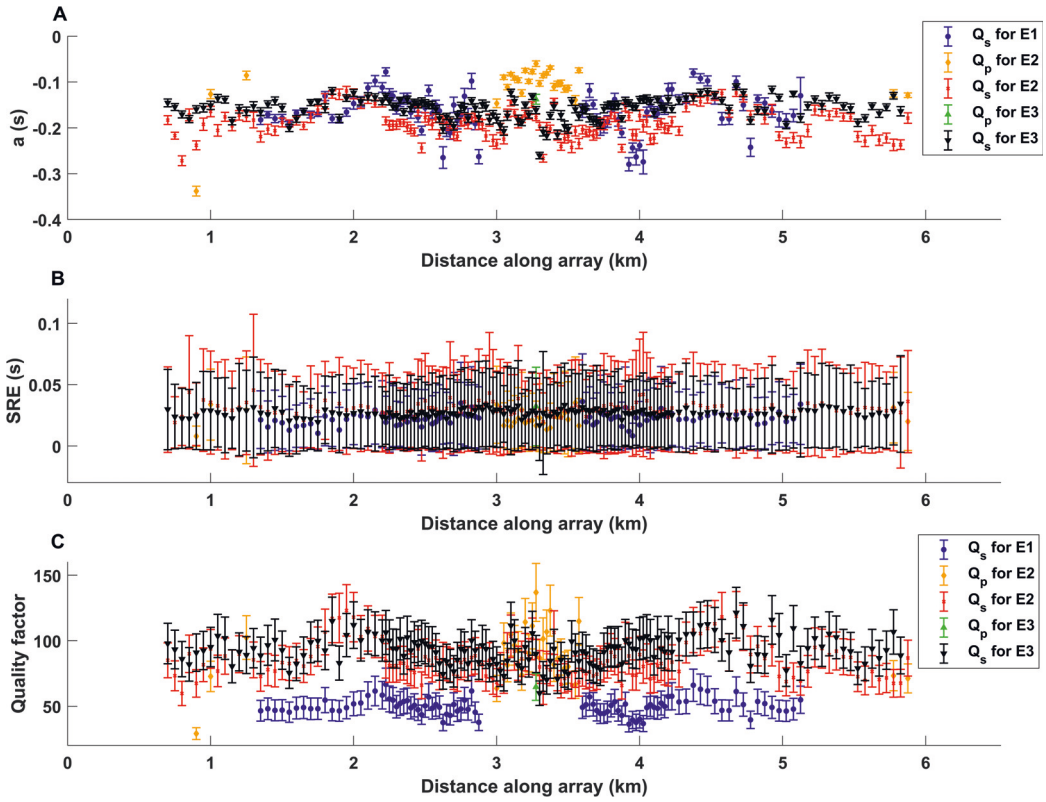

Figure 4.7: (A) Estimated slopes from the P- and S-waves with a 95% confidence interval for E1, E2, and E3. (B) The SRE of the slope estimates. (C) Estimated Q_p and Q_s values with uncertainty computed using equation (4.17)

tomography to estimate Q_{Lg} values for the entire Eurasia plate and find the quality factor value to be $\simeq$900, i.e., a nonattenuating media, for the Oseberg area, whereas Dasgupta and Clark (1998) and Reid et al. (2001) find local quality factor values to be between 81 and 1000 for sedimentary and bedrock in the North Sea. Furthermore, Beckwith et al. (2017) find a quality factor between 161 and 182 over the Kinnoull oil and gas field. These studies provide the area's widest range of credible values, and a three-layered Q model is chosen based on them (see Figure 4.3 C). Furthermore, the exact thickness of the sediment package varies due to the Oseberg mega block and ranges typically from 5 to 7 km (Færseth and Ravnås 1998). This induces uncertainty in the estimated Q_{sed} values as the computed traveltimes in the sedimentary sequence depend on the thickness. Decreasing the thickness of the sediment layer will decrease the traveltime value in the sedimentary layer (T'_{sed}) and increase the traveltime in the bedrock (T'). The consequence is that the Q_{sed} value will decrease as the decrease in T'_{sed} has a bigger effect on the quality factor estimate than the increase in T'. Decreasing the thickness of the sedimentary layer

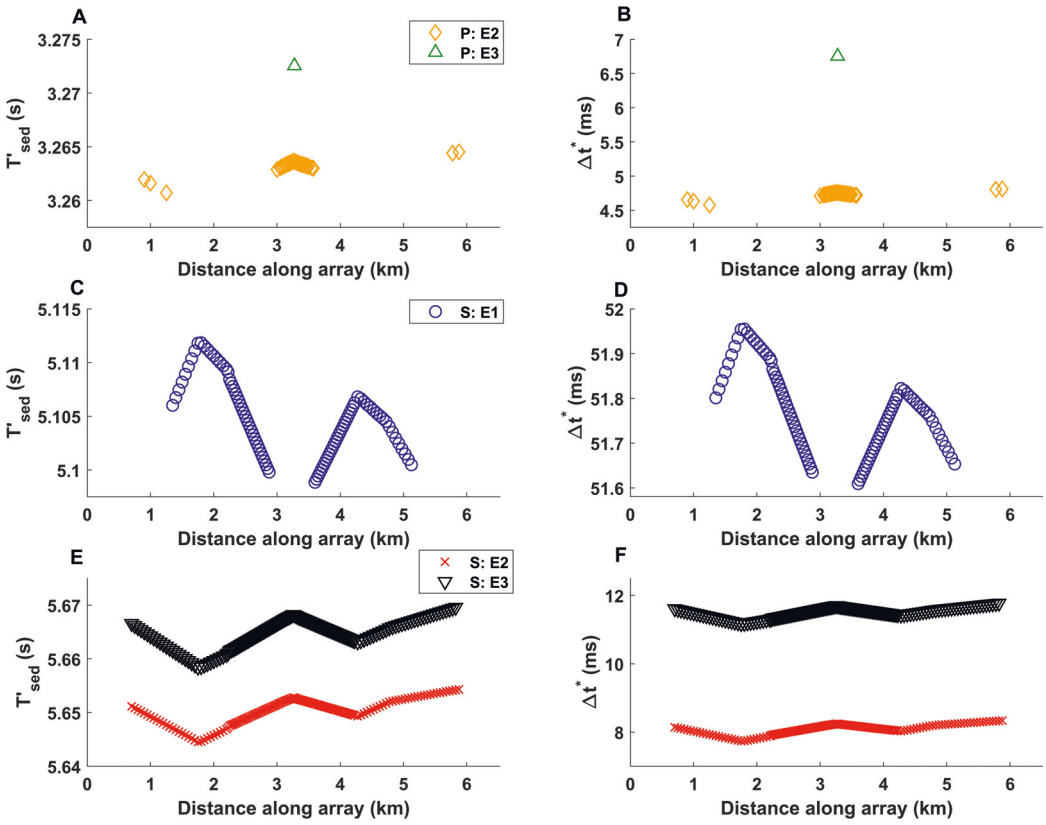

Figure 4.8: Traveltimes and Δt^* values based on the ray tracing from the earthquakes to OSE used in the Q estimation. (A) The traveltimes for P-waves through the sediment layer for E2 and E3. (B) Differences in t^* for the P-wave through the layered bedrock model for E1. (C, E) The traveltime for the S-wave through the sediment layers for (C) E1 and (E) E2 and E3. (D, F) Differences in t^* the S-wave through the layered bedrock model for (D) E1 and (F) E2 and E3.

from 7 km to 5 km gives an average quality factor decrease of 18 for the events studied. The results presented in Figure 4.7C are found using a sediment layer thickness of 7 km.

A 1D velocity model for the oceanic crust is used to estimate the traveltime values. As mentioned in the "Traveltime computation" subsection, it is created by combining a well near Oseberg (30/6-1) with a regional velocity model. The model provides reliable traveltime values for the raypaths close to the Oseberg PRM system, as the rays are propagating through geology captured by the sonic log used to create the velocity model. However, it will not provide the same accuracy for the raypaths to BER as the station is located on the continental crust. The rays to BER travel either through continental crust only (E2 and E3) or through a combination of oceanic and continental crust (E1). This introduces uncertainties to traveltimes, especially for rays propagating in the continental crust. Nevertheless, using a 1D model provides sufficient accuracy to the traveltimes to show the

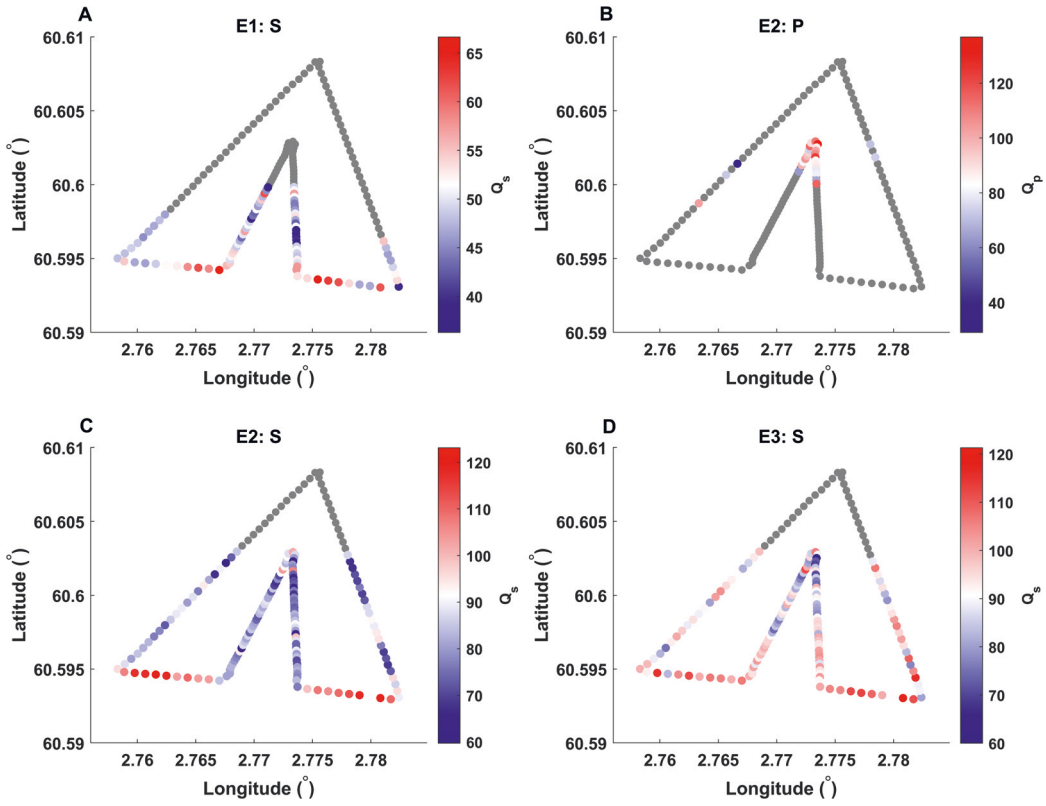

Figure 4.9: Spatial distribution of the Q_{sed} values along the array. Estimates for S-waves are given in (A) for E1, (C) for E2, and (D) for E3, whereas the estimates for P-waves are given in (B). Gray dots indicate receivers with SNR below 7.5 dB or the a priori omitted receivers.

reliability of this method. Further investigation into the effect of ray tracing using a 3D velocity model is outside the scope of this paper. This velocity model should capture all, or some, of the heterogeneity in the area including the effects of the Oseberg mega block and the differences in seismic velocities between oceanic and continental crust.

It is assumed that the source signature is canceled in the spectral division in equation (4.7). However, earthquakes are not isotropic sources. The effect of the source will be canceled when the stations are in the same azimuth direction from the earthquake. For the event in this study, the azimuth differences are 33°, 93° and 78° for E1, E2, and E3, respectively, which means that the source signature will not be the same and not entirely canceled out in the spectral ratios.

Notches due to free-surface multiples are observed in the hydrophone and geophone data. For the geophone data, four notches are observed at 3.5, 10.4, 17.4, and 24.4 Hz within the earthquake signal bandwidth, whereas the notches in the hydrophone recordings are

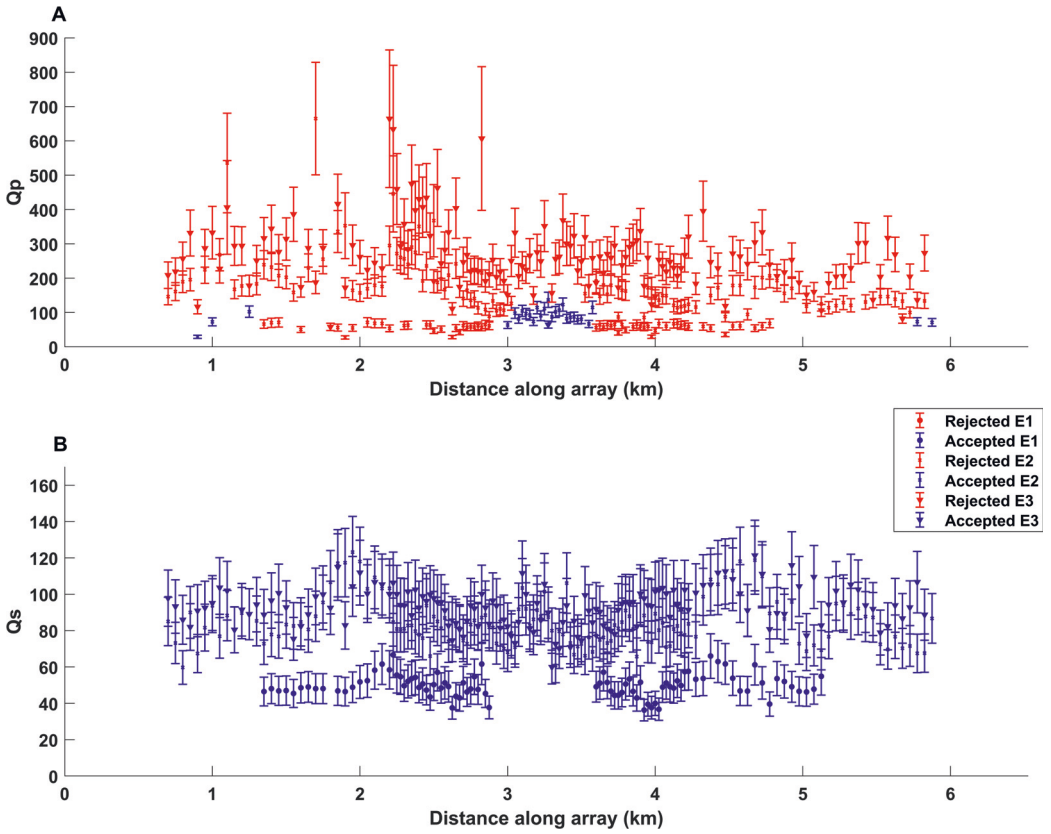

Figure 4.10: Raw Q estimation. The accepted (the blue) and rejected (the red) Q_p (A) and Q_s (B) estimates. Note that the Q_p values for E1 are rejected due to high noise contamination for all channels (see Figure 4.5), whereas Q_p values for E2 and E3 are rejected based on a combination of high noise levels and high errors in the regression analysis.

found at 0, 7.0, 13.9, and 20.9 Hz. Note that the notch at 0 Hz is a combination of the first free-surface multiple-related notch and that the hydrophone instrument response is close to 0 Hz at this frequency. These notches agree with the modeled first-order free-surface multiple notches for a 107 m water depth (see Appendix 4.C). However, compensating for their effect does not affect the estimated attenuation values and has not been included in the workflow but should be considered when estimating the sediment quality factor from similar OBN data.

4.4.3 Results E1

The epicenter of the earthquake recorded on 16 January 2014 was found to be 142 and 239 km southeast of the Oseberg PRM system and the BER seismometer, respectively (Figure 4.10). This M_L 2.11 earthquake was the lowest magnitude event used in this study, also reflected in the computed RMS and SNR values (Figure 4.5). From the SNR

and the clarity of first-break P- and S-phase arrivals, the ranges of the a priori omitted channels were increased to 1–27, 73–100, and 144–172. Furthermore, due to the event's low magnitude and remote location, Norwegian National Seismic Network (NNSN) and Norwegian Seismic Array (NORSAR) did not obtain a reliable depth estimation. A depth of 11 km, similar to the other events, was assumed for the earthquake. From the error ellipse presented in the NORSAR seismic bulletin (NORSAR 1971), the location of the earthquake was observed to contain significant uncertainty (Figure 4.10). Because the sediment attenuation estimates rely on modeled traveltimes from the event to the receivers, accurate hypocenter information was important, and uncertainty in the location induces uncertainty in the Q_{sed} estimation. Moreover, the travel paths from E1 to OSE and BER were primarily through the oceanic crust, with varying distances. From the ray tracing, the average traveltime differences were found to be $\simeq$34.7 s for the S-wave arrivals. Another effect of the long travel distance was that the seismic waves dive deeper into the subsurface and encounter the sediment package at higher angles (relative to the horizontal axis), decreasing the traveltimes in the sedimentary sequence. Using the traveltimes, slopes, and assumed values, 89 Q_{sed} values adhered to the first SNR condition and were estimated with a mean and one standard deviation of 50 ± 6, where the standard deviation represents the spread in the estimated values. The low estimated quality factor and low variability over the different estimates were due to the big traveltime difference systematically decreasing the final estimates; this will be discussed in more detail in the "Comparison" section. Moreover, the average total uncertainty related to the estimates was found to be 8.7 over the estimated values using equation (4.17). The individual Q_{sed} estimates, with related uncertainty, are shown in Figure 4.7C.

4.4.4 Results E2 and E3

The second (M_L 2.35) and third (M_L 2.57) earthquakes recorded on 22 January 2014 and 23 January 2014 have epicenters of $\simeq$88 and $\simeq$107 km northeast of OSE, respectively, and $\simeq$107 and $\simeq$119 km northwest of BER. These events also have uncertainties related to their hypocenter estimates inducing uncertainty in the computed traveltimes (Figure 4.1). Moreover, the seismic waves generated by the earthquakes travel through different geology to OSE and BER. The propagation to OSE is mainly through the oceanic crust, whereas it propagates through the continental crust to BER. The traveltimes to the receivers are similar, with an average P-wave traveltime difference of $\simeq$0.8 s for both E2 and E3. The average S-wave traveltime difference is $\simeq$1.45 s. Furthermore, due to the shorter travel distance (compared with E1), the rays will not dive as deep into the subsurface, hence encountering the sediment package at a lower angle, increasing the traveltimes in the sediment package (Table 4.2).

Figure 4.7C displays the 26 P-wave attenuation values and 145 S-wave attenuation values estimated for E2, with values ranging from 64 to 137 and from 60 to 123, respectively. In the same plot, the single estimated P-wave value and the 144 S-wave attenuation values for E3 are shown. The Q_p value for E3 is 65, while the Q_s values range from 60 to 121,

Table 4.3: Q_{sed} estimation results are given as the mean, with one standard deviation (Q_p for E3 has one value), of all stations adhering to the first SNR condition. The Q_s/Q_p values are taken for central channels with estimations for both wave types. N denotes the number of data points for the different estimates.

Name	N_p	Q_p	N_s	Q_s	$N_{Qs/Qp}$	Q_s/Q_p
E1	0	-	89	50 ± 6	0	-
E2	26	92 ± 18	145	84 ± 13	22	0.9 ± 0.2
E3	1	65	144	93 ± 13	1	1.4

resulting in an average Q_s estimation with one standard deviation of 93 ± 13 over the estimated values. The related mean uncertainties for Q_p and Q_s are, respectively, 10.3 and 14.7, as computed from equation (4.17). Furthermore, the Q_p and Q_s average estimates for E2 are 92 ± 19 and 85 ± 13, with average uncertainties of 14.2 and 13.3. It is also possible to compute the Q_s/Q_p value for E2 by taking the ratio between values obtained from corresponding channels. Using the central channels at distances 3.0-3.58 km (channels 77-100, excluding channels 78 and 98 due to low SNR), a ratio of 0.9 ± 0.2 is found. Similarly, the ratio between the single Q_p value for E3 and the corresponding Q_s is 1.4. However, we will not put any emphasis on this value due to it being obtained by only one data point. The ratio found for E2 is considered more reliable due to it being estimated from 22 data points. Table 4.3 summarises the estimated values.

4.4.5 Comparison

There are obvious differences between the travel path from E1 and E2-E3. (1) The travel distances from E1 to the receivers are longer than for E2 and E3. (2) The traveltime differences are larger for E1. (3) The seismic waves propagate through different media. The travel distances only change the depths the rays reach, and hence the traveltime in the sediment layer (T'_{sed}). From the ray tracing, the estimated S-wave traveltimes in the sedimentary sequence decrease $\simeq$11.8% from E1 to E2 and E3. Moreover, when a large traveltime difference is present in the Δt^* term of equation (4.11), it will influence the Q_{sed} estimates. For E1, this term is the same as the average slope term value ($-a/\pi$), with the same sign, which creates a systematic decrease in the attenuation estimation of the sediment package (see Table 4.2). Comparing E1 with E2 and E3, these terms are only $\simeq$14% and $\simeq$23% of the obtained average slope term values, respectively. Hence, the hypocenter position relative to the receiver pair will affect the end estimates of the attenuation value. If the traveltime difference term is neglected, and only the average slope values are considered, the estimates would be similar for the three events. From the slope values listed in Table 4.2 and depicted in Figure 4.7A the Q_{sed} values of E1 would be estimated around the E2 and E3 values. Therefore, a too large traveltime difference might introduce a systematic error in the method, whereas more reliable values are obtained when the difference is low. However, this depends on the accuracy of the assumed bedrock

Q model. The dependence on the bedrock Q model can be avoided by choosing the receiver pair and the earthquake carefully. The emerging distributed acoustic sensing technology will increase the station coverage on land and in the ocean worldwide (Lindsey et al. 2017, Williams et al. 2019), and choosing a station pair that optimizes the estimation procedure will be easier.

From Figure 4.9 the Q_{sed} values are plotted for the array layout. The values for Q_s for all events show a frequency-dependent array response, especially clear for E2, where the segment oriented in the north–south direction shows an all-over lower Q_s value than the east-west-oriented segments. Moreover, looking only at the quality factor values for the north–south-oriented segment, the standard deviation of the Q_s estimates over the array decreases to 5.4 (E1), 8.8 (E2), and 9.7 (E3), a decrease of, respectively, 0.9, 4.1, and 0.9. The Fresnel zones of the events are, on average, 6.2 km (E1), 5.3 km (E2), and 5.6 km (E3), which is considerably larger than the maximum array aperture of 1.75 km. From these Fresnel zones, there should not be large variations along the array. The exact nature of the response along the array is not known and is beyond the scope of the work in this paper. However, the fact that amplitudes along various branches of the array are aligned indicates a frequency-dependent array effect caused by the cable orientation. Another possible explanation for the variation can be near-surface effects. These effects can affect the observed amplitudes on the array. Malme et al. (2005) investigate effects of overburden diffractors and shallow lenses and find that they lead to considerable local amplitude variation. The diffraction leads to rapid oscillation in the amplitude level observed, whereas the lenses distort reflection events. Near-surface effects such as these have not been studied in the current work.

From the robust regression algorithm used, the 95% confidence interval (Figure 4.7A) and the SRE (Figure 4.7B) are estimated for the three earthquakes. The latter show similar values over all earthquakes, where the lowest average SRE is related to E1 (0.023 s), the highest is related to E2 (0.030 s), and E3 is between the two (0.027 s). The lower SRE value for E1 is related to the lower portion of the frequency spectra used in the regression analysis, which behavior is better represented by a linear regression line (see, e.g., supplemental Figures D.2, D.3 for E1, Figure D.4 for E2 and Figures D.5, D.6, D.7 for E3). Furthermore, using equation (4.17) the uncertainty as a function of the different variables in equation (4.11) is found. Figures 4.11 and 4.12 show the total uncertainty in Q_p and Q_s, respectively, for E2, as a function of the different variables (see supplemental Figure D.9 for equivalent plots for E1 and supplemental Figures D.10, D.11 for E3). By varying the slope a, a strong dependence is observed, where an increase in the slope value is related to a higher uncertainty, whereas a decrease is related to a lower uncertainty. By increasing T'_{sed}, the uncertainty will also increase. Conversely, the uncertainty related to Δt^* will decrease when its value increases. Furthermore, a decrease in the velocity model is related to a higher uncertainty than an increase in the velocity model.

The estimated Q_p and Q_s values found in this work agree with previously published

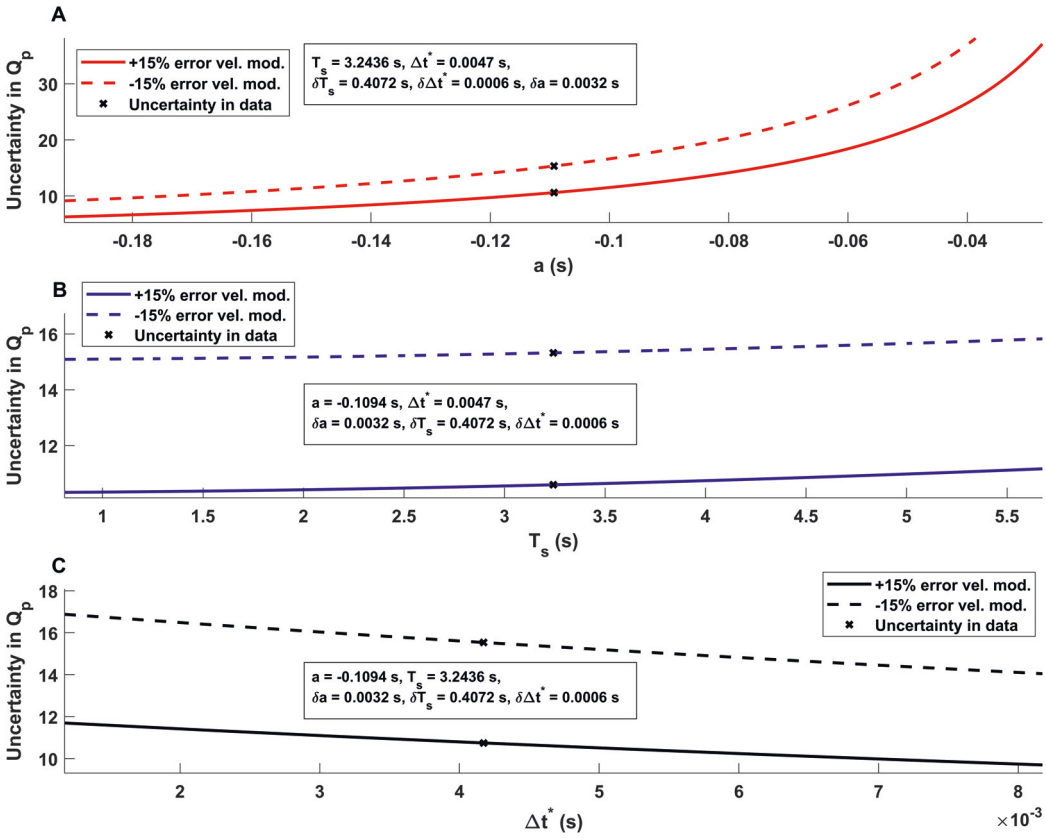

Figure 4.11: The total uncertainty in the estimated average quality factor obtained from P-waves, E2. (A) Uncertainty as a function of slope values. (B) Uncertainty as a function of travel-times through the sedimentary sequence. (C) Uncertainty as a function of Δt^* values (see equation (4.12)). For each plot, the range is taken as $\pm 75\%$ of the average values obtained from the analysis (the black crosses). The dashed lines are associated with an -15% error in the velocity model, whereas the solid line an $+15\%$ error.

values for sedimentary successions, including values estimated from North Sea deposits. Sheriff and Geldart (1995) mapped general Q_p values for different rock types and find the value to range from 20 to 200 for sediments. Others have found attenuation values in sediments between 20 and 200 for the North Sea (Kang and McMechan 1994, Dasgupta and Clark 1998, Reid et al. 2001, Allmark et al. 2018, Carter et al. 2020), providing the widest range of credible values. From the three earthquakes recorded in January 2014, values ranging from 64 to 137 for P-waves and 29 to 123 for S-waves have been found, with an average total uncertainty of 14.0 and 12.7, respectively. E2 and E3 show similar values, which are expected for seismic waves propagating through similar geology.

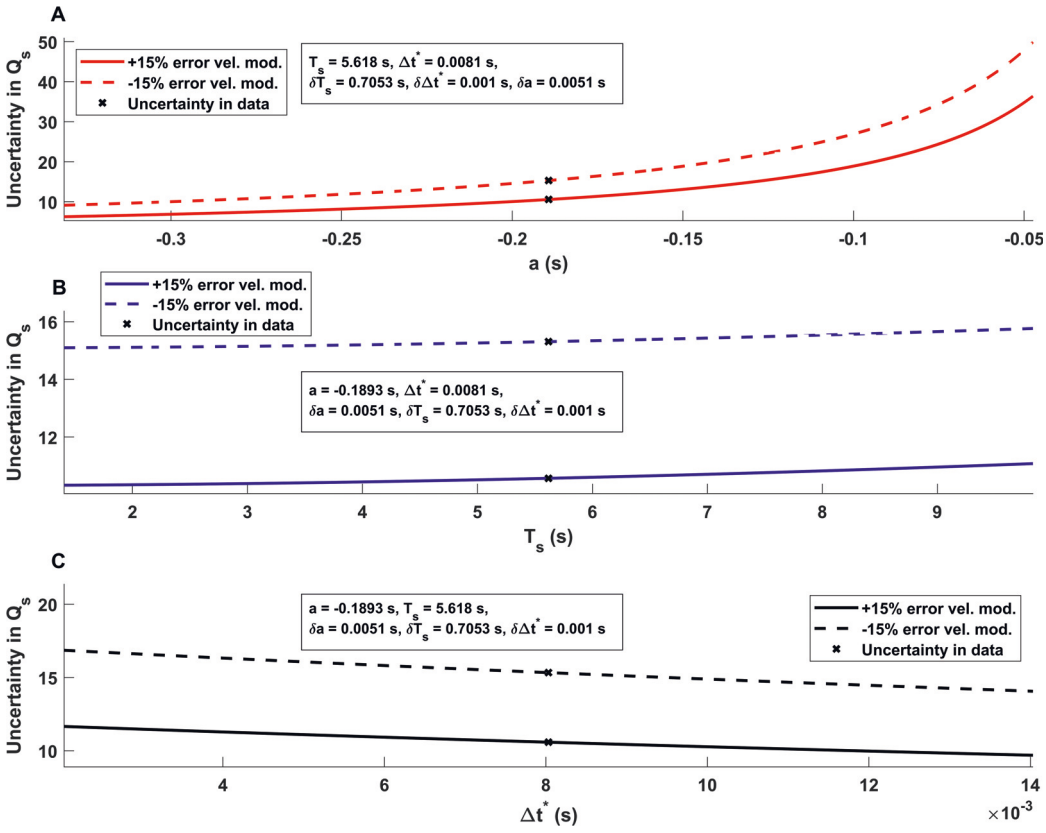

Figure 4.12: The total uncertainty in the estimated average quality factor obtained from P-waves, E2. (A) Uncertainty as a function of slope values. (B) Uncertainty as a function of traveltimes through the sedimentary sequence. (C) Uncertainty as a function of Δt^* values (see equation (4.12)). For each plot, the range is taken as $\pm 75\%$ of the average values obtained from the analysis (the black crosses). The dashed lines are associated with an -15% error in the velocity model, whereas the solid line an $+15\%$ error.

4.5 Conclusion

We developed a new method that estimates average quality factors for a given sedimentary package for recorded P- and S-waves, Q_p and Q_s, using the spectral ratio for a station pair, one located on sediment and one located on bedrock. Exploiting three earthquakes (E1, E2, and E3) recorded on 172 seabed receivers in the Oseberg PRM system and a seismometer in Bergen, a total of 27 Q_p and 378 Q_s values were estimated for the sediment package under the PRM system at Oseberg. The mean estimated Q_p values are 92 ± 18, where the confidence interval represents the spread in the estimated values. Furthermore, similar Q_s values were found for E2 and E3, respectively, 84 ± 13 and 93 ± 13. Moreover, the average uncertainty for the Q_p and Q_s estimates over the array was found to be 14.0

for both. Estimated Q_p and Q_s values from E2 give a Q_s/Q_p of 0.9 ± 0.2, while E3 estimates gives a Q_s/Q_p of 1.4. The estimated P-attenuation value for E2 was the most reliable value because of more estimated values for E2 (22) than E3 (1). The ratio suggested a bigger attenuation for S-waves than P-waves in this sedimentary layer

Acknowledgments

We thank the Oseberg partners, Equinor Energy AS, Petoro AS, TotalEnergies EP Norge AS, and ConocoPhillips Skandinavia AS, for making the Oseberg PRM data for January 2014 available. We thank the Norwegian Research Council and the industry partners of the GAMES consortium at NTNU for the financial support (grant no. 294404) and the Centre for Geophysical Forecasting at NTNU (grant no. 309960). The Digimon ACT project (grant no. 299622) also is acknowledged. We also would like to thank the University of Bergen formaking their earthquake data and arrival times available and NORSAR for access to their earthquake bulletin. The authors also would like to thank Shearwater GeoServices Software for the Reveal software used in our analysis. Finally, we thank the reviewers for the many good and helpful comments that improved the work.

Data and materials Availability

Data associated with this research are confidential and cannot be released.

Appendix

4.A Signal-to-Noise Ratio

The SNR for the P- and S-wave signals was computed by

$$\text{SNR} = 20 \cdot \log_{10} \left(\frac{u_{\text{signal}}}{u_{\text{noise}}} \right), \tag{4.18}$$

where u_{signal} denotes the RMS of the P- or S-wave signals, and u_{noise} denotes the RMS of a part of the signal assumed to only contain noise. The RMS was given by

$$u_{\text{RMS}} = \sqrt{\frac{1}{N} \sum_{i=1}^{N} u_i^2}. \tag{4.19}$$

The second SNR condition, for each frequency component, was computed by

$$U_k = 20 \cdot \log_{10} \left(\frac{|U_{k,\text{signal}}|}{|U_{k,\text{noise}}|} \right), \tag{4.20}$$

where U_k denotes component k of the frequency-domain representation of the signal ($u \leftrightarrow U$).

4.B Observed signals and arrival time picks

To compute the spectral division, we need the arrival times for P- and S-waves. This has been done visually by one observer, looking for a sudden amplitude and frequency change in the data corresponding to the onset of the P- and S-waves. There are many automatic picking algorithms that can be used to extract this information from the signal and decrease the observer's subjective bias at the cost of other potential limitations in the applied algorithms. For example, the phase detector algorithm has been developed by

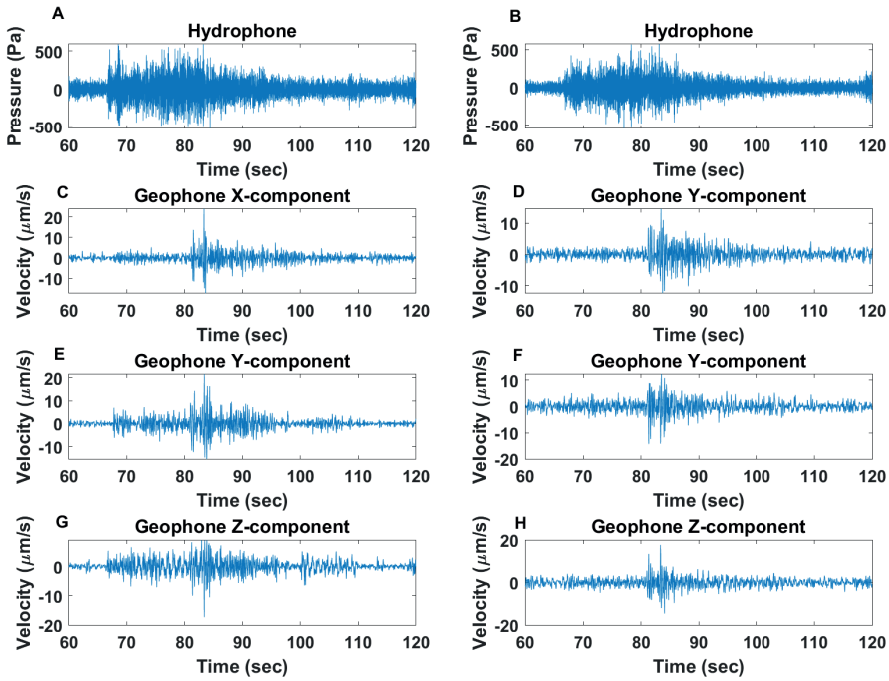

Figure 4.B.1: Example of high and low SNR waveforms at Oseberg. (A, B) Hydrophone component with a clear P-wave onset. (C, D) Geophone (east–west) component, clear S arrival. (E, F) Geophone (north–south) component, clear S arrival. (G, H) Geophone vertical component is clear P arrival in (G) and unclear in (H). (A, C, E, G) The recordings on node 90 and (B, D, F, H) node 60.

Earle and Shearer (1994), the phase picker by Baer and Kradolfer (1987), the artificial neural network approach for P- and S-phase by Gentili and Michelini (2006), or the automatic P-phase picker by Kalkan (2016). The P-wave arrivals have been picked using the vertical geophone and the hydrophone component. The vertical geophone component is, in general, noisier than the hydrophone component (see Figure 4.B.1), and a visual comparison between the two gives a more certain pick of the first break. On the other hand, the S-wave arrivals have a relatively high SNR for all earthquakes for the geophone data, hardly visible in the hydrophone data, and a total of 378 S-wave arrivals have been picked using the horizontal components, using the (east–west) component mainly.

4.C Free-surface multiple related notches in the data

In the Oseberg PRM data, we observe notches due to free-surface multiples (see Figure 4.C.1). The water depth at Oseberg has been measured to be $d \simeq 107$ m and the sound

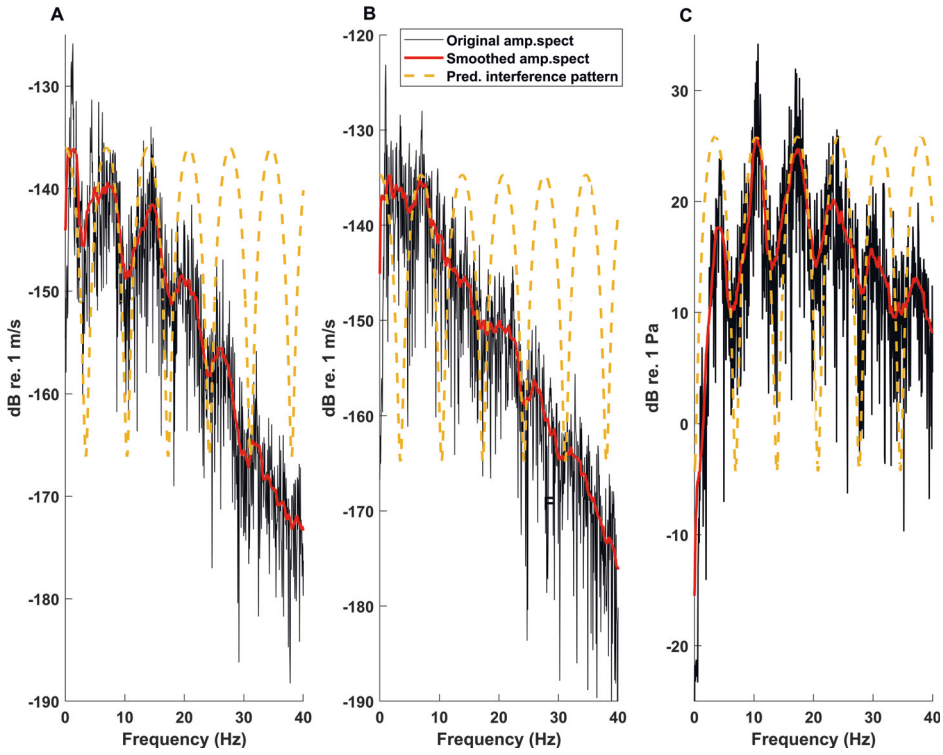

Figure 4.C.1: Notches observed on node 30 in the PRM system compared with the predicted interference pattern for a water depth of $\simeq$107 m. (A) The predicted interference pattern (the dashed yellow line) matches the observed P-wave train amplitude spectrum recorded by the geophone at Oseberg. The black line shows the original amplitude spectrum, whereas the red shows the smoothed version. (B) How the predicted interference partly fits the observed S-wave train amplitude spectrum, not as well as for the P-wave. Most likely because the S-wave does not propagate in liquids, and an S–P conversion is needed to create the notches. (C) The predicted interference pattern for the hydrophone correlates well with the observed amplitude spectrum.

speed in water (v_p) is assumed to be 1480 m/s. We can model the first-order free-surface notches in the received signal for the hydrophone ($G_H(\omega)$) and the geophone ($G_G(\omega)$) component:

$$|G_H(\omega)| = \left|1 - c_0 \exp\left(i\omega \frac{2d\cos(\theta)}{v_p}\right)\right|, \tag{4.21}$$

$$|G_G(\omega)| = \left|1 + c_0 \exp\left(i\omega \frac{2d\cos(\theta)}{v_p}\right)\right|. \tag{4.22}$$

c_0 is the reflection coefficients of the sea-surface and θ is the offset angle the ray enters the sea column with, measured from the vertical.

We can define the observed amplitude spectrum at OSE $|P(\omega)|$ as

$$|P(\omega)|^2 = |S(\omega)|^2 |H(\omega)|^2, \tag{4.23}$$

where $|S(\omega)|$ is the received amplitude spectrum unaffected by multiples; $|H(\omega)|^2 = |G(\omega)G(\omega)^*|$ is the predicted ghost power spectrum; and $*$ denotes the complex conjugate. To remove the ghosts in the Oseberg PRM data, we rearrange equation (4.23) to a spectral division and add a constant factor (υ) to avoid division by zero:

$$|S(\omega)| = \sqrt{\frac{|P(\omega)|^2}{|H(\omega)|^2 + \upsilon}}. \tag{4.24}$$

Figure 4.C.1 shows the predicted interference pattern plotted together with the original amplitude spectrum (the black) for the geophone (Figures 4.C.1A, B), the hydrophone recording (Figure 4.C.1C), and the smoothed (30 sample moving average) version (the red). A clear correlation between the notches from the data and the predicted interference pattern using the water depth at Oseberg is observed.

Chapter 5

Concluding remarks

5.1 Summary

In this work, several datasets have been acquired and analyzed to study how dense receiver arrays can extract new information about underwater and subsurface processes using acoustic and seismic sources. A wide range of applications have been studied and is summarized in the following paragraphs.

In Chapter 2, it is described how two distributed acoustic sensing (DAS) arrays in Svalbard were used to localize and track several whales simultaneously over a 60 km range of fiber-optic cable, as depicted in Figure 2.5. Geo-references of air gun shots were also acquired and used to quantify the errors associated with the localization methods used in the tracking, shown in Figure 2.2. Average errors of $\simeq$100 m were found for both methods, demonstrating the capabilities of establishing a near-real-time whale tracking system. Such a system could be applied anywhere in the world with whales and fiber-optic cables. For example, the fiber-optic tracking system could be coupled with ship detection and/or fused with data from other sources, such as automatic identification system (AIS), to create a ship-strike avoidance system.

In Chapter 3, we describe how a dedicated DAS array was trenched $\simeq$40 cm into a known quick clay area in Rissa, Norway, to monitor the subsurface parameters of the clay (the shear stiffness in particular) as a new road was built. Rayleigh waves produced by active sledgehammer shots and the ambient background noise were recorded on the DAS array and used to estimate the shear-wave velocity depth profiles. Shear-wave velocity (β) is used as it is related to the shear stiffness (μ) through $\beta = (\mu/\rho)^{1/2}$, where ρ is the density of the material. The surface wave data were acquired before, during, and after the road construction period to monitor the subsurface parameters. We extracted the dispersion curves inherent in the Rayleigh waves and used them as input to two different inversion algorithms (one linearized and one non-linear inversion). This allowed us to estimate the

shear-wave velocity depth profiles for a selection of dates during the acquisition period (see Table 3.2). The obtained dispersion curves and shear-wave velocity profiles for both the active and passive data did not change significantly during the acquisition period, as can be seen in Figures 3.10 and 3.11. This suggests that the quick clay properties remained stable during the construction period. Nevertheless, the results provide reference velocity trends in undistributed conditions and valuable information for future comparison to potential failure scenarios. Furthermore, the work illustrates the feasibility of using active and passive data recorded using DAS arrays in an early-warning system for quick clay avalanches. However, more work is needed to increase the system's sensitivity to depth and to detect smaller-scale velocity changes.

In Chapter 4, it is described how the Permanent Reservoir Monitoring (PRM) system at Oseberg was used with a broadband seismometer in Bergen to estimate average quality factors for the sedimentary package under the PRM system. A new spectral ratio method was developed using one station on sediment (in this case, stations part of the PRM system) and one on bedrock (the broadband seismometer). Exploiting three earthquakes (E1, E2, and E3) recorded on the receivers, a total of 27 Q_p and 378 Q_s values were estimated. The mean standard deviation Q_p estimates were 92 ± 18 for E2, with the Q_s values for E2 and E3 found to be 84 ± 13 and 93 ± 13. Moreover, plotting the obtained S-wave quality factor values along the array layout (Figure 4.9), we found the values for all events to have a frequency-dependent array response. The North-South-oriented segments showed an all over lower Q_s value than the East-West-oriented segments, especially clear for E2. Using the obtained quality factor values, we could estimate the Q_s/Q_p for E2 to be 0.9 ± 0.2, suggesting more attenuation for the S-waves than the P-waves in the sedimentary layer.

In Appendix A, we used data recorded on one of two fiber-optic cables connecting Svalbard and Ny-Ålesund during the field campaign of 2020 to analyze a local earthquake. We used various preprocessing techniques and a simple 2D beamforming procedure to increase the signal-to-noise ratio of the received earthquake signal. Additionally, the beamforming estimated the apparent velocity and angle of incidence of both P- and S-wave signals. The enhanced SNR was used to pick out P- and S-wave arrival times to estimate the earthquake epicenter location. We estimated an epicenter location in agreement with the conventional sensor networks in Norway, where the locations were within 17 km of each other.

5.2 Other work performed during this Ph.D.

This section summarizes other scientific work performed during the four-year Ph.D. period. The work is either published with the undersigned as co-author (subsections 5.2.1-5.2.4) or un-published work carried out over several months (subsection 5.2.5).

5.2.1 Sensing whales, storms, ships, and earthquakes using an Arctic fiber-optic cable

A journal paper by Landrø et al. (2022) published in Nature Scientific reports. The abstract of the paper is given in Appendix D.1, and a summary is given in the following.

This work shows how the first 120 km of the inner fiber-optical telecommunication cable connecting Longyearbyen and Ny-Ålesund (see Figure 2.1) can be used to observe and analyze signals from baleen whales, storms, ships, and earthquakes.

A range of whales were detected to 95 km along the cable during the 44 day recording period. The analysis identified different call types from at least two low-frequency baleen whale species: North Atlantic Blue whales and fin whales. Different calls were observed through the sample period, e.g., down-sweep calls from various whales and Blue whale stereotyped calls.

We could detect ocean surface gravity waves from distant storms by investigating the low-frequency portion of the data (0.04 to 0.1 Hz) over several days. These events were observed as near-linear narrow-band events in the time-frequency representation (spectrogram) of the data. Using their gradient, we could estimate the storms' rough origin position and time. One event was confirmed to be the Tropical Storm Edouard, roughly 4100 km from Longyearbyen, while the storm detected furthest from Svalbard was 13000 km away. A total of 12 events were detected, each lasting for 50 to 100 hours.

A number of ships crossed the cable during the acquisition period, where the crossing of the general cargo ship, Nordbjørn, was analyzed. Nordbjørn was successfully detected and tracked using the DAS data corresponding well with the reported AIS track ($\pm$50 m). Additionally, the Doppler shift as the vessel crosses the fiber was detected, from which its speed could be estimated to be 11.7 kn, in close agreement with the AIS data.

We analyzed seismic signals from a local and a teleseismic event. By investigating the local earthquake, we could estimate the epicenter location using only DAS data, in close agreement with reported values by earthquake catalogs in Norway (NNSN and NORSAR). We also observe the effect of deeper-diving waves passing through regions of higher velocity and the interaction with local bathymetry (the analysis of the local earthquake is also detailed in Appendix A).

5.2.2 Eavesdropping at the speed of light: Distributed acoustic sensing of baleen whales in the Arctic.

A journal paper by Bouffaut et al. (2022) published in Frontiers in Marine Science. The abstract of the paper is given in Appendix F, and a summary is given in the following.

This work builds on the whale analysis presented in subsection 5.2.1, where data from the same fiber-optic cable was used. We present the first case of wildlife monitoring em-

ploying DAS using the detected vocalization of baleen whales. These vocalizations are further used to find the 3D position of a vocalizing whale and exploited as a fully-passive method for seismic exploration. Beamforming was used with the localization method to get a track from a 10 min recording of a blue whale. In addition to estimating the track of the whale, the apparent swim speed was successfully estimated to be 5.4 km/h. The second part of the paper investigates the combined use of a non-stereotyped whale down-sweep vocalization and DAS to provide interpretable seismic profiles. The seismic profiles are found by first estimating the whale down-sweep signal and subsequently cross-correlating it with the received signal along the DAS array. Using this method for two different positions along the array, various arrivals are emphasized: direct waves, subsurface reflections, and strong water-layer multiple reflections. The subsurface reflections varied for the two studied locations due to the differences in the first sedimentary layer thicknesses.

5.2.3 Distributed acoustic sensing of ocean-bottom seismo-acoustics and distant storms: A case study from Svalbard, Norway.

A journal paper by Taweesintananon et al. (2023) published in Geophysics. The abstract of the paper is given in Appendix G, and a summary is given in the following.

This work also builds on subsection 5.2.1, emphasizing the infrasound acoustic signals. As mentioned, we can use DAS data to successfully trace ocean surface waves produced by distant storms back to the origin as far as 13000 km away from the cable. In addition, we find signals in the frequency range 0.5 to 4 Hz directly from the frequency-distance ($f - x$) representation of the data, corresponding to shear-wave modes (resonance) in the seafloor sediments directly below the DAS array. Using established equations by Godin and Chapman (1999), we can use the observed first S-wave resonance frequency to estimate the thickness of the sedimentary layer, which can then be used to determine the subsurface structures of this sedimentary layer. Other signals generated by dynamics in the atmosphere, ocean, and solid earth are also observed. These include ocean-bottom loading pressure fluctuation of ocean surface waves generated by storms, winds, and airflow turbulence, acoustic resonances in the water column, and propagating seismic waves.

5.2.4 Developing experimental skills: A hands-on course in acoustical measurement techniques at the Norwegian University of Science and Technology.

A journal paper by Dong et al. (2022) published in The Journal of the Acoustical Society of America (JASA). The abstract of the paper is given in Appendix H, and a summary is given in the following.

This paper was written for a special issue of JASA focusing on education in Acoustics. The paper describes the hands-on course "Acoustic Measurement Techniques - TTT4250" offered by the Acoustic Group at the Department of Electronic Systems, Norwegian Uni-

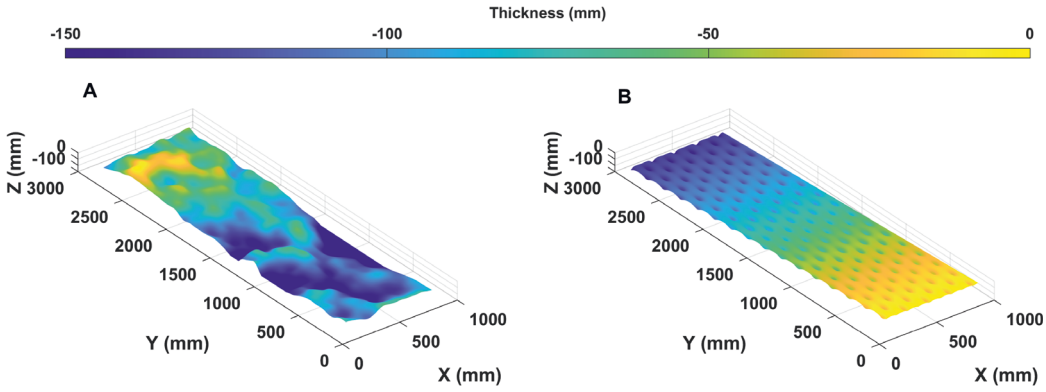

Figure 5.1: Geological models. (A) Utsira formation, (B) fin-scale elliptical model of caprock surface (Gasda et al. 2012).

versity of Science and Technology. The paper outlines the topics covered and the involvement of the academic staff as well as invited industry and research guest speakers as teachers. This paper also outlines aspects essential to carrying out five different acoustical measurement labs. These aspects include introducing the problems to be addressed in the assignment, the relevant ISO standards, the needed programming knowledge, as well as needed measurement uncertainty and statistical analysis of the recorded data. The labs include measurement of sound power, sound insulation, acoustic impedance, underwater acoustics, and human hearing.

5.2.5 Test tank for CO_2 monitoring studies

In this work a controlled tank experiment for CO_2 monitoring studies was installed and initial tests of the system were executed. First, the lab setup will be describe before the initial tests.

Experimental set-up

The setup consists of three main elements. The fundamental element is the Verasonics multichannel recording instrument containing the software used to: (1) Generate the ultrasound signal emitted into the experimental setup to be studied and (2) analyze the received signals. The second element of the system is transducers, which convert the signals defined in the Verasonics software into a physical acoustic excitation and later record the returning signal. Two transducer types with different central frequencies are used, one with 150 kHz center frequency (BII-7730; Benthowave-Instrument-INC. (2023b)) and another with 1 MHz (BII-7696; Benthowave-Instrument-INC. (2023a)). A total of 300 transducers are available, but only 50 of each type have been installed on a grid and tested so far. The final element of the setup is the water tank that will hold the geological models to be investigated. The tank is 2 m wide, 4 m long, and 1.2 m deep.

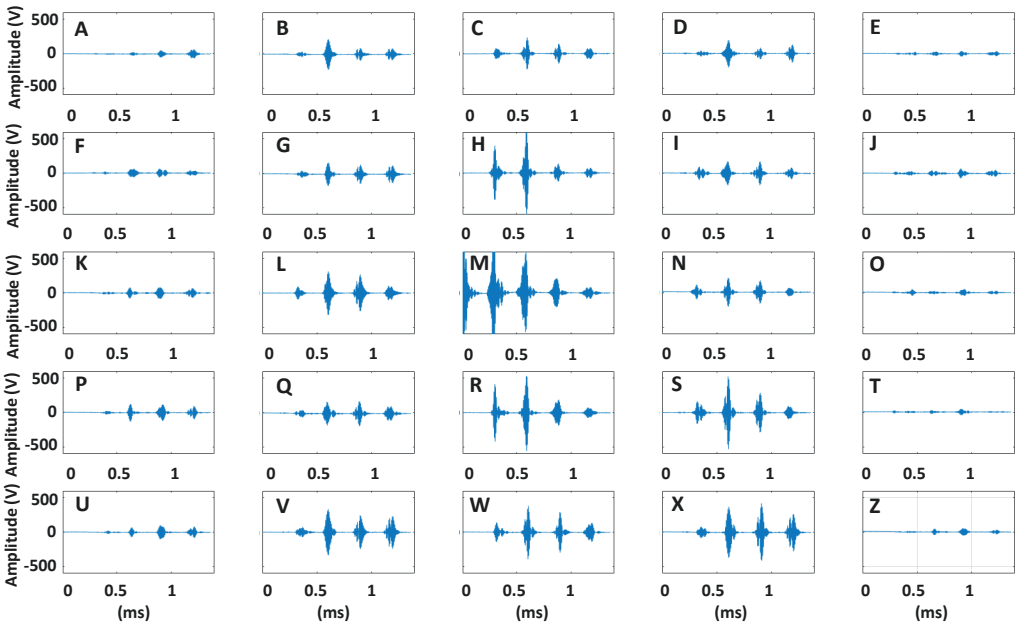

Figure 5.2: A grid of 25, 150 kHz, transducers recording the 150 kHz signal emitted by the central transducer in (M). No air was injected to the water column in this test.

The basic idea of the setup is to deploy geological models relevant for CO_2-storage and test them as CO_2 (or other gases) are injected below the geological models. The models are scaled by a factor of one to two thousand to fit them into the test setup. So far, two different models have been created, one based on the Utsira formation in the Sleipner field, the North Sea (see Figure 5.1A). The second model is a fine-scale elliptical model of caprock surfaces as presented by Gasda et al. (2012) (see Figure 5.1B).

The geological 3D models are made using PMMA-acryl material and will act as the cap rock of the reservoir. The models are divided into three 1×1 m pieces that create a 1×3 m model when fitted together. The thickness of each model varies from 10 to 20 cm. During deployment, the geological models are placed together and on top of a water-filled sand layer. Then, the transducer grid is placed on top of the flat top of the geological model (the $Z = 0$ mm plane in Figure 5.1) to simulate the acoustic monitoring system. This will, among other objectives, be used to test different acquisition geometries on the different geological models. Finally, at the bottom of the tank, three nozzles (or inlets) directly inject gas into the water-saturated sand.

Initial tests

Before working on the complex setups described above, we did initial tests in the tank only filled with water, air injected by one muzzle, and the receiver grid. This is done to better

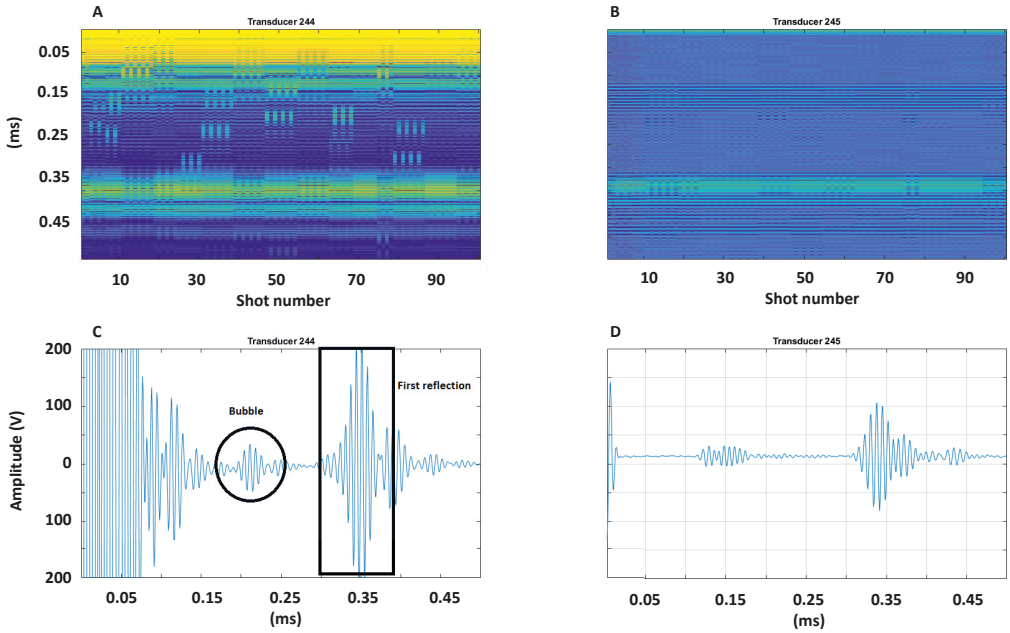

Figure 5.3: Recorded signal with bubbles emitted at a regular interval. (A) Source transducer. Bubbles migrating from the nuzzle can be observed as oblique events. (B) Neighboring transducer roughly 10 cm away. (C) Waveform of one signal. The signals before 0.15 ms is the emitted signal, the signal in the middle is diffraction of the air bubble bubble and the first reflection can be observed at 0.35 ms. (D) Same as (C) but for the neighboring transducer.

understand the Verasonics system and its software/algorithms and confirm that it behaves as expected. Figure 5.2 shows the first test, where a signal with a central frequency of 150 kHz was emitted into the tank, and the different order reflections from the bottom of the tank and the air-water interface were used to quality control (QC) the system. The QC was executed by using the known distance from the transducer placed 1–2 cm under the water surface, $\simeq$22.5 cm above the bottom of the tank, and the sound speed in water (assumed to be 1470 m/s) to confirm the observed arrival times of the reflections. The first reflection is predicted to arrive after $t = (2 \cdot 0.225 \text{ m})/1470 \text{ m/s} = 3.3 \cdot 10^{-4}$ s, corresponding well to observed arrivals in Figures 5.2M and 5.3C.

A second test was carried out by placing one of the muzzles at the bottom of the tank below the transducer grid and letting it inject air bubbles into the water column at regular intervals. We could see a clear signature of the air bubble by emitting a 150 kHz signal and recording it by the source transducer and a neighboring transducer 10 cm away. Figures 5.3A, B show 100 consecutive shots recorded for 0.5 ms, where the bubbles migrate from the air muzzle placed directly below transducer 244 (signal in Figure 5.3A), which can be observed as oblique events. Figures 5.3C, D can be compared to the same

situation without any bubbles, which is the case in Figures 5.2M, N. If we had a running movie of the arriving signal, we would see that bubbles propagate from the first reflection ($\simeq$0.33 ms) to the left (0 ms) in the display, which is expected as the bubbles are injected at a distance from the source transducer and migrate towards it.

This test shows that the system works as expected and that we can start with more complex experimental setups. The next test is to add the geological models to the setup and measure the resulting bubble signature. After which, water-saturated sand will be added.

5.3 Future outlook

Potential extensions and future research ideas related to the presented work are stated in the following.

I In future work, we aim to automate the procedures presented in Chapter 2 to develop a real-time ship-strike warning system. The first step is to develop an algorithm for the automatic detection of whales. Then the arrival time picking will be improved and made automatic, removing the bias related to manual picking and improving the obtained localization. These arrival times will be taken as input to the inversion algorithms presented in the paper to estimate the whale's location, speed, and heading in real time.

   Another extension is to use the geo-referenced seismic shots to correlate the distances estimated by the interrogator unit and those computed from the known position of the telecommunication cable with higher accuracy. This will improve the performance of the location procedures.

II The main limitation of using surface waves for monitoring quick clay, as discussed in Chapter 3, is the low depth penetration and the sensitivity to shear-wave velocity changes. Future work aims to test alternative methods previously shown to be sensitive to near-surface shear-wave velocity changes. Such methods include coda wave interferometry and a time-lapse reflection analysis from the bedrock boundary.

III We aim to apply the spectral method presented in Chapter 4 to other PRM receiver arrays (like the array near the Valhall or Grane fields) as well as data recorded by ocean-bottom fiber-optical cables (for example on the Svalbard data from 2020 or 2022). For the latter case, additional investigation into the directionality of the DAS array is needed. This will further be used to adjust the spectral ratio method to compensate for its effects. Additionally, more complex and reliable velocity models (both 2D and 3D) should be tested to see their effect on the final quality factor estimates. Finally, the effects of the different assumptions made in the work, like the frequency independent Q assumption, should be explored.

IV As only one local earthquake was analyzed for the work presented in Appendix A,

we aim to repeat it for all local events recorded during the 2020 and 2022 acquisition periods. This will include an uncertainty analysis of the obtained hypocenter locations, which will be compared to those reported by NORSAR and the Norwegian National Seismic Network (NNSN). This will give us essential information on the benefits of using one versus several DAS interrogators to analyze and localize earthquakes. Additionally, DAS arrays have a low sensitivity to P-waves impinging the fiber in a perpendicular direction (which is often the case for earthquakes, see, e.g., Papp et al. (2017), Lior et al. (2023)), and it has been argued that the P-wave arrivals observed on DAS arrays are mainly scattered P-waves, not the direct arrival. We aim to study how this affects the obtained localization and whether additional signal processing is needed to find more accurate P-wave onsets. We also aim to use other earthquake phases (e.g., the depth phase pP) to constrain the hypocenter depth better.

Appendix A

Conference paper 1: Analysis of a Local Earthquake in the Arctic using a 120 km long Fibre-Optic Cable

Robin André Rørstadbotnen[1,2], Martin Landrø[1,2], Kittinat Taweesintananon[1,2,3], Léa Bouffaut[4], John Potter[1,2], Ståle Johansen[1,2,5], Hannah Joy Kriesell[1,2], Jan Kristoffer Brenner[2,7], Aksel Haukanes[7], Olaf Schjelderup[2,6], Frode Storvik[2,6],

1 - Department of Electronic Systems, NTNU, 7491 Trondheim, Norway,

2 - Centre for Geophysical Forecasting, NTNU, 7491 Trondheim, Norway,

3 - PTT Exploration and Production Public Company Limited, Bangkok, Thailand,

4 - K. Lisa Yang Center for Conservation Bioacoustics, Cornell Lab of Ornithology, Cornell University, Ithaca, NY, United States,

5 - Department of Geoscience and Petroleum, NTNU, 7491 Trondheim, Norway,

6 - Sikt, 7037 Trondheim, Norway,

7 - Alcatel Submarine Networks Norway AS, 7075 Tiller, Norway,

Published and presented as conference paper in EAGE 83rd annual conference & exhibition.

A.1 Introduction

Spatial undersampling is a well-known problem when monitoring and characterizing the Earth's passive seismicity. The permanent seismic network available worldwide is typically installed close to the active seismic regions, rendering the inactive seismic areas highly undersampled. Moreover, the ocean receiver coverage is especially sparse due to the challenging and expensive nature of the installation and maintenance process. This bias in sensor coverage induces difficulties in many areas within passive seismology. Small-magnitude local earthquakes can go undetected and introduce biases in earthquake catalogs and develop problems when monitoring induced seismicity in areas of oil and gas production or carbon dioxide sequestration.

In the last decade, it has been demonstrated that standard Fibre-Optic (FO) telecommunication cables can be repurposed to sensor arrays of both high spatial and high-frequency samples. There are already more than 1.3 million km of FO cables trenched in the world's oceans, providing a unique possibility to increase the receiver density. These new types of sensors give the means to continuously measure low-frequency acoustic and seismic events over large distances via the Distributed Acoustic Sensing (DAS) technology and will significantly improve the spatial resolution of the seismic inactive regions and the ocean. The DAS technology measures the strain the acoustic waves induce on the cable by investigating the optical backscatter from the inherent impurities in the FO cable. For this work, the first 120 km of a 265 km long 'dark' cable stretching from Longyearbyen to Ny-Ålesund in Svalbard, Norway (see Figure A.1) were investigated. The FO cable was connected to an OptoDAS interrogator, recording the data.

Several studies have already applied DAS to geophysical problems. DAS has been used to map new geological structures beneath the length of FO cable (Jousset et al. 2018, Cheng et al. 2021), for source location of volcanic earthquakes and characterization of volcanic subsurfaces (Nishimura et al. 2021), for characterization of regional and teleseismic waveforms (Lindsey et al. 2017), and to detect weak earthquake signals below the noise level through template matching (Li and Zhan 2018).

This extended abstract reports how DAS alone can be used to locate a mid-Atlantic small-magnitude earthquake using arrival times, enhanced by various signal processing techniques, from the first 120 km of the FO cable. Ray tracing and a grid search procedure are used for the localization. It also investigated how near-field beamforming can be used to find the apparent direction and velocity of the event, how it can improve the signal-to-noise ratio (SNR) of the seismic signal, and how different cable segments can see different v_p/v_s ratios along the length of the cable.

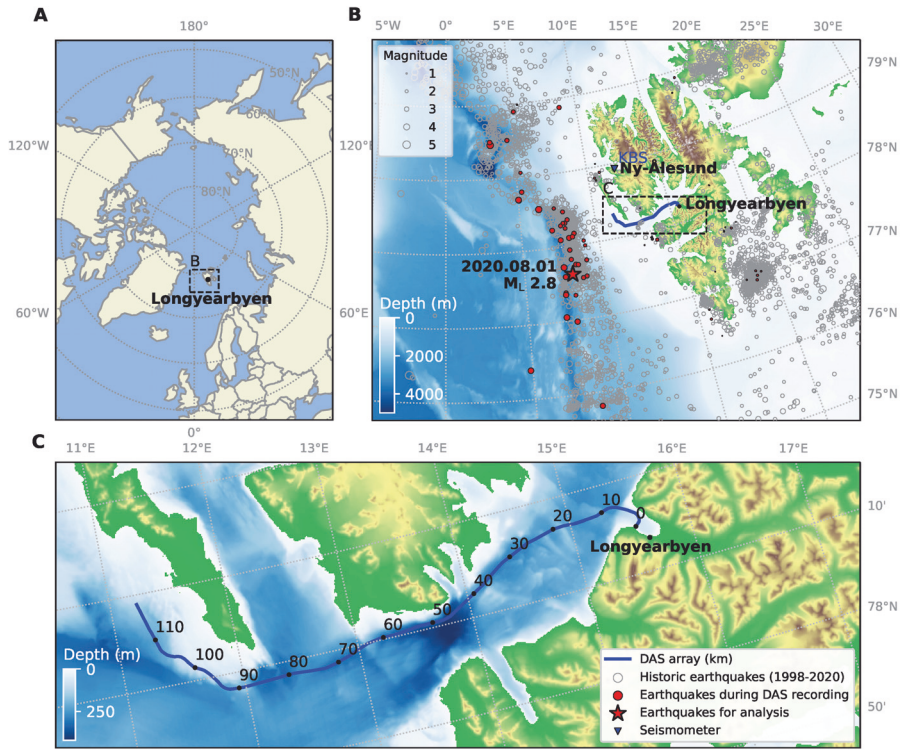

Figure A.1: (A) A polar stereographic map of the Arctic showing the location of the FO array near Longyearbyen. (B) A regional map displaying the epicenter of the M_L 2.8 earthquake near the mid-Atlantic ridge and other historic earthquakes recorded between 1998 and 2020. (C) A local map showing the layout of the DAS array.

A.2 Theory

A.2.1 Preprocessing

For the earthquake analysis, several processing steps were carried out to improve the data's SNR ratio and to extract more accurate P- and S-wave arrival times to estimate the hypocenter location. (1) A band-pass filter was applied to extract the dominant frequency, (2) $f-k$-filter and $f-x$ domain filter for swell noise attenuation and $f-x$ deconvolution, (3) 2D beamforming to extract the apparent velocity and angle of the arriving wave and the maximum channels used for coherent stacking.

The 2D time-domain beamforming was carried out using the known receiver position along the FO cable and possible apparent angles and velocities. Delay between adjacent sensor points $\delta t(v, \theta)$ can be found by

$$\delta t(v, \theta) = \frac{dr \sin(\theta)}{v}, \tag{A.1}$$

where dr denotes the distance between sensor points, θ the apparent angles, and v either the P- or S-wave velocity. The obtained delay was then used to align and sum the different traces. In order to investigate the maximum number of traces that stack coherently, the SNR was computed by finding Root-Mean-Square (RMS) of 2-second windows just before the P-wave arrival and immediately after the P- and S-wave arrivals.

A.2.2 Grid search for earthquake location using ray tracing

To invert for the hypocenter and origin time of an earthquake, a comparison between the observed and theoretical traveltimes is required. Here, the theoretical traveltimes, and hence the arrival times at the different receivers, were computed using a numerical implementation of the ray equations, a high-frequency approximate solution to the wave equation (Thomson and Chapman 1985, Keers et al. 1997). A variety of methods to find the hypocenter location exist (Havskov and Ottemoller 2010). In this work, a conventional grid search method (Havskov and Ottemoller 2010) has been implemented to estimate the location of an earthquake of interest using DAS recordings alone. A pre-defined grid of size ($81 \times 81 \times 301$) was constructed around an area assumed to contain the earthquake based on the catalog locations reported by NORSAR and the Norwegian National Seismic Network (NNSN). The RMS misfit $M(x, y, z)$ was computed for each grid point (x, y, z) by

$$M(x, y, z) = \left(\frac{\sum_{i=1}^{N} r_i^2(x, y, z)}{N} \right)^{1/2}, \tag{A.2}$$

where $r_i(x, y, z)$ denotes the residual for arrival time i and N the total number of arrivals. The location of the earthquake is the global minimum of the grid volume, i.e., the grid point with the lowest misfit.

A.3 Results

A local M_L 2.8 earthquake with a hypocenter close to the Mid-Atlantic ridge with origin time 01 August 2021 at 02:54:00 UTC was studied in this work. As shown in Figure A.1B, this earthquake is located in line with the majority of the cable positioned in the fjord. Other earthquakes located further to the North or the South will arrive from a more broadside direction offering a unique possibility to compare array effects and analyze apparent velocities for P- and S-waves from different earthquakes. For the earthquake investigated, after compensating for the apparent angle of arrival, the apparent velocity and the ratio of P- to S-wave velocity (v_p/v_s) are observed to increase with distance from the epicenter to

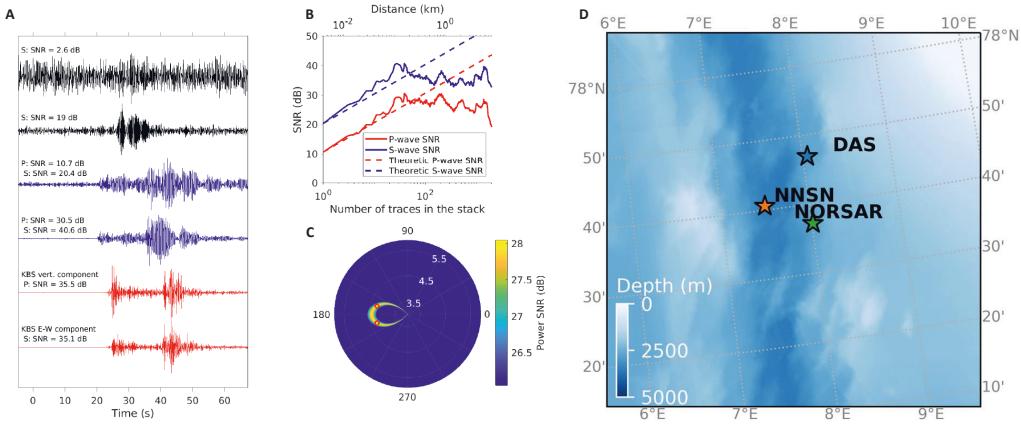

Figure A.2: (A) Comparison between a single trace and a stack of 39 traces for channels at 114 km (the black) and 61.3 km (the blue), against the vertical and east-west component of the KBS seismometer data (the red). (B) SNR versus stacking length for P- and S-waves recorded at 61.3 km along the cable. The dashed line corresponds to an improved SNR model ($\sqrt{N}$). (C) Beamforming results for apparent P-wave velocity and incidence angle using channels between 58.0-64.5 km with the same middle channel at 61.3 km. (D) Localization of the M_L 2.8 local earthquake using 53 DAS sensor points (the black start) compared to the catalogue locations reported by NNSN (the orange start) and NORSAR (the red star).

the DAS sensors. The arrival times for the P-waves of two segments at increasing cable lengths give velocities of 6.21 and 8.66 km/s, while the same segments for S-waves yield 3.75 and 5.14 km/s, resulting in two v_p/v_s ratios of 1.65 and 1.69, respectively. This rise in velocity is most likely due to eigenrays traveling at increasing depth to reach sensor points at increasing distances from the epicenter and thus encountering higher velocities zones. In addition to displaying the increasing velocity with cable distance, the observed seismic signals show a variation in response to the varying geology along the length of the cable.

By exploiting the aperture of the DAS array, it is possible to increase the SNR of the observed signals by stacking and beamforming. This is displayed in Figure A.2A, where it is first shown how a signal otherwise drowned in noise can be stacked above the noise level by beamforming. Furthermore, it is shown how the SNR of a signal initially well above the noise floor is further enhanced and how these compare to the conventional seismometer KBS located North of the array. Figure A.2B illustrates how the SNR increases with a growing number of traces in the stack and that it follows the trend predicted in theory (for coherently stacked traces as $\sqrt{N}$). Figure A.2C displays the result of the 2D beamforming. The highest SNR values are found for angles of 193° and 192° relative to the cable axis, with velocities of 4.25 and 2.45 km/s for the P- and S-wave, respectively. Furthermore, applying the obtained apparent angles and velocities to equation (A.1) in-

creases the SNR from 10.7 to 30.5 dB for the P-wave signal and from 20.4 to 40.6 dB for the S-wave signal.

The investigated earthquake has an epicenter 110–190 km from the DAS array according to the locations found by NORSAR and NNSN applying the seismometer network in the vicinity of Svalbard. An independent hypocenter estimation was found using only recordings from the FO cable in Isfjorden and compared to the catalog locations. The signal processing techniques were initially used to enhance the first-break arrivals required for the localization. After this, ray tracing was used to compute the theoretical eigenrays to the receivers. Finally, the observed and theoretical arrival time was used in the grid search optimization algorithm (equation (A.2)) to estimate the hypocenter location. As shown in Figure A.2D, this resulted in a location in close agreement with that reported by NORSAR and NNSN. However, the depth resolution is poor when locating an earthquake outside the receiver array's aperture, and it is only possible to constrain the maximum depth of the event using the DAS cable and the grid search method. Nevertheless, fixing the depth to 10 km, similar to the depth used by NORSAR and NNSN, the three hypocenter locations are within $\simeq$17 km of each other.

A.4 Conclusions

This work illustrates how a 120 km long FO cable can be used to enhance the SNR of the recorded P- and S-wave signals and estimate earthquake hypocenter locations. Exploiting one earthquake recorded during the summer of 2020, it has been shown how a simple beamforming procedure can find the direction of the earthquake and the apparent velocity and help increase the onset of P- and S-waves. It has also demonstrated how a local earthquake can be located in close agreement with those found by the conventional seismic receivers using the DAS arrival times only. In conclusion, the long antenna offered by fiber cables, like the one in Isfjorden, offers unique complementary methods to enhance received seismic signals and to traditional source localization for earthquakes and other seismic sources.

A.5 Acknowledgements

We thank the Norwegian Research Council and the industry partners of the GAMES consortium at NTNU for the financial support (grant no. 294404), and the Centre for Geophysical Forecasting at NTNU (grant no. 309960). We would also thank the University of Bergen and NORSAR for access to their earthquake bulletin. The author would also like to thank Shearwater GeoServices Software for the Reveal software used in our analysis.

Appendix B

Paper 1: Simultaneous Tracking of Multiple Whales using two Fiber-Optic cables - Supplemental information

Robin André Rørstadbotnen[1,2], Jo Eidsvik[2,3], Léa Bouffaut[4], Martin Landrø[1,2], John Potter[1,2], Kittinat Taweesintananon[1,2,5], Ståle Johansen[1,2,6], Frode Storvik[2,7], Joacim Jacobsen[3], Olaf Schjelderup[2,7], Susann Wienecke[3], Tor Arne Johansen[9], Bent Ole Ruud[9], Andreas Wuestefeld[2,10], Volker Oye[2,10]

1 - Department of Electronic Systems, NTNU, 7491 Trondheim, Norway,

2 - Centre for Geophysical Forecasting, NTNU, 7491 Trondheim, Norway,

3 - Department of Mathematical Sciences, NTNU, 7491 Trondheim, Norway,

4 - K. Lisa Yang Center for Conservation Bioacoustics, Cornell Lab of Ornithology, Cornell University, Ithaca, NY, United States,

5 - PTT Exploration and Production Public Company Limited, Bangkok, Thailand,

6 - Department of Geoscience and Petroleum, NTNU, 7491 Trondheim, Norway,

7 - Sikt, 7037 Trondheim, Norway,

8 - Alcatel Submarine Networks Norway AS, 7075 Tiller, Norway,

9 - Department of Earth Science, University of Bergen, 5007 Bergen, Norway,

10 - NORSAR, Gunnar Randers vei 15, 2007 Kjeller, Norway.

Supplemental information published together with the paper presented in Chapter 2.

Supplemental material and figures that support the ideas presented in the main text (Chapter 2) can be found in this Appendix. Section B.1 presents the theory behind the likelihood and traveltime derivative calculations, while Section B.2 gives the theory behind the Bayesian filter computations. In Section B.3, the supplemental figures are presented.

B.1 Likelihood and traveltime derivative calculations

The log-likelihood function at one vocalization time is defined by

$$l(x,y) = -\frac{\sum_{j=1}^{2}\sum_{i=1}^{n_j}\left(T_{i,j}^{(obs)} - T_{i,j}(x,y)\right)^2}{2\tau^2}, \tag{B.1}$$

where the modeled traveltime $T_{i,j} = T_{i,j}(x,y)$ is defined in equation (2.1). The derivatives of this log-likelihood with respect to lateral position (x,y) and the time shift are

$$\begin{aligned}
\frac{dl}{dx} &= \frac{-1}{\tau^2}\sum_{j=1}^{2}\sum_{i=1}^{n_j}\left(T_{i,j}^{(obs)} - T_{i,j}\right)\frac{dT_{i,j}}{dx} = \frac{-1}{\tau^2}\sum_{j=1}^{2}\sum_{i=1}^{n_j}\left(T_{i,j}^{(obs)} - T_{i,j}\right)\frac{(x-x_{i,j})}{c^2(T_{i,j}-\eta)},\\
\frac{dl}{dy} &= \frac{-1}{\tau^2}\sum_{j=1}^{2}\sum_{i=1}^{n_j}\left(T_{i,j}^{(obs)} - T_{i,j}\right)\frac{dT_{i,j}}{dy} = \frac{-1}{\tau^2}\sum_{j=1}^{2}\sum_{i=1}^{n_j}\left(T_{i,j}^{(obs)} - T_{i,j}\right)\frac{(y-y_{i,j})}{c^2(T_{i,j}-\eta)},\\
\frac{dl}{d\eta} &= \frac{-1}{\tau^2}\sum_{j=1}^{2}\sum_{i=1}^{n_j}\left(T_{i,j}^{(obs)} - T_{i,j}\right)\frac{dT_{i,j}}{d\eta} = \frac{-1}{\tau^2}\sum_{j=1}^{2}\sum_{i=1}^{n_j}\left(T_{i,j}^{(obs)} - T_{i,j}\right).
\end{aligned}$$

Considering a fixed (x,y), the latter equation defines a linear solution for η when setting $\frac{dl}{d\eta} = 0$. For the position (x,y), the second derivatives can be computed similarly:

$$\begin{aligned}
\frac{d^2l}{dx^2} &= \frac{1}{\tau^2}\sum_{j=1}^{2}\sum_{i=1}^{n_j}\left(T_{i,j}^{(obs)} - T_{i,j}\right)\left[\frac{dT_{i,j}}{dx}\right]^2 - \frac{1}{\tau^2}\sum_{j=1}^{2}\sum_{i=1}^{n_j}\left(T_{i,j}^{(obs)} - T_{i,j}\right)\frac{d^2T_{i,j}}{dx^2},\\
\frac{d^2l}{dxdy} &= \frac{1}{\tau^2}\sum_{j=1}^{2}\sum_{i=1}^{n_j}\left(T_{i,j}^{(obs)} - T_{i,j}\right)\left[\frac{dT_{i,j}}{dx}\right]\left[\frac{dT_{i,j}}{dy}\right] - \frac{1}{\tau^2}\sum_{j=1}^{2}\sum_{i=1}^{n_j}\left(T_{i,j}^{(obs)} - T_{i,j}\right)\frac{d^2T_{i,j}}{dxdy},\\
\frac{d^2l}{dy^2} &= \frac{1}{\tau^2}\sum_{j=1}^{2}\sum_{i=1}^{n_j}\left(T_{i,j}^{(obs)} - T_{i,j}\right)\left[\frac{dT_{i,j}}{dy}\right]^2 - \frac{1}{\tau^2}\sum_{j=1}^{2}\sum_{i=1}^{n_j}\left(T_{i,j}^{(obs)} - T_{i,j}\right)\frac{d^2T_{i,j}}{dy^2}.
\end{aligned}$$

The traveltime derivatives are

$$\begin{aligned}
\frac{dT_{i,j}}{dx} &= \frac{(x - x_{i,j})}{c\sqrt{(x - x_{i,j})^2 + (y - y_{i,j})^2 + (z - z_{i,j})^2}}, \\
\frac{dT_{i,j}}{dy} &= \frac{(y - y_{i,j})}{c\sqrt{(x - x_{i,j})^2 + (y - y_{i,j})^2 + (z - z_{i,j})^2}}, \\
\frac{d^2T_{i,j}}{dx^2} &= \frac{1}{c\sqrt{(x - x_{i,j})^2 + (y - y_{i,j})^2 + (z - z_{i,j})^2}} \\
&- \frac{(x - x_{i,j})^2}{c\left[(x - x_{i,j})^2 + (y - y_{i,j})^2 + (z - z_{i,j})^2\right]^{3/2}}, \\
\frac{d^2T_{i,j}}{dxdy} &= -\frac{(x - x_{i,j})(y - y_{i,j})}{c\left[(x - x_{i,j})^2 + (y - y_{i,j})^2 + (z - z_{i,j})^2\right]^{3/2}}, \\
\frac{d^2T_{i,j}}{dy^2} &= \frac{1}{c\sqrt{(x - x_{i,j})^2 + (y - y_{i,j})^2 + (z - z_{i,j})^2}} \\
&- \frac{(y - y_{i,j})^2}{c\left[(x - x_{i,j})^2 + (y - y_{i,j})^2 + (z - z_{i,j})^2\right]^{3/2}}.
\end{aligned}$$

Given a known or estimated position $(\hat{x}, \hat{y})$, the measurement noise variance τ^2 is estimated by

$$\hat{\tau}^2 = \frac{1}{n_1 + n_2} \sum_{j=1}^{2} \sum_{i=1}^{n_j} \left(T_{i,j}^{(obs)} - T_{i,j}(\hat{x}, \hat{y}) \right)^2. \tag{B.2}$$

B.2 Bayesian filtering calculations

For completeness, we give a brief account of the recursive methods for computing the filtering and prediction steps for state space models. A recent description of these approaches is provided by Särkkä (2013).

We denote the traveltime data at time s_k by $\boldsymbol{d}_k = \{T_{i,j,k}^{(obs)}; i = 1, \ldots, n_j, j = 1, 2\}$. All the traveltime data available up to this time are given by $\boldsymbol{D}_k = \{\boldsymbol{d}_k, \ldots, \boldsymbol{d}_1\}$.

We have the filtering state probability density function (PDF) at time s_{k-1} denoted $p(\boldsymbol{m}_{k-1}|\boldsymbol{D}_{k-1})$. Assume this is Gaussian with mean $\hat{\boldsymbol{m}}\boldsymbol{u}_{k-1}$ and covariance matrix $\hat{\boldsymbol{\Sigma}}_{k-1}$. The prediction PDF at time s_k is achieved by marginalizing over the previous state variable:

$$p(\boldsymbol{m}_k|\boldsymbol{D}_{k-1}) = \int p(\boldsymbol{m}_k, \boldsymbol{m}_{k-1}|\boldsymbol{D}_{k-1}) d\boldsymbol{m}_{k-1}. \tag{B.3}$$

Assuming a Gaussian approximation for the filtering distribution at time s_{k-1} and relying on the linear dynamical model in equation (2.6), we can solve equation (B.3) to see that

the predictive PDF is also Gaussian with mean $\bar{\boldsymbol{m}}u_k = \boldsymbol{A}_{k-1,k}\hat{\boldsymbol{m}}u_{k-1}$ and covariance matrix $\bar{\boldsymbol{\Sigma}}_k = \boldsymbol{A}_{k-1,k}\hat{\boldsymbol{\Sigma}}_{k-1}\boldsymbol{A}_{k-1,k}^t + \boldsymbol{S}_{k-1,k}$.

We denote this predicted state PDF at time s_k by $p(\boldsymbol{m}_k|\boldsymbol{D}_{k-1})$ (at the first time step, this is only the initial model $p(\boldsymbol{m}_1)$). The model is updated with data $\boldsymbol{d}_k$ to form the filtering PDF:

$$\begin{aligned} p(\boldsymbol{m}_k|\boldsymbol{D}_k) &= \frac{p(\boldsymbol{m}_k|\boldsymbol{D}_{k-1})p(\boldsymbol{d}_k|\boldsymbol{m}_k)}{p(\boldsymbol{d}_k|\boldsymbol{D}_{k-1})} \\ &\propto p(\boldsymbol{m}_k|\boldsymbol{D}_{k-1})p(\boldsymbol{d}_k|\boldsymbol{m}_k), \end{aligned} \tag{B.4}$$

where we assume conditionally-independent data; $p(\boldsymbol{d}_k|\boldsymbol{m}_k, \boldsymbol{D}_{k-1}) = p(\boldsymbol{d}_k|\boldsymbol{m}_k)$. We approximate the PDF in equation (B.4) by a Gaussian model with mean at the mode of equation (B.4) and covariance defined from the curvature at this mode. The optimization is done similarly to the single-time approach described in equation (2.4). We now start with the position prediction $\boldsymbol{m}_k^0 = \bar{\boldsymbol{m}}u_k$ and the iteration proceeds by $r = 1, \ldots$:

$$\boldsymbol{m}_k^r = \boldsymbol{m}_k^{r-1} - \left[\frac{d^2 l_k(\boldsymbol{m}_k^{r-1})}{d\boldsymbol{m}_k^2}\right]^{-1} \frac{dl_k(\boldsymbol{m}_k^{r-1})}{d\boldsymbol{m}_k}, \tag{B.5}$$

where the log filtering PDF in equation (B.4) at this time s_k is defined by

$$l_k(\boldsymbol{m}_k) = -\frac{1}{2}(\boldsymbol{m}_k - \bar{\boldsymbol{m}}u_k)^t \bar{\boldsymbol{\Sigma}}_k^{-1}(\boldsymbol{m}_k - \bar{\boldsymbol{m}}u_k) - \frac{1}{2\tau^2}[\boldsymbol{d}_k - \boldsymbol{T}_k(\boldsymbol{m}_k)]^t[\boldsymbol{d}_k - \boldsymbol{T}_k(\boldsymbol{m}_k)], \tag{B.6}$$

using $\boldsymbol{T}_k$ to denote the vector of modeled traveltime data at all fiber pick locations. The required derivatives are as calculated in Supplemental Material Section B.1. The fitted mean is the mode $\hat{\boldsymbol{m}}_k$ obtained by the iterative scheme in equation (B.5) and the fitted covariance of the Gaussian approximation is

$$\hat{\boldsymbol{\Sigma}}_k^{-1} = -\frac{d^2 l_k(\hat{\boldsymbol{m}}_k)}{d\boldsymbol{m}_k^2}. \tag{B.7}$$

The prediction and filtering equations in equations (B.3) and (B.4) are common in tracking. They represent online calculations. Smoothing or posterior expressions can be used similarly for offline inspection. An effective backward calculation from an end time point s_K, moving in a stepwise manner to the first time s_1, defines the expression for the posterior PDF:

$$p(\boldsymbol{m}_k|\boldsymbol{D}_K) = \int \frac{p(\boldsymbol{m}_{k+1}|\boldsymbol{m}_k)p(\boldsymbol{m}_k|\boldsymbol{D}_k)}{p(\boldsymbol{m}_{k+1}|\boldsymbol{D}_k)} p(\boldsymbol{m}_{k+1}|\boldsymbol{D}_K) d\boldsymbol{m}_{k+1}. \tag{B.8}$$

This relation builds on the Markovian state space modeling assumptions in equation (2.6) and the conditionally-independent assumptions of the data. Relying again on Gaussian

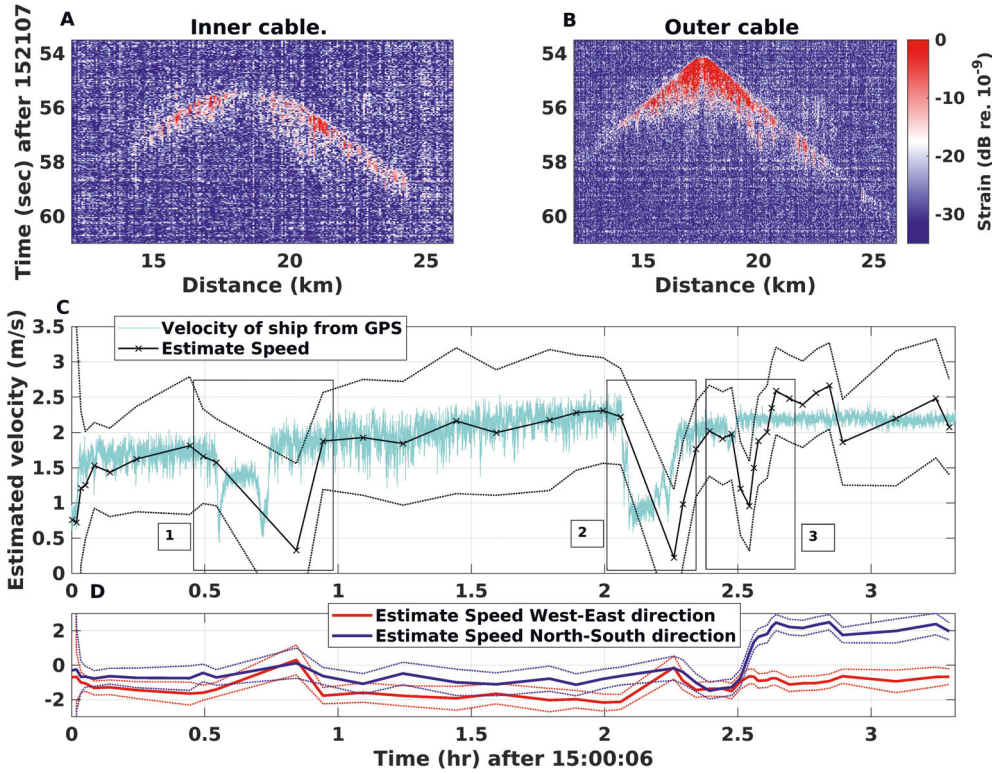

Figure B.1: Supplemental information from the air gun processing. (A) An air gun shot received on the inner cable. (B) The same airgun shot on the outer cable. In this example, the air gun was fired directly above the outer cable. (C) A comparison between the velocity computed using GPS position recorded by a GNSS receiver and the Bayesian filter. (D) The decomposed velocities in West-East and North-South directions. The dashed lines in (C) and (D) are uncertainties related to the velocities. The numbers in (C) indicate where the ships made sharp turns, (1) and (3), and a loop, (2).

approximations for the PDFs, all expressions in equation (B.8) are available from the Gaussian approximations to the filtering and predictive PDF, as well as the smoothing PDF at the latter time t_{k+1} in the backward recursion. We can hence complete the integral to get an associated Gaussian approximation to the smoothing PDF at time t_k. Denoting the mean and covariance matrix of this smoothing PDF by $\tilde{\boldsymbol{m}}u_k$ and $\tilde{\boldsymbol{\Sigma}}_k$, we have

$$\begin{aligned} \boldsymbol{J}_k &= \hat{\boldsymbol{\Sigma}}_k \boldsymbol{A}_{k,k+1}^t \bar{\boldsymbol{\Sigma}}_{k+1}^{-1}, \\ \tilde{\boldsymbol{m}}u_k &= \hat{\boldsymbol{m}}u_k + \boldsymbol{J}_k(\tilde{\boldsymbol{m}}u_{k+1} - \bar{\boldsymbol{m}}u_{k+1}) \\ \tilde{\boldsymbol{\Sigma}}_k &= \hat{\boldsymbol{\Sigma}}_k + \boldsymbol{J}_k(\tilde{\boldsymbol{\Sigma}}_{k+1} - \bar{\boldsymbol{\Sigma}}_{k+1})\boldsymbol{J}_k^t. \end{aligned} \tag{B.9}$$

For details, see (Särkkä 2013, Chapter 8).

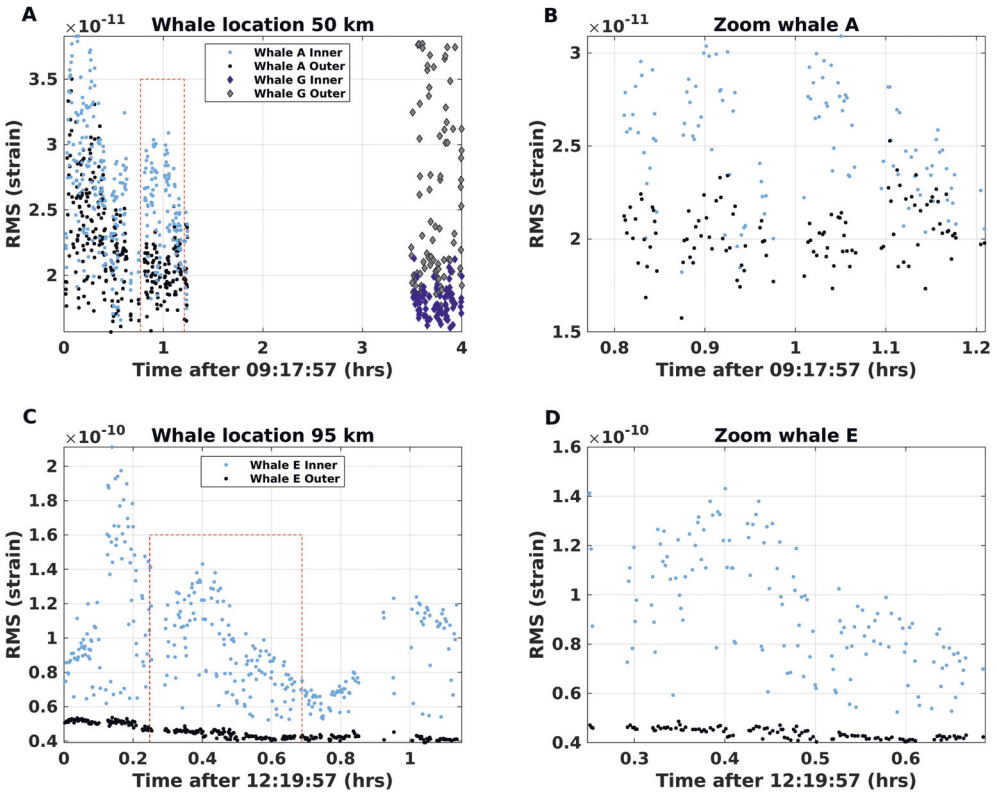

Figure B.2: Observed RMS amplitudes of all fin whale vocalizations computed by a rectangular window around the calls. (A, C) The vocalization for the whales in the two whale locations (45 and 95 km) as given in Figure 2.5. (B, D) Zoomed-in versions are meant to show the periods with whale calls and inter-call breaks.

B.3 Supplemental figures

Two supplemental figures are given. Figures B.1A, B show an example of recorded air gun signals received on the inner (A) and outer cable (B). Furthermore, it also shows the comparison between the velocity of the ship derived from the GPS log (from a GNSS receiver) and the velocities in North-South and East-West directions from the estimators.

Figure B.2 shows RMS levels for whale tracks (A), (G), and (E) computed in the same way as Figure 2.6. The first column of Figure B.2 shows the RMS levels as a function of time. The second column of Figure B.2 shows a zoomed-in version highlighting the inter-call and inter-series intervals for the various whale tracks.

Appendix C

Paper 2: Quick clay monitoring using distributed acoustic sensing: A case study from Rissa, Norway - Supplemental information

Robin André Rørstadbotnen[1,2], Hefeng Dong[1,2], Martin Landrø[1,2], Kenneth Duffaut[2,3], Kevin Growe[1,2], Umedzhon Kakhkorov[2,3], Susann Wienecke[2,4], Joacim Jacobsen[2,4]

1 - Department of Electronic Systems, NTNU, 7491 Trondheim, Norway

2 - Centre for Geophysical Forecasting, NTNU, 7491 Trondheim, Norway,

3 - Department of Geoscience and Petroleum, NTNU, 7491 Trondheim, Norway

4 - Alcatel Submarine Networks Norway AS, 7075 Tiller, Norway

Supplemental information submitted together with the paper presented in Chapter 3.

C.1 Analysis of construction noise

The channel on the segment investigated closest to well 1 ($\simeq$413 m along the cable) is chosen as the virtual source in the analysis of the construction noise, as for the quiet period (see "Data analysis" subsection). To find stable Virtual Shot Gathers (VSGs) for the industrial noise periods, the Phase-Weighted Stack (PWS) is applied directly to 3-s segments of construction noise. Less than 1 hour of data are needed to converge. However, due to the variation in noise sources, there are oscillations in the convergence curve (see supplemental Figure C.7B).

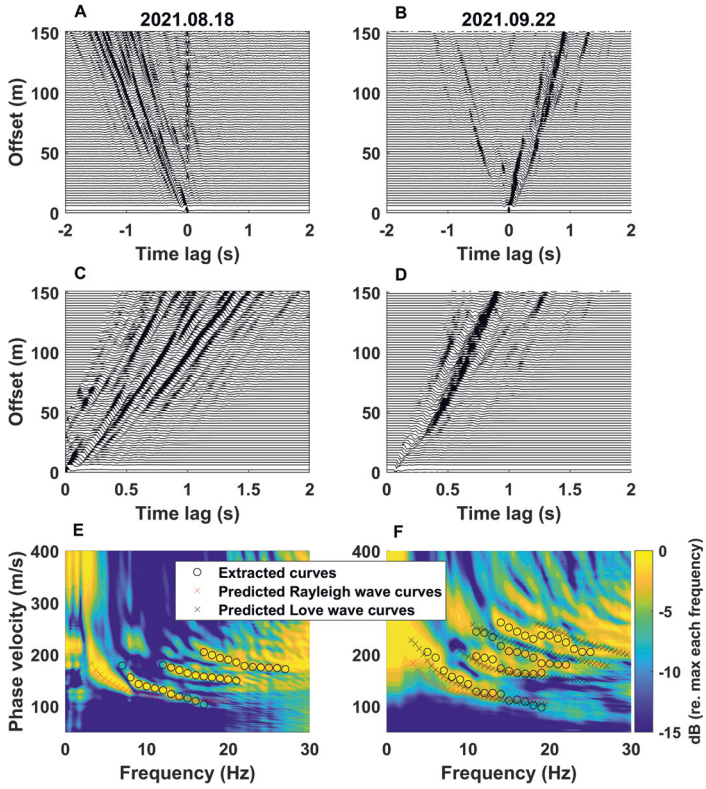

Figure C.1: Virtual shot gathers and resulting dispersion images for construction noise recorded on 18 August 2021 (column one) and 22 September 2021 (column two). (A, B) The two-sided VSG. (C, D) Muted one-sided VSG, i.e., the average of each side in the two-sided VSG. (E, F) The resulting dispersion image overlaid with the extracted Rayleigh wave dispersion curves (black circles), predicted Love wave fundamental mode (red crosses), and four predicted Rayleigh modes (black crosses). In (F), neither the predicted Rayleigh nor the Love dispersion curve fits the extracted dispersion curve. This is attributed to the construction work being carried out broadside to the array.

Figure C.1 displays the VSG from the seismic interferometry for ambient noise recordings for two construction periods, one day when the work is by the barn holding the interrogator, 200 m from the studied segment slightly broadside (18 August 2021, column one) and another day when the work is broadside to the array (22 September 2021, column two). Industrial traffic is, in general, more efficient in generating surface waves, and less then one hour of the stack is needed to compute the VSG for both examples. However, since the traffic on 18 August 2021 is not perfectly in-line with the DAS array, it generated Love waves in addition to Rayleigh waves as depicted by the red crosses in Figure C.1E (modeled by the estimated velocity profile from the active data 12 August 2021). For the traffic on 22 September 2021, a stable VSG is obtained, but the dispersion is not well

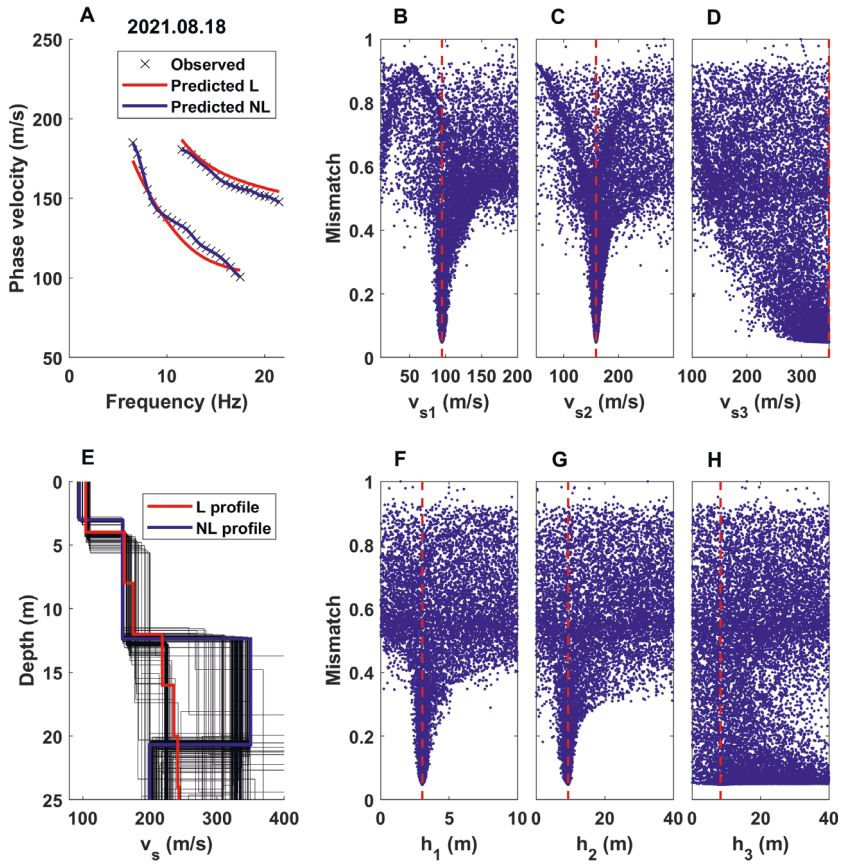

Figure C.2: Inversion results for 18 August 2021. (A) The match between observed and predicted modes. (B, C, D) Shear-wave velocity sensitivity from the multidimensional sensitivity analysis. (E) The resulting inversion profiles. (F, G, H) Layer thickness sensitivity.

resolved (see Figure C.1F). This is mainly due to the industrial activity on the broadside of the array. Furthermore, Figures C.1C, D show the portion of the VSG kept for computing the dispersion images. The resulting dispersion image for the industrial noise on 18 August 2021 shows clear fundamental modes for Love and Rayleigh waves and probably a mix for the higher-order modes. Comparing these results to that of quiet periods and active shots (Figure 3.4), the construction work contains less energy and fewer modes than the sledgehammer shots, but more than the quiet periods. This is also clear from the amplitudes shown in Figure 3.2.

Figure C.2A shows the predicted and observed dispersion modes, while Figure C.2E displays the inversion results. One high-velocity layer is obtained from the non-linear inversion result using two modes from the industrial noise data recorded on 18 August 2021. This is due to the dispersion curves being disrupted by the Love wave energy generated by

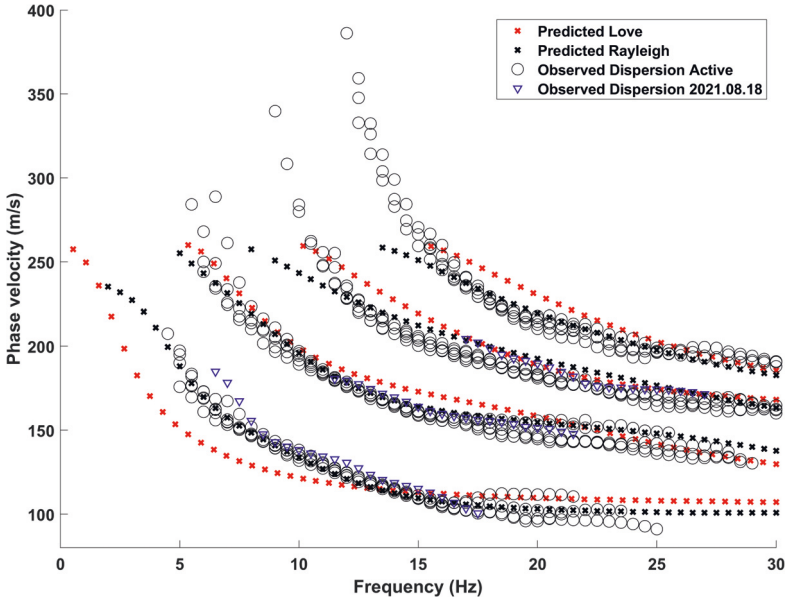

Figure C.3: Modeled dispersive curves for four Love and Rayleigh modes overlaid with observed data from all active data acquisitions and the industrial noise 18 August 2021. The velocity profile obtained from the active shots on 12 August 2021 was used to obtain the predicted dispersive curves.

broadside construction activity. The additional Love wave energy introduces a bias to the inversion result, where the depth and shear-wave velocity of the third layer is poorly estimated. It is also observed that the fit between observed and predicted dispersion curves for the linearized inversion is worse than the non-linear inversion. The effect of this difference is particularly pronounced for depths below 13 m. The associated MDS analysis for the velocity estimates is given in Figures C.2B, C, D and Figures C.2F, G, H for the thickness. Both the velocity and the thickness are well estimated for the first two layers and similar to those obtained using the active data and quiet ambient noise data (Figure 3.10). Contrarily, the shear-wave velocity of the third layer (v_{s3}) approaches the upper bound, and a change in this bound would alter the result, while the third layer thickness (h_3) has a flat mismatch response, indicating that the data cannot resolve the layer thickness. Hence, only the first two layers of the industrial noise data are reliable. However, these results are considered less reliable than those from the active data and the quiet periods due to Love waves generated by the construction noise. The presence of the Love wave energy disrupts the fundamental Rayleigh mode (also the higher-order modes) as seen in the deviation in the shape of the extracted curve at frequencies between 10 and 16 Hz in Figure C.1E, whereas in frequencies below 10 Hz the Love and Rayleigh modes are separated. This interpretation is supported by modeled Love and Rayleigh dispersion curves as depicted in Figure C.3.

C.2 Comparison with area northern segment

To better understand the behavior of the surface waves along the array, an additional survey is carried out on the northern segment of the array (Figure 3.1), an area previously shown to contain little-to-no quick clay (see segment P13B-11 in Solberg et al. (2012)). The dispersion image obtained from this area (Figure C.4A) is different from the ones achieved from the segment studied within the quick clay area (Figure 3.5). This is also evident from comparing the extracted dispersion curves from the two areas as depicted in Figure C.4A, where light gray dots indicate dispersion curves from the quick clay segment and black dots those from the northern segment. The modes found on the northern segment contain more modes, higher frequencies, and higher velocities than the segment in the quick clay. This agrees with the results presented by Solberg et al. (2012). They found different near-surface layers in the area containing the northern segment than in the area containing the quick clay segment. The first layer under the northern segment contains a crust layer ($\simeq$4 m), the second 5–15 m of dry clay, and the third unleached clay. Like the quick clay segment, the top 13–20 m can be resolved, and the surface waves are mainly affected by the crust and dry clay layers. The difference in the dispersion modes between the northern segment and the segment in the quick clay can therefore be attributed to the differences in subsurface material.

C.3 Supplemental figures

This document contains supplemental text and figures to support the content of the main text. Figure C.5 shows the comparison between P- and S-shots in various representations. The time-distance ($t - x$) domain (Figure C.5A), the amplitude spectrum (Figure C.5B) and the phase-velocity spectrum (Figures C.5C, D, E). Figure C.6 depicts the Radon transform representation of the surface wave data. Furthermore, the convergence plot for the passive interferometry is given for the different passive data types in Figure C.7. After which, the weather data (wind speed, temperature, and precipitation) for the acquisition period is given in Figure C.8. Finally, the virtual shot gathers and resulting dispersion images for the remaining quiet periods studied are presented in Figure C.9.

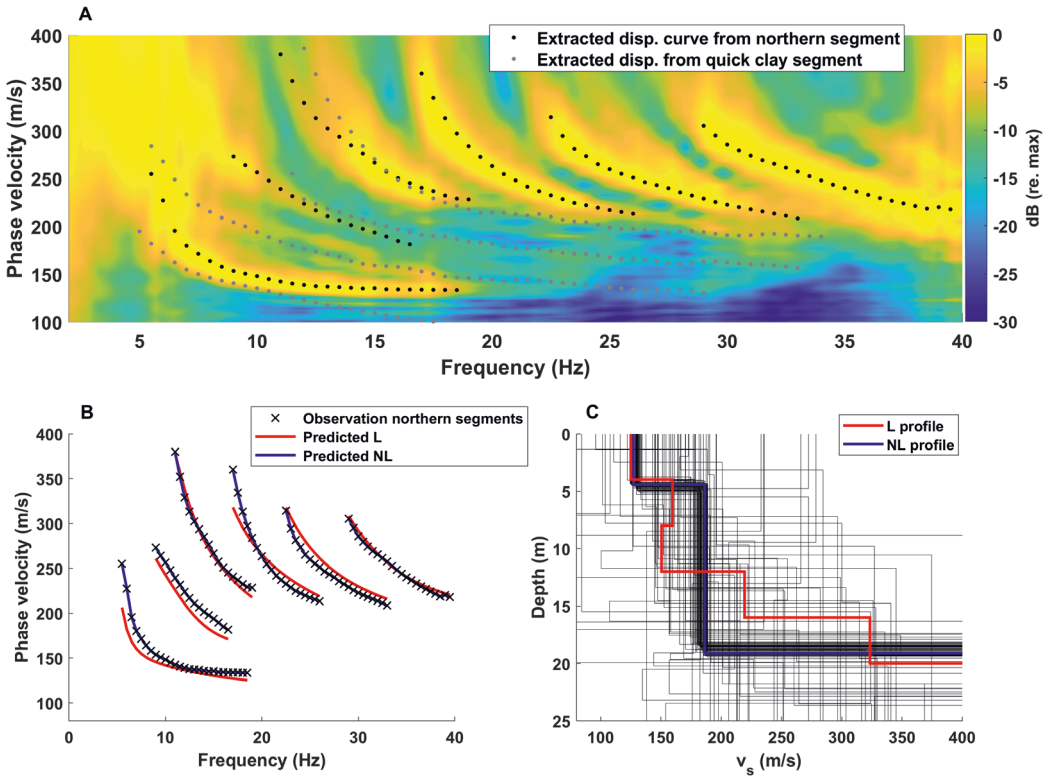

Figure C.4: (A) Phase velocity spectrum from a stack of 35 active shots on the northern segment (see Figure 3.1C) overlaid by the mean extracted dispersion curves (the dark gray) and dispersion curves from the quick clay segment (the light gray) to see the difference better. (B) The fit between the observed (the black) and the predicted (the red for linearized, the blue for ASSA) dispersion curves for the six modes extracted from shots recorded on the northern segment. (C) The estimated shear-wave velocity profiles from the linearized (L; the red) and ASSA non-linear (NL; the blue) inversion overlay a subset of the velocity profiles (the black) generated by the ASSA inversion. The ensemble illustrated the uncertainty of the parameter estimation.

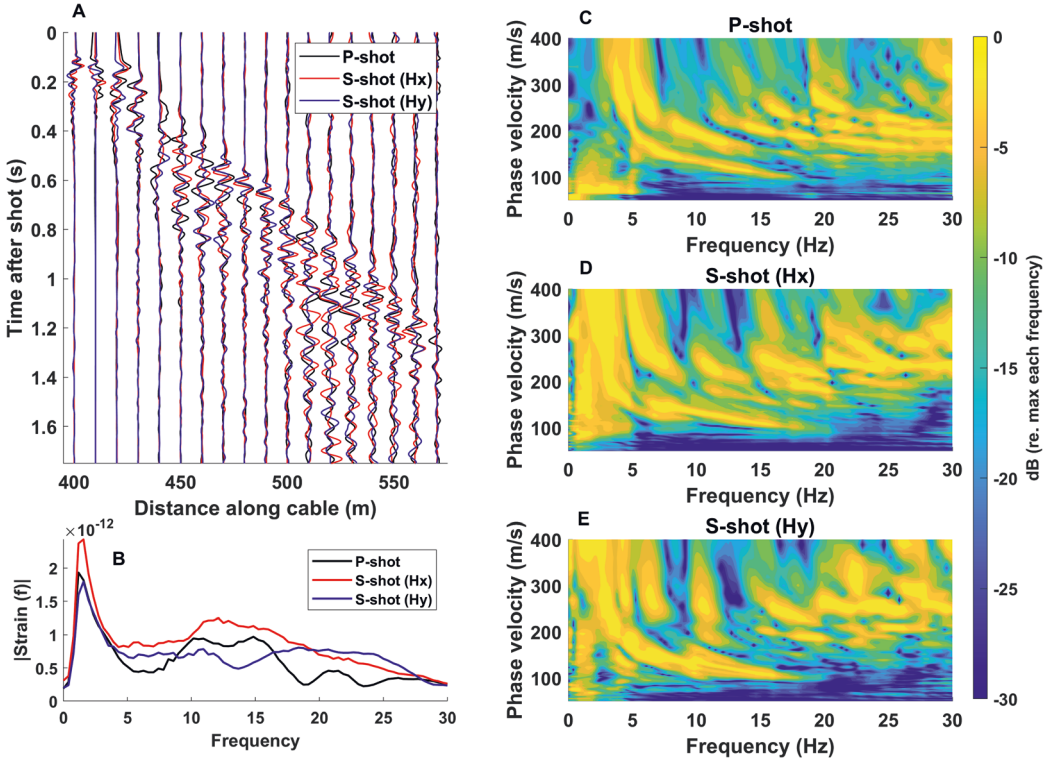

Figure C.5: Comparison between P- and S-shots. The S-shots are carried out in-line (Hx) and cross-line (Hy) to the segment under interest. (A) Waveform comparison. (B) Average frequency content from 28 shots. (C, D, E) Dispersion image comparison. The P-shots show mostly Rayleigh wave arrivals, while the S-shots show a superposition of Rayleigh and Love waves. Note that in (A), only traces every 10 m starting 400 m from the interrogator are shown for easier visualization of the waveforms.

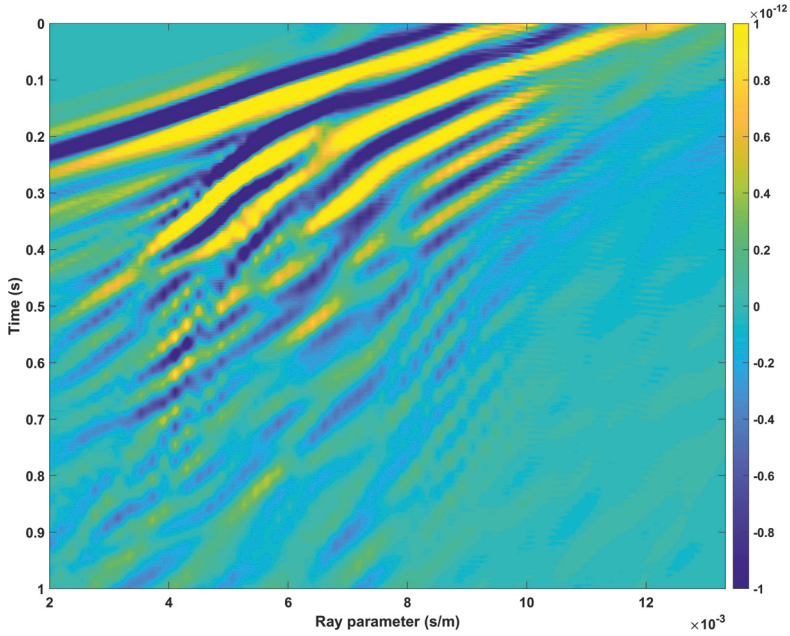

Figure C.6: Radon transform representation of an example shot from 01 June 2021. Clear dispersive arrivals can be observed.

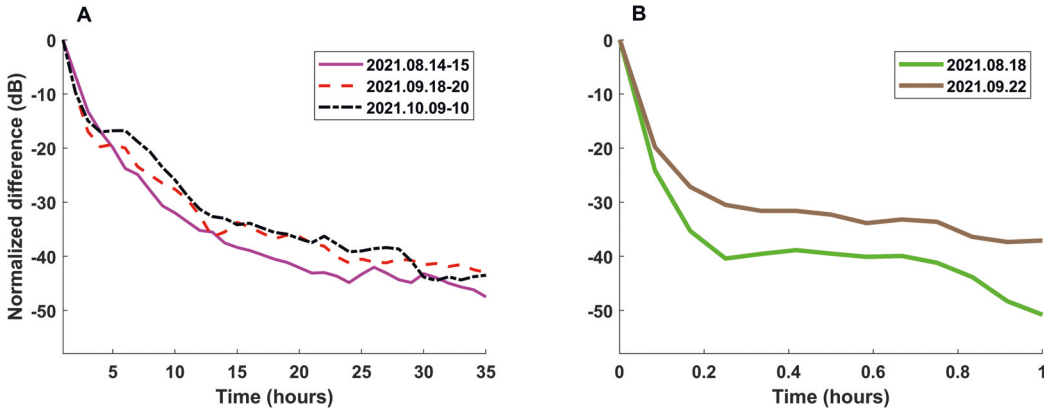

Figure C.7: Convergence plot for the passive interferometry to obtain stable VSG for (A) the quiet periods and (B) the construction period. In (B), every 5 minutes has been extracted to show the convergence.

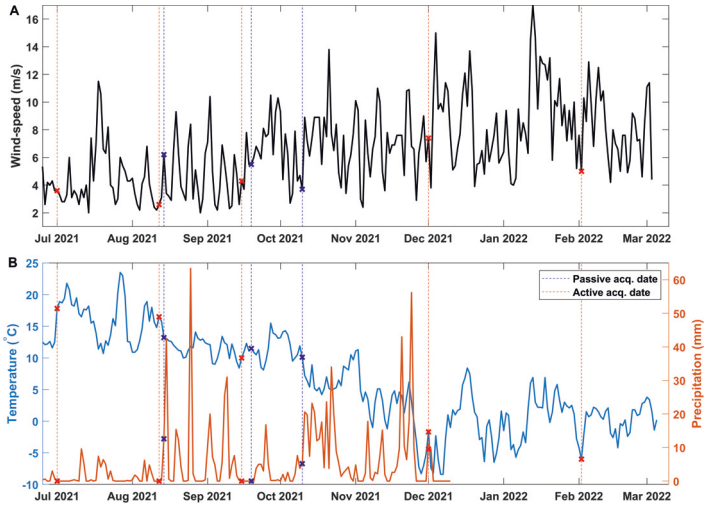

Figure C.8: Weather data for the acquisition period. (A) Wind speed as a function of date. (B) Temperature (the blue) and precipitation (the orange) as a function of time (weather data from seklima.met.no (2022)). Dates used in the analyses are marked as red (active) and blue (passive). Note that no precipitation data are available after 10 December 2021.

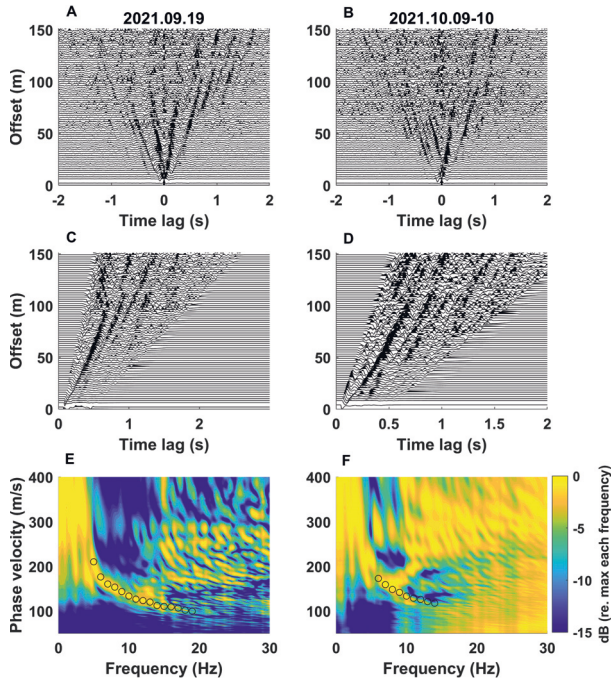

Figure C.9: Virtual shot gathers and resulting dispersion images for quiet periods on 19 September 2021 (column one) and 09-10 October 2021 (column two). (A, B) The two-sided VSG. (C, D) Muted one-sided VSG, i.e., the average of each side in the two-sided VSG. (E, F) The resulting dispersion image overlaid with the extracted Rayleigh wave dispersion curves (black circles).

Appendix D

Paper 3: Average Q_p and Q_s estimation in marine sediments using a dense receiver array - Supplemental information

Robin André Rørstadbotnen[1,2], Martin Landrø[1,2]

1 - Department of Electronic Systems, NTNU, 7491 Trondheim, Norway,

2 - Centre for Geophysical Forecasting, NTNU, 7491 Trondheim, Norway,

Supplemental information published together with the paper presented in Chapter 4.

D.1 Supplemental figures

This section contain supplemental figures to support the content of the main text in Chapter 4. Figure D.1 depicts the typical noise pattern for the PRM array. Furthermore, different examples of computed slopes are shown in Figures D.2 to D.7. After which, rays computed in the ray tracing are presented in Figure D.8. Finally, plots of the uncertainty for E1 and E3 related to the parameters in equation (4.13) are given in Figures D.9 to D.11.

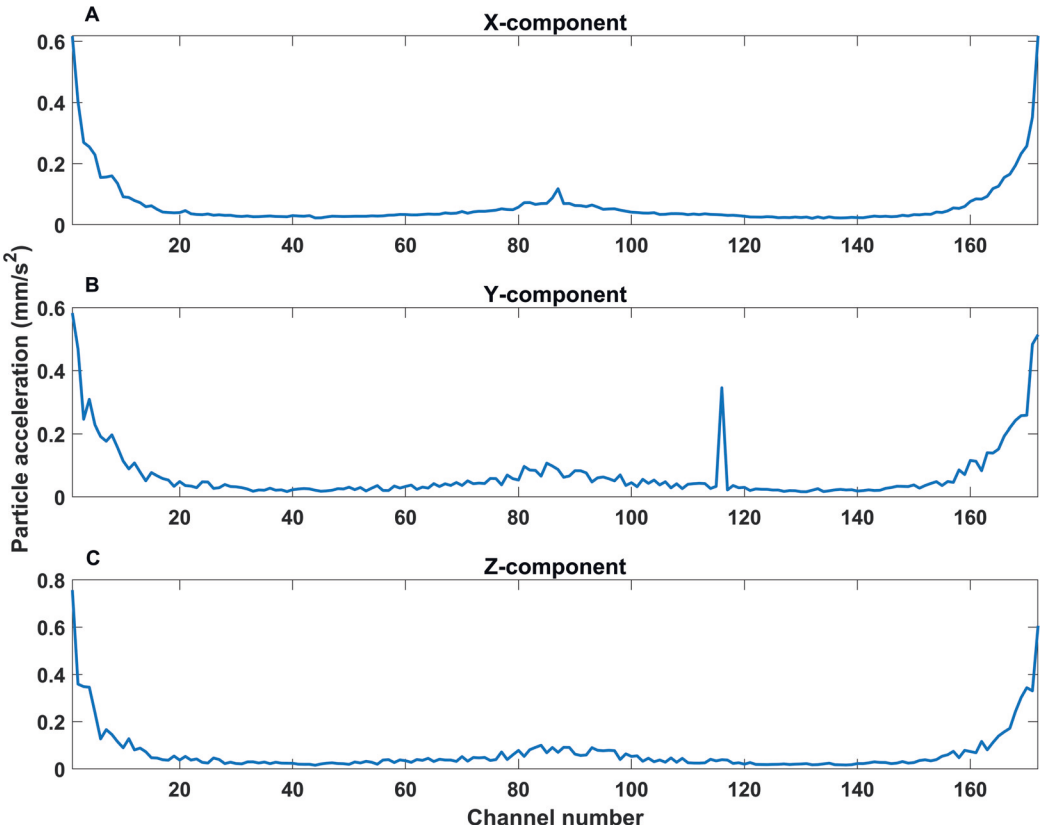

Figure D.1: Average noise RMS for the (E-W)-component (A), (N-S)-component (B) and vertical-component (C) for a random selection of 10 min noise section between 14 January 2014 and 25 January 2014, accumulating to a 3 hour period.

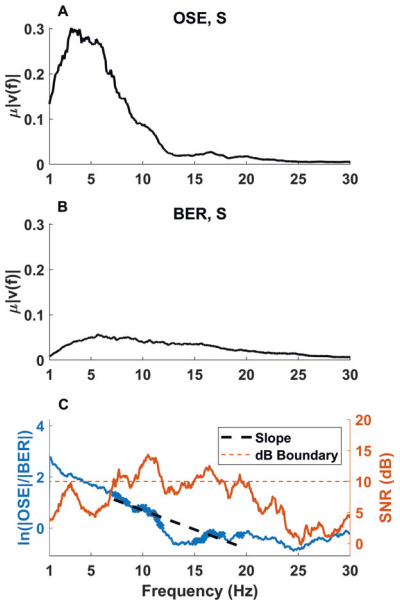

Figure D.2: Computation of the slope from E1 using node 60. (A) The smoothed amplitude spectrum for the S-wave phase recorded on the Oseberg PRM data. (B) The smoothed amplitude spectrum for the S-wave for BER. (C) The computation of the slope (the black dashed line) using the frequency components (the bold blue segments) with SNR above 10 dB (the orange dashed line), used in the Q_{sed} estimation.

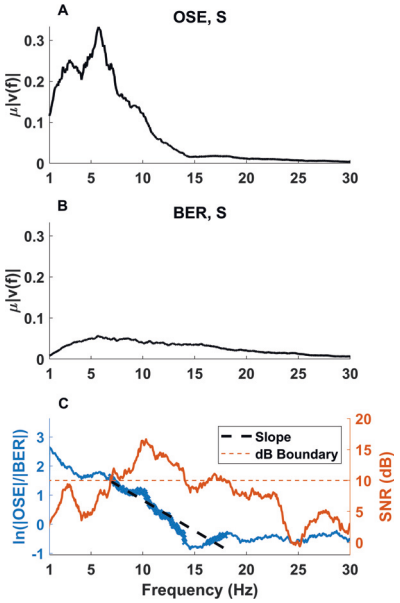

Figure D.3: Same as Figure D.2 but using node 112.

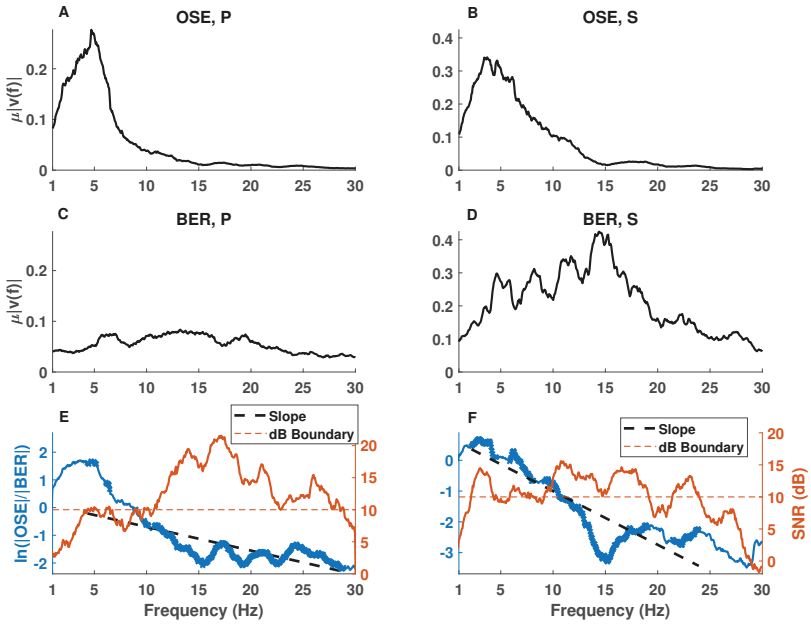

Figure D.4: Computation of the slope from E2 using node 26. (A, B) The smoothed amplitude spectrum for the P- and S-wave phases recorded on the Oseberg PRM data. (C, D) The smoothed amplitude spectrum for the P- and S-wave for BER. (E, F) The computation of the slope (the black dashed line) using the frequency components (the bold blue segments) with SNR above 10 dB (the orange dashed line) is used in the Q_{sed} estimation.

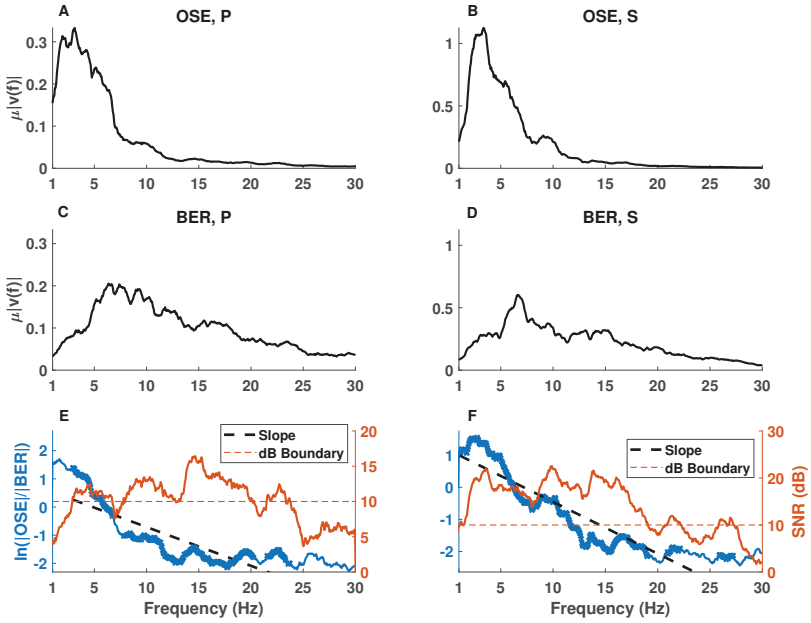

Figure D.5: Same as Figure D.4 but for E3 using node 88.

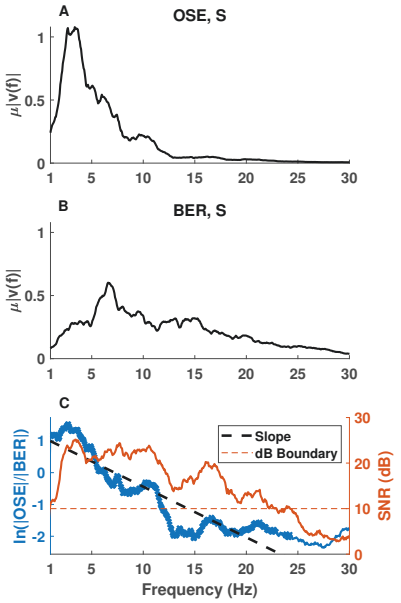

Figure D.6: Computation of the slope from E3 using node 60. (A) The smoothed amplitude spectrum for the S-wave phase recorded on the Oseberg PRM data. (B) The smoothed amplitude spectrum for the S-wave for BER. (C) The computation of the slope (the black dashed line) using the frequency components (the bold blue segments) with SNR above 10 dB (the orange dashed line) is used in the Q_{sed} estimation.

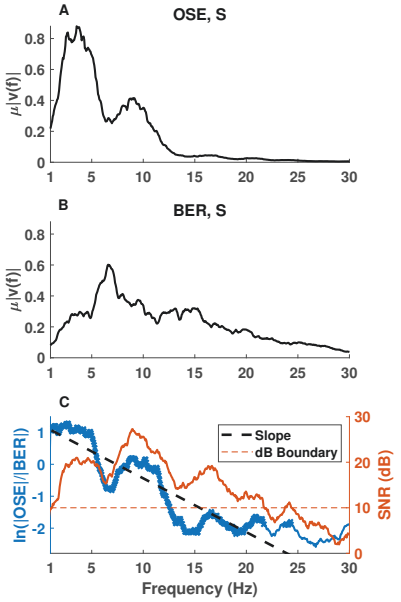

Figure D.7: Same as Figure D.6 but for node 115.

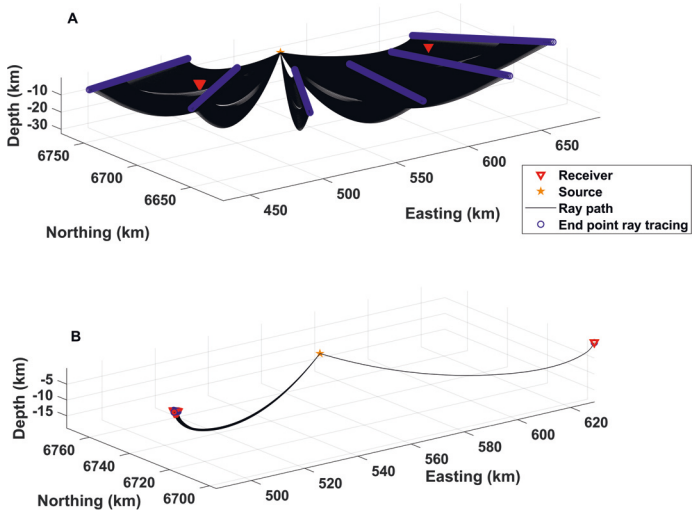

Figure D.8: Obtained ray paths from the ray tracing. (A) The one-point rays are traced to arbitrary points on the surface. (B) The eigenrays are traced from the source to all receivers. Found by triangulation of the end-points obtained in the one-point ray tracing.

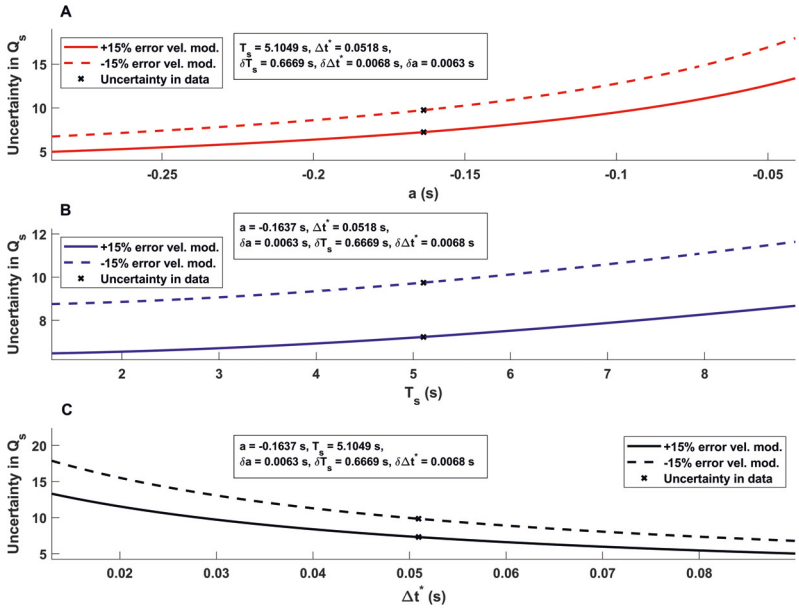

Figure D.9: Total uncertainty obtained from S-waves, E1. (A) Uncertainty in the estimated average quality factor as a function of slope values. (B) Uncertainty in the estimated average quality factor as a function of traveltimes through the sedimentary sequence. (C) Uncertainty in the estimated average quality factor as a function of Δt^* values. For each plot, the range is taken as $\pm 75\%$ of the average values obtained from the analysis (indicated by black crosses). The dashed lines are associated with an -15% error in the velocity model, whereas the solid line an $+15\%$ error.

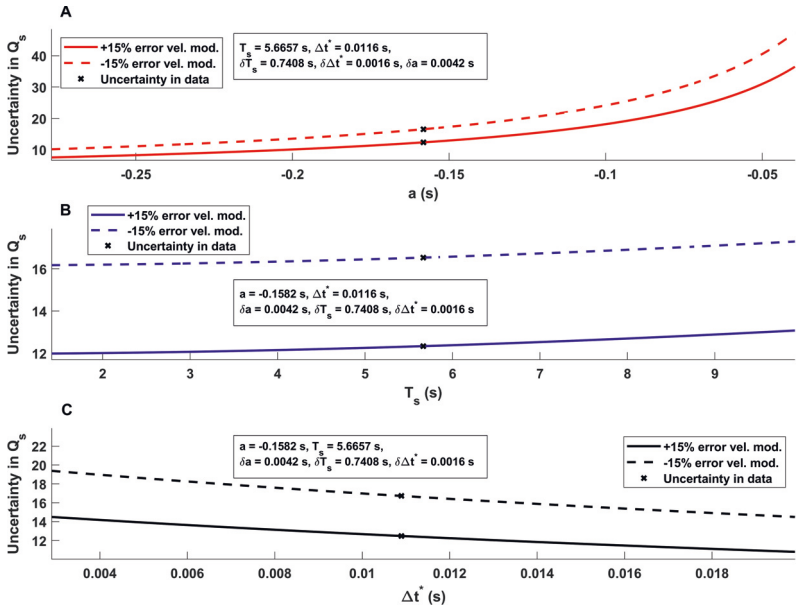

Figure D.10: Total uncertainty obtained from S-waves, E3. (A) Uncertainty in the estimated average quality factor as a function of slope values. (B) Uncertainty in the estimated average quality factor as a function of traveltimes through the sedimentary sequence. (C) Uncertainty in the estimated average quality factor as a function of Δt^* values. For each plot the range is taken as $\pm 75\%$ of the average values obtained from the analysis (indicated by black crosses). The dashed lines are associated with an -15% error in velocity model, whereas the solid line an $+15\%$ error.

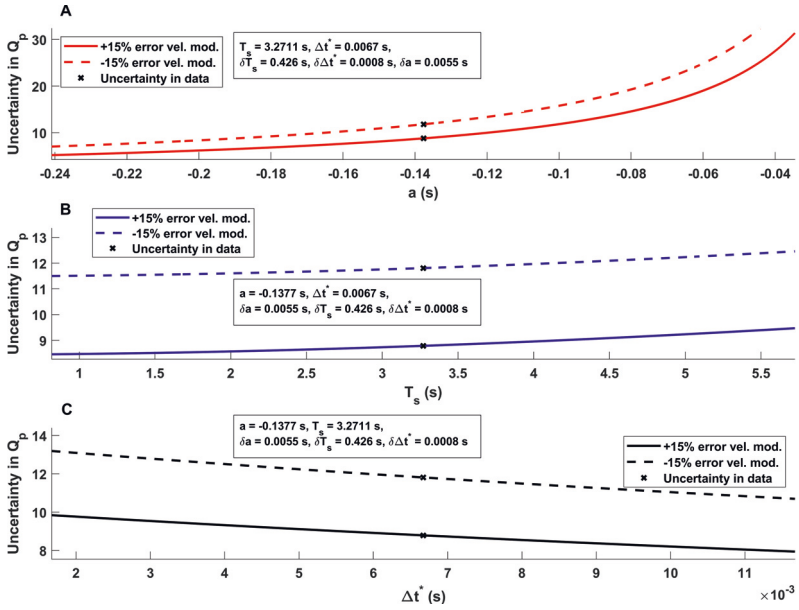

Figure D.11: Same as Figure D.10 but for P-waves.

Appendix E

Abstract: Sensing whales, storms, ships, and earthquakes using an Arctic fiber-optic cable

Martin Landrø[1,2], Léa Bouffaut[1,2,3], Hannah Joy Kriesell[1,2], John Potter[1,2], Robin André Rørstadbotnen[1,2], Kittinat Taweesintananon[1,2,4], Ståle Johansen[2,5], Jan Kristoffer Brenner[2,6], Aksel Haukanes[6], Olaf Schjelderup[2,7], Frode Storvik[2,7],

1 - Department of Electronic Systems, NTNU, 7491 Trondheim, Norway,

2 - Centre for Geophysical Forecasting, NTNU, 7491 Trondheim, Norway,

3 - K. Lisa Yang Center for Conservation Bioacoustics, Cornell Lab of Ornithology, Cornell University, Ithaca, NY, United States,

4 - PTT Exploration and Production Public Company Limited, Bangkok, Thailand,

5 - Department of Geoscience and Petroleum, NTNU, 7491 Trondheim, Norway,

6 - Sikt, 7037 Trondheim, Norway,

7 - Alcatel Submarine Networks Norway AS, 7075 Tiller, Norway,

Published by Nature Scientific Reports 10 November 2022 (Landrø et al. 2022).

Abstract

Our oceans are critical to the health of our planet and its inhabitants. Increasing pressures on our marine environment are triggering an urgent need for continuous and comprehensive monitoring of the oceans and stressors, including anthropogenic activity. Current ocean observational systems are expensive and have limited temporal and spatial coverage. However, there exists a dense network of fibre-optic (FO) telecommunication cables, covering both deep ocean and coastal areas around the globe. FO cables have an untapped potential for advanced acoustic sensing that, with recent technological break-throughs, can now fill many gaps in quantitative ocean monitoring. Here we show for the first time that an advanced distributed acoustic sensing (DAS) interrogator can be used to capture a broad range of acoustic phenomena with unprecedented signal-to-noise ratios and distances. We have detected, tracked, and identified whales, storms, ships, and earthquakes. We live-streamed 250 TB of DAS data from Svalbard to mid-Norway via Uninett's research network over 44 days; a first step towards real-time processing and distribution. Our findings demonstrate the potential for a global Earth-Ocean-Atmosphere-Space DAS monitoring network with multiple applications, e.g., marine mammal forecasting combined with ship tracking, to avoid ship strikes. By including automated processing and fusion with other remote-sensing data (automated identification systems, satellites, etc.), a low-cost ubiquitous real-time monitoring network with vastly improved coverage and resolution is within reach. We anticipate that this is a game-changer in establishing a global observatory for Ocean-Earth sciences that will mitigate current spatial sampling gaps. Our pilot test confirms the viability of this 'cloud-observatory' concept.

Appendix F

Abstract: Eavesdropping at the speed of light: Distributed acoustic sensing of baleen whales in the Arctic.

Léa Bouffaut[1,2,3], Kittinat Taweesintananon[1,2,4], Hannah Joy Kriesell[1,2], Robin André Rørstadbotnen[1,2], John Potter[1,2], Martin Landrø[1,2], Ståle Johansen[2,5], Jan Kristoffer Brenner[2,6], Aksel Haukanes[6], Olaf Schjelderup[2,7], Frode Storvik[2,7],

1 - Department of Electronic Systems, NTNU, 7491 Trondheim, Norway,

2 - Centre for Geophysical Forecasting, NTNU, 7491 Trondheim, Norway,

3 - K. Lisa Yang Center for Conservation Bioacoustics, Cornell Lab of Ornithology, Cornell University, Ithaca, NY, United States,

4 - PTT Exploration and Production Public Company Limited, Bangkok, Thailand,

5 - Department of Geoscience and Petroleum, NTNU, 7491 Trondheim, Norway,

6 - Sikt, 7037 Trondheim, Norway,

7 - Alcatel Submarine Networks Norway AS, 7075 Tiller, Norway,

Published by Frontiers in Marine Science 05 July 2022 (Bouffaut et al. 2022).

Abstract

In a post-industrial whaling world, flagship and charismatic baleen whale species are indicators of the health of our oceans. However, traditional monitoring methods provide spatially and temporally undersampled data to evaluate and mitigate the impacts of increasing climatic and anthropogenic pressures for conservation. Here we present the first case of wildlife monitoring using distributed acoustic sensing (DAS). By repurposing the globally-available infrastructure of sub-sea telecommunication fiber-optic (FO) cables, DAS can (1) record vocalizing baleen whales along a 120 km FO cable with a sensing point every 4 m, from a protected fjord area out to the open ocean; (2) estimate the 3D position of a vocalizing whale for animal density estimation; and (3) exploit whale non-stereotyped vocalizations to provide fully-passive conventional seismic records for subsurface exploration. This first example's success in the Arctic suggests DAS's potential for realtime and low-cost monitoring of whales worldwide with unprecedented coverage and spatial resolution.

Appendix G

Abstract: Distributed acoustic sensing of ocean-bottom seismo-acoustics and distant storms: A case study from Svalbard, Norway.

Kittinat Taweesintananon[1,2,3], Martin Landrø[1,2], John Potter[1,2], Ståle Johansen[2,4], Robin André Rørstadbotnen[1,2], Léa Bouffaut[1,2,4], Hannah Joy Kriesell[1,2], Jan Kristoffer Brenner[2,6], Aksel Haukanes[6], Olaf Schjelderup[2,7], Frode Storvik[2,7],

1 - Department of Electronic Systems, NTNU, 7491 Trondheim, Norway,

2 - Centre for Geophysical Forecasting, NTNU, 7491 Trondheim, Norway,

3 - PTT Exploration and Production Public Company Limited, Bangkok, Thailand,

4 - Department of Geoscience and Petroleum, NTNU, 7491 Trondheim, Norway,

5 - K. Lisa Yang Center for Conservation Bioacoustics, Cornell Lab of Ornithology, Cornell University, Ithaca, NY, United States,

6 - Sikt, 7037 Trondheim, Norway,

7 - Alcatel Submarine Networks Norway AS, 7075 Tiller, Norway,

Published by Geophysics 01 Mai 2023 (Taweesintananon et al. 2023).

Abstract

Distributed acoustic sensing (DAS) leverages an ocean-bottom telecommunication fiber-optic cable into a densely sampled array of strain sensors. We demonstrate DAS applications to passive acoustic monitoring through an experiment on a submarine fiber-optic cable in Longyearbyen, Svalbard, Norway. We find that DAS can measure many types of signals in the frequency range from 0.01 to 20 Hz generated by dynamics in the atmosphere, ocean, and solid earth. These include ocean-bottom loading pressure fluctuation of ocean surface waves generated by storms, winds, and airflow turbulence, shear-wave resonances in low-velocity near-surface sediments, acoustic resonances in the water column, and propagating seismic waves. We find that DAS can record high-quality low-frequency seismo-acoustic waves down to 0.01 Hz, which could be used for subsurface exploration. Using the shear-wave resonances recorded by DAS, we can determine the subsurface structure of near-surface sediments with low velocity. In addition, we can trace ocean swells back to their origins of distant storms as far as 13,000 km away from the cable. Because DAS is capable of seismo-acoustic monitoring with a high spatial resolution of approximately 1 m over a cable of approximately 100 km long and with a broadband sensitivity down to 0.01 Hz on the low end, it can deliver great scientific value to the ocean observation and geophysics community.

Appendix H

Abstract: Developing experimental skills: A hands-on course in acoustical measurement techniques at the Norwegian University of Science and Technology[1].

Hefeng Dong[2], U. Peter Svensson[2], Guillaume Dutilleux[2], Sara R. Martin[2], Tim Cato Netland[2], Robin André Rørstadbotnen[2], Andreas Sørbrøden Talberg[3]

1 - This paper is part of the special issue of Education in Acoustics,

2 - Department of Electronic Systems, NTNU, 7491 Trondheim, Norway,

3 - NDT Global AS, Bergen 5106, Norway.

Published by JASA 10 June 2022 (Dong et al. 2006).

Abstract

The course "Acoustical Measurement Techniques TTT4250," offered by the Acoustics Group at the Department of Electronic Systems, Norwegian University of Science and Technology, is a fourth-year course in the specialization of acoustics in the five-year master program "Electronics Systems Design and Innovation" or MTELSYS, and the two-year international master program "Electronic Systems Design" or MSELSYS. It is one of the four required courses for MTELSYS and one of the two required courses for MSELSYS. It offers a hands-on approach to acoustics. This paper outlines the topics covered in this course and the involvement of several academic staff members, as well as invited industry and research institute guest speakers, as teachers. The assessment of laboratory reports is described, and general lecture topics, including measurement uncertainty and statistics, the introduction of standards, and programming, are also described. All aspects of the course aim to maximize students' experience with a broad range of acoustic measurements and their interest in acoustics.

Bibliography

Abadi, S. H., Tolstoy, M., and Wilcock, W. S. (2017). Estimating the location of baleen whale calls using dual streamers to support mitigation procedures in seismic reflection surveys. *Plos one*, 12(2):e0171115.

Ahonen, H., Stafford, K. M., de Steur, L., Lydersen, C., Wiig, Ø., and Kovacs, K. M. (2017). The underwater soundscape in western Fram Strait: Breeding ground of Spitsbergen's endangered bowhead whales. *Marine pollution bulletin*, 123(1-2):97–112.

Ahonen, H., Stafford, K. M., Lydersen, C., Berchok, C. L., Moore, S. E., and Kovacs, K. M. (2021). Interannual variability in acoustic detection of blue and fin whale calls in the Northeast Atlantic High Arctic between 2008 and 2018. *Endangered Species Research*, 45:209–224.

Ajo-Franklin, J. B., Dou, S., Lindsey, N. J., Monga, I., Tracy, C., Robertson, M., Rodriguez Tribaldos, V., Ulrich, C., Freifeld, B., Daley, T., et al. (2019). Distributed acoustic sensing using dark fiber for near-surface characterization and broadband seismic event detection. *Scientific reports*, 9(1):1–14.

Aki, K. (1980). Attenuation of shear-waves in the lithosphere for frequencies from 0.05 to 25 hz. *Physics of the Earth and Planetary Interiors*, 21(1):50–60.

Aki, K. and Richards, P. G. (2002). *Quantitative seismology*.

Allmark, C., Curtis, A., Galetti, E., and de Ridder, S. (2018). Seismic attenuation from ambient noise across the North Sea Ekofisk permanent array. *Journal of Geophysical Research: Solid Earth*, 123(10):8691–8710.

Amalokwu, K., Best, A. I., Sothcott, J., Chapman, M., Minshull, T., and Li, X.-Y. (2014). Water saturation effects on elastic wave attenuation in porous rocks with aligned fractures. *Geophysical Journal International*, 197(2):943–947.

Amiri, P., Kordrostami, Z., and Ghoddus, H. (2020). Design and simulation of a flat cap mushroom shape microelectromechanical systems piezoelectric transducer with the application as hydrophone. *IET Science, Measurement & Technology*, 14(2):157–164.

Araya, A., Takamori, A., Morii, W., Miyo, K., Ohashi, M., Hayama, K., Uchiyama, T., Miyoki, S., and Saito, Y. (2017). Design and operation of a 1500-m laser strainmeter installed at an underground site in Kamioka, Japan. *Earth, Planets and Space*, 69:1–7.

Arisona, A., Nawawi, M., Khalil, A. E., Nuraddeen, U., Hariri, M., Fathi, M., et al. (2017). Evaluation Study of Boundary and Depth of the Soil Structure for Geotechnical Site Investigation using MASW. *Journal of Geoscience, Engineering, Environment, and Technology*, 2(1):31–38.

Baer, M. and Kradolfer, U. (1987). An automatic phase picker for local and teleseismic events. *Bulletin of the Seismological Society of America*, 77(4):1437–1445.

Barzilai, A., VanZandt, T., and Kenny, T. (1998). Improving the performance of a geophone through capacitive position sensing and feedback. In *ASME International Mechanical Engineering Congress and Exposition*, volume 15861, pages 629–636. American Society of Mechanical Engineers.

Baumgartner, M. F., Bonnell, J., Van Parijs, S. M., Corkeron, P. J., Hotchkin, C., Ball, K., Pelletier, L.-P., Partan, J., Peters, D., Kemp, J., et al. (2019). Persistent near real-time passive acoustic monitoring for baleen whales from a moored buoy: System description and evaluation. *Methods in Ecology and Evolution*, 10(9):1476–1489.

Beckwith, J., Clark, R., and Hodgson, L. (2017). Estimating frequency-dependent attenuation quality factor values from prestack surface seismic data. *Geophysics*, 82(1):O11–O22.

Benioff, H. (1959). Fused-quartz extensometer for secular, tidal, and seismic strains. *Geological Society of America Bulletin*, 70(8):1019–1032.

Bensen, G., Ritzwoller, M., Barmin, M., Levshin, A. L., Lin, F., Moschetti, M., Shapiro, N., and Yang, Y. (2007). Processing seismic ambient noise data to obtain reliable broad-band surface wave dispersion measurements. *Geophysical Journal International*, 169(3):1239–1260.

Benthowave-Instrument-INC. (2023a). BII-7690 Series NDT & Imaging Transducers: High Axial and Lateral Resolutions. Accessed: 2023-04-18.

Benthowave-Instrument-INC. (2023b). BII-7730 Series Broadband Transducer: Low Qm, Single and Dual Beams. Accessed: 2023-04-18.

Bjerrum, L., Løken, T., Heiberg, S., and Foster, R. (1971). A field study of factors responsible for quick clay slides. pages 17–26.

Bouffaut, L., Landrø, M., and Potter, J. R. (2021). Source level and vocalizing depth estimation of two blue whale subspecies in the western Indian Ocean from single sensor observations. *The Journal of the Acoustical Society of America*, 149(6):4422–4436.

Bouffaut, L., Taweesintananon, K., Kriesell, H. J., Rørstadbotnen, R. A., Potter, J. R., Landrø, M., Johansen, S. E., Brenne, J. K., Haukanes, A., Schjelderup, O., et al. (2022). Eavesdropping at the speed of light: distributed acoustic sensing of baleen whales in the arctic. *Frontiers in Marine Science*, page 994.

Boussinesq, J. (1885). *Application des potentiels à l'étude de l'équilibre et du mouvement des solides élastiques: principalement au calcul des déformations et des pressions que produisent, dans ces solides, des efforts quelconques exercés sur une petite partie de leur surface ou de leur intérieur: mémoire suivi de notes étendues sur divers points de physique, mathematique et d'analyse*, volume 4. Gauthier-Villars.

Brincker, R., Lagö, T. L., Andersen, P., and Ventura, C. (2005). Improving the classical geophone sensor element by digital correction. In *Conference Proceedings: IMAC-XXIII: A Conference & Exposition on Structural Dynamics*. Society for Experimental Mechanics.

Bussat, S., Bjerrum, L., Dando, B., Bergfjord, E., Iranpour, K., and Oye, V. (2016). Offshore injection and overburden surveillance using real-time passive seismic. *First Break*, 34(7).

Caiti, A., Akal, T., and Stoll, R. D. (1994). Estimation of shear wave velocity in shallow marine sediments. *IEEE Journal of Oceanic Engineering*, 19(1):58–72.

Carter, A. J., Torres Caceres, V. A., Duffaut, K., and Stovas, A. (2020). Velocity-attenuation model from check-shot drift trends in North Sea well data. *Geophysics*, 85(2):D65–D74.

Cervenỳ, V. (2001). *Seismic ray theory*, volume 110. Cambridge university press Cambridge.

Cheng, F., Chi, B., Lindsey, N. J., Dawe, T. C., and Ajo-Franklin, J. B. (2021). Utilizing distributed acoustic sensing and ocean bottom fiber optic cables for submarine structural characterization. *Scientific reports*, 11(1):1–14.

Clark, C. W., Gagnon, G. J., and Frankel, A. S. (2019). Fin whale singing decreases with increased swimming speed. *Royal Society open science*, 6(6):180525.

Comiso, J. C., Parkinson, C. L., Gersten, R., and Stock, L. (2008). Accelerated decline in the Arctic sea ice cover. *Geophysical research letters*, 35(1).

Cummings, W. C. and Thompson, P. O. (1971). Underwater sounds from the blue whale, Balaenoptera musculus. *The journal of the Acoustical Society of America*, 50(4B):1193–1198.

Dasgupta, R. and Clark, R. A. (1998). Estimation of Q from surface seismic reflection data. *Geophysics*, 63(6):2120–2128.

de Lorenzo, S., Del Pezzo, E., and Bianco, F. (2013). Q_C, Q_β, Q_i and Q_S attenuation parameters in the Umbria–Marche (Italy) region. *Physics of the Earth and Planetary Interiors*, 218:19–30.

Dean, T., Cuny, T., and Hartog, A. H. (2017). The effect of gauge length on axially incident P-waves measured using fibre optic distributed vibration sensing. *Geophysical Prospecting*, 65(1):184–193.

Delarue, J., Todd, S. K., Van Parijs, S. M., and Di Iorio, L. (2009). Geographic variation in Northwest Atlantic fin whale (Balaenoptera physalus) song: Implications for stock structure assessment. *The Journal of the Acoustical Society of America*, 125(3):1774–1782.

Dong, H., Hovem, J. M., and Kristensen, Å. (2006). Estimation of shear wave velocity in shallow marine sediment by multi-component seismic data: a case study. In *Procs. of the 8th European Conference on Underwater Acoustics*, volume 2, pages 497–502.

Dong, H., Svensson, U. P., Dutilleux, G., Martin, S. R., Netland, T. C., Rørstadbotnen, R. A., and Talberg, A. S. (2022). Developing experimental skills: A hands-on course in acoustical measurement techniques at the Norwegian University of Science and Technology. *The Journal of the Acoustical Society of America*, 151(6):3919–3926.

Dosso, S. E., Wilmut, M. J., and Lapinski, A.-L. (2001). An adaptive-hybrid algorithm for geoacoustic inversion. *IEEE Journal of Oceanic Engineering*, 26(3):324–336.

Dou, S., Lindsey, N., Wagner, A. M., Daley, T. M., Freifeld, B., Robertson, M., Peterson, J., Ulrich, C., Martin, E. R., and Ajo-Franklin, J. B. (2017). Distributed acoustic sensing for seismic monitoring of the near surface: A traffic-noise interferometry case study. *Scientific reports*, 7(1):1–12.

Douglas, A. (1992). Q for short-period P-waves: is it frequency dependent? *Geophysical journal international*, 108(1):110–124.

Dumouchel, W. and O'Brien, F. (1989). Integrating a robust option into a multiple regression computing environment. In *Computer science and statistics: Proceedings of the 21st symposium on the interface*, pages 297–302. American Statistical Association Alexandria.

Earle, P. S. and Shearer, P. M. (1994). Characterization of global seismograms using an automatic-picking algorithm. *Bulletin of the Seismological Society of America*, 84(2):366–376.

Eidsvik, J. and Hokstad, K. (2006). Positioning drill-bit and look-ahead events using seismic traveltime data. *Geophysics*, 71(4):F79–F90.

Ewing, W. M., Jardetzky, W. S., and Press, F. (1957). *Elastic waves in layered media*. McGraw-Hill Book Company.

Færseth, R. and Ravnås, R. (1998). Evolution of the Oseberg fault-block in context of the northern North Sea structural framework. *Marine and Petroleum Geology*, 15(5):467–490.

Fayemendy, C., Sadikhov, E., and Schuberth, M. (2021). PRM seismic acquisition real-time monitoring. An example of how digitalization can enables acquisition productivity and efficiency. In *EAGE GeoTech 2021 Third EAGE Workshop on Practical Reservoir Monitoring*, volume 2021, pages 1–5. EAGE Publications BV.

Garcia, H. A., Zhu, C., Schinault, M. E., Kaplan, A. I., Handegard, N. O., Godø, O. R., Ahonen, H., Makris, N. C., Wang, D., Huang, W., et al. (2019). Temporal–spatial, spectral, and source level distributions of fin whale vocalizations in the Norwegian Sea observed with a coherent hydrophone array. *ICES Journal of Marine Science*, 76(1):268–283.

Gasda, S. E., Nilsen, H. M., Dahle, H. K., and Gray, W. G. (2012). Effective models for CO_2 migration in geological systems with varying topography. *Water Resources Research*, 48(10).

Gavrilov, A. N. and Mikhalevsky, P. N. (2006). Low-frequency acoustic propagation loss in the Arctic Ocean: Results of the Arctic climate observations using underwater sound experiment. *The Journal of the Acoustical Society of America*, 119(6):3694–3706.

GEBCO, C. G. (2021). GEBCO 2021 Grid.

Gella, K. (2017). Geotechnical and Geological charaterisation of a quick clay site at Flotten.

Gentili, S. and Michelini, A. (2006). Automatic picking of P and S phases using a neural tree. *Journal of Seismology*, 10(1):39–63.

Gervaise, C., Simard, Y., Aulanier, F., and Roy, N. (2021). Optimizing passive acoustic systems for marine mammal detection and localization: Application to real-time monitoring north Atlantic right whales in Gulf of St. Lawrence. *Applied Acoustics*, 178:107949.

Godin, O. A. and Chapman, D. M. (1999). Shear-speed gradients and ocean seismo-acoustic noise resonances. *The Journal of the Acoustical Society of America*, 106(5):2367–2382.

Google, M. (2022). Overview map Rissa, Norway. Accessed: 2022-02-04.

Greene, C. H. and Pershing, A. J. (2004). Climate and the conservation biology of North Atlantic right whales: the right whale at the wrong time? *Frontiers in Ecology and the Environment*, 2(1):29–34.

Gregersen, O. et al. (1981). The quick clay landslide in Rissa, Norway. *Norwegian Geotechnical Institute Publication*, 135:1–6.

Hagen, J. O., Liestøl, O., Roland, E., and Jørgensen, T. (1993). *Glacier atlas of Svalbard and Jan Mayen*, volume 129. Norsk Polarinstitutt Oslo.

Hamilton, C. D., Lydersen, C., Aars, J., Biuw, M., Boltunov, A. N., Born, E. W., Dietz, R., Folkow, L. P., Glazov, D. M., Haug, T., et al. (2021). Marine mammal hotspots in the Greenland and Barents Seas. *Marine Ecology Progress Series*, 659:3–28.

Harcourt, R., Van der Hoop, J., Kraus, S., and Carroll, E. L. (2019). Future directions in Eubalaena spp.: comparative research to inform conservation. *Frontiers in Marine Science*, 5:530.

Hardin, B. O. and Blandford, G. E. (1989). Elasticity of particulate materials. *Journal of Geotechnical Engineering*, 115(6):788–805.

Hartog, A. H. (2017). *An Introduction to Distributed Optical Fibre Sensors*. CRC Press, 1 edition.

Hauge, P. S. (1981). Measurements of attenuation from vertical seismic profiles. *Geophysics*, 46(11):1548–1558.

Hauksson, E. and Shearer, P. M. (2006). Attenuation models (Q_P and Q_S) in three dimensions of the southern California crust: Inferred fluid saturation at seismogenic depths. *Journal of Geophysical Research: Solid Earth*, 111(B5).

Havshov, J. and Bungum, H. (1987). Source parameters for earthquakes in the northern North Sea. *Norsk Geologisk Tidsskrift*, 67:51–58.

Havskov, J. and Alguacil, G. (2010). *Instrumentation in earthquake seismology*, volume 358. Springer.

Havskov, J. and Ottemoller, L. (2010). *Routine data processing in earthquake seismology: With sample data, exercises and software*. Springer Science & Business Media.

Hearn, S., Strong, S., and Kinmont, A. (2019). Observations of geophone spurious resonance. *ASEG Extended Abstracts*, 2019(1):1–5.

Hendricks, B., Wray, J. L., Keen, E. M., Alidina, H. M., Gulliver, T. A., and Picard, C. R. (2019). Automated localization of whales in coastal fjords. *The Journal of the Acoustical Society of America*, 146(6):4672–4686.

High Tech, I. (2023). HTI-97-DA. Accessed: 2023-01-29.

Höschle, C., Cubaynes, H. C., Clarke, P. J., Humphries, G., and Borowicz, A. (2021). The potential of satellite imagery for surveying whales. *Sensors*, 21(3):963.

Hovem, J. M. (2012). *Marine acoustics: The physics of sound in underwater environments*. Peninsula publishing Los Altos, CA.

Hwang, Y. K., Ritsema, J., and Goes, S. (2009). Spatial variations of P wave attenuation in the mantle beneath North America. *Journal of Geophysical Research: Solid Earth*, 114(B6).

IPCC (2022). Summary for Policymakers. In *Climate Change 2022: Mitigation of Climate Change*. (Cambridge University Press, Cambridge, UK and New York, NY, USA.). Intergovernmental Panel on Climate Contribution: Contribution from working Group III to the Sixth Assessment Report.

Jaskólski, M. W. (2021). For human activity in Arctic coastal environments–a review of selected interactions and problems. *Miscellanea Geographica*, 25(2):127–143.

Jerkins, A. E., Shiddiqi, H. A., Kværna, T., Gibbons, S. J., Schweitzer, J., Ottemöller, L., and Bungum, H. (2020). The 30 June 2017 North Sea earthquake: location, characteristics, and context. *Bulletin of the Seismological Society of America*, 110(2):937–952.

Jousset, P., Reinsch, T., Ryberg, T., Blanck, H., Clarke, A., Aghayev, R., Hersir, G. P., Henninges, J., Weber, M., and Krawczyk, C. M. (2018). Dynamic strain determination using fibre-optic cables allows imaging of seismological and structural features. *Nature communications*, 9(1):1–11.

Kähler, S. and Meissner, R. (1983). Radiation and receiver pattern of shear and compressional waves as a function of Poisson's ratio. *Geophysical Prospecting*, 31(3):421–435.

Kalkan, E. (2016). An automatic P-phase arrival-time picker. *Bulletin of the Seismological Society of America*, 106(3):971–986.

Kang, I. B. and McMechan, G. A. (1994). Separation of intrinsic and scattering Q based on frequency-dependent amplitude ratios of transmitted waves. *Journal of Geophysical Research: Solid Earth*, 99(B12):23875–23885.

Keers, H., Dahlen, F., and Nolet, G. (1997). Chaotic ray behaviour in regional seismology. *Geophysical Journal International*, 131(2):361–380.

Klinck, H., Nieukirk, S. L., Mellinger, D. K., Klinck, K., Matsumoto, H., and Dziak, R. P. (2012). Seasonal presence of cetaceans and ambient noise levels in polar waters of the North Atlantic. *The Journal of the Acoustical Society of America*, 132(3):EL176–EL181.

Landrø, M. and Amundsen, L. (2018). *Introduction to exploration geophysics with recent advances*. Bivrost.

Landrø, M., Bouffaut, L., Kriesell, H. J., Potter, J. R., Rørstadbotnen, R. A., Taweesintananon, K., Johansen, S. E., Brenne, J. K., Haukanes, A., Schjelderup, O., et al. (2022). Sensing whales, storms, ships and earthquakes using an Arctic fibre optic cable. *Scientific Reports*, 12(1):1–10.

Landrø, M. (2002). Uncertainties in quantitative time-lapse seismic analysis. *Geophysical prospecting*, 50(5):527–538.

Langhammer, J., Eriksrud, M., and Nakstad, H. (2010). Performance characteristics of 4C fiber optic ocean bottom cables for permanent reservoir monitoring. In *SEG Technical Program Expanded Abstracts 2010*, pages 66–70. Society of Exploration Geophysicists.

Lavery, T. J., Roudnew, B., Seymour, J., Mitchell, J. G., Smetacek, V., and Nicol, S. (2014). Whales sustain fisheries: blue whales stimulate primary production in the Southern Ocean. *Marine Mammal Science*, 30(3):888–904.

L'Heureux, J.-S., Long, M., and Lunne, T. (2015). Korrelasjoner mellom skjærbølgehastighet og geotekniske parametere i Norsk leirer, SP8-GEODIP.

Li, C., Dosso, S. E., Dong, H., Yu, D., and Liu, L. (2012). Bayesian inversion of multimode interface-wave dispersion from ambient noise. *IEEE Journal of Oceanic Engineering*, 37(3):407–416.

Li, Y., Karrenbach, M., and Ajo-Franklin, J. (2022). *Distributed acoustic sensing in geophysics: Methods and applications*, volume 268. John Wiley & Sons.

Li, Z. and Zhan, Z. (2018). Pushing the limit of earthquake detection with distributed acoustic sensing and template matching: A case study at the Brady geothermal field. *Geophysical Journal International*, 215(3):1583–1593.

Lin, S., Wang, Z., Xiong, J., Fu, Y., Jiang, J., Wu, Y., Chen, Y., Lu, C., and Rao, Y. (2019). Rayleigh fading suppression in one-dimensional optical scatters. *IEEE Access*, 7:17125–17132.

Lindsey, N. J., Martin, E. R., Dreger, D. S., Freifeld, B., Cole, S., James, S. R., Biondi, B. L., and Ajo-Franklin, J. B. (2017). Fiber-optic network observations of earthquake wavefields. *Geophysical Research Letters*, 44(23):11–792.

Lindsey, N. J., Rademacher, H., and Ajo-Franklin, J. B. (2020). On the broadband instrument response of fiber-optic das arrays. *Journal of Geophysical Research: Solid Earth*, 125(2):e2019JB018145.

Lior, I., Rivet, D., Ampuero, J.-P., Sladen, A., Barrientos, S., Sánchez-Olavarría, R., Villarroel Opazo, G. A., and Bustamante Prado, J. A. (2023). Magnitude estimation and ground motion prediction to harness fiber optic distributed acoustic sensing for earthquake early warning. *Scientific Reports*, 13(1):424.

Liu, N., Zhang, B., Gao, J., Gao, Z., and Li, S. (2018). Seismic attenuation estimation using the modified log spectral ratio method. *Journal of Applied Geophysics*, 159:386–394.

Long, M., Trafford, A., McGrath, T., and O'Connor, P. (2020). Multichannel analysis of surface waves (MASW) for offshore geotechnical investigations. *Engineering Geology*, 272:105649.

Lundström, K., Larsson, R., and Dahlin, T. (2009). Mapping of quick clay formations using geotechnical and geophysical methods. *Landslides*, 6(1):1–15.

Lydersen, C., Vacquié-Garcia, J., Heide-Jørgensen, M. P., Øien, N., Guinet, C., and Kovacs, K. M. (2020). Autumn movements of fin whales (Balaenoptera physalus) from Svalbard, Norway, revealed by satellite tracking. *Scientific reports*, 10(1):1–13.

L'Heureux, J.-S. and Long, M. (2017). Relationship between shear-wave velocity and geotechnical parameters for Norwegian clays. *Journal of geotechnical and Geoenvironmental engineering*, 143(6):04017013.

Malme, T. N., Landrø, M., and Mittet, R. (2005). Overburden distortions—implications for seismic avo analysis and time-lapse seismic. *Journal of Geophysics and Engineering*, 2(2):81–89.

Maraschini, M. and Foti, S. (2010). A Monte Carlo multimodal inversion of surface waves. *Geophysical Journal International*, 182(3):1557–1566.

Martin, E., Lindsey, N., Dou, S., Ajo-Franklin, J., Daley, T., Freifeld, B., Robertson, M., Ulrich, C., Wagner, A., and Bjella, K. (2016). Interferometry of a roadside DAS array in Fairbanks, AK. In *SEG Technical Program Expanded Abstracts 2016*, pages 2725–2729. Society of Exploration Geophysicists.

Martin, E. R. and Biondi, B. L. (2017). Ambient noise interferometry across two-dimensional DAS arrays. In *SEG Technical Program Expanded Abstracts 2017*, pages 2642–2646. Society of Exploration Geophysicists.

Matsumoto, H., Araki, E., Kimura, T., Fujie, G., Shiraishi, K., Tonegawa, T., Obana, K., Arai, R., Kaiho, Y., Nakamura, Y., et al. (2021). Detection of hydroacoustic signals on a fiber-optic submarine cable. *Scientific reports*, 11(1):1–12.

Maturilli, M., Herber, A., and König-Langlo, G. (2013). Climatology and time series of surface meteorology in Ny-Ålesund, Svalbard. *Earth System Science Data*, 5(1):155–163.

Mayeda, K., Malagnini, L., and Walter, W. R. (2007). A new spectral ratio method using narrow band coda envelopes: Evidence for non-self-similarity in the Hector Mine sequence. *Geophysical Research Letters*, 34(11).

McDonald, M. A. and Fox, C. G. (1999). Passive acoustic methods applied to fin whale population density estimation. *The Journal of the Acoustical Society of America*, 105(5):2643–2651.

McDonald, M. A., Hildebrand, J. A., and Webb, S. C. (1995). Blue and fin whales observed on a seafloor array in the Northeast Pacific. *J. Acoust. Soc. Am.*, 98(2):712–721.

McDonald, M. A., Mesnick, S. L., and Hildebrand, J. A. (2006). Biogeographic characterization of blue whale song worldwide: using song to identify populations. *Journal of cetacean research and management*, 8(1):55–65.

Mellinger, D. K. and Clark, C. W. (2000). Recognizing transient low-frequency whale sounds by spectrogram correlation. *The Journal of the Acoustical Society of America*, 107(6):3518–3529.

Mestayer, J., Cox, B., Wills, P., Kiyashchenko, D., Lopez, J., Costello, M., Bourne, S., Ugueto, G., Lupton, R., Solano, G., et al. (2011). Field trials of distributed acoustic sensing for geophysical monitoring. In *SEG technical program expanded abstracts 2011*, pages 4253–4257. Society of Exploration Geophysicists.

Mitchell, B. J. (1995). Anelastic structure and evolution of the continental crust and upper mantle from seismic surface wave attenuation. *Reviews of Geophysics*, 33(4):441–462.

Mitchell, B. J., Cong, L., and Ekström, G. (2008). A continent-wide map of 1-Hz Lg coda Q variation across Eurasia and its relation to lithospheric evolution. *Journal of Geophysical Research: Solid Earth*, 113(B4).

Moore, S. E., Haug, T., Víkingsson, G. A., and Stenson, G. B. (2019). Baleen whale ecology in Arctic and subarctic seas in an era of rapid habitat alteration. *Progress in Oceanography*, 176:102118.

NGI (2011). The Quick Clay Landslide at Rissa - 1978 (english commentary). Accessed: 2022-01-24.

Nishimura, T., Emoto, K., Nakahara, H., Miura, S., Yamamoto, M., Sugimura, S., Ishikawa, A., and Kimura, T. (2021). Source location of volcanic earthquakes and subsurface characterization using fiber-optic cable and distributed acoustic sensing system. *Scientific reports*, 11(1):1–12.

Nordli, Ø., Przybylak, R., Ogilvie, A. E., and Isaksen, K. (2014). Long-term temperature trends and variability on Spitsbergen: the extended Svalbard Airport temperature series, 1898–2012. *Polar research*, 33(1):21349.

NORSAR (1971). NORSAR seismic bulletins.

Nowacek, D. P., Christiansen, F., Bejder, L., Goldbogen, J. A., and Friedlaender, A. S. (2016). Studying cetacean behaviour: new technological approaches and conservation applications. *Animal behaviour*, 120:235–244.

Ocean-Acoustic-Library (2022). Acoustic Toolbox. Accessed: 2023-02-12.

Offshore-Energy (2019). CGG to process Johan Sverdrup PRM seismic data. Accessed: 2023-04-17.

Olafsdottir, E. A., Bessason, B., and Erlingsson, S. (2018). Combination of dispersion curves from MASW measurements. *Soil Dynamics and Earthquake Engineering*, 113:473–487.

Oleson, E. M., Širović, A., Bayless, A. R., and Hildebrand, J. A. (2014). Synchronous seasonal change in fin whale song in the North Pacific. *PloS one*, 9(12):e115678.

Papp, B., Donno, D., Martin, J. E., and Hartog, A. H. (2017). A study of the geophysical response of distributed fibre optic acoustic sensors through laboratory-scale experiments. *Geophysical Prospecting*, 65(5):1186–1204.

Reid, F. J., Nguyen, P. H., MacBeth, C., and Clark, R. A. (2001). Q estimates from North sea VSPs. In *SEG Technical Program Expanded Abstracts 2001*, pages 440–443. Society of Exploration Geophysicists.

Renalier, F., Bièvre, G., Jongmans, D., Campillo, M., and Bard, P. (2010). Clayey landslide investigations using active and passive VS measurements. *Advances in near-surface seismology and ground-penetrating radar, Geophys. dev. Ser*, 15:397–414.

Richard, G., Mathias, D., Collin, J., Chauvaud, L., and Bonnel, J. (2023). Three-dimensional anthropogenic underwater noise modeling in an Arctic fjord for acoustic risk assessment. *Marine Pollution Bulletin*, 187:114487.

Rivet, D., de Cacqueray, B., Sladen, A., Roques, A., and Calbris, G. (2021). Preliminary assessment of ship detection and trajectory evaluation using distributed acoustic sensing on an optical fiber telecom cable. *The Journal of the Acoustical Society of America*, 149(4):2615–2627.

Rodríguez Tribaldos, V. and Ajo-Franklin, J. B. (2021). Aquifer monitoring using ambient seismic noise recorded with distributed acoustic sensing (DAS) deployed on dark fiber. *Journal of Geophysical Research: Solid Earth*, 126(4):e2020JB021004.

Romagosa, M., Nieukirk, S., Cascão, I., Marques, T. A., Dziak, R., Royer, J.-Y., O'Brien, J., Mellinger, D. K., Pereira, A., Ugalde, A., et al. (2022). Fin whale singalong: evidence of song conformity. *bioRxiv*, pages 2022–10.

Roman, J., Estes, J. A., Morissette, L., Smith, C., Costa, D., McCarthy, J., Nation, J., Nicol, S., Pershing, A., and Smetacek, V. (2014). Whales as marine ecosystem engineers. *Frontiers in Ecology and the Environment*, 12(7):377–385.

Romanowicz, B. and Mitchell, B. (2007). Deep Earth structure Q of the earth from crust to core. *Treatise on geophysics*, pages 731–774.

Rørstadbotnen, R. A., Eidsvik, J., Bouffaut, L., Landrø, M., Potter, J. R., Taweesintananon, K., Johansen, S. E., Storvik, F., Jacobsen, J., Schjelderup, O., Wienecke, S., Johansen, T. A., Ruud, B. O., Wuestefeld, A., and Oye, V. (2023). Simultaneous tracking of multiple whales using two fiber-optic cables in the arctic. *Frontiers in Marine Science*.

Rørstadbotnen, R. A. and Landrø, M. (2023). Average Q_P and Q_S estimation in marine sediments using a dense receiver array. *Geophysics*, 88(2):L11–L25.

Ryan, I. and Riekeles, H. (2021). Årsaken til kvikkleireskredet i Gjerdrum 2020.

Rørstadbotnen, R. A., Landrø, M., Taweesintananon, K., Bouffaut, L., Potter, J. R., Johansen, S. E., Kriesell, H. J., Brenne, J. K., Haukanes, A., Schjelderup, O., and Storvik, F. (2022). Analysis of a Local Earthquake in the Arctic Using a 120 KM Long Fibre-Optic Cable. In *83rd EAGE Annual Conference & Exhibition*, volume 2022 of *Conference Proceedings*, pages 1–5. European Association of Geoscientists & Engineers.

Salas-Romero, S., Malehmir, A., Snowball, I., Lougheed, B. C., and Hellqvist, M. (2016). Identifying landslide preconditions in Swedish quick clays—insights from integration of surface geophysical, core sample-and downhole property measurements. *Landslides*, 13(5):905–923.

Sams, M., Neep, J., Worthington, M., and King, M. (1997). The measurement of velocity dispersion and frequency-dependent intrinsic attenuation in sedimentary rocks. *Geophysics*, 62(5):1456–1464.

Särkkä, S. (2013). *Bayesian filtering and smoothing*. Cambridge university press.

Sauvin, G., Lecomte, I., Bazin, S., Hansen, L., Vanneste, M., and L'Heureux, J.-S. (2014). On the integrated use of geophysics for quick-clay mapping: The Hvittingfoss case study, Norway. *Journal of Applied Geophysics*, 106:1–13.

Schimmel, M. and Paulssen, H. (1997). Noise reduction and detection of weak, coherent signals through phase-weighted stacks. *Geophysical Journal International*, 130(2):497–505.

Schonewille, M., Vigner, A., and Ryder, A. (2008). Swell-noise attenuation using an iterative FX prediction filtering approach. In *SEG Technical Program Expanded Abstracts 2008*, pages 2647–2651. Society of Exploration Geophysicists.

Schuler, T. V., Kohler, J., Elagina, N., Hagen, J. O. M., Hodson, A. J., Jania, J. A., Kääb, A. M., Luks, B., Małecki, J., Moholdt, G., et al. (2020). Reconciling Svalbard glacier mass balance. *Frontiers in Earth Science*, 8:156.

Seis Tech, I. (2023). Low Frequency Geophone 2.5 Hz. Accessed: 2023-01-30.

seklima.met.no (2022). Seklima - Observations and weather statistics. Accessed: 2022-03-24.

Sheriff, R. E. and Geldart, L. P. (1995). *Exploration seismology*. Cambridge university press.

Shiu, Y., Palmer, K., Roch, M. A., Fleishman, E., Liu, X., Nosal, E.-M., Helble, T., Cholewiak, D., Gillespie, D., and Klinck, H. (2020). Deep neural networks for automated detection of marine mammal species. *Scientific reports*, 10(1):607.

Shragge, J., Yang, J., Issa, N., Roelens, M., Dentith, M., and Schediwy, S. (2021). Low-frequency ambient distributed acoustic sensing (DAS): case study from Perth, Australia. *Geophysical Journal International*, 226(1):564–581.

Širović, A., Williams, L. N., Kerosky, S. M., Wiggins, S. M., and Hildebrand, J. A. (2013). Temporal separation of two fin whale call types across the eastern North Pacific. *Marine biology*, 160(1):47–57.

Sketsiou, P., De Siena, L., Gabrielli, S., and Napolitano, F. (2021). 3-D attenuation image of fluid storage and tectonic interactions across the Pollino fault network. *Geophysical Journal International*, 226(1):536–547.

Solberg, I.-L., Dalsegg, E., and L'Heureux, J.-S. (2012). Resistivitetsmålinger for løsmassekartlegging ved Rein kirke i Rissa, Sør-Trøndelag. Data og tolkninger.

Solomon, S. C. (1973). Shear wave attenuation and melting beneath the Mid-Atlantic Ridge. *Journal of Geophysical Research*, 78(26):6044–6059.

Song, Z., Zeng, X., and Thurber, C. H. (2021). Surface-wave dispersion spectrum inversion method applied to Love and Rayleigh waves recorded by distributed acoustic sensing. *Geophysics*, 86(1):EN1–EN12.

Spica, Z. J., Nishida, K., Akuhara, T., Pétrélis, F., Shinohara, M., and Yamada, T. (2020). Marine sediment characterized by ocean-bottom fiber-optic seismology. *Geophysical Research Letters*, 47(16):e2020GL088360.

Stainsby, S. and Worthington, M. (1985). Q estimation from vertical seismic profile data and anomalous variations in the central North Sea. *Geophysics*, 50(4):615–626.

Stein, S. and Wysession, M. (2003). *An introduction to seismology, earthquakes, and earth structure*. John Wiley & Sons.

Stimpert, A. K., DeRuiter, S. L., Falcone, E. A., Joseph, J., Douglas, A. B., Moretti, D. J., Friedlaender, A. S., Calambokidis, J., Gailey, G., Tyack, P. L., et al. (2015). Sound production and associated behavior of tagged fin whales (Balaenoptera physalus) in the Southern California Bight. *Animal Biotelemetry*, 3(1):1–12.

Storrie, L., Lydersen, C., Andersen, M., Wynn, R. B., and Kovacs, K. M. (2018). Determining the species assemblage and habitat use of cetaceans in the Svalbard Archipelago, based on observations from 2002 to 2014. *Polar Research*, 37(1):1463065.

Stroeve, J., Holland, M. M., Meier, W., Scambos, T., and Serreze, M. (2007). Arctic sea ice decline: Faster than forecast. *Geophysical research letters*, 34(9).

Taweesintananon, K., Landrø, M., Brenne, J. K., and Haukanes, A. (2021). Distributed acoustic sensing for near-surface imaging using submarine telecommunication cable: A case study in the Trondheimsfjord, Norway. *Geophysics*, 86(5):B303–B320.

Taweesintananon, K., Landrø, M., Potter, J. R., Johansen, S. E., Rørstadbotnen, R. A., Bouffaut, L., Kriesell, H. J., Brenne, J. K., Haukanes, A., Schjelderup, O., et al. (2023). Distributed acoustic sensing of ocean-bottom seismo-acoustics and distant storms: A case study from Svalbard, Norway. *Geophysics*, 88(3):1–65.

Teng, T.-L. (1968). Attenuation of body waves and the Q structure of the mantle. *Journal of Geophysical Research*, 73(6):2195–2208.

Thode, A. M., D'Spain, G., and Kuperman, W. (2000). Matched-field processing, geoacoustic inversion, and source signature recovery of blue whale vocalizations. *The Journal of the Acoustical Society of America*, 107(3):1286–1300.

Thomas, P. O., Reeves, R. R., and Brownell Jr, R. L. (2016). Status of the world's baleen whales. *Marine Mammal Science*, 32(2):682–734.

Thompson, M., Amundsen, L., Karstad, P. I., Langhammer, J., Nakstad, H., and Eriksrud, M. (2006). Field trial of fibre-optic multi-component sensor system for application in ocean bottom seismic. In *2006 SEG Annual Meeting*. OnePetro.

Thompson, M. and Andersen, M. (2008). Focused seismic monitoring. *The Leading Edge*, 27(12):1626–1631.

Thompson, P. O., Findley, L. T., and Vidal, O. (1992). 20-Hz pulses and other vocalizations of fin whales, Balaenoptera physalus, in the Gulf of California, Mexico. *The Journal of the Acoustical Society of America*, 92(6):3051–3057.

Thomson, C. and Chapman, C. (1985). An introduction to Maslov's asymptotic method. *Geophysical Journal International*, 83(1):143–168.

Timmermans, M. L. and Labe, Z. (2022). Sea Surface Temperature. Accessed: 2022-01-13.

Tonn, R. (1991). The Determination of the seismic quality factor Q from VSP data: a comparison of different computational methods. *Geophysical Prospecting*, 39(1):1–27.

Townhill, B. L., Reppas-Chrysovitsinos, E., Sühring, R., Halsall, C. J., Mengo, E., Sanders, T., Dähnke, K., Crabeck, O., Kaiser, J., and Birchenough, S. N. (2021). Pollution in the Arctic Ocean: An overview of multiple pressures and implications for ecosystem services. *Ambio*, pages 1–13.

USGS (2022). Search earthquake catalog. Accessed: 2022-06-22.

Van Gestel, J.-P., Kommedal, J. H., Barkved, O. I., Mundal, I., Bakke, R., and Best, K. D. (2008). Continuous seismic surveillance of Valhall Field. *The Leading Edge*, 27(12):1616–1621.

van Weelden, C., Towers, J. R., and Bosker, T. (2021). Climate Change Ecology. *Climate Change Ecology*, 1,1009.

Verschuur, D. J. (2013). *Seismic multiple removal techniques: past, present and future*. EAGE publications Houten, The Netherlands.

Waagaard, O. H., Rønnekleiv, E., Haukanes, A., Stabo-Eeg, F., Thingbø, D., Forbord, S., Aasen, S. E., and Brenne, J. K. (2021). Real-time low noise distributed acoustic sensing in 171 km low loss fiber. *OSA Continuum*, 4(2):688–701.

Watkins, W. A., Tyack, P., Moore, K. E., and Bird, J. E. (1987). The 20-Hz signals of finback whales (Balaenoptera physalus). *The Journal of the Acoustical Society of America*, 82(6):1901–1912.

White, R. (1992). The accuracy of estimating Q from seismic data. *Geophysics*, 57(11):1508–1511.

Wilcock, W. S. (2012). Tracking fin whales in the northeast Pacific Ocean with a seafloor seismic network. *The Journal of the Acoustical Society of America*, 132(4):2408–2419.

Wilcock, W. S., Abadi, S., and Lipovsky, B. P. (2023). Distributed acoustic sensing recordings of low-frequency whale calls and ship noise offshore Central Oregon. *JASA Express Letters*, 3(2):026002.

Williams, E. F., Fernández-Ruiz, M. R., Magalhaes, R., Vanthillo, R., Zhan, Z., González-Herráez, M., and Martins, H. F. (2019). Distributed sensing of microseisms and teleseisms with submarine dark fibers. *Nature communications*, 10(1):1–11.

Williams, E. F., Zhan, Z., Martins, H. F., Fernández-Ruiz, M. R., Martín-López, S., González-Herráez, M., and Callies, J. (2022). Surface gravity wave interferometry and ocean current monitoring with ocean-bottom DAS. *Journal of Geophysical Research: Oceans*, 127(5):e2021JC018375.

Wu, G., Dong, H., Ke, G., and Song, J. (2020). Shear-Wave Tomography Using Ocean Ambient Noise with Interference. *Remote Sensing*, 12(18):2969.

Wuestefeld, A., Greve, S. M., Näsholm, S. P., and Oye, V. (2018). Benchmarking earthquake location algorithms: A synthetic comparison. *Geophysics*, 83(4):KS35–KS47.

Xia, J., Miller, R. D., Park, C. B., and Tian, G. (2003). Inversion of high frequency surface waves with fundamental and higher modes. *Journal of Applied Geophysics*, 52(1):45–57.

Yigit, C. O., Gikas, V., Alcay, S., and Ceylan, A. (2014). Performance evaluation of short to long term GPS, GLONASS and GPS/GLONASS post-processed PPP. *Survey Review*, 46(336):155–166.

Yuan, S., Lellouch, A., Clapp, R. G., and Biondi, B. (2020). Near-surface characterization using a roadside distributed acoustic sensing array. *The Leading Edge*, 39(9):646–653.

Zeng, X., Lancelle, C., Thurber, C., Fratta, D., Wang, H., Lord, N., Chalari, A., and Clarke, A. (2017). Properties of noise cross-correlation functions obtained from a distributed acoustic sensing array at Garner Valley, California. *Bulletin of the Seismological Society of America*, 107(2):603–610.

Zollo, A. and de Lorenzo, S. (2001). Source parameters and three-dimensional attenuation structure from the inversion of microearthquake pulse width data: Method and synthetic tests. *Journal of Geophysical Research: Solid Earth*, 106(B8):16287–16306.

ISBN 978-82-326-7256-1 (printed ver.)
ISBN 978-82-326-7255-4 (electronic ver.)
ISSN 1503-8181 (printed ver.)
ISSN 2703-8084 (online ver.)

NTNU
Norwegian University of
Science and Technology